THE UNIVERSITY OF
WARWICK

AUTHOR: **Gábor Szepesi** DEGREE: **Ph.D.**

TITLE: **Modelling of Turbulent Particle Transport in Finite-Beta and Multiple Ion Species Plasma in Tokamaks**

DATE OF DEPOSIT: .....

I agree that this thesis shall be available in accordance with the regulations governing the University of Warwick theses.

I agree that the summary of this thesis may be submitted for publication.

I **agree** that the thesis may be photocopied (single copies for study purposes only).

Theses with no restriction on photocopying will also be made available to the British Library for microfilming. The British Library may supply copies to individuals or libraries. subject to a statement from them that the copy is supplied for non-publishing purposes. All copies supplied by the British Library will carry the following statement:

> "Attention is drawn to the fact that the copyright of this thesis rests with its author. This copy of the thesis has been supplied on the condition that anyone who consults it is understood to recognise that its copyright rests with its author and that no quotation from the thesis and no information derived from it may be published without the author's written consent."

AUTHOR'S SIGNATURE: .....

USER'S DECLARATION

1. I undertake not to quote or make use of any information from this thesis without making acknowledgement to the author.
2. I further undertake to allow no-one else to use this thesis while it is in my care.

DATE SIGNATURE ADDRESS

.....

.....

.....

.....

.....

THE UNIVERSITY OF WARWICK

Library Declaration and Deposit Agreement

1. STUDENT DETAILS

Please complete the following:

Full name: ……

University ID number: ……

2. THESIS DEPOSIT

2.1 I understand that under my registration at the University, I am required to deposit my thesis with the University in BOTH hard copy and in digital format. The digital version should normally be saved as a single pdf file.

2.2 The hard copy will be housed in the University Library. The digital version will be deposited in the University's Institutional Repository (WRAP). Unless otherwise indicated (see 2.3 below) this will be made openly accessible on the Internet and will be supplied to the British Library to be made available online via its Electronic Theses Online Service (EThOS) service.
[At present, theses submitted for a Master's degree by Research (MA, MSc, LLM, MS or MMedSci) are not being deposited in WRAP and not being made available via EthOS. This may change in future.]

2.3 In exceptional circumstances, the Chair of the Board of Graduate Studies may grant permission for an embargo to be placed on public access to the hard copy thesis for a limited period. It is also possible to apply separately for an embargo on the digital version. (Further information is available in the *Guide to Examinations for Higher Degrees by Research*.)

2.4 *If you are depositing a thesis for a Master's degree by Research, please complete section (a) below. For all other research degrees, please complete both sections (a) and (b) below:*

(a) Hard Copy

I hereby deposit a hard copy of my thesis in the University Library to be made publicly available to readers (please delete as appropriate) EITHER immediately OR after an embargo period of ……..... months/years as agreed by the Chair of the Board of Graduate Studies.

I agree that my thesis may be photocopied. YES / NO (*Please delete as appropriate*)

(b) Digital Copy

I hereby deposit a digital copy of my thesis to be held in WRAP and made available via EThOS.

Please choose one of the following options:

EITHER My thesis can be made publicly available online. YES / NO (*Please delete as appropriate*)

OR My thesis can be made publicly available only after…..[date] (Please give date)
YES / NO (*Please delete as appropriate*)

OR My full thesis cannot be made publicly available online but I am submitting a separately identified additional, abridged version that can be made available online.
YES / NO (*Please delete as appropriate*)

OR My thesis cannot be made publicly available online. YES / NO (*Please delete as appropriate*)

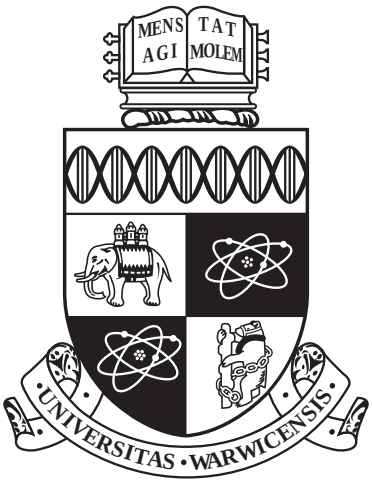

Modelling of Turbulent Particle Transport in Finite-Beta and Multiple Ion Species Plasma in Tokamaks

by

Gábor Szepesi

Thesis

Submitted to the University of Warwick

for the degree of

Doctor of Philosophy

Department of Physics

March 2013

THE UNIVERSITY OF WARWICK

Contents

Acknowledgments

I would like to say thanks to all the people who taught me during my life. Parents and friends, teachers, coaches, colleagues and lecturers. Without them I would not have been able to start my postgraduate studies and arrive to this point. Knowledge is of great value, providing it is kindness, and I am deeply grateful to them.

I would like to express my special gratitude to my supervisors, Arthur Peeters and Michele Romanelli. Although Arthur left the university before I could finish my PhD, he provided excellent guidance during the first year and a half of my course. He helped me with understanding the basic idea of gyrokinetic theory and the structure of the gyrokinetic code GKW, of which he is the principal developer. His physical sense and intuitive way of thinking has been, and will remain, an example to follow during my scientific career.

Michele took over the role of my supervisor for the remaining two and a half years while I stayed at Culham. During our many discussions he provided me with crystal clear explanations and enlightening analogies of various physical topics, most notably of transport theory. His sense of grasping the main point of a problem is exemplary, it improved all my writings and I hope I have been able to learn some of his skills. His guidance, optimism and encouragement was especially helpful when I felt that my thesis was not going anywhere.

A big thanks goes to Fulvio Militello who sparing no time and effort, explained many subtleties of fluid theory to me. His theoretical knowledge and precision stands as yet another major example that I will remember and try to follow.

The gyrokinetic code I used for my work has been developed by the GKW group, Yann Camenen, Francis Casson, William Hornsby and Andrew Snodin under

the guidance of Arthur Peeters. They explained various parts of the code to me and provided plenty of support with running it. Many thanks to all of them.

My thanks goes to the FTU and MAST teams, as well, who provided the experimental data for my simulations.

I would also like to mention my good friends and fellow PhD students, Kornél Jahn and Dávid Wágner, with whom we discussed several issues that arose during our studies.

I would like to express my respect and gratitude to Natia Sopromadze for her encouragement and constant emotional support during my course, and for her unique ability of making me smile even during my desperate periods.

My PhD course at the University of Warwick has been funded by the Engineering and Physical Sciences Research Council.

This thesis was typeset with LaTeX 2$_\varepsilon$[1] by the author.

[1] LaTeX 2$_\varepsilon$ is an extension of LaTeX. LaTeX is a collection of macros for TeX. TeX is a trademark of the American Mathematical Society. The style package *warwickthesis* was used.

Declarations

I hereby declare that this thesis has been completely written by me, and the material presented in it is my work. Experimental data has been provided by the FTU and MAST teams. All sources used for the results and discussions have been referenced. The majority of the results in chapter 3 and chapter 5 has been published in Nuclear Fusion [45]. The thesis has not been submitted for a degree at any other university.

Abstract

Recent experimental results carried out on Frascati Tokamak Upgrade (FTU) with the use of Liquid Lithium Limiter (LLL) show that the presence of lithium impurity can give rise to an improved particle confinement regime in which the main plasma constituents are transported towards the core whereas the impurity particles are driven outwards. The aim of our research was to further investigate this process using gyrokinetic simulations with the GKW code to calculate the particle flux in FTU-LLL discharges, and to provide a physical explanation of the above phenomena with a simplified multi-fluid description. The fluctuations in the FTU tokamak are dominantly electro-static (ES), magnetic perturbations are expected to be important in high beta tokamak plasmas, such as those in the Mega Ampère Spherical Tokamak (MAST). The effects of impurities on the electro-magnetic (EM) terms of turbulent particle transport are investigated in a typical MAST H-mode discharge.

The first chapter of the thesis is dedicated to provide an understandable but thorough introduction to the gyrokinetic equation and the code GKW. It summarizes the concept of the Lie-transform perturbation method which forms the basis of the modern approach to gyrokinetics. The gyrokinetic Vlasov–Maxwell system of equations including the full electro-magnetic perturbation is derived in the Lagrangian formalism in a rotating frame of reference. The simulation code GKW is briefly introduced and the calculation of the particle fluxes is explained.

In the second chapter the FTU-LLL and MAST experiments are introduced and the gyrokinetic simulations of the two discharges are presented. It is shown that in an ES case the ITG driven electron transport is significantly reduced at high lithium concentration. This is accompanied by an ion flow separation in order to maintain quasi-neutrality, and an inward deuterium pinch is obtained by a sufficiently high impurity density gradient. The EM terms are found to be negligible in the ion particle flux compared to the ExB contribution even at relatively high plasma beta. However, the EM effects drive a strong non-adiabatic electron response and thus prevent the ion flow separation in the analyzed cases.

The third chapter provides a detailed description of a multi-fluid model that is used to gain insight into the diffusive, thermo-diffusive and pinch terms of the anomalous particle transport. It is based on the collisionless Weiland model, however, the trapped electron collisions are introduced (Nilsson & Weiland, NF 1994) in order to capture the micro-stability properties of the gyrokinetic simulations. The model is compared with analytical and numerical results in the two-fluid, adiabatic electron and large aspect ratio limits, showing good qualitative agreement.

In the fourth chapter the fluid analysis of the FTU-LLL discharge is presented. It is shown that the inward deuterium pinch is achieved by a reduction of the diffusive term of the ITG driven main ion flux in presence of lithium impurities. The ITG mode responsible for the majority of the radial particle transport has been found to be the only unstable eigenmode rotating in the ion diamagnetic direction. Eigenmodes associated with the deuterium and lithium temperature gradients can be separately obtained when the Larmor-radius of the two ion species are more distinct, in which case the effect of lithium on the main ion transport is reduced and the inward deuterium flux is weaker.

Abbreviations

FTU	Frascati Tokamak Upgrade
MAST	Mega Ampere Spherical Tokamak
LLL	Liquid Lithium Limiter
GKW	GyroKinetics at Warwick
ITG	Ion Temperature Gradient (Driven Mode)
ETG	Electron Temperature Gradient (Driven Mode)
TEM	Trapped Electron Mode
KBM	Kinetic Ballooning Mode
ES	Electro-static
EM	Electro-magnetic
MCF	Magnetic Confinement Fusion
ICF	Inertial Confinement Fusion
NBI	Neutral Beam Injection

Chapter 1

Introduction to Anomalous Transport in Tokamak Plasmas

1.1 Magnetic Confinement Fusion

From the peaked shape of the mean nuclear binding energy per nucleon as a function of the atomic number, it is clear that nuclear energy can be potentially released either by splitting large nuclei to parts or by fusing small ones together (see any textbook on nuclear physics, for example [1]). While commercial reactors based on nuclear fission have been in operation since the mid 20th century, using nuclear fusion for controlled energy production has still not been achieved.

Any kind of fusion reaction is resisted by the Coulomb-force between the two approaching nuclei of the same charge. In order to make fusion possible, the fuel particles must be accelerated to sufficient speed to overcome this barrier. The effective cross-section of a fusion reaction thus depends on the type as well as the energy of the colliding particles. The reaction with the highest effective fusion cross section at the lowest required energy is that between a deuterium and a tritium ion, resulting in an energetic helium nucleus and a neutron [2]:

$$\begin{array}{ccccccc} {}_1\mathrm{D}^2 + {}_1\mathrm{T}^3 & \rightarrow & {}_2\mathrm{He}^4 & + & {}_0\mathrm{n}^1 & & \\ & & \downarrow & & \downarrow & & \\ & & 3.5\mathrm{MeV} & & 17.6\mathrm{MeV} & & \end{array} \tag{1.1}$$

In any medium containing fusion fuel, a self-sustaining reaction will take place when the energy deposited by the fusion products is larger than the energy lost to the environment. This is the phenomenological condition of the so-called ignition, and it has been quantified by the Lawson-criterion [3]. The fusion energy

production is proportional to the densities of the fuel ions, n_{f1} and n_{f2}, whilst the energy loss rate is estimated as the total stored energy divided by the time it takes for this energy to be fully depleted (the energy confinement time). Since the total energy is proportional to the sum fuel densities, this line of thought leads to the inequality

$$\frac{n_{f1}n_{f2}}{n_{f1}+n_{f2}}\tau_E > C \tag{1.2}$$

where τ_E is the energy confinement time and C is a constant determined by temperature of the medium and the type of the fusion reaction considered. This estimate does not take into account the external energy required for the initial heating, and therefore it is not the condition for overall positive energy balance.

The inequality in equation 1.2 suggests that ignition in a fusion experiment at a given temperature can be achieved by increasing either the density of the fuel particles or the energy confinement time, and sets the direction of the two main paths of fusion research. In inertial confinement fusion (ICF) a small solid D-T pellet is imploded in an elaborate way by shooting high energy lasers at its surface. The confinement time is relatively short as it is determined by the inertia of the pellet material, hence the name of the method, but a very high particle density can be achieved during the implosion. In contrast, in magnetic confinement fusion (MCF) a relatively low density and high temperature plasma containing the fuel ions is confined for an extended period of time using strong external magnetic fields. The energy required for fusion reactions is provided by the thermal energy of the particles, therefore this method is also called thermo-nuclear fusion.

Two main approaches to fusion-relevant experiments exist within MCF: the tokamak and the stellarator concepts. Tokamaks are toroidal, axi-symmetric devices in which the main toroidal magnetic field is generated by external coils [2] [1]. The poloidal magnetic field, required to balance the pressure gradient of the plasma, is induced by driving toroidal plasma current. In stellarators both the toroidal and the poloidal magnetic fields are generated by external coils, therefore there is no need for driving plasma current. However, they require careful design and optimization. The rest of this thesis focuses on particle transport in tokamaks.

1.2 Turbulent Transport in Tokamaks

The quality of the confinement in a tokamak is determined by the rate particles, energy, momentum, or any physical quantity is transported across the confining

[1] The word tokamak is a Russian abbreviation, it stands for toroidal chamber with magnetic coils.

magnetic field. It is typically characterized by the confinement time, defined as the time needed for a given quantity stored in the plasma to be exhausted to the environment. On this bases one can talk about particle, energy, momentum, etc. confinement times, respectively.

It is easy to understand that particle and energy confinement times play a central role in determining the feasibility of a future fusion reactor. Not long after the beginning of tokamak research it has been realized that confinement time calculations based on collisional transport processes (classical transport) are severely overestimated (see for example [4] and references therein). These estimates have been improved by the inclusion of toroidal effects, giving rise to the so called neo-classical transport theory [5], but they still could not explain the rapid heat loss observed in experiments. The process leading to this unexpectedly high level of transport was therefore labelled anomalous.

It is now commonly accepted that the source of anomalous transport arises from plasma turbulence. By plasma turbulence we mean structured, small-scale fluctuations of the quantities, such as the density of the plasma particles or the electro-static potential. It is associated with the forming of turbulent eddies transporting heat and particles across the confining magnetic field more effectively than collisions. Eddies in tokamaks are small scale structures, typically a few ion Larmor-radii across the confining magnetic field while are elongated in the direction parallel to the magnetic field. The origin of these eddies is associated with the non-linear saturation phase of different micro-instabilities of the plasma, most notably the drift-like instabilities.

1.2.1 Drift Instabilities

There is a wide range of micro-instabilities that can occur in a tokamak plasma. One practical way of categorizing these instabilities is by determining the source of free energy required for their onset [6]. In every case, the free energy comes from some kind of deviation from the perfect thermo-dynamical equilibrium. The most important type of instabilities in terms of turbulent transport are those driven unstable by the spatial gradients of density, temperature or velocity [7]. Since these gradients give rise to diamagnetic drift currents in the plasma, these modes are called drift-instabilities. Historically, it was believed that there is always available free energy for this type of modes whenever the plasma occupies a finite volume of space, hence they are also denoted as universal instabilities [6]. Although this is not always the case, they are indeed commonly observed in typical tokamak conditions, and believed to be the main reason for anomalous transport.

The simplest form of a drift-mode occurs in presence of finite density gradient. In an ideal plasma with no dissipative effects, this mode is a wave propagating in the diamagnetic direction of the species at the diamagnetic frequency. It is driven unstable only if a dissipative mechanism, such as collisions or Landau-damping, is present [2, 7], since in a collisionless plasma thermal equilibrium is maintained even when the density is not uniform in space. In typical tokamak conditions the collision frequency in the plasma core is sufficiently low that this mode remains sub-dominant. The dominant instabilities driving turbulence in present day tokamaks are typically the so called ion temperature gradient (ITG) driven, electron temperature gradient (ETG) driven and trapped electron (TE) modes [8].

While TEM and ETG are responsible for the majority of electron particle and heat transport in tokamaks, the cross-field ion particle transport is typically driven by ITG and TE modes. ITG modes are drift modes coupled with ion sound modes along the magnetic field lines, driven unstable by the ion temperature gradient [9, 10, 11]. In tokamaks they develop two branches, the slab and the curvature variety [2]. Both of these branches are characterized by wavelengths of the order of the ion Larmor-radius ($k_\perp \rho_{\mathrm{L,i}} \sim 1$), and modified ion diamagnetic frequencies depending on the parallel ion transit frequency and the magnetic drift frequency, respectively [2].

1.2.2 Modelling of Turbulent Transport in Tokamaks

Micro-instabilities are typically studied in the framework of gyrokinetic or multi-fluid theory. It is important to capture the difference between the ion and electron response for the analysis of these modes, and therefore a single-fluid approach (magneto-hydrodynamics) is not sufficient.

Gyrokinetic theory is based on a transformation of the Vlasov–Maxwell system of equation in order to average out the rapid gyro-motion of the charged particles around the equilibrium magnetic field [12]. It is therefore applicable whenever the physical processes under investigation are characterized by much lower frequencies than the Larmor-frequency, which is typically true for drift instabilities. A more detailed introduction to gyrokinetic theory and a derivation of the fully electromagnetic gyrokinetic Vlasov–Maxwell system in a rotating frame of reference is found in chapter 2.

Fluid theory is derived by taking moments of the kinetic equation in velocity space. It is therefore applicable when the velocity distribution of the particles is close to Maxwellian, and any physical processes related to a non-Maxwellian state are expected to be weak. This is generally true in a strongly collisional plasma, in

which case the collisional fluid equations derived by Braginskii [13] are applicable. Although in the core of a typical tokamak plasma the collision frequency is low and the plasma can often be considered collisionless, the presence of strong magnetic field provides sufficient organization of the particles and enables an asymptotic closure of the fluid equations [14]. The fluid equations used in this thesis are based on a Weiland-type diamagnetic closure [15], their derivation is detailed in chapter 4.

1.3 Purpose of this Thesis

The main focus of this thesis is to assess the effect of light impurities, most importantly lithium, on the turbulent particle transport in a tokamak plasma. The study is motivated by the recent experimental observations on the Frascati Tokamak Upgrade (FTU) [16] following the installation of a Liquid Lithium Limiter (LLL) [17]: Discharges performed with LLL exhibit significantly increased particle confinement properties and density peaking compared to the previous standard metallic limiter scenarios [18, 19].

The presence of large lithium concentration can have several different effects on plasma performance, for example, it is known that lithium coating greatly increases the deuterium retention capabilities of the plasma facing components [20, 21, 22, 23, 24]. However, since impurity induced improved confinement has been reported from various other tokamaks [25, 26, 27], it seems probable that a large impurity concentration has a significant impact on plasma turbulence, and hence on anomalous transport. This has been confirmed, for example, in [28] with gyrokinetic simulations of a standard test case with helium impurities.

In this thesis a comprehensive particle transport analysis using gyrokinetic and fluid methods of the FTU-LLL #30582 discharge is presented in chapters 3 and 5, respectively. Emphasis is laid on how the impurities change the radial turbulent flux of the main plasma constituents, deuterium ions and electrons, and why are light impurities, especially lithium, effective in this process.

The effects of impurities on particle transport are also studied in the Mega Ampère Spherical Tokamak (MAST) [29]. Although electro-magnetic perturbations in FTU are typically not significant due to the high toroidal magnetic field and low plasma beta, they have to be taken into account when estimating the particle transport in MAST. The gyrokinetic transport analysis of MAST #24541 is found in the second part of chapter 3.

Chapter 2

Derivation of Gyrokinetic Equations for Finite-Beta Plasmas for GKW

2.1 Introduction

In this chapter the derivation of the gyrokinetic Vlasov–Maxwell system of equations is presented. First, in section 2.2, the main motivation and the basic mathematical concept of the gyrokinetic transformation based on the Lie-transform perturbation method is outlined. A constructive derivation of the gyrokinetic equations is shown in section 2.3. This calculation is based on the work by Dannert presented in his thesis [30]. The main difference is that my derivation includes plasma rotation and is formulated in a co-rotating frame of reference. The gyrokinetic Maxwell-equations are shown in more detail, in particular the parallel component of Ampère's law where a minor correction of the equation is suggested.

The equations derived in this chapter are solved by the gyrokinetic code GKW [31], and form the basis of the analysis described in the following chapter. The parallel Ampère's law has recently been implemented in the code and is required for an accurate modelling of high beta discharges. Estimating the radial particle transport in tokamaks is a crucial part of this thesis. Therefore, the calculation of the radial particle flux, as performed in GKW, is introduced in section 2.3.7.

2.2 Motivation and Basic Mathematical Concept of Gyrokinetics

Modelling the turbulent processes in a tokamak plasma is a difficult task. Despite the fact that the forces acting on individual plasma particles can be analytically expressed, the solution of the equation of motion for every single particle is presently impossible. However, in order to characterize the macroscopic behaviour of the plasma, such detailed knowledge is not required. A statistical method, based on describing the evolution of the distribution function of the particles both in real and velocity space, is sufficient. The underlying theory is called the kinetic theory and the equation governing the dynamics of the distribution function is the Vlasov-equation (see any textbook on plasma physics, for example [32]):

$$\frac{\partial f}{\partial t} + \mathbf{v} \cdot \frac{\partial f}{\partial \mathbf{x}} + \mathbf{a} \cdot \frac{\partial f}{\partial \mathbf{v}} = 0 \tag{2.1}$$

where $f = f(\mathbf{x}, \mathbf{v}, t)$ is the distribution of the particles in the six-dimensional phase space, $\mathbf{x}$ is the real spatial coordinate, $\mathbf{v}$ is the velocity space coordinate, t is time and $\mathbf{a}$ is the acceleration of particles determined by the force acting on them. Binary interactions between particles can be included in this equation with a collision operator on the right hand side. The study of collisions is in itself a complex theory, and for the purpose of this introduction a collisionless case is considered.

Without collisions the particles are accelerated only by electromagnetic forces. The electromagnetic fields are determined by the density and current of the plasma through Maxwell's equations, which are expressed as moments of the distribution function. The acceleration is therefore a non-trivial function of the distribution function and the third term on the left hand side becomes non-linear in f. This means that the Vlasov-equation is a complicated integro-differential equation. And the fact that it is six-dimensional (not counting the different species of the plasma), makes its numerical treatment challenging.

Gyrokinetic theory is basically a method that enables the numerical solution of the Vlasov-equation. The idea is based on the fact that one component of the single particle motion in a magnetized plasma is always a gyration around the magnetic field lines. Although gyro-motion leads to fundamental physical phenomena, such as drifts, and therefore strongly influences plasma turbulence, the exact knowledge of where the particles reside on their respective gyro-orbits is not required for estimating macroscopic plasma confinement and transport. The gyro-motion can be averaged out and the orbiting particles replaced by an associated gyro-centre

that moves according to the particle drifts. The advantage of gyro-averaging is twofold: first, in an appropriately chosen coordinate system (where the gyro-angle is one of the coordinates), it reduces the dimensionality of the problem from six to five. Second, the gyro-motion typically takes place on a much faster time scale than the turbulent processes of interest. Therefore, once the gyro-averaging has been performed, there is no need to resolve the particles' rapid gyromotion, and a significantly larger time-step can be applied in the numerical scheme.

In a stationary plasma with uniform magnetic field the projection of the particle orbits onto the plane perpendicular to the magnetic field is a circle. Integrating the particle motion along the gyro-orbit in this case is straightforward since none of the quantities depend on the gyro-phase. However, turbulence in plasmas is characterized by small scale and small amplitude fluctuations superimposed on the quasi-stationary equilibrium. These fluctuations vary on the length scale of the Larmor-radius and therefore they reintroduce the gyro-phase dependence to the system. Although a direct averaging over the gyro-angle is still possible, in modern gyrokinetic theory the averaging process is regarded as a phase space transformation. The basic idea is that the six-dimensional phase space manifold is mapped onto itself in a way that the gyro-phase dependence of the fluctuations are asymptotically removed from the equations of motion up to a certain order [12]. A rigorous mathematical treatment of the problem is based on the Lie-transform perturbation method [33].

2.2.1 The Lie-transform Perturbation Method

The Lie transform perturbation method is a general way of treating small-amplitude perturbations to arbitrary orders with near-identity, continuous mappings of manifolds. The underlying idea is that the points of the manifold are infinitesimally transported along a pre-defined vector field. The vector field can be pictured as a breeze blowing the points of the manifold, like grains of sand[1]. This defines a mapping Φ of the manifold M onto itself generated by a vector field G: $\Phi : M \to M$.

Pull-back, push-forward

As a result of this mapping not only the points of the manifold are transported, the functions (mapping of the manifold to the real numbers) and curves (mapping of the real numbers to the manifold) change, as well. Figure 2.1 introduces two important concepts arising from this: the pull-back and push-forward operators. For the sake

[1] Note, however, that unlike what generally happens when sand is blown by the wind, the movement of the grains must be small.

of generality we define a non-invertible mapping Φ between two manifolds M and N. We assume that there exists a curve on the original manifold M represented by the mapping $\gamma : \mathbb{R} \to M$. One possible definition of a vector space upon a manifold is through finding equivalence classes of curves (for details see [34] or any textbook on differential geometry). A vector space upon manifold M will be denoted by $\mathcal{T}^1(M)$ indicating that the vectors lie in the local tangent plane to the manifold. The upper index shows that this is a special, one times contravariant, case of a general $\mathcal{T}^p_q$ tensor space. Note, that a vector space $\mathcal{T}^1(M)$ is not the same as one particular vector field G generating the transform. Usually $G \subset \mathcal{T}^1(M)$. The curve γ is therefore related to a vector at point x denoted with $\dot{\gamma} \in \mathcal{T}^1(x)$. If we now apply the mapping Φ, the points of curve $\gamma \subset M$ are simply transported to N and thus a curve $\Phi \circ \gamma$ and an associated vector in $\Phi(x)$ naturally arise. The two-step process of moving along the arrows γ and Φ can be substituted by a single mapping from $\mathbb{R}$ directly to N. In other words, the curve γ and the vector $\dot{\gamma}$ are *pushed forward* from manifold M to N by the mapping Φ. The push-forward operator acting on the vector space is denoted by Φ_* and the new vector by $\Phi_*\dot{\gamma}$. Note, that this process does not work in the opposite direction: if a curve originally existed on N it could not be pushed forward to M unless Φ was invertible. However, if a function $\Psi : N \to \mathbb{R}$ is defined on the target manifold N it can be *pulled back* to M. Any point on N that is mapped to a certain real value by Ψ has an origin in M. Thus, following the two-step process of moving along Φ and then Ψ can be replaced by a single effective arrow from M to $\mathbb{R}$ $\Psi \circ \Phi$.

For our present purpose, the application of Lie-transform method in gyrokinetics, we have to consider an other mathematical object: functions mapping the vectors on a manifold to the real numbers. These can also be thought of as elements of the dual space of the original vector space and denoted as $\mathcal{T}_1(M)$. If we replace M and N on figure 2.1 with $\mathcal{T}^1(M)$ and $\mathcal{T}^1(N)$, such a mapping will be analogous to $\Psi : N \to \mathbb{R}$ in the previous example. They are therefore pulled back from the vector space upon the target manifold N to that upon M. The pull-back operator acting on the dual space $\mathcal{T}_1(N)$ will be denoted by Φ^*. The reason why we have to consider this object is because in the Lagrangian formalism of the gyrokinetic transformation the Lagrangian itself is represented by a differential one-form on the phase space. A complete introduction to differential forms is beyond the scope of this thesis. We simply state that differential one-forms are elements of the dual vector space upon a manifold. We can therefore conclude, that when the gyrokinetic transformation is applied, the Lagrangian will be transformed by the pull-back operator.

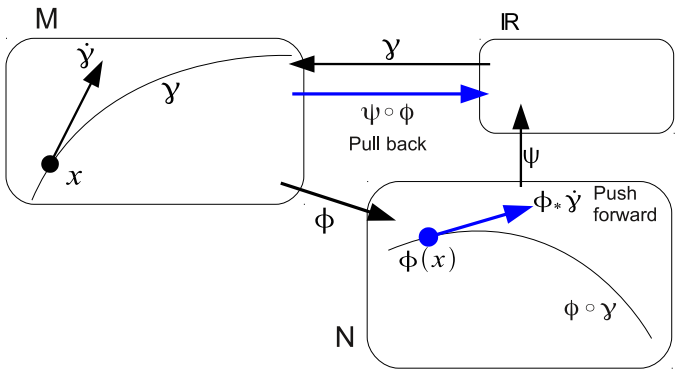

Figure 2.1: The pull-back and push-forward operators induced by a general continuous mapping Φ between two differentiable manifolds M and N. Since Φ is generally not invertible, the existence of a mapping $\mathbb{R} \to M$ induces a mapping $\mathbb{R} \to N$ but not the other way around. Similarly $\Psi : N \to \mathbb{R}$ naturally leads to $\Psi \circ \Phi : M \to \mathbb{R}$.

Transformation of a one-form

Let us assume that the infinitesimal transport Φ on manifold M generated by the vector field G can be expressed as a function of a small parameter ε. If we want to calculate how a general covariant tensor field $A \in \mathcal{T}_q(M)$ changes due to the transport, we have to compare it with its original state *at the same point*. In order to do this, we have to pull the resulting tensor space back to the original manifold. This operation is expressed by the Lie-derivative:

$$\mathcal{L}_G A = \frac{\mathrm{d}}{\mathrm{d}\varepsilon}\bigg|_0 \Phi_\varepsilon^* A \qquad \Longrightarrow \tag{2.2}$$

$$\Phi_\varepsilon^* A = A + \varepsilon \mathcal{L}_G A + \mathcal{O}(\varepsilon^2) \qquad \varepsilon \ll 1. \tag{2.3}$$

Note, that the above formula is generally true if Φ_ε^*, and therefore Φ, is differentiable. Φ is usually assumed to be an exponential function of ε: $\Phi = \mathrm{e}^{\varepsilon G}$ [35]. This means that the pull-back operator can also be written as an exponential containing the Lie-derivative. If the manifold M is such that Taylor-series converge (M is C^ω class [34]) then it can be approximated as

$$\Phi_\varepsilon^* = e^{\varepsilon \mathcal{L}_G} = 1 + \varepsilon \mathcal{L}_G + \frac{\varepsilon^2}{2!} \mathcal{L}_G \mathcal{L}_G + \mathcal{O}(\varepsilon^3). \tag{2.4}$$

Let $\Gamma \in \mathcal{T}_1(M)$ an arbitrary one-form on M. If it was defined on N then it could simply be pulled back to M by Φ^*. However, if we want to evaluate it on

the target manifold, we have to apply the inverse of the pull-back operator. The inverse generally exists if Φ itself is invertible. This, together with the condition on differentiability, requires Φ to be a diffeomorphism. In this particular case the exponential form of Φ satisfies this condition and one can write

$$(\Phi_\varepsilon^*)^{-1} = e^{-\varepsilon \mathcal{L}_G} = 1 - \varepsilon \mathcal{L}_G + \frac{\varepsilon^2}{2!} \mathcal{L}_G \mathcal{L}_G + \mathcal{O}(\varepsilon^3) \tag{2.5}$$

and the one-form on the target manifold as

$$\bar{\Gamma} = (\Phi_\varepsilon^*)^{-1} \Gamma + \mathrm{d}S \tag{2.6}$$

where $\bar{\Gamma} \in \mathcal{T}_1(N)$. $\mathrm{d}S$ expresses gauge freedom, that is, we allow for a constant additional term in the one-form. This is related to the motion being independent up to an additive constant in the Lagrangian. Finally, the Lie-derivative of the one-form in terms of the generating vector field can be calculated using the homotopy formula [35]:

$$(\mathcal{L}_G \Gamma)_i = G^j \left(\frac{\partial \Gamma_i}{\partial x^j} - \frac{\partial \Gamma_j}{\partial x^i} \right) \tag{2.7}$$

where x^i are contravariant coordinates and G^i are the components of the generating vector field.

Perturbations

So far we have expressed how an arbitrary one-form changes under an infinitesimal transformation of the manifold. The reason why this is interesting from a practical point of view is perturbations. Perturbations can be modelled by writing the one-form as a sum of contributions of different orders:

$$\Gamma = \Gamma_0 + \varepsilon \Gamma_1 + \varepsilon^2 \Gamma_2 + \dots . \tag{2.8}$$

A series of transformations associated to each of these terms can be introduced and the overall inverse pull-back operator written as

$$\begin{aligned} (\Phi_\varepsilon^*)^{-1} &= \dots e^{-\varepsilon^2 \mathcal{L}_{G_2}} e^{-\varepsilon \mathcal{L}_{G_1}} \\ &= 1 - \varepsilon \mathcal{L}_{G_1} + \varepsilon^2 \left(\frac{1}{2} \mathcal{L}_{G_1}^2 - \mathcal{L}_{G_2} \right) + \mathcal{O}(\varepsilon^3) \end{aligned}$$

where the second line is obtained by using equation 2.5 for each of the factors. Finally, substituting to equation 2.6 and separating the orders lead to:

$$\begin{aligned}
\bar{\Gamma}_0 &= \Gamma_0 + \mathrm{d}S_0 \\
\bar{\Gamma}_1 &= \Gamma_1 - \mathcal{L}_G\Gamma_0 + \mathrm{d}S_1 \\
\bar{\Gamma}_2 &= \Gamma_2 - \mathcal{L}_{G_1}\Gamma_1 + \left(\frac{1}{2}\mathcal{L}^2_{G_1} - \mathcal{L}_{G_2}\right)\Gamma_0 + \mathrm{d}S_2 \\
&\vdots
\end{aligned}$$

This introduction shows how the perturbation method can be applied up to arbitrary orders. In the present work perturbations only up to first order in an appropriate small parameter will be considered. Choosing the zeroth order gauge function S_0 to be zero and using the homotopy formula 2.7, the first order perturbation can be finally expressed as

$$\bar{\Gamma}_0 = \Gamma_0 \tag{2.9}$$

$$\bar{\Gamma}_{1,i} = \Gamma_{1,i} - G^j_1\left(\frac{\partial\Gamma_{0,i}}{\partial x^j} - \frac{\partial\Gamma_{0,j}}{\partial x^i}\right) + \frac{\partial S_1}{\partial x^i}. \tag{2.10}$$

2.2.2 Lagrangian Formalism and Lie-transform in Gyrokinetics

In this work the derivation of the gyrokinetic equations in Lagrangian formalism is presented. In general kinetic theory the Lagrangian is used to derive the equations of motion through the Euler–Lagrange equations (2.52). The time derivatives of the coordinates enter the Vlasov equation which is solved for the distribution function. As mentioned in the introduction of the chapter, the Vlasov-equation is coupled with Maxwell's equations through the dependence of the electro-magnetic fields on the distribution function. An analytical solution of the Vlasov–Maxwell system is rarely possible, typically an iterative method outlined in figure 2.2 is used in numerical schemes. In the first iteration an initial estimate of the electro-magnetic fields is used for the calculations of the distribution function. Then, the fields are updated by solving the Maxwell-equations are solved with the first approximation of the distribution function. The process is continued until convergence is reached.

In the previous section (2.2.1) it was shown what happens to an arbitrary differential one-form under an infinitesimal transformation of the manifold described by a generating vector field. In gyrokinetics the aim is to find an appropriate transformation of the six-dimensional phase space so that the gyro-angle dependence of the perturbations are asymptotically removed from the Lagrangian. This is now an

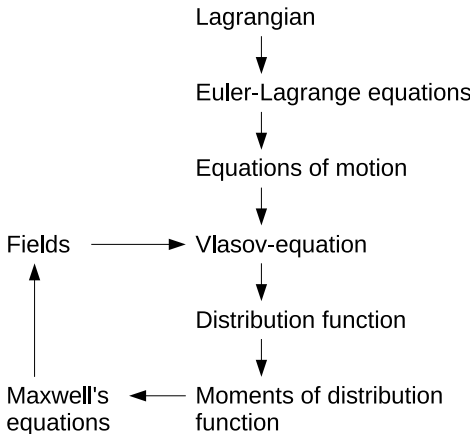

Figure 2.2: Iterative solution of the Vlasov–Maxwell system in Lagrangian formalism.

inverse problem: the vector field generating the transport is not specified, its components are derived based on prescribed conditions on the gyrokinetic Lagrangian.

If the new Lagrangian, the starting point of the graph on figure 2.2 is known, why is it still needed to derive the generating vector field? The gyrokinetic Lagrangian leads to the equations of motion in the transformed coordinates and a Vlasov-equation describing the evolution of the transformed gyrokinetic distribution function. However, the electro-magnetic fields depend on the actual, untransformed positions and velocities of the plasma particles. The transformed distribution function has to be pulled back to the original manifold in order to solve Maxwell's equations. The transformation rule, i.e. the components of the generating vector field, must be derived in order to carry out this pull-back operation.

2.3 Derivation of the Fully Electro-magnetic Gyrokinetic Equations

The derivation outlined here closely follows the structure of the calculation described by Dannert in his thesis [30]. The major difference is that in this work the derivation is performed in presence of finite plasma rotation in a co-rotating frame of reference.

The derivation of the gyrokinetic equations is carried out through a two-step coordinate transformation method. The first step is a change of coordinates performed in equilibrium without perturbations. The new coordinates are the so

called *guiding-centre* coordinates (and the manifold the guiding-centre phase space) which are more suitable to describe the gyrating motion of the charged particles in the stationary magnetic field. The derivation of the guiding-centre Lagrangian is detailed in section 2.3.3.

The second step is performed when the perturbations are introduced. It is based on the Lie-transform perturbation method and decouples the gyro-angle dependence of the Lagrangian in the presence of small scale fluctuations. The transformation takes us from the guiding-centre phase space to the so called *gyro-centre* phase space. This process is explained in section 2.3.4.

Before proceeding to the derivation of the gyro-kinetic Lagrangian, the ordering assumptions are clarified in section 2.3.1 and the notation required for the rotating frame of reference is introduced in section 2.3.2.

2.3.1 Notes on Ordering

It has been emphasized in the previous section that the Lie-transform method is applicable for small perturbations. In the general theory this has been expressed by the smallness of the parameter ε and the linear approximation of the exponential transformation formulae. In gyrokinetic theory the aim is to decouple the effect of small-scale, small amplitude fluctuations of the plasma in the Lagrangian. It is therefore natural to choose either of these properties of the fluctuations as the small parameter in this problem. These statements can be formalized by the usual ordering assumptions applied in gyrokinetic theory [12]

$$\frac{|\mathbf{A}_1|}{|\mathbf{A}_0|} \sim \frac{\Phi_1}{\Phi_0} \sim \varepsilon_\delta \ll 1 \tag{2.11}$$

$$\rho\frac{\nabla B_0}{B_0} \sim \rho\frac{\nabla E_0}{E_0} \sim \frac{\rho}{L_B} \sim \varepsilon_B \ll 1 \tag{2.12}$$

$$k_\perp \rho \sim \varepsilon_\perp \sim 1 \tag{2.13}$$

$$\frac{\omega}{\omega_\mathrm{L}} \sim \varepsilon_\omega \ll 1 \tag{2.14}$$

where $\mathbf{A}$ and Φ are the vector and scalar potentials, $\mathbf{B}$ and $\mathbf{E}$ are the magnetic and electric fields, ω and $k_\perp$ are the typical mode frequency and perpendicular wavenumber, ρ and ω_L are the Larmor-radius and Larmor-frequency. The equilibrium quantities are denoted with 0 and the fluctuations with 1 subscript. The above equations express that the fluctuations have a much smaller magnitude than the corresponding equilibrium values, their typical time scale is much slower than the Larmor-frequency, their characteristic length scale is of the order of the Larmor-radius and it is typically much shorter than the equilibrium spatial variation scale.

The gyrokinetic equation as derived in this document is valid if these ordering assumptions are true. The three different small parameters described here arise for different physical reasons. However, the general practice is to assume that they are of similar order and substitute them with one parameter. In this work the ratio of the reference thermal Larmor-radius and the equilibrium magnetic length scale $\rho_* = \frac{\rho_{\text{ref}}}{L_B} = \frac{m_{\text{ref}} v_{th,ref}}{eB_{\text{ref}}} \sim \varepsilon_B \sim \varepsilon_\delta \sim \varepsilon_\omega$ is chosen for this purpose, and the equations are derived up to first order in this quantity.

2.3.2 Plasma Rotation

Turbulence in a rotating plasma can be conveniently described in a co-rotating frame of reference. Although plasma rotation is outside the main scope of this thesis, for the sake of generality the derivation of the gyrokinetic equations is shown in a reference frame rigidly rotating with velocity $\mathbf{u}_0$. The plasma rotation is assumed to be toroidal, its poloidal component is typically much smaller and neglected. The reference frame is therefore chosen to rotate in the toroidal direction, and its velocity can be expressed with a constant angular frequency in the form

$$\mathbf{u}_0 = \mathbf{\Omega} \times \mathbf{x} = R^2 \Omega \nabla \varphi \tag{2.15}$$

where φ is the toroidal angle and $R\nabla\varphi$ is the unit vector in the toroidal direction [36].

The rotation of the plasma in the laboratory frame is typically not a rigid body rotation, it is characterized by a radial profile of angular velocity $\hat{\Omega}(\psi)$. The rotating frame is chosen in a way that its angular frequency Ω matches the plasma rotation at a certain radial point: $\Omega = \hat{\Omega}(\psi_r)$. This method is suitable for local gyrokinetic studies, since in the rotating frame on the surface labelled by ψ_r the plasma rotation vanishes. However, a finite gradient of the rotation profile has to be taken into account. The plasma rotation in the co-rotating frame of reference will be denoted as $\omega_\varphi(\psi) = \hat{\Omega}(\psi) - \Omega$. The associated plasma rotation speed along the magnetic field line in the co-rotating frame can be expressed as

$$u_\parallel = \frac{RB_{\text{t}}}{B} \omega_\varphi(\psi) \tag{2.16}$$

where B_{t} is the toroidal component of the magnetic field [36].

2.3.3 Lagrangian in Guiding-centre Coordinates

The particle phase space consists of three real space and three velocity space components: $(\mathbf{x}, \mathbf{v})$. A point in this space describes a particle at a certain position travelling according to a certain velocity vector. The Lagrangian, or fundamental one-form, of a particle with mass m and charge number Z in an electro-magnetic field is written as

$$\gamma = \gamma_\nu \mathrm{d}z^\nu = (m\mathbf{v} + Ze\mathbf{A}(\mathbf{x})) \cdot \mathrm{d}\mathbf{x} - \left(\frac{1}{2}mv^2 + Ze\Phi(\mathbf{x})\right) \mathrm{d}t, \tag{2.17}$$

where ν indexes the six coordinates, and summation over repeated indices is meant [37]. $\mathbf{A}$ and Φ are the vector and scalar potentials, respectively. The first term, multiplied by the differential of the spatial coordinates, is called the symplectic part and the second is the Hamiltonian: $H(\mathbf{x}, \mathbf{v})$.

In order to write the Lagrangian in a rotating frame of reference, both the velocity coordinates and the fields have to be modified according to the Lorentz-transformation:

$$\mathbf{v} \to \mathbf{v} + \mathbf{u}_0 \qquad \mathbf{E} \to \mathbf{E} + \mathbf{u}_0 \times \mathbf{B} \qquad \Phi \to \Phi + \mathbf{A} \cdot \mathbf{u}_0. \tag{2.18}$$

Following the calculation outlined in [36] the Lagrangian becomes

$$\gamma = (m\mathbf{v} + m\mathbf{u}_0 + Ze\mathbf{A}(\mathbf{x})) \cdot \mathrm{d}\mathbf{x} - \left(\frac{1}{2}mv^2 + Ze\Phi(\mathbf{x}) - \frac{1}{2}mu_0^2\right) \mathrm{d}t. \tag{2.19}$$

Let us introduce the guiding-centre phase space with the following coordinate transformation:

$$\begin{aligned}
\mathbf{X}(\mathbf{x}, \mathbf{v}) &= \mathbf{x} - \mathbf{r} = \mathbf{x} - \rho(\mathbf{x}, \mathbf{v})\mathbf{a}(\mathbf{x}, \mathbf{v}) && (2.20)\\
v_\parallel(\mathbf{x}, \mathbf{v}) &= \mathbf{v} \cdot \mathbf{b}(\mathbf{x}) && (2.21)\\
\mu(\mathbf{x}, \mathbf{v}) &= \frac{mv_\mathrm{L}^2(\mathbf{x})}{2B(\mathbf{x})} && (2.22)\\
\theta(\mathbf{x}, \mathbf{v}) &= \cos^{-1}\left(\frac{1}{v_\mathrm{L}(\mathbf{x})}(\mathbf{b}(\mathbf{x}) \times \mathbf{v}) \cdot \mathbf{e}_1\right). && (2.23)
\end{aligned}$$

The new coordinates are the position of the centre of the particle's gyro-orbit, or guiding-centre $\mathbf{X}$, the particle velocity parallel to the equilibrium magnetic field $v_\parallel$, the magnetic moment μ and the gyrophase θ. $\mathbf{b}(\mathbf{x})$ is the unit vector in the direction of the equilibrium magnetic field and $\rho(\mathbf{x}, \mathbf{v})\mathbf{a}(\mathbf{x}, \mathbf{v})$ is the vector pointing from the guiding-centre to the particle's position. Its direction is determined by the unit

vector $\mathbf{a}$ and its length is the Larmor-radius

$$\rho(\mathbf{x}, \mathbf{v}) = \frac{m v_{\mathrm{L}}(\mathbf{x})}{|Z| e B(\mathbf{x})} \tag{2.24}$$

where v_{L} is the velocity of the gyro-motion, or Larmor-velocity. The absolute value of the charge number is needed so the ion and electron Larmor-radii are both positive. The fact that their gyration is in opposite direction is expressed by the vectorial factor $\mathbf{a}$. The unit vector $\mathbf{a}$ can be expressed in a local orthonormal basis as the function of the gyro-angle:

$$\mathbf{a}(\theta) = \mathbf{e}_1 \cos\theta + \mathbf{e}_2 \sin\theta. \tag{2.25}$$

The vectors $\mathbf{b}$, $\mathbf{e}_1$ and $\mathbf{e}_2$ form a local righthanded Cartesian coordinate system at the guiding-centre position.

The transformation of the one-form due to the change of coordinates can be expressed as

$$\Gamma_\eta = \gamma_\nu \frac{\mathrm{d}z^\nu}{\mathrm{d}Z^\eta} \tag{2.26}$$

where Γ_η is a component of the guiding-centre fundamental one-form [37]. In order to calculate these new components the transformation equations 2.20, 2.21, 2.22 and 2.23 have to be inverted in order to provide the old coordinates as functions of the new ones: $z(Z)$. It is clear that the direct transformation is uniquely determined if the magnetic field is known at the particle's position. However, when the inverse is taken and particle coordinates are calculated, the particle position can not be explicitly expressed due to the dependence of the Larmor-radius on $\mathbf{x}$ through the magnetic field. The coordinates are therefore Taylor-expanded in space around the guiding-centre location $\mathbf{X}$:

$$\begin{aligned} \mathbf{x} &= \mathbf{X} + \rho(\mathbf{x})\mathbf{a}(\theta) \\ \rho(\mathbf{x}) &\approx \rho(\mathbf{X}) + \left(\frac{\partial \rho(\mathbf{x})}{\partial \mathbf{x}}\right)_{\mathbf{X}} \rho(\mathbf{x})\mathbf{a}(\theta) + \mathcal{O}((\rho(\mathbf{x})\mathbf{a}(\theta))^2). \end{aligned}$$

It can be shown that the first order correction in the Taylor-expansion containing $\rho\frac{\partial \rho}{\partial \mathbf{x}} \sim \rho^2$ leads to second order terms in ρ_*. It is thus sufficient to keep only $\rho(\mathbf{x}) \approx \rho(\mathbf{X})$ which gives

$$\mathbf{x}(\mathbf{X}, \theta) \approx \mathbf{X} + \rho(\mathbf{X})\mathbf{a}(\theta). \tag{2.27}$$

Note that the Larmor radius ρ also depends on the velocity space coordinates $\mathbf{v}$

in particle phase space, or the magnetic moment μ in guiding-centre phase space through the formula $\rho(\mathbf{X},\mu) = \frac{1}{Ze}\sqrt{\frac{2\mu m}{B(\mathbf{X})}}$. This dependence will not be explicitly indicated unless greater clarity is called for.

The particle velocity is the sum of three contributions: the velocity along the magnetic field, the gyration velocity and the drift velocities. It will be shown later that the particle drifts are described by the motion of the guiding centre. Hence the velocity in the guiding-centre frame can be written as

$$\mathbf{v} = v_\parallel \mathbf{b}(\mathbf{x}) + \mathbf{v}_\mathrm{L} = v_\parallel \mathbf{b}(\mathbf{x}) + \rho(\mathbf{x})\dot{\mathbf{a}}(\theta)$$

Applying Taylor expansion again around $\mathbf{X}$ we obtain

$$\mathbf{v}(\mathbf{X}, v_\parallel, \mu, \theta) \approx v_\parallel \left[\mathbf{b}(\mathbf{X}) + \frac{\partial \mathbf{b}(\mathbf{X})}{\partial \mathbf{X}} \cdot \mathbf{a}(\theta)\rho(\mathbf{X},\mu)\right] + \rho(\mathbf{X},\mu)\dot{\mathbf{a}}(\theta) \tag{2.28}$$

The transformation formula (2.26) can now be applied to express the fundamental one-form in the new coordinates. The $\mathbf{X}$ component takes the form

$$\Gamma_{X^i} = \gamma_{x^j}\frac{\mathrm{d}x^j}{\mathrm{d}X^i} + \underbrace{\gamma_{v^j}}_{0}\frac{\mathrm{d}v^j}{\mathrm{d}X^i} + \gamma_t \underbrace{\frac{\mathrm{d}t}{\mathrm{d}X^i}}_{0}.$$

The required derivative is

$$\frac{\mathrm{d}x^j}{\mathrm{d}X^i} = \delta_i^j + \frac{\mathrm{d}\rho(\mathbf{X})}{\mathrm{d}X^i}a^j(\theta)$$

which substituted into (2.26) gives

$$\begin{aligned}\Gamma_{X^i} &= \left(mv_j + mu_{0j} + ZeA_j(\mathbf{x})\right)\frac{\mathrm{d}x^j}{\mathrm{d}X^i} \\ &= \left(mv_\parallel b_j(\mathbf{x}) + m\rho(\mathbf{x})\dot{a}_j(\theta) + mu_{0j} + ZeA_j(\mathbf{x})\right)\left(\delta_i^j + \frac{\mathrm{d}\rho(\mathbf{X})}{\mathrm{d}X^i}a^j(\theta)\right).\end{aligned}$$

Expanding the quantities into Taylor-series around $\mathbf{X}$ and keeping terms up to first order in ρ results

$$\begin{aligned}\Gamma_{X^i} &= mv_\parallel\left[b_i(\mathbf{X}) + \frac{\partial b_i(\mathbf{X})}{\partial X^k}a^k(\theta)\rho(\mathbf{X})\right] + m\rho(\mathbf{X})\dot{a}_i + mu_{0i} \\ &\quad + Ze\left[A_i(\mathbf{X}) + \frac{\partial A_i(\mathbf{X})}{\partial X^k}a^k(\theta)\rho(\mathbf{X})\right] + \left(ZeA_j(\mathbf{X}) + mu_{0j}\right)\frac{\mathrm{d}\rho(\mathbf{X})}{\mathrm{d}X^i}a^j(\theta).\end{aligned}$$

Note that $\mathbf{a}$ is perpendicular to both $\mathbf{b}$ and $\dot{\mathbf{a}}$ and the term containing $\rho\frac{\partial\rho}{\partial\mathbf{X}}$ can be

neglected.

The gyro-averaging operator in guiding-centre phase space is simply an integral over the gyro-phase θ:

$$\langle \dots \rangle = \frac{1}{2\pi} \int_0^{2\pi} \dots \, \mathrm{d}\theta. \tag{2.29}$$

It follows from the definition of the vector $\mathbf{a}$ (equation 2.25) that first order terms in $\mathbf{a}$ or $\dot{\mathbf{a}}$ disappear under gyro-averaging. Hence the θ-integral yields

$$\langle \Gamma_{X^i} \rangle = m v_\parallel b_i(\mathbf{X}) + m u_{0i} + Z e A_i(\mathbf{X}). \tag{2.30}$$

The remaining components are expressed in an analogous way. The parallel velocity component according to equation 2.26 becomes

$$\Gamma_{v_\parallel} = \gamma_\nu \frac{\mathrm{d}z^\nu}{\mathrm{d}v_\parallel} = \gamma_{x^i} \underbrace{\frac{\mathrm{d}x^i}{\mathrm{d}v_\parallel}}_{0} + \underbrace{\gamma_{v^i}}_{0} \frac{\mathrm{d}v^i}{\mathrm{d}v_\parallel} = 0 \tag{2.31}$$

meaning that this component remains zero in the guiding-centre approximation.

The μ-component takes the form

$$\begin{aligned}
\Gamma_\mu &= \gamma_\nu \frac{\mathrm{d}z^\nu}{\mathrm{d}\mu} = \gamma_{x^i} \frac{\mathrm{d}x^i}{\mathrm{d}\mu} = \left(m v_i + m u_{0i} + Z e A_i(\mathbf{x})\right) \frac{\partial \rho(\mathbf{X}, \mu)}{\partial \mu} a^i(\theta) \\
&= \left(m v_\parallel b_i(\mathbf{x}) + m \rho(\mathbf{x}) \dot{a}_i(\theta) + m u_{0i} + Z e A_i(\mathbf{x})\right) \frac{\partial \rho(\mathbf{X}, \mu)}{\partial \mu} a^i(\theta) \\
&= \left[m u_{0i} + Z e \left(A_i(\mathbf{X}) + \frac{\partial A_i(\mathbf{X})}{\partial X^k} a^k(\theta) \rho(\mathbf{X}, \mu) \right) \right] \frac{\partial \rho(\mathbf{X}, \mu)}{\partial \mu} a^i(\theta).
\end{aligned}$$

Since $\frac{\partial \rho}{\partial \mu} \sim \frac{\rho}{\mu}$, the term containing $\rho \frac{\partial \rho}{\partial \mu}$ leads to second order terms in ρ_* and therefore it can be neglected. Finally, gyro-averaging gives

$$\langle \Gamma_\mu \rangle = 0. \tag{2.32}$$

Using relations $\dot{\mathbf{a}}(\theta) = \frac{\partial \mathbf{a}(\theta)}{\partial \theta} \dot{\theta}$ and $\dot{\theta} = \omega_\mathrm{L} = \frac{ZeB}{m}$, the gyration velocity can be written as $\rho(\mathbf{X}) \dot{\theta} = \frac{Z}{|Z|} v_\mathrm{L}(\mathbf{X})$. Since $\frac{\partial a_i}{\partial \theta} \frac{\partial a^i}{\partial \theta} = 1$ (see equations 2.25 and 2.28) the θ-component becomes

$$\Gamma_\theta = \gamma_{x^i} \frac{\mathrm{d}x^i}{\mathrm{d}\theta} \implies \langle \Gamma_\theta \rangle = m \rho(\mathbf{X}) \frac{Z}{|Z|} v_\mathrm{L}(\mathbf{X}) = \frac{2 \mu m}{Z e}. \tag{2.33}$$

Time is not transformed thus the Hamiltonian part in guiding-centre coordinates remains

$$\langle \Gamma_t \rangle = -\left(\frac{1}{2} m v_\parallel^2 + \mu B(\mathbf{X}) - \frac{1}{2} m u_0^2 + Ze\Phi(\mathbf{X}) \right). \tag{2.34}$$

Using equations 2.30, 2.31, 2.32, 2.33 and 2.34 describing the components of the fundamental one-form in guiding-centre coordinates we finally obtain

$$\begin{aligned} \langle \Gamma \rangle &= \left(m v_\parallel \mathbf{b}(\mathbf{X}) + m\mathbf{u}_0 + Ze\mathbf{A}(\mathbf{X}) \right) \cdot \mathrm{d}\mathbf{X} + \frac{2\mu m}{Ze} \mathrm{d}\theta \\ &\quad - \left(\frac{1}{2} m v_\parallel^2 + \mu B(\mathbf{X}) - \frac{1}{2} m u_0^2 + Ze\Phi(\mathbf{X}) \right) \mathrm{d}t. \end{aligned} \tag{2.35}$$

The equations of motion can be derived from equation 2.35 with the Euler–Lagrange equations (2.52). The results are the well known drifts of the guiding centre and are not detailed here. However, it is important to note that as a consequence of of the Lagrangian being independent of the gyro-phase θ, the magnetic moment μ (the associated conjugate coordinate pair of θ) becomes an invariant of the motion: $\dot{\mu} = 0$.

2.3.4 Lagrangian in Gyro-centre Coordinates

In this section the fluctuations are added to the guiding-centre Lagrangian, and a transformation is derived that removes the gyro-phase dependence of the perturbations up to first order in ρ_*. The derivation is based on a list of requirements on the new Lagrangian and the transformation is defined in terms of the generating vector field.

Perturbed guiding-centre one-form

Let us introduce small scale perturbations of the electromagnetic fields in the form

$$\mathbf{A} = \mathbf{A}_0 + \mathbf{A}_1 \qquad \Phi = \Phi_0 + \Phi_1.$$

The equilibrium electric field is typically assumed zero in a stationary plasma, but it has to be kept in case of finite plasma rotation. According to the gyrokinetic ordering the perturbations are first order in the typical small parameters used in gyrokinetics: $\frac{A_1}{A_0} \sim \frac{\Phi_1}{\Phi_0} \sim \rho_*$. The perturbations appear in the particle phase space

Lagrangian as

$$\begin{aligned}\gamma &= \gamma_0 + \gamma_1 \\ \gamma_0 &= (m\mathbf{v} + m\mathbf{u}_0 + Ze\mathbf{A}_0(\mathbf{x})) \cdot \mathrm{d}\mathbf{x} - \left(\frac{1}{2}mv^2 - \frac{1}{2}mu_0^2 + Ze\Phi_0(\mathbf{x})\right)\mathrm{d}t \\ \gamma_1 &= Ze\mathbf{A}_1(\mathbf{x}) \cdot \mathrm{d}\mathbf{x} - Ze\Phi_1(\mathbf{x})\mathrm{d}t.\end{aligned}$$

The total Lagrangian has to be transformed first to the guiding-centre and then to gyro-centre phase space. The guiding-centre transformation of the equilibrium part has been completed in section 2.3.3. The transformation of the perturbed part of the Lagrangian γ_1 is analogous to the calculation shown there. An important difference arises from the fact that fluctuating quantities vary on a small length scale and therefore Taylor expansion around the guiding-centre is not advantageous. Their values have to be taken at the particle position which is a function of the gyro-angle in guiding-centre coordinates.

The spatial components of the perturbed guiding-centre one-form are calculated as

$$\begin{aligned}\Gamma_{1,X^i} &= \gamma_{1,\nu}\frac{\mathrm{d}z^\nu}{\mathrm{d}X^i} = ZeA_{1,j}(\mathbf{x})\left(\delta_i^j + \frac{\mathrm{d}\rho(\mathbf{X})}{\mathrm{d}X^i}a^j(\theta)\right) \\ &= ZeA_{1,i}(\mathbf{x}) + Ze\frac{\mathrm{d}\rho(\mathbf{X})}{\mathrm{d}X^i}A_{1,j}(\mathbf{x})a^j(\theta) \\ &\approx ZeA_{1,i}(\mathbf{x}).\end{aligned}$$

The final approximation can be made because the second term contains $\frac{\partial\rho}{\partial\mathbf{x}}\mathbf{A}_1 \sim \rho^2$ and therefore can be neglected. The parallel velocity component remains zero since there are no terms added in the perturbed part

$$\Gamma_{1,v_\parallel} = 0. \tag{2.36}$$

The perturbed μ component is

$$\Gamma_{1,\mu} = ZeA_{1,j}(\mathbf{x})\frac{\rho(\mathbf{X})}{2\mu}a^j(\theta) = \frac{Z}{|Z|}\frac{1}{v_\mathrm{L}(\mathbf{X},\mu)}\mathbf{A}_1(\mathbf{x}) \cdot \mathbf{a}(\theta), \tag{2.37}$$

the θ component is

$$\Gamma_{1,\theta} = ZeA_{1,j}(\mathbf{x})\rho(\mathbf{X})\frac{\mathrm{d}a^j(\theta)}{\mathrm{d}\theta} = \frac{Z}{|Z|}\frac{2\mu}{v_\mathrm{L}(\mathbf{X},\mu)}\mathbf{A}_1(\mathbf{x}) \cdot \frac{\mathrm{d}\mathbf{a}(\theta)}{\mathrm{d}\theta}, \tag{2.38}$$

and the Hamiltonian becomes

$$\Gamma_{1,t} = -Ze\Phi_1(\mathbf{x}). \tag{2.39}$$

The perturbed part of the one-form in the guiding-centre phase space can be written as

$$\Gamma_1 = Ze\mathbf{A}_1(\mathbf{x}) \cdot \mathrm{d}\mathbf{X} + \frac{Z}{|Z|}\frac{\mathbf{A}_1(\mathbf{x}) \cdot \mathbf{a}}{v_\mathrm{L}}\mathrm{d}\mu + \frac{Z}{|Z|}\frac{2\mu}{v_\mathrm{L}}\mathbf{A}_1(\mathbf{x}) \cdot \frac{\mathrm{d}\mathbf{a}}{\mathrm{d}\theta}\mathrm{d}\theta - Ze\Phi_1(\mathbf{x})\mathrm{d}t. \tag{2.40}$$

The complete guiding-centre Lagrangian including perturbations is the sum of equations 2.35 and 2.40.

Gyro-centre transformation

The aim is now to find a transformation that removes the gyro-angle dependence introduced by the fluctuations from the Lagrangian. Since the perturbations are first order in ρ_*, this one-form can be transformed into the gyro-centre phase space according to equation 2.10. Note, that the transformation is an inverse pull-back operator, which means that the new Lagrangian in the gyro-centre phase space is expressed in guiding-centre coordinates $(\mathbf{X}, v_\parallel, \mu, \theta)$ in order to allow the comparison of the two one-forms. However, the transformation does give rise to a new set of gyro-centre coordinates $(\bar{\mathbf{X}}, \bar{v}_\parallel, \bar{\mu}, \bar{\theta})$ which are not being used in the present section. The gyro-centre Lagrangian will be distinguished from its guiding-centre counterpart with an overbar $\bar{\Gamma}$.

It is not obvious which vector field to use to generate a transformation that removes the fluctuating quantities from the Lagrangian. Therefore, we do not perform a direct transformation. The vector field is derived based on a simple set of requirements on the gyro-centre Lagrangian suggested by Dannert [30]:

$$\begin{aligned}
G_{1,t} = 0 \quad &\rightarrow \quad \text{no transformation in time} \\
\bar{\Gamma}_{1,v_\parallel} = 0 \quad &\rightarrow \quad \text{no } v_\parallel \text{ component} \\
\bar{\Gamma}_{1,\mu} = 0 \quad &\rightarrow \quad \text{no } \mu \text{ component} \\
\bar{\Gamma}_{1,\theta} = 0 \quad &\rightarrow \quad \text{no change in } \theta \text{ component} \\
\bar{\Gamma}_{1,\mathbf{X}} = Ze\langle\mathbf{A}_1(\mathbf{x})\rangle \quad &\rightarrow \quad \text{the transformation leads to the gyro-average}
\end{aligned}$$

Let us now apply equation 2.10 and the requirements above to express the components of the generator vector field that provides the desired Lagrangian. As it was mentioned in section 2.2.2, this can be considered as an inverse problem. The

equation for the μ component is written as

$$\begin{aligned}\bar{\Gamma}_{1,\mu} &= \frac{Z}{|Z|}\frac{\mathbf{A}_1(\mathbf{x})\cdot\mathbf{a}(\theta)}{v_{\mathrm{L}}(\mathbf{X},\mu)} + G_1^{\theta}\frac{2m}{Ze} + \frac{\partial S_1}{\partial \mu} = 0 \quad \Longrightarrow \\ G_1^{\theta} &= -\frac{Ze}{2m}\left(\frac{Z}{|Z|}\frac{\mathbf{A}_1(\mathbf{x})\cdot\mathbf{a}(\theta)}{v_{\mathrm{L}}(\mathbf{X},\mu)} + \frac{\partial S_1}{\partial \mu}\right). \end{aligned} \tag{2.41}$$

The equation for the θ component gives

$$\begin{aligned}\bar{\Gamma}_{1,\theta} &= \frac{Z}{|Z|}\frac{mv_{\mathrm{L}}(\mathbf{X},\mu)}{B_0(\mathbf{X})}\mathbf{A}_1(\mathbf{x})\cdot\frac{\mathrm{d}\mathbf{a}(\theta)}{\mathrm{d}\theta} - G_1^{\mu}\frac{2m}{Ze} + \frac{\partial S_1}{\partial \theta} = 0 \quad \Longrightarrow \\ G_1^{\mu} &= \frac{Ze}{2m}\left(\frac{\partial S_1}{\partial \theta} + \frac{Z}{|Z|}\frac{mv_{\mathrm{L}}(\mathbf{X},\mu)}{B_0(\mathbf{X})}\mathbf{A}_1(\mathbf{x})\cdot\frac{\mathrm{d}\mathbf{a}(\theta)}{\mathrm{d}\theta}\right). \end{aligned} \tag{2.42}$$

The $v_{\parallel}$ component leads to

$$\begin{aligned}\bar{\Gamma}_{1,v_{\parallel}} &= G_1^{\mathbf{X}}\cdot m\mathbf{b}_0 + \frac{\partial S_1}{\partial v_{\parallel}} = 0 \quad \Longrightarrow \\ G_1^{\mathbf{X}}\cdot\mathbf{b}_0 &= -\frac{1}{m}\frac{\partial S_1}{\partial v_{\parallel}}. \end{aligned} \tag{2.43}$$

The spatial components' transformation can be written as

$$\begin{aligned}\bar{\Gamma}_{1,\mathbf{X}} &= Ze\mathbf{A}_1(\mathbf{x}) + ZeG_1^{\mathbf{X}}\times\underbrace{\nabla\times\left(\mathbf{A}_0(\mathbf{X}) + \frac{m}{Ze}(v_{\parallel}\mathbf{b}_0(\mathbf{X}) + \mathbf{u}_0)\right)}_{\equiv\mathbf{B}_0^*(\mathbf{X})\equiv\nabla\times\mathbf{A}_0^*(\mathbf{X})} + \\ &\quad mG_1^{v_{\parallel}}\mathbf{b}_0(\mathbf{X}) + \nabla S_1 = Ze\langle\mathbf{A}_1(\mathbf{x})\rangle \quad \Longrightarrow \\ 0 &= Ze\underbrace{\left(\mathbf{A}_1(\mathbf{x}) - \langle\mathbf{A}_1(\mathbf{x})\rangle\right)}_{\widetilde{\mathbf{A}}_1(\mathbf{x})} + ZeG_1^{\mathbf{X}}\times\mathbf{B}_0^*(\mathbf{X}) - mG_1^{v_{\parallel}}\mathbf{b}_0(\mathbf{X}) + \nabla S_1 \end{aligned} \tag{2.44}$$

where the notation $\mathbf{B}_0^*(\mathbf{X}) = \nabla\times\left(\mathbf{A}_0(\mathbf{X}) + \frac{m}{Ze}(v_{\parallel}\mathbf{b}_0(\mathbf{X}) + \mathbf{u}_0)\right)$ has been introduced. The scalar and vector potential perturbations are formally separated into a gyro-averaged and an oscillating part:

$$\mathbf{A}_1 = \widetilde{\mathbf{A}}_1 + \langle\mathbf{A}_1\rangle \tag{2.45}$$

$$\Phi_1 = \widetilde{\Phi}_1 + \langle\Phi_1\rangle. \tag{2.46}$$

In order to express the required component of the generating vector field, first we take the scalar product of equation 2.44 with B_0^* to obtain $G_1^{v_{\parallel}}$, then the vector

product with $\mathbf{b}_0$ to obtain $G_1^{\mathbf{X}}$.

$$G_1^{v_\parallel} = \frac{1}{mB_{0\parallel}^*(\mathbf{X})}\left(Ze\widetilde{\mathbf{A}}_1(\mathbf{x})\cdot\mathbf{B}_0^*(\mathbf{X}) + \nabla S_1\cdot\mathbf{B}_0^*(\mathbf{X})\right) \tag{2.47}$$

$$G_1^{\mathbf{X}} = -\frac{1}{B_{0\parallel}^*(\mathbf{X})}\left(\widetilde{\mathbf{A}}_1(\mathbf{x})\times\mathbf{b}_0(\mathbf{X}) + \frac{1}{m}\frac{\partial S_1}{\partial v_\parallel}\mathbf{B}_0^*(\mathbf{X}) + Ze\nabla S_1\times\mathbf{b}_0(\mathbf{X})\right) \tag{2.48}$$

where equation 2.43 and $B_{0\parallel}^* = \mathbf{B}_0^*\cdot\mathbf{b}_0$ have been used. Finally, the transformation of the Hamiltonian part yields

$$\begin{aligned}
\bar{\Gamma}_{1,t} &= -Ze\Phi_1(\mathbf{x}) + G_1^{\mathbf{X}}\cdot(\mu\nabla B_0(\mathbf{X}) + Ze\nabla\Phi_0(\mathbf{X})) + G_1^{v_\parallel}mv_\parallel + G_1^{\mu}B_0(\mathbf{X}) + \frac{\partial S_1}{\partial t}\\
&= -Ze\Phi_1(\mathbf{x}) - \frac{1}{B_{0\parallel}^*}\left(\widetilde{\mathbf{A}}_1(\mathbf{x})\times\mathbf{b}_0(\mathbf{X}) + \frac{1}{m}\frac{\partial S_1}{\partial v_\parallel}\mathbf{B}_0^*(\mathbf{X}) + Ze\nabla S_1\times\mathbf{b}_0(\mathbf{X})\right)\cdot\\
&\quad (\mu\nabla\mathbf{B}_0(\mathbf{X}) + Ze\nabla\Phi_0(\mathbf{X})) + \frac{v_\parallel}{B_{0\parallel^*}}\left(Ze\widetilde{\mathbf{A}}_1(\mathbf{x})\cdot\mathbf{B}_0^*(\mathbf{X}) + \nabla S_1\cdot\mathbf{B}_0^*(\mathbf{X})\right) +\\
&\quad \frac{Ze}{2m}\left(\frac{\partial S_1}{\partial\theta} + \frac{Z}{|Z|}\frac{mv_{\mathrm{L}}(\mathbf{X},\mu)}{B_0(\mathbf{X})}\mathbf{A}_1(\mathbf{x})\cdot\frac{\mathrm{d}\mathbf{a}(\theta)}{\mathrm{d}\theta}\right)B_0(\mathbf{X}) + \frac{\partial S_1}{\partial t}.
\end{aligned}$$

Let us now take a closer look on the gauge transformation function S_1 and its derivatives. According to equations 2.13-2.14 the ordering of these derivatives is as follows:

$$\begin{aligned}
\partial_t S_1 &\sim \omega S_1 \sim \varepsilon_\omega\omega_{\mathrm{L}}S_1 \sim \rho_*\omega_{\mathrm{L}}S_1\\
\nabla_\parallel S_1 &\sim \frac{1}{L_B}S_1 \sim \frac{\rho_*}{\rho}S_1\\
\nabla_\perp S_1 &\sim \frac{1}{\rho}S_1\\
\partial_{v_\parallel} S_1 &\sim \frac{1}{v_{\mathrm{th}}}S_1\\
\partial_\mu S_1 &\sim \frac{B_0}{T}S_1\\
\partial_\theta S_1 &\sim 1.
\end{aligned}$$

Note that the characteristic length scale of the perturbations along the magnetic field lines is of order L_B and that the characteristic parallel velocity and Larmor-speed is of order of the thermal velocity. Using the above assumptions and $|\mathbf{B}_0^*| = \left|\mathbf{B}_0 + \frac{mv_\parallel}{e}\nabla\times\mathbf{b}_0\right| \sim B_0 + \rho_*B_0$, the ordering of the terms containing S_1 in the

gyro-centre Hamiltonian can be written as

$$\begin{aligned}
\frac{\mathbf{B}_0^*}{B_{0\|}^*}\frac{1}{m}\frac{\partial S_1}{\partial v_\|}\cdot(\mu\nabla B_0 + Ze\nabla\Phi_0) &\sim \rho_*\omega_{\mathrm{L}}\left(1+\frac{Ze\Phi_0}{\mu B_0}\right)S_1 \\
\frac{1}{B_{0\|}^*}Ze\nabla S_1\times\mathbf{b}_0\cdot(\mu\nabla B_0 + Ze\nabla\Phi_0) &\sim \rho_*\omega_{\mathrm{L}}\left(1+\frac{Ze\Phi_0}{\mu B_0}\right)S_1 \\
\frac{\mathbf{B}_0^*}{B_{0\|}^*}\cdot\nabla S_1 v_\| \sim \frac{v_\|}{\rho}\varepsilon_B S_1 &\sim \rho_*\omega_{\mathrm{L}}S_1 \\
\frac{Ze}{2m}\frac{\partial S_1}{\partial\theta}B_0 &\sim \omega_{\mathrm{L}}S_1 \\
\frac{\partial S_1}{\partial t} &\sim \rho_*\omega_{\mathrm{L}}S_1
\end{aligned}$$

Note that $\nabla_\perp S_1\cdot\mathbf{B}_0 = 0$ and $\nabla_\| S_1\times\mathbf{b}_0 = 0$. Let us assume that the order of $\frac{Ze\Phi_0}{\mu B_0}$ is no larger than 1 (Φ_0 is zero in a non-rotating plasma). Terms that are explicitly second order in ρ_* have been neglected. Since S_1 is the first order gauge function, $\rho_* S_1$ gives rise to second order terms and therefore can be neglected, as well. The only term that remains is the one containing the θ derivative of S_1. Using the above orderings and applying the decomposition in equation 2.46 gives

$$\begin{aligned}
\bar{\Gamma}_{1,t} = & -Ze\left(\widetilde{\Phi}_1(\mathbf{x}) + \langle\Phi_1(\mathbf{x})\rangle\right) - \frac{1}{B_{0\|}^*}\widetilde{\mathbf{A}}_1(\mathbf{x})\times\mathbf{b}_0(\mathbf{X})\cdot(\mu\nabla B_0(\mathbf{X}) + Ze\nabla\Phi_0(\mathbf{X})) \\
& +\omega_{\mathrm{L}}\frac{\partial S_1}{\partial\theta} + \frac{v_\|}{B_{0\|}^*}Ze\widetilde{\mathbf{A}}_1(\mathbf{x})\cdot\mathbf{B}_0^*(\mathbf{X}) \\
& +Ze\left(\langle\mathbf{A}_1(\mathbf{x})\cdot\mathbf{v}_{\mathrm{L}}(\mathbf{X},\mu,\theta)\rangle + (\mathbf{A}_1(\mathbf{x})\cdot\mathbf{v}_{\mathrm{L}}(\mathbf{X},\mu,\theta))^{\mathrm{osc}}\right)
\end{aligned}$$

where $\mathbf{v}_{\mathrm{L}}(\mathbf{X},\mu,\theta) = v_{\mathrm{L}}(\mathbf{X},\mu)\frac{\partial\mathbf{a}(\theta)}{\partial\theta}$. The word "osc" in superscript is the same as $\widetilde{\ }$, it denotes the oscillating part of the quantity between the brackets.

In order to remove the oscillating quantities from the Lagrangian, the term $\omega_{\mathrm{L}}\frac{\partial S_1}{\partial\theta}$ has to cancel them all. This leads to the following equation for S_1:

$$\begin{aligned}
\frac{\partial S_1}{\partial\theta} = & \frac{1}{\omega_{\mathrm{L}}}\left(Ze\widetilde{\Phi}_1(\mathbf{x}) + \frac{1}{B_{0\|}^*}\widetilde{\mathbf{A}}_1(\mathbf{x})\times\mathbf{b}_0(\mathbf{X})\cdot(\mu\nabla B_0(\mathbf{X}) + Ze\nabla\Phi_0(\mathbf{X})) - \right. \\
& \left. \frac{v_\|}{B_{0\|}^*}Ze\widetilde{\mathbf{A}}_1(\mathbf{x})\cdot\mathbf{B}_0^*(\mathbf{X}) - Ze\left(\mathbf{A}_1(\mathbf{x})\cdot\mathbf{v}_{\mathrm{L}}(\mathbf{X},\mu,\theta)\right)^{\mathrm{osc}}\right).
\end{aligned}$$

As a result, the total gyro-centre Lagrangian becomes

$$\begin{aligned}\bar{\Gamma} &= \bar{\Gamma}_0 + \bar{\Gamma}_1 = \left(mv_\parallel \mathbf{b}_0(\mathbf{X}) + m\mathbf{u}_0 + Ze\mathbf{A}_0(\mathbf{X}) + Ze\langle \mathbf{A}_1(\mathbf{x})\rangle\right)\cdot \mathrm{d}\mathbf{X} + \frac{2\mu m}{Ze}\mathrm{d}\theta - \\ &\left(\frac{1}{2}m\left(v_\parallel^2 - u_0^2\right) + \mu B_0(\mathbf{X}) + Ze\left(\Phi_0(\mathbf{X}) + \langle\Phi_1(\mathbf{x})\rangle\right) - Ze\langle \mathbf{A}_1(\mathbf{x})\cdot\mathbf{v}_\mathrm{L}(\mathbf{X},\mu,\theta)\rangle\right)\mathrm{d}t.\end{aligned} \tag{2.49}$$

The oscillating quantities have thus been systematically removed from the gyro-centre Lagrangian and added to the gauge function. The components of the gyro-centre Lagrangian are again independent of the gyro-phase, and therefore the magnetic moment in the new phase space remains invariant during the particles' motion.

Bessel functions

Gyro-averaging of the fluctuations can be performed in Fourier-space by separating the quantities' dependence on the gyro-centre position and the Larmor-radius vector:

$$\begin{aligned}\langle \mathbf{A}_1(\mathbf{x})\rangle &= \langle \mathbf{A}_1(\mathbf{X}+\mathbf{r})\rangle = \langle \int \hat{\mathbf{A}}_1(\mathbf{k})\mathrm{e}^{i\mathbf{k}\cdot(\mathbf{X}+\mathbf{r})}\mathrm{d}\mathbf{k}\rangle \\ &= \frac{1}{2\pi}\int_0^{2\pi}\int \hat{\mathbf{A}}_1(\mathbf{k})\mathrm{e}^{i\mathbf{k}\cdot\mathbf{X}}\mathrm{e}^{ik_\perp\rho\cos\theta}\mathrm{d}\mathbf{k}\mathrm{d}\theta \\ &= \int \hat{\mathbf{A}}_1(\mathbf{k})\mathrm{e}^{i\mathbf{k}\cdot\mathbf{X}}\underbrace{\frac{1}{2\pi}\int_0^{2\pi}\mathrm{e}^{ik_\perp\rho\cos\theta}\mathrm{d}\theta}_{J_0(\rho k_\perp)}\mathrm{d}\mathbf{k} \\ &= \int J_0(\rho k_\perp)\hat{\mathbf{A}}_1(\mathbf{k})\mathrm{e}^{i\mathbf{k}\cdot\mathbf{X}}\mathrm{d}\mathbf{k} = J_0(\lambda)\mathbf{A}_1(\mathbf{X})\end{aligned}$$

where the vector $\mathbf{r}$ is used in the sense of equation 2.20, and the direction of the basis vector $\mathbf{e}_1$ has been aligned with the wavenumber vector so that $\mathbf{k} = \mathbf{e}_1 k_\perp$ leading to $\mathbf{k}\cdot\mathbf{r} = \rho k_\perp \cos\theta$. J_0 is a zeroth order Bessel function of the first kind as defined in [39]. Its argument becomes $\lambda = i\rho\nabla_\perp$ during the inverse Fourier transformation.

Gyro-averaging of the $\langle \mathbf{A}_1 \cdot \mathbf{v}_\mathrm{L}\rangle$ can be performed in a similar fashion, although through some lengthy algebra. The detailed calculation can be found in Appendix C of [30]. The gyro-averaging process eventually gives

$$\begin{aligned}\langle\Phi_1(\mathbf{x})\rangle &= J_0(\lambda)\Phi_1(\mathbf{X}) \\ \langle \mathbf{A}_1(\mathbf{x})\rangle &= J_0(\lambda)\mathbf{A}_1(\mathbf{X}) \\ Ze\langle \mathbf{A}_1(\mathbf{x})\cdot\mathbf{v}_\mathrm{L}(\mathbf{X},\mu,\theta)\rangle &= -\hat{J}_1(\lambda)\mu B_{1\parallel}(\mathbf{X})\end{aligned}$$

where $\hat{J}_1(z) = \frac{2}{z}J_1(z)$ is a modified first order Bessel function of the first kind.

Substituting the above expressions into the gyro-centre Lagrangian gives

$$\begin{aligned}\bar{\Gamma} &= \left(mv_{\parallel}\mathbf{b}_0(\mathbf{X}) + Ze\mathbf{A}_0(\mathbf{X}) + m\mathbf{u}_0 + ZeJ_0(\lambda)\mathbf{A}_1(\mathbf{X})\right)\cdot \mathrm{d}\mathbf{X} + \frac{2\mu m}{Ze}\mathrm{d}\theta - \\ &\quad \left(\frac{1}{2}m\left(v_{\parallel}^2 - u_0^2\right) + Ze\left(\Phi_0(\mathbf{X}) + J_0(\lambda)\Phi_1(\mathbf{X})\right) + \mu\left(B_0(\mathbf{X}) + \hat{J}_1(\lambda)B_{1\parallel}(\mathbf{X})\right)\right)\mathrm{d}t \\ &= \left(Ze\mathbf{A}_0^*(\mathbf{X}) + Ze\bar{\mathbf{A}}_1(\mathbf{X})\right)\cdot \mathrm{d}\mathbf{X} + \frac{2\mu m}{Ze}\mathrm{d}\theta - \\ &\quad \left(\frac{1}{2}m\left(v_{\parallel}^2 - u_0^2\right) + Ze\left(\Phi_0(\mathbf{X}) + \bar{\Phi}_1(\mathbf{X})\right) + \mu\left(B_0(\mathbf{X}) + \bar{B}_{1\parallel}(\mathbf{X})\right)\right)\mathrm{d}t \qquad (2.50)\end{aligned}$$

where we used $\mathbf{A}_0^* = \mathbf{A}_0 + \frac{m}{Ze}(v_{\parallel}\mathbf{b}_0 + \mathbf{u}_0)$ again and introduced the shorter notations $J_0(\lambda)\Phi_1 = \bar{\Phi}_1$, $J_0(\lambda)\mathbf{A}_1 = \bar{\mathbf{A}}_1$ and $\hat{J}_1(\lambda)B_{1\parallel} = \bar{B}_{1\parallel}$.

2.3.5 Gyrokinetic Vlasov-equation

The time evolution of the distribution function in the phase space is described by the Vlasov equation. In particle phase space without collisions it can be written as

$$\frac{\partial f}{\partial t} + \dot{\mathbf{x}}\cdot\frac{\partial f}{\partial \mathbf{x}} + \dot{\mathbf{v}}\cdot\frac{\partial f}{\partial \mathbf{v}} = 0.$$

Since in gyro-centre phase space the gyro-phase is an ignorable coordinate and the total time derivative of the gyro-centre magnetic moment is zero (see equation (2.53)), the Vlasov equation takes the form

$$\frac{\partial f_{\mathrm{gy}}}{\partial t} + \dot{\mathbf{X}}\cdot\frac{\partial f_{\mathrm{gy}}}{\partial \mathbf{X}} + \dot{v}_{\parallel}\frac{\partial f_{\mathrm{gy}}}{\partial v_{\parallel}} = 0 \qquad (2.51)$$

where f_{gy} is the distribution function of they gyro-centres instead of the particles. In the remainder of this section the "gy" underscript will be dropped for simplicity and f will denote the gyro-centre distribution function unless otherwise stated.

Two important modifications have to be performed on equation 2.51: first, the terms $\dot{\mathbf{X}}$ and $\dot{v}_{\parallel}$ have to be expressed from the gyro-centre Lagrangian through of the Euler–Lagrange equations, and second, the total distribution function f will be decomposed into a sum of an equilibrium and a perturbation part: $f = F + \delta f$ where $\frac{\delta f}{F} \sim \varepsilon_\delta$. The latter step is the so called delta-f approximation.

The Euler–Lagrange equations

According to Scott [37] the Euler–Lagrange equations can be written as

$$\left(\frac{\partial \gamma_j}{\partial z^i} - \frac{\partial \gamma_i}{\partial z^j}\right)\frac{\mathrm{d}z^j}{\mathrm{d}t} = \frac{\partial H}{\partial z^i} + \frac{\partial \gamma_i}{\partial t}. \tag{2.52}$$

After substituting equation 2.50 the equations of motion are directly obtained as

$$\begin{aligned} &m\dot{v}_\parallel \mathbf{b}_0 - Ze\dot{\mathbf{X}} \times \mathbf{B}_0^* - Ze\dot{\mathbf{X}} \times \left(\nabla \times \bar{\mathbf{A}}_1\right) = \\ &\qquad \underbrace{-Ze\nabla\left(\Phi_0 + \bar{\Phi}_1\right) - Ze\frac{\mathrm{d}}{\mathrm{d}t}\bar{\mathbf{A}}_1}_{Ze\bar{\mathbf{E}}} - \mu\nabla\left(B_0 + \bar{B}_{1\parallel}\right) + \frac{1}{2}m\nabla u_0^2 \\ &v_\parallel = \mathbf{b}_0 \cdot \dot{\mathbf{X}} \qquad \dot{\mu} = 0 \qquad \dot{\theta} = \omega_\mathrm{L} - \frac{Ze}{m}\frac{\partial}{\partial \mu}\left(Ze\bar{\mathbf{A}}_1 \cdot \dot{\mathbf{X}} - Ze\bar{\Phi}_1 - \mu\bar{B}_{1\parallel}\right) \end{aligned} \tag{2.53}$$

where the relation $\left(\nabla\mathbf{A} - (\nabla\mathbf{A})^T\right) \cdot \dot{\mathbf{X}} = \dot{\mathbf{X}} \times (\nabla \times \mathbf{A})$ has been applied. Using equation 2.15 the last term in the first equation of 2.53 can be rewritten as $\frac{1}{2}m\nabla u_0^2 = mR\Omega^2\nabla R$.

By introducing the notation $\nabla \times \bar{\mathbf{A}}_1 = \bar{\mathbf{B}}_1$ and taking the cross product with $\mathbf{b}_0$ the time evolution of the gyro-centre position $\dot{\mathbf{X}}$ can be expressed as

$$\begin{aligned} \dot{\mathbf{X}} &= \mathbf{b}_0 v_\parallel + \frac{mv_\parallel^2}{ZeB_0}\left(\nabla \times \mathbf{b}_0\right)_\perp + \frac{\bar{\mathbf{B}}_{1\perp}}{B_0}v_\parallel - \frac{1}{B_0}\bar{\mathbf{E}} \times \mathbf{b}_0 + \\ &\quad \frac{\mu}{ZeB_0}\nabla\left(B_0 + \bar{B}_{1\parallel}\right) \times \mathbf{b}_0 + \frac{2mv_\parallel}{ZeB_0}\boldsymbol{\Omega}_\perp - \frac{mR\Omega^2}{ZeB_0}\nabla R \times \mathbf{b}_0 \\ &= \mathbf{b}_0 v_\parallel + \underbrace{\mathbf{v}_{\bar{\mathbf{B}}_{1\perp}} + \mathbf{v}_{\bar{\mathbf{E}}\times\mathbf{B}_0} + \mathbf{v}_{\nabla\bar{B}_{1\parallel}}}_{\mathbf{v}_\chi} + \underbrace{\mathbf{v}_\mathrm{C} + \mathbf{v}_{\nabla\mathbf{B}_0} + \mathbf{v}_\mathrm{co} + \mathbf{v}_\mathrm{cf}}_{\mathbf{v}_\mathrm{D}}. \end{aligned} \tag{2.54}$$

To obtain equation 2.54 the Taylor expansion

$$\frac{1}{B_{0\parallel}^* + \bar{B}_{1\parallel}} = \frac{1}{B_0}\left(1 - \frac{m}{ZeB_0}\mathbf{b}_0 \cdot \nabla \times \left(v_\parallel \mathbf{b}_0 + \mathbf{u}_0\right) - \frac{\bar{B}_{1\parallel}}{B_0} + O(\rho^2)\right)$$

has been used and the terms were kept up to first order in ρ_*.

The subsequent terms in the first two lines of equation 2.54 denote streaming along the equilibrium magnetic field ($\mathbf{b}_0 v_\parallel$), curvature drift ($\mathbf{v}_\mathrm{C}$), streaming along the perpendicular perturbed magnetic field ($\mathbf{v}_{\bar{\mathbf{B}}_{1\perp}}$), $E \times B$ drift in the total electric field ($\mathbf{v}_{\bar{\mathbf{E}}\times\mathbf{B}_0}$), and grad-$B$ drifts in the gradients of the equilibrium as well as the parallel perturbed magnetic fields ($\mathbf{v}_{\nabla\bar{B}_{1\parallel}}$ and $\mathbf{v}_{\nabla\mathbf{B}_0}$), the Coriolis ($\mathbf{v}_\mathrm{co}$) and centrifugal ($\mathbf{v}_\mathrm{cf}$) drifts, respectively.

Note that the motion along the parallel component of the perturbed magnetic field is missing in equation 2.54, it would only appear in higher orders. The perpendicular component of the perturbed vector potential $\bar{\mathbf{A}}_{1\perp}$ is related to the parallel perturbation of the magnetic field and it has been kept in $\bar{\mathbf{E}}$. However, according to typical normalization assumptions in gyrokinetics (see for example [31]) one can easily show that the time derivative of the vector potential is one order smaller than the gradient of the electrostatic potential and therefore its contribution can be neglected in the $\mathbf{v}_{\bar{\mathbf{E}}\times\mathbf{B}_0}$ velocity.

After dropping the vector potential term from $\mathbf{v}_{\bar{\mathbf{E}}\times\mathbf{B}_0}$, the velocities due to the perturbation of the fields can be written in a more compact form. Let us define the quantity χ as

$$\chi = \underbrace{\Phi_0 + \bar{\Phi}_1}_{\bar{\Phi}} - v_\parallel \bar{A}_{1\parallel} + \frac{\mu}{Ze}\bar{B}_{1\parallel}$$

with which one can write

$$\mathbf{v}_\chi = \frac{\mathbf{b}\times\nabla\chi}{B_0} = \mathbf{v}_{\bar{\mathbf{B}}_{1\perp}} + \mathbf{v}_{\bar{\mathbf{E}}\times\mathbf{B}_0} + \mathbf{v}_{\nabla\bar{B}_{1\parallel}}.$$

The equation for $\dot{v}_\parallel$ is obtained by taking the scalar product of the first equation of equation 2.53 with $\dot{\mathbf{X}}$:

$$\dot{v}_\parallel = \frac{\dot{\mathbf{X}}}{mv_\parallel}\cdot\left(Ze\bar{\mathbf{E}} - \mu\nabla(B_0 + \bar{B}_{1\parallel}) + \frac{1}{2}m\nabla u_0^2\right). \tag{2.55}$$

By substituting the obtained drift velocities it can be shown that the acceleration of the $\bar{\mathbf{E}}\times\mathbf{B}_0$ velocity by the mirror force of the perturbed magnetic field $\mu\nabla\bar{B}_{1\parallel}$ and the acceleration of the $\nabla\bar{B}_{1\parallel}\times\mathbf{B}_0$ velocity by the electric field cancel each other. Noting that $\nabla\bar{\Phi}\perp\nabla\bar{\Phi}\times\mathbf{b_0}$ and $\nabla\bar{B}_{1\parallel}\perp\nabla\bar{B}_{1\parallel}\times\mathbf{b_0}$, the equation of motion for the parallel velocity becomes

$$\dot{v}_\parallel = \frac{\dot{\mathbf{X}}}{mv_\parallel}\cdot\left(-\mu\nabla B_0 + \frac{1}{2}m\nabla u_0^2\right) + \frac{\mathbf{v}_D + \mathbf{v}_{\mathbf{B}_{1\perp}}}{mv_\parallel}\cdot(Ze\bar{\mathbf{E}} - \mu\nabla\bar{B}_{1\parallel}). \tag{2.56}$$

The delta-f approximation

Substituting equations 2.55 and 2.54 into the gyro-centre Vlasov equation 2.51 and applying the delta-f approximation $f = F + \delta f$ leads to

$$\frac{\partial\delta f}{\partial t} + \dot{\mathbf{X}}\cdot\nabla\delta f - \frac{\mathbf{b}_0}{m}\cdot(\nabla\Phi_0 - mR\Omega^2\nabla R + \nabla B_0)\frac{\partial\delta f}{\partial v_\parallel} = \underbrace{-\dot{\mathbf{X}}\cdot\nabla F - \dot{v}_\parallel\frac{\partial F}{\partial v_\parallel}}_{S}. \tag{2.57}$$

Note that in equation 2.57 only the highest order term of $\dot{v}_\parallel$ has to be kept in $\dot{v}_\parallel \frac{\partial \delta f}{\partial v_\parallel}$, the contributions of $\bar{B}_{1\parallel}$ and $\bar{\Phi}_1$ can be neglected.

The equilibrium distribution function is assumed to be a Maxwellian. In a toroidally rotating plasma, a finite radial equilibrium electric field arises in order to balance the centrifugal force (in the co-rotating frame). A combined energy term associated with the kinetic energy of the rotation and the energy stored in the equilibrium electric field has to be included in the Maxwellian. According to [36], in the rotating frame this term can be written as

$$\mathcal{E} = Ze\langle\Phi_0\rangle - \frac{1}{2}m\omega_\varphi^2(R^2 - R_0^2)$$

where the angled brackets denote flux-surface averaging, ω_φ is the plasma rotation frequency profile in the rotating frame as introduced in section 2.3.2, R is the local major radius and R_0 is an integration constant which can be chosen, for example, as the major radius of the plasma or the flux surface average of the major radius [38]. The Maxwellian is written as

$$F = F_\mathrm{M} = \frac{n_0}{(2\pi T/m)^{\frac{3}{2}}} \exp\left(-\frac{\frac{1}{2}m(v_\parallel - u_\parallel)^2 + \mu B_0 + \mathcal{E}}{T}\right) = F_\mathrm{M}(\mathbf{X}, v_\parallel, \mu) \quad (2.58)$$

where n_0 is the equilibrium particle density and $u_\parallel$ is rotation speed of the plasma in the rotating frame parallel to the magnetic field. In a local description, a reference frame rotating with $u_\parallel$ can be chosen in which case $u_\parallel$ vanishes but its gradient has to be taken into account. According to [36] the derivatives of the Maxwellian can be expressed as

$$\begin{aligned}
\nabla F_\mathrm{M} &= \left[\frac{\nabla n_0}{n_0} + \left(\frac{\frac{1}{2}mv_\parallel^2 + \mu B_0 + \mathcal{E}}{T} - \frac{3}{2}\right)\frac{\nabla T}{T} - \frac{\mu B_0}{T}\frac{\nabla B_0}{B_0} + \right. \\
&\quad \left.\left(\frac{mv_\parallel R B_\mathrm{t}}{BT} + m\Omega(R^2 - R_0^2)\right)\nabla\omega_\varphi\right] F_\mathrm{M} \\
\frac{\partial F_\mathrm{M}}{\partial v_\parallel} &= -\frac{mv_\parallel}{T}F_\mathrm{M} \qquad \frac{\partial F_\mathrm{M}}{\partial \mu} = -\frac{B_0}{T}F_\mathrm{M}
\end{aligned} \quad (2.59)$$

where the $\nabla\omega_\varphi$ terms in the gradient are coming from the derivatives of the $u_\parallel$ and $\mathcal{E}$ terms, respectively, and evaluated at zero rotation speed locally in the co-rotating frame. Using equations 2.54, 2.55 and 2.59 it can be shown that the ∇B_0 term in $-\dot{\mathbf{X}}\cdot\nabla F_\mathrm{M}$ cancels with $\frac{\dot{\mathbf{X}}}{mv_\parallel}\mu\nabla B_0\frac{\partial F_\mathrm{M}}{\partial v_\parallel}$. In case of purely toroidal rotation $\nabla R \perp \boldsymbol{\Omega}$, and $\nabla R \perp \nabla R \times \mathbf{b}_0$. Using these expression the source term can be finally written

as

$$\begin{aligned} S &= -\left(\mathbf{v}_\chi + \mathbf{v}_\mathrm{D}\right)\cdot\nabla_p F_\mathrm{M} - \frac{Zev_\parallel}{T}\frac{\partial \bar{A}_{1\parallel}}{\partial t}F_\mathrm{M} \\ &\quad -\frac{F_\mathrm{M}}{T}\left(v_\parallel \mathbf{b}_0 + \mathbf{v}_D + \mathbf{v}_{\mathbf{B}_{1\perp}}\right)\cdot\left(Ze\nabla\bar{\Phi} + \mu\nabla\bar{B}_{1\parallel}\right) \end{aligned}$$

where ∇_p means that only the ∇n, ∇T and $\nabla\omega_\varphi$ terms of ∇F_M are considered [31].

The term containing the time derivative of the perturbed vector potential is computationally difficult to handle. Therefore a modified distribution function g is defined as

$$g = \delta f + \frac{Zev_\parallel}{T}\bar{A}_{1\parallel}F_\mathrm{M}. \tag{2.60}$$

Note that g is not the non-adiabatic part of the distribution function, as it typically appears in the literature. The perturbed part of the distribution function δf is replaced with g in the first term of the left hand side of the Vlasov-equation 2.57, and also in the second term where it is multiplied by $\mathbf{v}_\chi$. In the remaining part of the second term, where it is multiplied by $\mathbf{b}_0 v_\parallel + \mathbf{v}_\mathrm{D}$ the original distribution function is kept. It can be easily shown that as a result of this substitutions the $\mathbf{v}_{\mathbf{B}_{1\perp}}$ term in the source cancels out and the equation simplifies to

$$\frac{\partial g}{\partial t} + \mathbf{v}_\chi\cdot\nabla g + \left(v_\parallel\mathbf{b}_0 + \mathbf{v}_\mathrm{D}\right)\cdot\nabla\delta f - \frac{\mathbf{b}_0}{m}\cdot\left(\nabla\Phi_0 - mR\Omega^2\nabla R + \nabla B_0\right)\frac{\partial\delta f}{\partial v_\parallel} = S \tag{2.61}$$

with the source term being

$$S = -\left(\mathbf{v}_\chi + \mathbf{v}_\mathrm{D}\right)\cdot\nabla_p F_\mathrm{M} + \frac{F_\mathrm{M}}{T}\left(v_\parallel\mathbf{b}_0 + \mathbf{v}_D\right)\cdot\left(-Ze\nabla\bar{\Phi}_1 - \mu\nabla\bar{B}_{1\parallel}\right). \tag{2.62}$$

This is the form of the Vlasov-equation currently implemented in the code GKW. The normalized version of its terms is found in [31]. The effect of the magnetic compression on the Vlasov-equation is that a new velocity term, $\mathbf{v}_{\nabla\bar{B}_{1\parallel}}$ describing the grad-B drift in the parallel perturbation of the magnetic field, and an associated mirror force in the source term appear.

2.3.6 Maxwell's Equations in Gyro-centre Coordinates

In order to obtain a self-consistent system of equations, the perturbed electromagnetic fields must be calculated with Maxwell's equations. In typical fusion plasmas the Gauss law is replaced by the quasi-neutrality condition. This expresses that any deviation from neutrality can only happen at small length scales (within the Debye-length) and on a time scale much shorter than that of the fluctuations. The

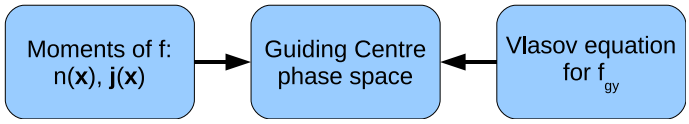

Figure 2.3: Idea of gyrokinetic Maxwell's equations: The density and current of particles as well as the gyro-centre distribution function are expressed in guiding centre phase space.

displacement current in Ampère's law is also neglected due to the non-relativistic time scale of the turbulence. With these assumptions the Maxwell-equations can be written as

$$\sum_{\mathrm{sp}} Z_{\mathrm{sp}} e n_{\mathrm{sp}} = 0 \qquad \nabla \times \mathbf{E}_1 = -\frac{\partial \mathbf{B}_1}{\partial t}$$
$$\nabla \cdot \mathbf{B}_1 = 0 \qquad \nabla \times \mathbf{B}_1 = \mu_0 \sum_{\mathrm{sp}} \mathbf{j}_{\mathrm{sp}}.$$

These equations contain densities and currents of particles that can be expressed by taking the moments of the particle phase space distribution function. The Vlasov equation, however, describes the evolution of the distribution function in the gyro-centre phase space. The connection between them is recovered by expressing the particle moments with the guiding-centre distribution function and by pulling back the gyro-centre distribution function to the guiding-centre phase space. That is, Maxwell's equations in gyrokinetic theory are written in the guiding-centre phase space (see figure 2.3).

As a first step, the particle densities and currents of one species are expressed with the guiding-centre distribution function:

$$n(\mathbf{x}) = \int f(\mathbf{x},\mathbf{v})\mathrm{d}\mathbf{v} = \frac{B_0}{m}\int \delta(\mathbf{X}+\mathbf{r}-\mathbf{x}) f_{\mathrm{gc}} \mathrm{d}\mathbf{X}\mathrm{d}v_\parallel \mathrm{d}\theta \mathrm{d}\mu \tag{2.63}$$
$$j_\parallel = Ze\int v_\parallel f(\mathbf{x},\mathbf{v})\mathrm{d}\mathbf{v} = \frac{ZeB_0}{m}\int \delta(\mathbf{X}+\mathbf{r}-\mathbf{x}) v_\parallel f_{\mathrm{gc}} \mathrm{d}\mathbf{X}\mathrm{d}v_\parallel \mathrm{d}\theta \mathrm{d}\mu \tag{2.64}$$
$$\mathbf{j}_\perp = Ze\int \mathbf{v}_{\mathrm{L}} f(\mathbf{x},\mathbf{v})\mathrm{d}\mathbf{v} = \frac{ZeB_0}{m}\int \delta(\mathbf{X}+\mathbf{r}-\mathbf{x}) \mathbf{v}_{\mathrm{L}} f_{\mathrm{gc}} \mathrm{d}\mathbf{X}\mathrm{d}v_\parallel \mathrm{d}\theta \mathrm{d}\mu \tag{2.65}$$

where $\mathbf{r}$ is the vector pointing from the centre of the Larmor orbit to the particle's position. The $\frac{B_0}{m}$ factor is the Jacobian. Formally, the delta function appears since the change of coordinates affects the whole phase space while the integral goes only

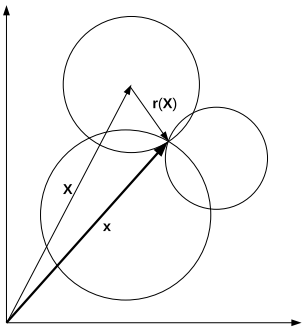

Figure 2.4: The connection between the density of particles and density of guiding-centres.

over the velocity subspace. It guarantees that the spatial region taken into account in the integral remains unchanged during the coordinate transformation. Physically, this expresses a condition that all the particles that have a Larmor orbit crossing a given point $\mathbf{x}$ in real space contribute to the particle density there (see figure 2.4).

The second step is to express the guiding-centre distribution function with the gyro-centre one and write it into equations 2.63-2.65. Since the distribution function is a regular function (or zero-form) on the manifold, it is transformed by the pull-back operator:

$$f_{\mathrm{gc}} = \Phi^* f_{\mathrm{gy}} = \mathrm{e}^{\varepsilon \mathcal{L}_{G_1}} f_{\mathrm{gy}} \approx (1 + \varepsilon \mathcal{L}_{G_1})\, f_{\mathrm{gy}} = f_{\mathrm{gy}} + G_1^{\nu} \frac{\partial f_{\mathrm{gy}}}{\partial Z^{\nu}}. \tag{2.66}$$

Substituting the components of the generator vector field derived in section 2.3.4, the expressions that connect the gyro-centre and guiding-centre distribution function are directly obtained. The delta-f approximation is applied once again and the equilibrium part of the gyro-centre distribution function f_{gy} is assumed Maxwellian (equation 2.58). Since the generator functions are already first order in ρ_*, in the second part of equation 2.66 only the equilibrium distribution function F_{M} must be taken into account. Also, as ∇F_{M} only contains first order terms in ρ_* the term

$G_1^{\mathbf{X}} \cdot \nabla F_{\mathrm{M}}$ can be dropped. The resulting transformation formula is

$$\begin{aligned} G_1^{\mu}\frac{\partial F_{\mathrm{M}}}{\partial \mu} &= \frac{1}{B_0}\left(Ze\widetilde{\Phi}_1 - Zev_{\parallel}\widetilde{A}_{1\parallel} - Ze\left(\widetilde{\mathbf{A}_1 \cdot \mathbf{v}_{\mathrm{L}}}\right) + Zev_{\mathrm{L}}\left|\mathbf{A}_{1\perp}\right|\right)\frac{\partial F_{\mathrm{M}}}{\partial \mu} \\ &= \frac{1}{B_0}\left(Ze\widetilde{\Phi}_1 - Zev_{\parallel}\widetilde{A}_{1\parallel} - Ze\langle \mathbf{A}_1 \cdot \mathbf{v}_{\mathrm{L}}\rangle\right)\frac{\partial F_{\mathrm{M}}}{\partial \mu} \\ &= -\frac{1}{T}\left(Ze\widetilde{\Phi}_1 - Zev_{\parallel}\widetilde{A}_{1\parallel} + \mu\bar{B}_{1\parallel}\right)F_{\mathrm{M}} \end{aligned}$$

$$G_1^{v_{\parallel}}\frac{\partial F_{\mathrm{M}}}{\partial v_{\parallel}} = -Ze\frac{v_{\parallel}}{T}\widetilde{A}_{1\parallel}F_{\mathrm{M}}$$

$$f_{\mathrm{gc}} = f_{\mathrm{gy}} + G_1^{\mu}\frac{\partial F_{\mathrm{M}}}{\partial \mu} + G_1^{v_{\parallel}}\frac{\partial F_{\mathrm{M}}}{\partial v_{\parallel}} = f_{\mathrm{gy}} - \frac{F_{\mathrm{M}}}{T}\left(Ze\widetilde{\Phi}_1 - \mu\bar{B}_{1\parallel}\right). \quad (2.67)$$

The two correction terms appearing in equation 2.67 containing the fluctuations of the electro-magnetic fields are the results of the pull-back transformation from the gyro-centre to the guiding centre phase space. Physically, they describe the polarization and magnetization effects of the fluctuations on the gyro-orbit [12].

Normalization

The field equations derived in the following sections will be normalized as detailed in [31]. The definition of the normalized quantities is reiterated here for the sake of completeness. A reference mass m_{ref}, density n_{ref}, temperature T_{ref}, magnetic field B_{ref} and major radius R_{ref} is chosen. These are then used to define the reference thermal velocity $T_{\mathrm{ref}} = \frac{1}{2}m_{\mathrm{ref}}v_{\mathrm{th,ref}}^2$ and reference thermal Larmor radius $\rho_{\mathrm{ref}} = \frac{m_{\mathrm{ref}}v_{\mathrm{th,ref}}}{eB_{\mathrm{ref}}}$. The normalized major radius and equilibrium magnetic field are simply $R = R_{\mathrm{ref}}R_{stN}$ and $B = B_{\mathrm{ref}}B_{\mathrm{N}}$. For convenience, the small parameter ρ_* is redefined with the reference values as $\rho_* = \frac{\rho_{\mathrm{ref}}}{R_{\mathrm{ref}}}$. The reference quantities are used to define the dimensionless relative quantities

$$m_{\mathrm{R}} = \frac{m}{m_{\mathrm{ref}}} \qquad n_{\mathrm{R}} = \frac{n}{n_{\mathrm{ref}}} \qquad T_{\mathrm{R,sp}} = \frac{T}{T_{\mathrm{ref}}} \qquad v_{\mathrm{R}} = \frac{v_{\mathrm{th}}}{v_{\mathrm{th,ref}}}. \quad (2.68)$$

The fluctuating fields are normalized as

$$\Phi_1 = \rho_*\frac{T_{\mathrm{ref}}}{e}\Phi_{1\mathrm{N}} \qquad A_{1\parallel} = B_{\mathrm{ref}}R_{\mathrm{ref}}\rho_*^2 A_{1\parallel\mathrm{N}} \qquad B_{1\parallel} = \rho_* B_{\mathrm{ref}}B_{1\parallel\mathrm{N}}. \quad (2.69)$$

The time and the angular rotation frequency are normalized using the reference thermal velocity as

$$t = \frac{R_{\mathrm{ref}}}{v_{\mathrm{th,ref}}} t_{\mathrm{N}} \qquad \Omega = \frac{v_{\mathrm{th,ref}}}{R_{\mathrm{ref}}} \Omega_{\mathrm{N}} \tag{2.70}$$

whereas the velocity space coordinates and the distribution functions are normalized with the thermal velocity to maintain their species dependence:

$$v_{\parallel} = v_{\mathrm{th}} v_{\parallel \mathrm{N}} \qquad \mu = \frac{m v_{\mathrm{th}}^2}{e B_{\mathrm{ref}}} \qquad \delta f = \rho_* \frac{n}{v_{\mathrm{ref}}^3} \delta f_{\mathrm{N}} \qquad F_{\mathrm{M}} = \frac{n}{v_{\mathrm{ref}}^3} F_{\mathrm{M,N}}. \tag{2.71}$$

Finally, the parallel and perpendicular gradients of the equilibrium and the wavenumber of the fluctuations are normalized, respectively, as

$$\nabla_{\perp} = \frac{1}{R_{\mathrm{ref}}} \nabla_{\perp \mathrm{N}} \qquad \nabla_{\parallel} = \frac{1}{R_{\mathrm{ref}}} \nabla_{\parallel \mathrm{N}} \qquad k = \frac{k_{\mathrm{N}}}{\rho_*}. \tag{2.72}$$

Gyrokinetic Poisson equation

The derivation of the gyrokinetic Maxwell-equations is now straightforward: the distribution function transformed from gyro-centre to guiding-centre phase space by equation 2.67 has to be substituted to the guiding-centre particle density and current equations 2.63-2.65. Equation 2.63 takes the form

$$\begin{aligned} n(\mathbf{x}) &= \frac{B_0}{m} \int \delta(\mathbf{X} + \mathbf{r} - \mathbf{x}) \left(f_{\mathrm{gy}}(\mathbf{X}) - \frac{F_{\mathrm{M}}}{T} \left(Ze\widetilde{\Phi}_1(\mathbf{X} + \mathbf{r}) - \bar{B}_{1\parallel}(\mathbf{X}) \right) \right) \mathrm{d}\mathbf{X} \mathrm{d}v_{\parallel} \mathrm{d}\theta \mathrm{d}\mu \\ &= \bar{n}(\mathbf{x}) - \frac{B_0}{m} \int \delta(\mathbf{X} + \mathbf{r} - \mathbf{x}) \left(Ze\widetilde{\Phi}_1(\mathbf{X} + \mathbf{r}) - \mu \bar{B}_{1\parallel}(\mathbf{X}) \right) \frac{F_{\mathrm{M}}}{T} \mathrm{d}\mathbf{X} \mathrm{d}v_{\parallel} \mathrm{d}\theta \mathrm{d}\mu \end{aligned}$$

where the density of gyro-centres $\bar{n}$ has been introduced. Note that the distribution functions f_{gy} depends on $\mathbf{X}$ as well as the velocity coordinates $v_{\parallel}$, μ and θ. Here, however, only the spatial dependence is indicated for the gyroaveraging. Writing the oscillating part of the perturbed potential as $\widetilde{\Phi}_1(\mathbf{X} + \mathbf{r}) = \Phi_1(\mathbf{X} + \mathbf{r}) - \bar{\Phi}_1(\mathbf{X})$ and integrating the $\Phi_1(\mathbf{X} + \mathbf{r})$ term yields

$$\begin{aligned} n(\mathbf{x}) &= \bar{n}(\mathbf{x}) - \frac{Ze\Phi_1(\mathbf{x})}{T} n_0(\mathbf{x}) \\ &\quad + \frac{B_0}{m} \int \delta(\mathbf{X} + \mathbf{r} - \mathbf{x}) \left(Ze\bar{\Phi}_1(\mathbf{X}) + \mu \bar{B}_{1\parallel}(\mathbf{X}) \right) \frac{F_{\mathrm{M}}}{T} \mathrm{d}\mathbf{X} \mathrm{d}v_{\parallel} \mathrm{d}\theta \mathrm{d}\mu \end{aligned}$$

where n_0 is the equilibrium particle density. The factor $\frac{F_{\mathrm{M}}}{T}$ changes on the equilibrium length scale. Therefore, its weak spatial dependence has been neglected in the previous step compared to the fast variation of the fluctuating Φ_1. The integral over $\mathbf{X}$ together with the delta function changes the arguments of the fields to $\mathbf{x} - \mathbf{r}$.

After integrating over θ this results

$$\begin{aligned} n(\mathbf{x}) &= \bar{n}(\mathbf{x}) - \frac{Ze\Phi_1(\mathbf{x})}{T} n_0(\mathbf{x}) \\ &\quad + \frac{2\pi B_0}{m} \int J_0(\lambda) \left(Ze\bar{\Phi}_1(\mathbf{x}) + \mu \bar{B}_{1\parallel}(\mathbf{x}) \right) \frac{F_\mathrm{M}}{T} \mathrm{d}v_\parallel \mathrm{d}\mu \end{aligned}$$

where $\lambda^2 = -\rho^2 \nabla_\perp^2$. Performing the $v_\parallel$ integral is straightforward as it is only the Maxwellian that depends on it:

$$\begin{aligned} F_\mathrm{M} &= F_\mathrm{M}(\mu) \mathrm{e}^{-\frac{m(v_\parallel - u_\parallel)^2}{2T}} \mathrm{e}^{-\frac{\mathcal{E}}{T}} \\ n(\mathbf{x}) &= \bar{n}(\mathbf{x}) - \frac{Ze\Phi_1(\mathbf{x})}{T} n_0(\mathbf{x}) \\ &\quad + \frac{B_0}{\sqrt{T}} \left(\frac{2\pi}{m} \right)^{\frac{3}{2}} \mathrm{e}^{\frac{-\mathcal{E}}{T}} \int F_\mathrm{M}(\mu) J_0(\lambda) \left(Ze\bar{\Phi}_1(\mathbf{x}) + \mu \bar{B}_{1\parallel}(\mathbf{x}) \right) \mathrm{d}\mu. \end{aligned}$$

In order to evaluate the integrals of the Bessel functions, let us introduce the new variable $x = \frac{\mu B}{T}$, leading to $\lambda^2 = 2xb$, $b = -\rho_\mathrm{th}^2 \nabla_\perp^2$, where ρ_th is the thermal Larmor radius. The two remaining integrals are of the form

$$\int_0^\infty J_0^2(\sqrt{2bx}) \mathrm{e}^{-x} \mathrm{d}x \qquad \int_0^\infty J_0(\sqrt{2bx}) \hat{J}_1(\sqrt{2bx}) \sqrt{x} \mathrm{e}^{-x} \mathrm{d}x.$$

For the details of evaluating these integrals see appendix A. The results are

$$\mathrm{e}^{-b} I_0(b) \qquad \mathrm{e}^{-b} \left(I_0(b) - I_1(b) \right),$$

respectively, where I_n is the n-th order modified Bessel function of the first kind. Using the notation $\Gamma_n(b) = I_n(b)\mathrm{e}^{-b}$, the expression for the particle density can be written as

$$n(\mathbf{x}) = \bar{n}(\mathbf{x}) - \frac{Ze\Phi_1(\mathbf{x})}{T} n_0(\mathbf{x}) + n_0 \mathrm{e}^{\frac{-\mathcal{E}}{T}} \left(\Gamma_0(b) \frac{Ze\Phi_1(\mathbf{x})}{T} + (\Gamma_0(b) - \Gamma_1(b)) \frac{B_{1\parallel}(\mathbf{x})}{B_0} \right).$$

The quasineutrality equation $\sum_\mathrm{sp} Z_\mathrm{sp} e n_\mathrm{sp} = 0$ gives

$$\begin{aligned} &\sum_\mathrm{sp} Z_\mathrm{sp} e \left(1 - \mathrm{e}^{\frac{-\mathcal{E}_\mathrm{sp}}{T_\mathrm{sp}}} \Gamma_0(b_\mathrm{sp}) \right) \frac{Z_\mathrm{sp} e \Phi_1(\mathbf{x}) n_{0,\mathrm{sp}}}{T_\mathrm{sp}} = \\ &\qquad \sum_\mathrm{sp} Z_\mathrm{sp} e \left(\bar{n}_\mathrm{sp} + \mathrm{e}^{\frac{-\mathcal{E}_\mathrm{sp}}{T_\mathrm{sp}}} \left(\Gamma_0(b_\mathrm{sp}) - \Gamma_1(b_\mathrm{sp}) \right) \frac{B_{1\parallel}(\mathbf{x}) n_{0,\mathrm{sp}}}{B_0} \right). \end{aligned} \tag{2.73}$$

In order to bring this equation to the form implemented in GKW, the mod-

ified distribution function g has to be applied. When substituting equation 2.60 into the definition of the gyro-centre density, it can be seen that the second term provides zero contribution since it contains the product of F_M, which is symmetric in $v_\parallel$, with $v_\parallel$, which is antisymmetric:

$$\begin{aligned}\bar{n}(\mathbf{x}) &= \frac{B_0}{m}\int \delta(\mathbf{X}+\mathbf{r}-\mathbf{x}) f_\mathrm{gy}(\mathbf{X})\mathrm{d}\mathbf{X}\mathrm{d}v_\parallel \mathrm{d}\mu\mathrm{d}\theta \\ &= \frac{2\pi B_0}{m}\int J_0(\lambda)\left(g(\mathbf{x}) - \frac{F_\mathrm{M}}{T}v_\parallel Ze\bar{A}_{1\parallel}\right)\mathrm{d}v_\parallel\mathrm{d}\mu = \frac{2\pi B_0}{m}\int J_0(\lambda) g(\mathbf{x})\mathrm{d}v_\parallel\mathrm{d}\mu.\end{aligned}$$

After Fourier-transforming and applying the normalizing expressions of section 2.3.6, the gyrokinetic Poisson equation finally takes the form

$$\begin{aligned}&\sum_\mathrm{sp} Z_\mathrm{sp} n_\mathrm{R,sp}\left[2\pi B_\mathrm{N}\int J_0(k_\perp\rho_\mathrm{sp})\hat{g}_\mathrm{N,sp}\mathrm{d}v_{\parallel N}\mathrm{d}\mu_\mathrm{N} + \right. \\ &\left.\frac{Z_\mathrm{sp}}{T_\mathrm{R,sp}}\hat{\Phi}_{1\mathrm{N}}\left(\mathrm{e}^{\frac{-\mathcal{E}_\mathrm{N,sp}}{T_\mathrm{R,sp}}}\Gamma_0(b_\mathrm{sp}) - 1\right) + \frac{\hat{B}_{1\parallel\mathrm{N}}}{B_\mathrm{N}}\mathrm{e}^{\frac{-\mathcal{E}_\mathrm{N,sp}}{T_\mathrm{R,sp}}}\left(\Gamma_0(b_\mathrm{sp}) - \Gamma_1(b_\mathrm{sp})\right)\right] = 0 \quad (2.74)\end{aligned}$$

Since the equation does not contain spatial derivatives of the fields and the distribution function, and they are linear in every term, the Fourier transform simply results in the Fourier components $\hat{g}_\mathrm{N,sp}(\mathbf{k})$, $\hat{\Phi}_{1\mathrm{N}}(\mathbf{k})$ and $\hat{B}_{1\parallel\mathrm{N}}(\mathbf{k})$.

Equation for $A_{1\parallel}$

The method to calculate the equation of the parallel perturbation of the vector potential is analogous to that used for the Poisson-equation. The starting point is the parallel component of Ampère's law. It is first transformed into guiding-centre coordinates, then the guiding-centre distribution function is expressed with the pull-back of its gyro-centre counterpart.

The parallel component of Ampère's law using Coulomb gauge $\nabla\cdot\mathbf{A}_1 = 0$ can be written as

$$\nabla^2\mathbf{A}_{1\parallel} = \mu_0\mathbf{j}_{1\parallel}. \quad (2.75)$$

The parallel perturbation of the current density is expressed with equation 2.64.

After applying equation 2.67 it takes the form

$$\begin{aligned} j_{1\parallel} &= \frac{ZeB_0}{m}\int v_\parallel \delta(\mathbf{X}+\mathbf{r}-\mathbf{x})\left[f_{\mathrm{gy}}(\mathbf{X}) - \frac{F_{\mathrm{M}}}{T}\left(Ze\widetilde{\Phi}_1(\mathbf{X}+\mathbf{r}) - \mu\bar{B}_{1\parallel}(\mathbf{X})\right)\right]\mathrm{d}\mathbf{X}\mathrm{d}v_\parallel\mathrm{d}\mu\mathrm{d}\theta \\ &= \frac{ZeB_0}{m}\int v_\parallel \delta(\mathbf{X}+\mathbf{r}-\mathbf{x}) f_{\mathrm{gy}}(\mathbf{X})\mathrm{d}\mathbf{X}\mathrm{d}v_\parallel\mathrm{d}\mu\mathrm{d}\theta - \frac{ZeB_0}{m}\underbrace{\int v_\parallel F_{\mathrm{M}}(v_\parallel)\mathrm{d}v_\parallel}_{0}\int(\dots)\mathrm{d}\mathbf{X}\mathrm{d}\mu\mathrm{d}\theta \\ &= \frac{2\pi ZeB_0}{m}\int v_\parallel J_0(\lambda) f_{\mathrm{gy}}(\mathbf{x})\mathrm{d}v_\parallel\mathrm{d}\mu. \end{aligned}$$

Substituting equation 2.60 gives

$$j_{1\parallel} = \frac{2\pi ZeB_0}{m}\int v_\parallel J_0(\lambda) g\mathrm{d}v_\parallel\mathrm{d}\mu - \frac{2\pi ZeB_0}{m}\int v_\parallel^2 J_0(\lambda)\frac{F_{\mathrm{M}}}{T}Ze\bar{A}_{1\parallel}\mathrm{d}v_\parallel\mathrm{d}\mu.$$

In the second term the integral over $v_\parallel$ can be performed by parts leading to

$$-B_0 Zem^{-2}v_{\mathrm{th}}^{-2}\frac{n_0 A_{1\parallel}}{\sqrt{2}}\mathrm{e}^{\frac{-\mathcal{E}}{T}}\underbrace{\int J_0^2(\lambda)\mathrm{e}^{-\frac{\mu B_0}{T}}\mathrm{d}\mu}_{\frac{T}{B_0}\Gamma_0(b)},$$

and so the total expression for $j_{1\parallel}$ becomes

$$j_{1\parallel} = \frac{2\pi B_0 Ze}{m}\int v_\parallel J_0(\lambda) g\mathrm{d}v_\parallel\mathrm{d}\mu - \frac{Zen_0}{m}\mathrm{e}^{\frac{-\mathcal{E}}{T}}\Gamma_0(b)A_{1\parallel}.$$

Summing the above expression over the species, substituting into Ampère's law, Fourier transforming and applying the normalization equations yield

$$\begin{aligned} &\left[k_{\perp\mathrm{N}}^2 + \beta_{\mathrm{ref}}\sum_{\mathrm{sp}}\frac{Z_{\mathrm{sp}}^2 n_{\mathrm{R,sp}}}{m_{\mathrm{R,sp}}}\mathrm{e}^{\frac{-\mathcal{E}_{\mathrm{N,sp}}}{T_{\mathrm{R,sp}}}}\Gamma_0(b_{\mathrm{sp}})\right]\hat{A}_{1\parallel\mathrm{N}} = \\ &2\pi B_{\mathrm{N}}\beta_{\mathrm{ref}}\sum_{\mathrm{sp}} Z_{\mathrm{sp}} n_{\mathrm{R,sp}} v_{\mathrm{R,sp}}\int v_{\parallel N} J_0(k_\perp\rho_{\mathrm{sp}})\hat{g}_{\mathrm{N,sp}}\mathrm{d}v_{\parallel N}\mathrm{d}\mu_N \end{aligned} \tag{2.76}$$

where the reference plasma beta has been defined as

$$\beta_{\mathrm{ref}} = \frac{2\mu_0 n_{\mathrm{ref}} T_{\mathrm{ref}}}{B_{\mathrm{ref}}^2}. \tag{2.77}$$

Equation for $B_{1\parallel}$

The perpendicular component of Ampère's law can be written as

$$(\nabla \times \mathbf{B}_1)_\perp = \begin{pmatrix} \partial_y B_{1\parallel} - \partial_z B_{1y} \\ \partial_z B_{1x} - \partial_x B_{1\parallel} \end{pmatrix} = \mu_0 \mathbf{j}_{1\perp}$$

where z is the direction of the equilibrium magnetic field. The parallel gradients of the perturbed quantities can be neglected since they are one order smaller than perpendicular ones, giving

$$\begin{pmatrix} \partial_y B_{1\parallel} \\ -\partial_x B_{1\parallel} \end{pmatrix} = \nabla_\perp B_{1\parallel} \times \mathbf{b} = \mu_0 \mathbf{j}_{1\perp}.$$

Taking the cross-product of the above equation with $\mathbf{b}$ from the left gives

$$\mu_0 \mathbf{b} \times \mathbf{j}_{1\perp} = \mathbf{b} \times \nabla_\perp B_{1\parallel} \times \mathbf{b} = \nabla_\perp B_{1\parallel}.$$

Using equation 2.65, assuming zero equilibrium current $\mathbf{j}_0 = 0$, summing over species and dotting with $\mathbf{k}_\perp$ leads to

$$\begin{aligned}
\mathbf{k}_\perp \cdot \nabla_\perp B_{1\parallel} &= \mu_0 B_0 e \sum_{\text{sp}} \frac{Z_{\text{sp}}}{m_{\text{sp}}} \int \delta(\mathbf{X} + \mathbf{r} - \mathbf{x}) \underbrace{\mathbf{k}_\perp \cdot \mathbf{b} \times \mathbf{v}_{\text{L}}}_{\mathbf{v}_{\text{L}} \cdot (\mathbf{k}_\perp \times \mathbf{b})} \\
&\quad \left(f_{\text{gy,sp}} - \left(Z_{\text{sp}} e \widetilde{\Phi}_1 - \mu \bar{B}_{1\parallel} \right) \frac{F_{\text{M}}}{T_{\text{sp}}} \right) \mathrm{d}\mathbf{X} \mathrm{d}v_\parallel \mathrm{d}\mu \mathrm{d}\theta \\
&= \mu_0 B_0 e \sum_{\text{sp}} \frac{Z_{\text{sp}}}{m_{\text{sp}}} \left[\int \mathbf{v}_{\text{L}} \cdot (\mathbf{k}_\perp \times \mathbf{b}(\mathbf{x})) f_{\text{gy,sp}}(\mathbf{x} - \mathbf{r}) \mathrm{d}v_\parallel \mathrm{d}\mu \mathrm{d}\theta \right. \\
&\quad \left. + \int \mathbf{v}_{\text{L}} \cdot (\mathbf{k}_\perp \times \mathbf{b}(\mathbf{x})) \frac{F_{\text{M}}}{T_{\text{sp}}} \left(Z_{\text{sp}} e \bar{\Phi}_1(\mathbf{x} - \mathbf{r}) + \mu \bar{B}_{1\parallel}(\mathbf{x} - \mathbf{r}) \right) \mathrm{d}v_\parallel \mathrm{d}\mu \mathrm{d}\theta \right].
\end{aligned}$$

Performing the θ-integral gives (for details see [30], Appendix C)

$$\begin{aligned}
\mathbf{k}_\perp \cdot \nabla_\perp B_{1\parallel} &= -2\pi \mu_0 B_0 e \sum_{\text{sp}} \frac{Z_{\text{sp}}}{|Z_{\text{sp}}|} \frac{Z_{\text{sp}}}{m_{\text{sp}}} \left[v_{\text{L}} \int \frac{\mathrm{d}^3 k}{(2\pi)^3} \left(i k_\perp^2 (\mathbf{k}_\perp \times \mathbf{b} \cdot \mathbf{e}_1 \hat{f}_{\text{gy,sp}}) - \right. \right. \\
&\quad \left. i k_\perp^1 (\mathbf{k}_\perp \times \mathbf{b} \cdot \mathbf{e}_2 \hat{f}_{\text{gy,sp}}) \right) \frac{\rho_{\text{sp}}}{2} \hat{J}_1(k_\perp \rho_{\text{sp}}) \mathrm{e}^{i\mathbf{k}\cdot\mathbf{r}} \mathrm{d}v_\parallel \mathrm{d}\mu + \\
&\quad v_{\text{L}} \int \frac{\mathrm{d}^3 k}{(2\pi)^3} i k_\perp^2 \left(\mathbf{k}_\perp \times \mathbf{b} \cdot \mathbf{e}_1 \frac{F_{\text{M}}}{T_{\text{sp}}} \left(Z_{\text{sp}} e \hat{\bar{\Phi}}_1 + \mu \hat{\bar{B}}_{1\parallel} \right) \right) - \\
&\quad \left. i k_\perp^1 \left(\mathbf{k}_\perp \times \mathbf{b} \cdot \mathbf{e}_2 \frac{F_{\text{M}}}{T_{\text{sp}}} \left(Z_{\text{sp}} e \hat{\bar{\Phi}}_1 + \mu \hat{\bar{B}}_{1\parallel} \right) \right) \frac{\rho_{\text{sp}}}{2} \hat{J}_1(k_\perp \rho_{\text{sp}}) \mathrm{e}^{i\mathbf{k}\cdot\mathbf{r}} \mathrm{d}v_\parallel \mathrm{d}\mu \right].
\end{aligned}$$

It can be easily shown that $\mathbf{k}_\perp \times \mathbf{b} \cdot \mathbf{e}_1 = k_\perp^2$ and $\mathbf{k}_\perp \times \mathbf{b} \cdot \mathbf{e}_2 = -k_\perp^1$, where the upper indices represent contravariant components. Fourier transforming both sides, dividing by the perpendicular wavenumber and transforming back to real space results

$$\begin{aligned} ik_\perp^2 \hat{B}_{1\parallel} &= -2\pi B_0 e \mu_0 \sum_{\mathrm{sp}} \frac{Z_{\mathrm{sp}}}{|Z_{\mathrm{sp}}|} \frac{Z_{\mathrm{sp}}}{m_{\mathrm{sp}}} \left[v_{\mathrm{L}} \int ik_\perp^2 \hat{f}_{\mathrm{gy,sp}} \frac{\rho_{\mathrm{sp}}}{2} \hat{J}_1(k_\perp \rho_{\mathrm{sp}}) \mathrm{d}v_\parallel \mathrm{d}\mu + \right. \\ &\quad \left. v_{\mathrm{L}} \int ik_\perp^2 \left(Z_{\mathrm{sp}} e \hat{\tilde{\Phi}}_1 + \mu \hat{\tilde{B}}_{1\parallel} \right) \frac{F_{\mathrm{M}}}{T_{\mathrm{sp}}} \frac{\rho_{\mathrm{sp}}}{2} \hat{J}_1(k_\perp \rho_{\mathrm{sp}}) \mathrm{d}v_\parallel \mathrm{d}\mu \right] \\ B_{1\parallel} &= -2\pi B_0 \mu_0 \sum_{\mathrm{sp}} \frac{Z_{\mathrm{sp}}}{|Z_{\mathrm{sp}}|} \frac{1}{m_{\mathrm{sp}}} \left[\int \mu \frac{Z_{\mathrm{sp}}}{|Z_{\mathrm{sp}}|} \hat{J}_1(\lambda_{\mathrm{sp}}) f_{\mathrm{gy,sp}} \mathrm{d}v_\parallel \mathrm{d}\mu \right. \\ &\quad \left. + \int \mu \left(Z_{\mathrm{sp}} e J_0(\lambda_{\mathrm{sp}}) \Phi_1 + \mu \hat{J}_1(\lambda_{\mathrm{sp}}) B_{1\parallel} \right) \frac{F_{\mathrm{M}}}{T_{\mathrm{sp}}} \frac{Z_{\mathrm{sp}}}{|Z_{\mathrm{sp}}|} \hat{J}_1(\lambda_{\mathrm{sp}}) \mathrm{d}v_\parallel \mathrm{d}\mu \right]. \end{aligned}$$

Here the upper index in $k_\perp^2$ means second power. The integral over $v_\parallel$ is elementary as again it only appears in the Maxwellian. Using equation 2.60 and evaluating the integrals over μ according to equations A.8 in appendix A one obtains

$$\begin{aligned} B_{1\parallel} &= -\sum_{\mathrm{sp}} \frac{2\mu_0 T_{\mathrm{sp}} n_{0,\mathrm{sp}}}{B_0} \left[\frac{\pi B_0^2}{m_{\mathrm{sp}} n_{0,\mathrm{sp}} T_{\mathrm{sp}}} \int \mu \hat{J}_1(\lambda_{\mathrm{sp}}) g_{\mathrm{sp}} \mathrm{d}v_\parallel \mathrm{d}\mu + \right. \\ &\quad \left. \mathrm{e}^{\frac{-\mathcal{E}}{T_{\mathrm{sp}}}} \left(\Gamma_0(b_{\mathrm{sp}}) - \Gamma_1(b_{\mathrm{sp}}) \right) \left(\frac{Z_{\mathrm{sp}} e \Phi_1}{2T_{\mathrm{sp}}} + \frac{B_{1\parallel}}{B_0} \right) \right]. \end{aligned}$$

Normalization and rearrangement of the terms after writing the fields in Fourier-space yield

$$\begin{aligned} &\left[1 + \sum_{\mathrm{sp}} \beta_{\mathrm{sp}} \mathrm{e}^{\frac{-\mathcal{E}_{\mathrm{N,sp}}}{T_{\mathrm{R,sp}}}} \left(\Gamma_0(b_{\mathrm{sp}}) - \Gamma_1(b_{\mathrm{sp}}) \right) \right] \hat{B}_{1\parallel \mathrm{N}} = \\ &\qquad -\sum_{\mathrm{sp}} \beta_{\mathrm{sp}} \left[2\pi B_{\mathrm{N}}^3 \int \mu_N \hat{J}_1(k_\perp \rho_{\mathrm{sp}}) \hat{g}_{\mathrm{N,sp}} \mathrm{d}v_{\parallel N} \mathrm{d}\mu_{\mathrm{N}} + \right. \\ &\qquad \left. \mathrm{e}^{\frac{-\mathcal{E}_{\mathrm{N,sp}}}{T_{\mathrm{R,sp}}}} \left(\Gamma_0(b_{\mathrm{sp}}) - \Gamma_1(b_{\mathrm{sp}}) \right) \frac{Z_{\mathrm{sp}} B_{\mathrm{N}}}{2T_{\mathrm{R,sp}}} \hat{\Phi}_{1\mathrm{N}} \right]. \end{aligned} \tag{2.78}$$

Using the reference instead of the full value of the plasma beta ($\beta = \beta_{\mathrm{ref}} \beta_{\mathrm{R}} = \beta_{\mathrm{ref}} \frac{T_{\mathrm{R,sp}} n_{\mathrm{R,sp}}}{B_{\mathrm{N}}^2}$), the equation for the parallel magnetic perturbation can be finally

written as

$$\left[1+\sum_{\mathrm{sp}}\frac{T_{\mathrm{R,sp}}n_{\mathrm{R,sp}}}{B_{\mathrm{N}}^{2}}\beta_{\mathrm{ref}}\mathrm{e}^{\frac{-\varepsilon_{\mathrm{N,sp}}}{T_{\mathrm{R,sp}}}}\left(\Gamma_{0}(b_{\mathrm{sp}})-\Gamma_{1}(b_{\mathrm{sp}})\right)\right]\hat{B}_{1\|\mathrm{N}}=$$
$$-\sum_{\mathrm{sp}}\beta_{\mathrm{ref}}\left[2\pi B_{\mathrm{N}}T_{\mathrm{R,sp}}n_{\mathrm{R,sp}}\int\mu_{N}\hat{J}_{1}(k_{\perp}\rho_{\mathrm{sp}})\hat{g}_{\mathrm{N,sp}}\mathrm{d}v_{\|N}\mathrm{d}\mu_{\mathrm{N}}\right.$$
$$\left.+\,\mathrm{e}^{\frac{-\varepsilon_{\mathrm{N,sp}}}{T_{\mathrm{R,sp}}}}\left(\Gamma_{0}(b_{\mathrm{sp}})-\Gamma_{1}(b_{\mathrm{sp}})\right)\frac{Z_{\mathrm{sp}}n_{\mathrm{R,sp}}}{2B_{\mathrm{N}}}\hat{\Phi}_{1\mathrm{N}}\right]. \tag{2.79}$$

It can be seen that both the perpendicular (equation 2.76) and parallel (equation 2.78) components of the perturbed magnetic field depend strongly on the plasma β. Indeed, it has been commonly observed in gyrokinetic simulations that in low β plasmas the amplitude of the magnetic perturbations is much lower than that of the fluctuating scalar potential. However, in high β plasmas magnetic perturbations strongly impact mode stability and transport by destabilizing kinetic ballooning [40] and micro-tearing [41] modes.

The correction suggested in equation 2.78 compared to the calculation by Dannert in [30] is the missing $2b$ factor in the second term on the left hand side, which is the direct consequence of equation A.8. High β simulations with GKW using the corrected form of this equation have been successfully benchmarked against an other gyrokinetic code, GS2 [42].

2.3.7 The GKW Particle Flux

The aim of this section is to introduce one of the GKW output data types, the particle flux, that is extensively used in this work in the following chapters. The calculation of the particle flux, as it is performed in GKW, is shown, as well as its meaning in the linear and non-linear sense. It is also pointed out that the flux of gyro-centres is equal to the flux of particles up to first order in ρ_{*}.

GKW

GyroKinetics@Warwick (GKW) [31] is a fully electromagnetic, flux tube, initial value Eulerian code using delta-f approximation, including kinetic electrons, strong rotation and collisional effects. It uses a linearized Fokker–Planck collision operator consisting of pitch-angle scattering, energy scattering and friction terms, the exact form of the operator is detailed in [43]. It solves the self-consistent Vlasov–Maxwell system of equations 2.61, 2.62, 2.74, 2.76 and 2.79 in a normalized form. Being a local, flux-tube code, the spatial domain of the simulation is an elongated, three

dimensional tube along an equilibrium magnetic field line on a particular flux surface. The parallel dimension with respect to the magnetic field is described with a finite differences method in real space, while the solution is Fourier-transformed in the perpendicular plane. The extent of this domain largely depends on the characteristic mode driving the turbulence. Typically, several tens of toroidal periods along the field line in the parallel direction, and several tens of gyro-radii in the perpendicular direction is required for sufficiently capture the mode dynamics. The velocity space consisting of the parallel velocity and the magnetic moment are also treated with a finite differences scheme.

Numerically, solving the Vlasov–Maxwell system can be regarded as an inhomogeneous eigenvalue problem with the eigenfunction being the discretized vector of the combined distribution function and electro-magnetic fields, and the operator being the complex gyrokinetic operator. As suggested in section 2.2.2, the system is solved iteratively. GKW is highly parallelized in the parallel spatial and velocity directions and its performance scales well up to a processor number of 10^3. The details of the numerical methods and algorithms applied in the code are found in [31].

Calculating the particle flux

The radial (ψ) particle flux due to the fluctuating electro-magnetic fields can be written as

$$\Gamma^{\psi}_{\text{part}}(\mathbf{x}) = \left\{ \int \left(\mathbf{v}_{\mathbf{E}_1 \times \mathbf{B}_0} + \mathbf{v}_{\mathbf{B}_{1\perp}} + \mathbf{v}_{\nabla B_{1\parallel}} \right) \cdot \nabla\psi(\mathbf{x}) f(\mathbf{x}, \mathbf{v}) \mathrm{d}^3 v \right\} \tag{2.80}$$

where the three velocities are the $E \times B$, the magnetic flutter and the compressional velocities, respectively, $\nabla\psi$ is the radial unit vector, and the curly brackets denote flux surface averaging. The gyro-motion of the particles does not give a contribution to the flux and it vanishes from the definition. Equation 2.80 is not gyro-averaged, it is written in the particle phase space. However, GKW solves the gyrokinetic equation to obtain the distribution function in the gyro-centre phase space. Similar to the method applied in the derivation of the gyrokinetic Maxwell-equations, this equation will be transformed into the guiding-centre phase space and the guiding-centre distribution function will be expressed algebraically with the gyro-centre distribution function using equation 2.67. For the sake of simplicity, only the $E \times B$ term will be carried in the remainder of the derivation, which is related to the fluctuating potential, and typically provides the largest contribution to the flux.

Equation 2.80 in guiding-centre coordinates becomes

$$\Gamma^{\psi}_{E\times B}(\mathbf{x}) = \left\{ \int \delta(\mathbf{X}+\rho-\mathbf{x}) \frac{-\nabla\bar{\Phi}_1(\mathbf{X})\times\mathbf{b}}{B_0}\cdot\nabla\psi(\mathbf{X}) \right. \\ \left. f_{\mathrm{gc}}(\mathbf{X},v_\parallel,\mu,\theta)\frac{B_0}{m}\mathrm{d}\mathbf{X}\mathrm{d}v_\parallel\mathrm{d}\mu\mathrm{d}\theta \right\}. \tag{2.81}$$

Substituting equation 2.67 into equation 2.81 gives

$$\Gamma^{\psi}_{E\times B}(\mathbf{x}) = \left\{ \int \frac{B_0}{m}\frac{-\nabla\bar{\Phi}_1(\mathbf{X})\times\mathbf{b}}{B_0}\delta(\mathbf{X}+\rho-\mathbf{x})\cdot\nabla\psi(\mathbf{X}) \left(f_{\mathrm{GY}}(\mathbf{X},v_\parallel,\mu,\theta) \right.\right. \\ \left.\left. -\frac{F_{\mathrm{M}}}{T}(Ze\tilde{\phi}_1(\mathbf{X}+\rho)-\mu\bar{B}_{1\parallel}(\mathbf{X})) \right) \mathrm{d}\mathbf{X}\mathrm{d}v_\parallel\mathrm{d}\mu\mathrm{d}\theta \right\}. \tag{2.82}$$

The first term is the flux of gyro-centres driven by the fluctuating $E\times B$ velocity and is the only term in this expression calculated in GKW . The two remaining terms are related to the polarization and magnetization effects due to the fluctuating fields. They are first order terms in ρ_* and therefore kept in Maxwell's equations. However, in GKW the fields and the distribution function are represented as series of Fourier modes in the perpendicular direction:

$$\Phi_1(\mathbf{X}) = \sum_m \hat{\Phi}_{1,m}\mathrm{e}^{i\mathbf{k}_{\perp,m}\cdot\mathbf{X}} \quad\Longrightarrow\quad \mathbf{v}_{\mathbf{E}_1\times\mathbf{B}} = \sum_m \hat{\mathbf{v}}^m_{\mathbf{E}_1\times\mathbf{B}}\mathrm{e}^{i\mathbf{k}_{\perp,m}\cdot\mathbf{X}} \tag{2.83}$$

where $\hat{(.)}$ denotes a complex Fourier-component of the associated quantity. Therefore, each term in equation 2.82 is a product of two of such series. When performing the flux surface average in equation 2.82, only terms consisting of Fourier components in opposite phase give a non-zero contribution to the sum [31]. This implies

$$\{\mathbf{v}_{\mathbf{E}_1\times\mathbf{B}}\cdot\nabla\psi f_{\mathrm{gy}}\} = 2\sum_m \mathrm{Re}\left((\hat{\mathbf{v}}^m_{\mathbf{E}_1\times\mathbf{B}})^*\cdot\nabla\psi\hat{f}^m_{\mathrm{gy}} \right), \tag{2.84}$$

where $(.)^*$ denotes complex conjugation. That is, a flux associated to each Fourier-component can be defined. However, these are not the Fourier-components of the total flux itself. Equation 2.84 is valid both with the gyro-averaged and the oscillating components of the fluctuating scalar potential since gyro-averaging is performed along the independent θ coordinate. The real part of this expression is required since the Fourier-components are generally complex whereas the physical quantities are real. Therefore, if there is no phase difference between the two quantities combined in the sense of equation 2.84, the real part of this expression will vanish. Consequently, the flux associated with the polarization term $\widetilde{\Phi}_1$ in equation 2.82

is zero since its phase, with respect to the perpendicular Fourier-decomposition, is the same as that of the gyro-averaged $\bar{\Phi}_1$. The same exact cancellation cannot be said about the magnetization term including $\bar{B}_{1\parallel}$. As shown by equation 2.79, one term in the expression for the parallel magnetic perturbation is proportional to Φ_1, which therefore cancels in equation 2.82, but the other term is an integral over the gyro-centre distribution function that generally gives a finite contribution to the flux. This is caused by the fact that the partice gyro-orbits do not close on themselves in presence of magnetic compression. However, the magnetic perturbation scales roughly linearly with the plasma β, which is typically small (10^{-2}) in fusion experiments. Even in high β discharges its value is about 10^{-1}, hence the flux due to the magnetic perturbations is at least an order of magnitude smaller than the leading order gyro-centre flux due to the $E \times B$ convection.

In a linear simulation the solution given by GKW is normalized after every timestep against the sum of the mode amplitudes squared [31]. The normalizing factors in two consecutive timesteps are then used to calculate the growth rate of the mode but the time evolution is generally not kept. Convergence is reached when the growth rate is stabilized and its change is smaller than a user defined limit. This means that the eigenfunction and flux calculated by the code are also normalized and they are associated with the fastest growing eigenmode of the system. The magnitude of the flux therefore does not carry information about the saturated flux level. It is proportional to the phase difference between the density and potential fluctuations during the linear phase of the mode evolution, and its sign indicates whether the flux is radially inward (negative) or outward (positive) [44]. In a nonlinear simulation the above normalization scheme is not applied. Both the perturbed distribution function and velocities are calculated taking into account the full nonlinear Vlasov-equation. Their product is a second order term in ρ_* providing a physical radial flux on the transport time scale.

2.4 Summary of the Chapter

In this chapter the motivation and basic mathematical concept of the gyrokinetic transformation has been outlined. Based on the work by Dannert [30], a constructive derivation of the first order gyrokinetic Vlasov–Maxwell system using the Lie-transform perturbation method in Lagrangian formalism including toroidal rotation has been shown. The role of the parallel magnetic perturbations in gyrokinetic theory has been identified: it gives rise to an additional magnetic drift velocity, and leads to a magnetization term in the field equations. This magnetization term is

expected to give a non-zero correction to the radial gyro-centre flux, however, it is presently neglected due to its close to linear scaling with the typically small plasma β. The gyrokinetic equations derived here are solved by the GKW code and provide the basis for the particle transport analysis in the following chapter.

Chapter 3

Gyrokinetic Analysis of Particle Transport in FTU-LLL and High-Beta MAST Discharges

3.1 Analysis of FTU #30582

In this section we apply the gyrokinetic framework introduced in the previous chapter in order to understand the recent experimental observations on the Frascati Tokamak Upgrade (FTU) following the installation of a Liquid Lithium Limiter (LLL): discharges performed with LLL exhibit larger density peaking compared to the previous standard metallic limiter scenarios [19].

One of the possible explanations for the increased density peaking in FTU-LLL discharges is that the high concentration of lithium impurities alters the turbulent mode spectrum and the phase difference between density and potential fluctuations, and thus leads to an inward anomalous particle transport, in contrast with the standard plasma operation (without LLL). In order to test this hypothesis a local gyrokinetic analysis with the GKW code (Gyrokinetics@Warwick, [31]) of the FTU-LLL discharge #30582 has been performed. Most of the results presented in this section are published in [45].

3.1.1 Experimental Features of FTU-LLL Discharges

FTU is a medium size, fully metallic (stainless steel vacuum chamber), toroidal limiter (molybdenum) tokamak [19], its typical operating parameters are summarized in table 3.1. The most notable feature is the high toroidal magnetic field allowing FTU to generate high density discharges.

FTU parameters	Value	Dim.
Plasma major radius	0.935	m
Plasma minor radius	0.31	m
Maximum plasma current	1.6	MA
Toroidal magnetic field	8	T
Toroidal field flat-top duration	1.5	s

Table 3.1: Typical parameters of the FTU tokamak. Data from http://www.fusione.enea.it/FTU

FTU has been fitted with a Liquid Lithium Limiter (LLL) in the shadow of the original molybdenum limiter. The main impact of employing a LLL on plasma performance is twofold. First, the deuterium and light impurity retention capabilities of the lithium coated walls are greatly increased, resulting in a reduced deuterium recycling rate and a plasma containing only lithium impurities in large concentration (measured by UV emission). Second, the lithium ions are being removed from the plasma core during the discharge, and a $Z_{\text{eff}} \sim 1$ is typically observed during most of the current plateau phase. At the same time a more peaked electron and deuterium density profile occurs compared to standard metallic limiter experiments [19]. Figure 3.1 shows a comparison of a typical metallic limiter (#26671) and a LLL (#30583) discharge with otherwise similar parameters. The time evolution of the plasma current (top), the core and edge electron density (middle) and deuterium gas injection rate (bottom) are plotted. The electron density and temperature profiles are also indicated at two time instances. In the standard limiter scenario the increase of the density profile is approximately uniform, and the electron temperature becomes more peaked during the discharge. In contrast, in the LLL case an increasingly peaked density profile is accompanied by slightly reduced temperatures. The core electron density in the LLL discharge follows the increasing gas fuelling rate, indicating electron and deuterium particle pinch from the edge towards the core. The value of the fuelling rate is about three times as much as in the metallic limiter case. This is required to balance the larger density peaking and the increased deuterium retention of the walls.

The reference discharge selected for the analysis is FTU #30582. As it is clear from figure 3.2, the features described in the previous paragraph in connection with FTU #30583 are present, they are typical characteristics of FTU-LLL plasmas. FTU #30582 is preferable for the analysis since it displays a more clearly separated density ramp-up (up to ∼0.6s) and density plateau phases.

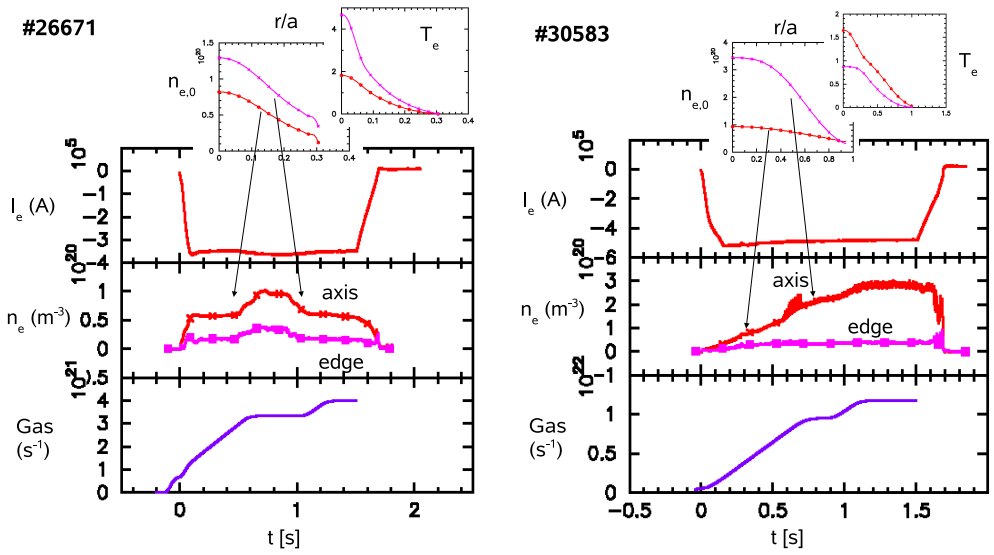

Figure 3.1: Comparison of the FTU #26671 (metallic limiter only, left) and FTU #30583 (LLL, right) discharges.

Since FTU is not fitted with a Neutral Beam Injection (NBI) system, the plasma rotation is typically of the order of the diamagnetic velocity. At this rotation speed centrifugal effects (implemented in GKW [38]) are not expected to affect the main ion and light impurity transport, and are not included in the present analysis.

3.1.2 Linear Gyrokinetic Analysis

The micro-stability and turbulent transport properties of FTU #30582 are investigated at two time instances: one during the transient ramp up phase of the discharge at $t = 0.3$s characterized by $Z_{\rm eff} = \sum_{\rm s} n_{\rm s} Z_{\rm s}^2 = 1.93$ due to the high lithium concentration ($c_{\rm Li} = n_{\rm Li}/n_{\rm e} = 0.15$), and one in the density plateau phase at $t = 0.8$s with $c_{\rm Li} = 0.01$ and $Z_{\rm eff} = 1.06$. The input parameters of the simulations are reported in table 3.2 [44]. The reference density is chosen to be the electron density, and the reference temperature the ion temperature. The thermal velocity is defined as $v_{\rm th} = \sqrt{2T_{\rm i}/m_{\rm i}}$, and the reference Larmor radius is the ion thermal Larmor radius on the magnetic axis: $\rho_{\rm i} = (m_{\rm ref} v_{\rm th,ref})/(eB_{\rm ref})$. The linear simulations have been performed using 264 points along the parallel direction covering 11 periods around the torus, 10 points in magnetic moment and 36 points in parallel velocity space. A non-shifted circular geometry described in [46] has been applied.

In the linear simulations both the parallel and perpendicular components

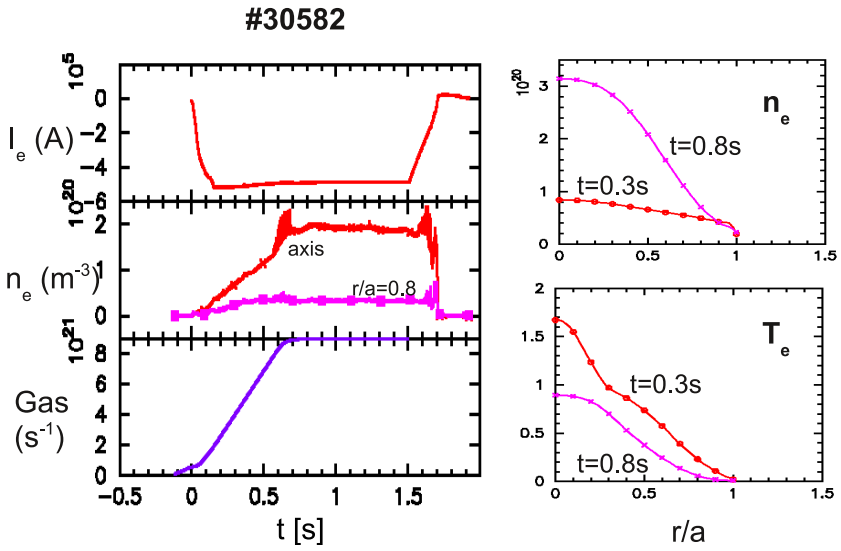

Figure 3.2: Experimental data from FTU #30582. Left: time traces of plasma current (top), core and edge electron density (middle) and gas injection rate (bottom). Edge refers to $r/a = 0.8$ with $a = 0.3$ m. Right: electron density (top) and temperature (bottom) profiles at $t_1 = 0.3$s and $t_2 = 0.8$s [44].

of the magnetic perturbations have been included. However, due to the strong toroidal magnetic field, the plasma beta, defined as the ratio of the magnetic and hydrodynamic pressures $\beta = \frac{p}{B^2/(2\mu_0)}$, is expected to be low. The plasma beta is related to the strength of the magnetic perturbations, as shown in section 2.3.6. Indeed, the amplitude of the normalized magnetic perturbations is approximately 10^{-3}-10^{-4} times of that of the electro-static perturbations. Consequently, when calculating the particle flux according to equation 2.80, only the first term (the flux associated with the fluctuating ExB velocity) is kept. The effect of high plasma beta will be discussed in section 3.2 in connection with a MAST discharge analysis.

The Density Ramp-up Phase

The top left and right panels of figure 3.3 show the linear growth rate and real frequency spectra of the bi-normal modes at the beginning of the discharge ($t = 0.3$s) for two different values of collision frequencies. Simulations performed with a Lorentz-type collision operator (pitch angle scattering only, blue crosses) and the full collision operator (pitch-angle scattering, energy scattering and friction terms, cyan diamonds) are included. The collision frequencies are given in terms of the

	$n[10^{19}\mathrm{m}^{-3}]$	$T[\mathrm{keV}]$	$-\frac{a\nabla T}{T}$	$-\frac{a\nabla n}{n}$
		$t = 0.3\mathrm{s}$		
D^+	3.21	0.47	2.14	0.89
e^-	6.03	0.57	3.07	0.89
Li^{3+}	0.94	0.47	2.14	0.89
	$R_{\mathrm{ref}} = 0.97\mathrm{m}$	$q = 2.76$	$\hat{s} = 0.97$	$\nu_{\mathrm{ii,N}} = 0.028$
		$t = 0.8\mathrm{s}$		
D^+	15.50	0.26	4.61	3.12
e^-	15.95	0.24	4.94	3.12
Li^{3+}	0.15	0.26	4.61	3.12
	$R_{\mathrm{ref}} = 0.98\mathrm{m}$	$q = 2.36$	$\hat{s} = 1.55$	$\nu_{\mathrm{ii,N}} = 0.220$

Table 3.2: Plasma parameters used in the gyrokinetic simulations of FTU #30582 at $r/a = 0.6$, $t_1 = 0.3$ s and $t_2 = 0.8$ s. $a = 0.3$ m.

normalized ion-ion collision frequency $\nu_{\mathrm{ii,N}}$ in units of $v_{\mathrm{th,ref}}/R_{\mathrm{ref}}$. The collision frequencies between the other species are calculated from $\nu_{\mathrm{ii,N}}$ within the code [31]. The reference value, as determined from the measured plasma parameters, is $\nu_{\mathrm{ii,N}} = 0.028$ (solid), and the increased value is $\nu_{\mathrm{ii,N}} = 0.1$ (dot dashed). Positive real frequencies correspond to modes rotating in the ion diamagnetic direction.

If collisions are not included in the simulation (x-es), the spectrum is fully dominated by trapped electron modes. When using a Lorentz-type collision operator (pitch angle scattering only, crosses), the spectrum contains both ITG (below $k_\theta \rho_{\mathrm{i}} \approx 1.4$) and TE modes. Increasing collisionality with respect to the reference value (dashed, crosses) weakly stabilizes ITG modes and destabilizes trapped electron modes. The latter observation is unexpected since TEM-s are typically stabilized by increasing collisionality even with pitch-angle scattering only. A similar behaviour is also observed at 1% lithium concentration (not shown). A peaked collisionality scaling of linear growth rates has been reported in [47], but there the increasing part of the $\gamma(\nu)$ function corresponds to significantly higher density gradients than those in the present simulation. When using the full collision operator (diamonds), it changes the ITG/TEM spectrum to an ITG only case via stabilization of the TE modes. If the collision frequency is increased to $\nu_{\mathrm{ii,N}} = 0.1$ (dashed, diamonds), a uniform stabilizing effect across the whole spectrum is obtained. If the collision frequency is further increased to the value of the $t = 0.8$s case ($\nu_{\mathrm{ii,N}} = 0.22$)

the modes are completely stabilized (not shown). When the impurity concentration is reduced to $c_{\mathrm{Li}} = 0.01$ while keeping the full collision operator (dots), the reference collision frequency slightly changes through the weak density dependence of the Coulomb-logarithm (the change is less than 2%). However, the frequency of the collisions with the two ion species is strongly affected: ν_{si} increases while ν_{sI} decreases due to the higher deuterium and lower impurity densities. The effective collision frequency of the species is proportional to the Z_{eff} of the plasma. The reduced Z_{eff} means that stabilization through collisions becomes weaker, the deuterium population less diluted, and the screening of the potential fluctuations less effective [48]. These effects together cause the main ion ITG modes to grow more unstable, the impurity ITG modes to disappear and the electron driven modes to become dominant above $k_\theta \rho_{\mathrm{i}} \approx 1.4$ (as observed in [44] with Lorentz collision operator).

The spectra of the corresponding quasi-linear deuterium and impurity fluxes are shown on the bottom left and right panels of figure 3.3, respectively. The ITG modes are found to drive an inward deuterium and outward lithium flux at the reference impurity concentration $c_{\mathrm{Li}} = 0.15$, both with pitch-angle scattering and the full collision operator, at both collision frequencies. The direction of the particle transport remains the same even if the collision frequency is reduced to about one third of the reference value to $\nu_{\mathrm{ii,N}} = 0.01$ (not shown). However, at the reduced impurity concentration of $c_{\mathrm{Li}} = 0.01$ the modes below $k_\theta \rho_{\mathrm{i}} \approx 0.6$ drive the deuterium ions outward. These modes are expected to provide the majority of the particle transport according to mixing length estimates and, consequently, to reverse the direction of the deuterium flux. This result is only obtained when the energy scattering and friction terms are taken into account in the collision operator and therefore it was missed in [44]. Although the impact of these terms on the linear fluxes are typically much smaller than that of the pitch-angle scattering operator, in this case it is enough to change the sign of the fluxes that are close to zero. The gyrokinetic simulations in the remainder of this thesis are performed using the full collision operator unless otherwise stated.

A scan of the impurity concentration in the $t = 0.3$s case is shown on figure 3.4. With reducing impurity concentration the main ITG modes become gradually more unstable, and the transition to the electron driven modes occurs at lower k_θ values. This trend is similar to as described in [44] with pitch-angle scattering only. However, below a certain lithium concentration the low-k modes (below $k_\theta \rho_{\mathrm{i}} \approx 0.5$ at $c_{\mathrm{Li}} = 0.1$) drive an outward deuterium flux (bottom left). Inward deuterium transport requires approximately $c_{\mathrm{Li}} > 0.05$ in this case. The outward impurity

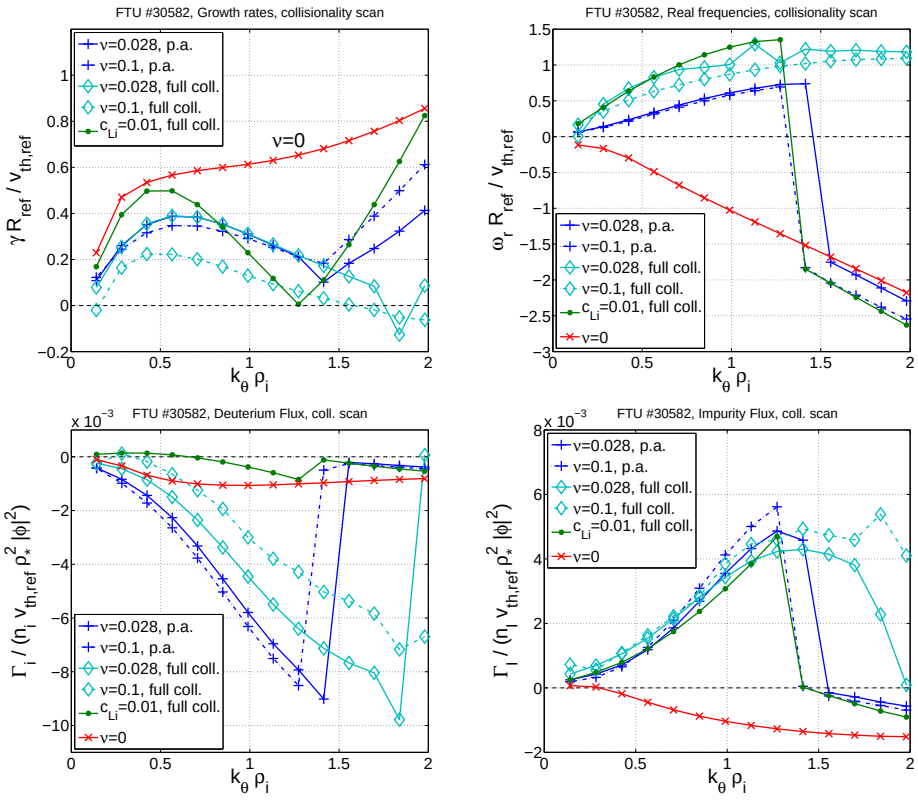

Figure 3.3: Collisionality scan of growth rate (top left), real frequency (top right), quasi-linear deuterium (bottom left) and lithium (bottom right) flux as a function of bi-normal wavenumber at $t = 0.3$s. The reference impurity concentration is $n_{\mathrm{Li}}/n_{\mathrm{e}} = 0.15$. Cases at the reference ($\nu_{\mathrm{ii,N}} = 0.028$, solid) and an increased ($\nu_{\mathrm{ii,N}} = 0.1$, dot dashed) collision frequency with both a Lorentz type (blue crosses) and the full (cyan diamonds) collision operator, together with a reduced impurity concentration ($n_{\mathrm{Li}}/n_{\mathrm{e}} = 0.01$, solid, green dots) and a collisionless (red x-es) case are shown.

flux driven by the ITG modes (bottom right) remains unchanged. As the impurity concentration is increased the outward electron flux driven by the low-k modes (top right) is also reduced. This can be attributed to the fact that the electrons are less sensitive to the ion scale modes, and tend to remain nearly adiabatic in ITG turbulence. When the impurity population is low the electrons must follow the ion transport due to quasi-neutrality. However, when the quasi-neutrality equation contains three major constituents, the restriction imposed by ambi-polarity can be satisfied with the two ion species. The fifth curve (dashed green) on the left and right panels shows a pure plasma simulation with zero impurity concentration, but with Z_{eff} manually set to its original value of 1.93. This provides approximately

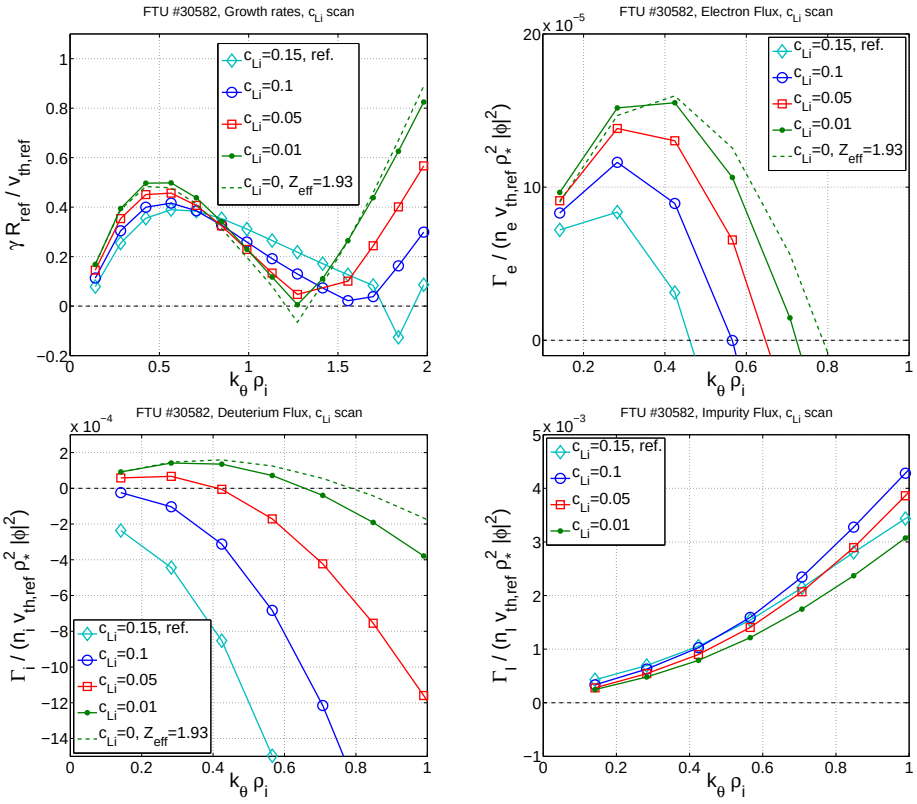

Figure 3.4: Lithium concentration scan of growth rate (top left), quasi-linear electron (top right), deuterium (bottom left) and lithium (bottom right) flux as a function of bi-normal wavenumber at $t = 0.3$s.

the same effective electron and ion collision frequencies as in the experimental case (within 2% difference due to the change of the Coulomb logarithm). The growth rates, frequencies and fluxes are nearly identical to the 1% impurity concentration results, showing that the main impact of the lithium impurities is not a collisional effect.

It has been pointed out by several authors (see for example [28, 49, 50]) that impurity transport is sensitive to the ion density gradient. In the previous simulations the same positive density gradient value has been used for all three species, that is, a centrally peaked impurity density profile has been assumed. However, experimentally the impurity profile is often found to be peaked towards the edge. The effect of varying the lithium density gradient on the quasi-linear ion flux is investigated in figure 3.5. The deuterium density gradient is kept at the reference value ($R_{\mathrm{ref}}/L_{\mathrm{n,D}} = 2.9$), the electron density gradient has been adjusted in order to maintain quasi-neutrality. The growth rates are slightly increased at lower

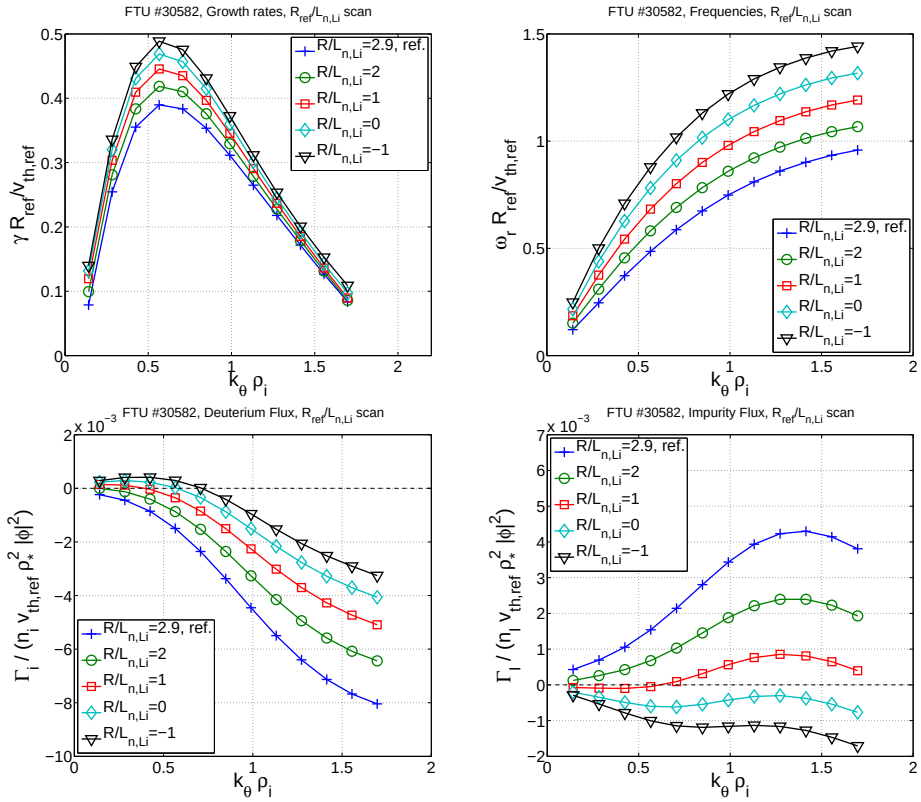

Figure 3.5: Impurity density gradient scan of the growth rates (top left), frequencies (top right), quasi-linear deuterium (bottom left) and lithium (bottom right) flux as a functions of bi-normal wavenumber at $t = 0.3$s.

lithium gradients due to the stronger drive of the lithium component of the ITG modes. An inward deuterium and outward impurity flux driven by the low-k modes is observed only with the two largest values of the lithium density gradient, that is $R_{\mathrm{ref}}/L_{\mathrm{n,Li}} = 2.9$ and 2.0. However, the reduction of the impurity flux in the latter case is already significant. At $R_{\mathrm{ref}}/L_{\mathrm{n,Li}} = 1$ the flux driven by the modes below $k_\theta \rho_{\mathrm{i}} \approx 0.4$ is reversed, expectedly leading to outward deuterium transport and core lithium accumulation in the saturated phase.

An impurity density gradient scan of the quasi-linear ion flux at three different impurity concentrations at $k_\theta \rho_{\mathrm{i}} = 0.28$ summarizes the above observations (figure 3.6). Since the electron response to the low-k modes is expected to be close to adiabatic in a highly contaminated plasma, the direction of the deuterium and lithium transport is determined by the balance of the drive of their respective fluxes. This drive strongly depends on the concentration and the density gradient of the impurity species, while the impact of these parameters on the low-k ITG mode sta-

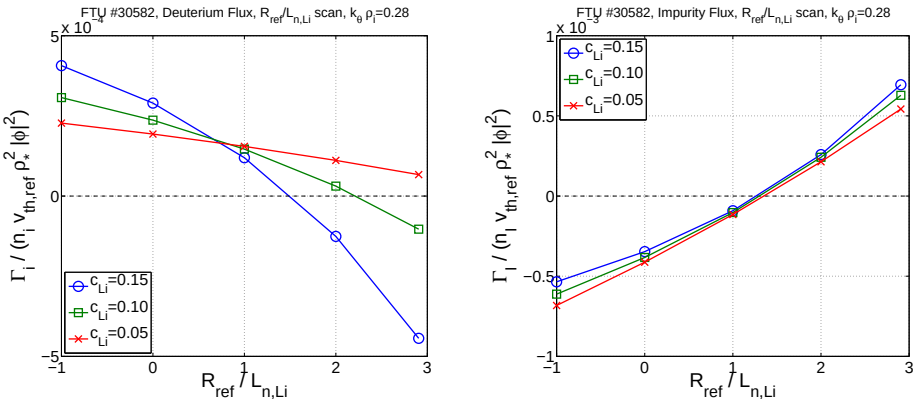

Figure 3.6: Impurity concentration and impurity density gradient scan of the quasi-linear deuterium (left) and lithium (right) fluxes at $t = 0.3$s and $k_\theta \rho_\mathrm{i} = 0.28$.

bility is relatively weak. If the impurity concentration is sufficiently high and its density profile sufficiently peaked, such as it is assumed during the density ramp-up of this FTU-LLL discharge, then the outward drive of the impurity flux outweighs that of the deuterium, and forces the main ions to be transported inward. This observation is qualitatively consistent with the results of [28] obtained with helium impurities in a standard test case.

The significance of the impurities being lithium ions is tested by a series of simulations using different light impurity species (carbon, tritium, helium) while keeping the deuterium concentration constant. A mixed deuterium-tritium-lithium case is also investigated due to its potential relevance in future burning plasma applications. The results are plotted in figure 3.7. The carbon (black circles) and lithium (cyan diamonds) are the most effective among the selected impurity species in reducing the quasi-linear electron flux and driving the deuterium flux inward. However, under the current circumstances, the increase of the ion collisionality due to 7% carbon concentration strongly stabilizes the modes. The helium impurity (blue squares) and the mixed D-T-Li case exhibit similar behaviour, but the results with 46% tritium (light green triangles) are close to the clear plasma simulations (1% lithium, green dots), both of them driving an outward deuterium flux. If the deuterium and impurity Larmor-radii are too close, they are expected to react similarly to the main ion ITG modes, and thus to be unable to reduce the electron transport and generate the deuterium pinch. Indeed, the quasi-linear tritium flux in both the D-T and D-T-Li cases follow that of the deuterium, although in the former case the flux is close to zero and only the three lowest k modes indicate an outward transport. The dynamics of the deuterium and lithium ions are sufficiently

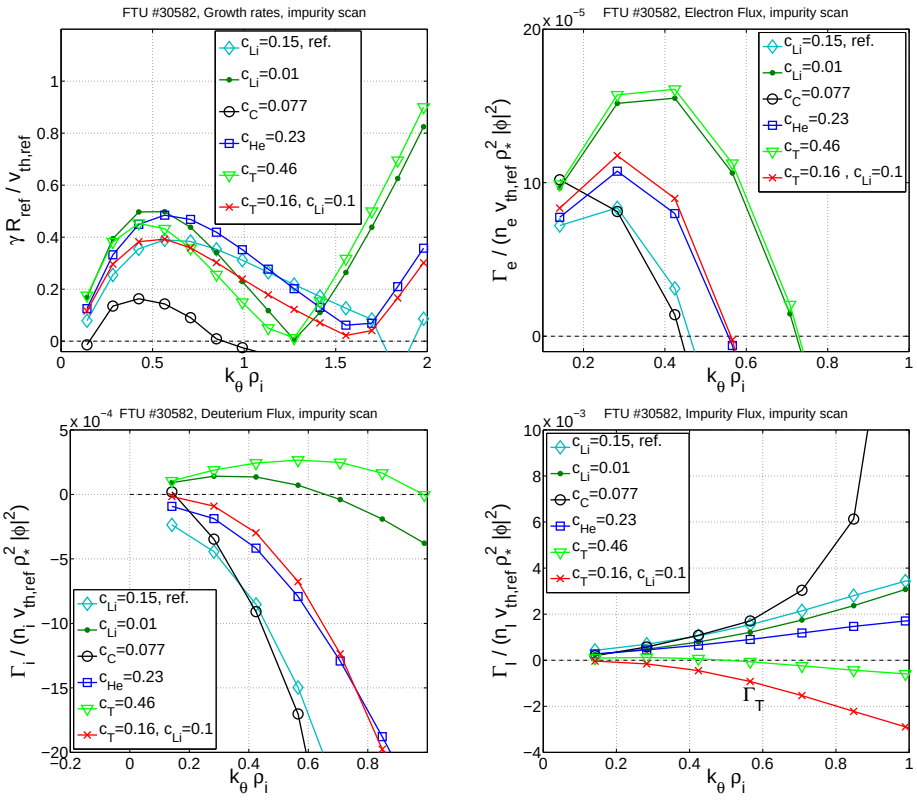

Figure 3.7: Growth rate (top left), electron (top right), deuterium (bottom left) and impurity (bottom left) quasi-linear flux spectra as a function of the bi-normal wavenumber using different impurity species.

different for the ion flow separation to occur. However, the typical D-ITG length scale is still sufficiently close to the lithium Larmor-radius that the lithium ions can have a significant effect on the low-k ITG transport. Moreover, Z_{Li} is low enough that it does not have a major qualitative impact on mode stability and it does not cause large radiative losses.

The dependence of the growth rates, real frequencies and ion particle flux on the magnetic shear ($\hat{s} = \frac{r}{q}\frac{\mathrm{d}q}{\mathrm{d}r}$, q is the safety factor) at $t = 0.3$s is presented in figure 3.8. Increasing magnetic shear in the range of $\hat{s} = 0.5-1.5$ stabilizes the ITG modes, also observed in more detailed studies on the impact of magnetic shear by Kinsey et al. [51], Moradi at al. [52] and Nordman at al. [53]. However, it should be noted that the actual effect of the magnetic shear strongly depends on the other plasma parameters and its stabilizing effect should be considered on a case-to-case basis. TEM-s are suppressed by the collisionality and they remain stable even at the lower shear value. The phase difference between potential and ion density perturbations

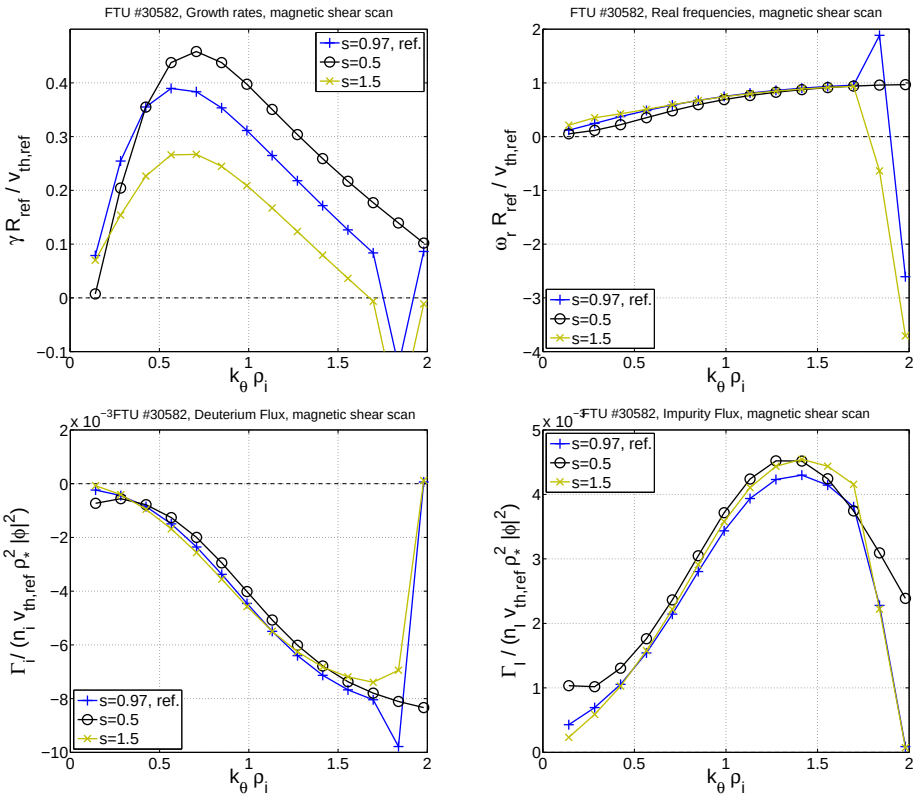

Figure 3.8: Magnetic shear $\hat{s}$ scan of growth rate (top left), real frequency (top right), quasi-linear deuterium (bottom left) and lithium (bottom right) flux as a function of the bi-normal wavenumber at $t = 0.3$s.

depends weakly on the variation of the magnetic shear.

The Density Plateau Phase

At $t = 0.3$s the plasma is not in steady-state. It is characterized by finite radial particle transport that, as it has been shown above, contributes to the dynamical build-up of the deuterium density profile and the reduction of impurity concentration. At $t = 0.8$s the plasma is described by significantly larger deuterium and electron density (and also temperature) gradients, reduced Z_{eff}, and a slightly increased magnetic shear. The reference collision frequency is approximately a factor of eight higher ($\nu_{\text{ii,N}} = 0.22$) due to the lower temperature and higher density values, leading to an increased effective collision frequency of the species despite the lower Z_{eff}.

The effect of increasing only the temperature or density gradients of all three species from $t = 0.3$s to their corresponding values at $t = 0.8$s while keeping the other

parameters constant is shown in figure 3.9. The higher temperature gradients (blue circles) provide a stronger drive for both ITG and TE modes, increasing the growth rates across the whole spectrum. The transition between ion and electron modes occur at approximately the same wavenumber value as in the $t = 0.3$s simulation (dashed, cyan diamonds), and the fluxes maintain their directions compared to the reference case. Increasing the density gradients only (yellow squares) is sufficient to reverse the direction of the deuterium transport from inward to outward, according to the expectations. However, the spectrum of modes exhibits a different nature compared to the $t = 0.3$s case: the modes below $k_\theta \rho_\mathrm{i} \approx 1.2$ rotate in the electron diamagnetic direction and their frequencies monotonically increase with the mode number. If both density and temperature gradients are increased (red x-es) a similar behaviour is found, but the real frequencies are shifted up and thus the transition point from ion to electron direction is moved to $k_\theta \rho_\mathrm{i} \approx 0.6$, and the modes below this value are further destabilized by the increased temperature gradient. As described in [54], the spectra in these two latter cases consist of trapped electron modes that are destabilized by the electron density gradient, and that obtain fluid-like character at higher mode numbers. These observations are in contrast with the results of the $t = 0.8$s case (solid, cyan diamonds). At $t = 0.8$s the modes are stabilized by the increased collisionality. The unstable modes below $k_\theta \rho_\mathrm{i} \approx 1$ show the characteristics of the ITG modes (positive real frequency) and drive an outward deuterium flux.

The microstability and particle transport properties of the $t = 0.8$s case can be further approached by sequentially increasing the reference collision frequency to $\nu_{\mathrm{ii,N}} = 0.2$, decreasing the lithium concentration to $c_\mathrm{Li} = 0.01$ and electron temperature to $T_\mathrm{e}/T_\mathrm{i} = 0.9$, as shown on figure 3.10. The graphs indicate that the high collisionality is essential in stabilizing the trapped electron modes but it is not, on its own, sufficient to obtain the mode structure and fluxes as observed at the later time stage. Only by reducing the lithium concentration (and thus decreasing the effective collisionality) can an ITG dominated spectrum and outward deuterium flux in the mid-k range ($k_\theta \rho_\mathrm{i} > 0.6$) be reproduced. The high-k modes are stabilized by the lower electron temperature, and the low-k ITG mode growth rates are reduced by the increased magnetic shear (not shown), finally providing the spectrum of the $t = 0.8$s case.

The impurity density scan at $t = 0.8$s, presented on figure 3.11, shows that the reversal of the deuterium flux can be retained again with high lithium concentration. However, the effect on the microstability is even more pronounced in this case. Both at $c_\mathrm{Li} = 0.1$ and $c_\mathrm{Li} = 0.15$ the growth rate and frequency (top left and right) spectra suggest the presence of three distinct modes rotating in the ion di-

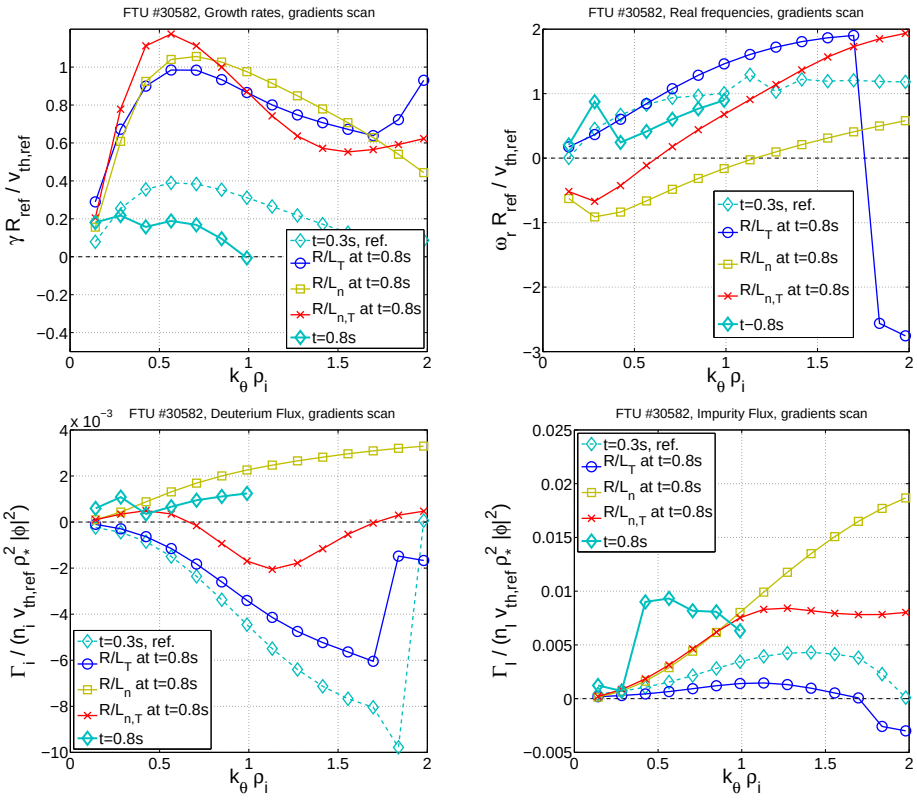

Figure 3.9: Effect of increasing the gradients on the growth rate (top left), real frequency (top right), quasi-linear deuterium (bottom left) and lithium (bottom right) flux as a function of the bi-normal wavenumber at $t = 0.3$s.

rection. The low-k peak can be associated with the D-ITG modes, the middle peak between $0.5 < k_\theta \rho_\mathrm{i} < 1.5$ with Li-ITG modes, and above $k_\theta \rho_\mathrm{i} \approx 1.5$ with ion drift modes. The stabilization of the D-ITG and destabilization of the ion drift modes is attributed to the significantly increased effective collisionality. In both the $c_\mathrm{Li} = 0.1$ and $c_\mathrm{Li} = 0.15$ cases the Li-ITG modes are characterized by strong potential and density phase difference and drive an inward deuterium flux. The ion drift modes also drive an outward deuterium flow but their contribution is likely to be small in the saturated phase due to their high k_θ values.

Separation of Ion ITG Modes

The above results highlight the role of lithium impurities in ITG driven turbulent transport. At $t = 0.8$s the impurity ITG modes can be distinguished from the D-ITG, the former driving inward and the latter outward deuterium flux (figure

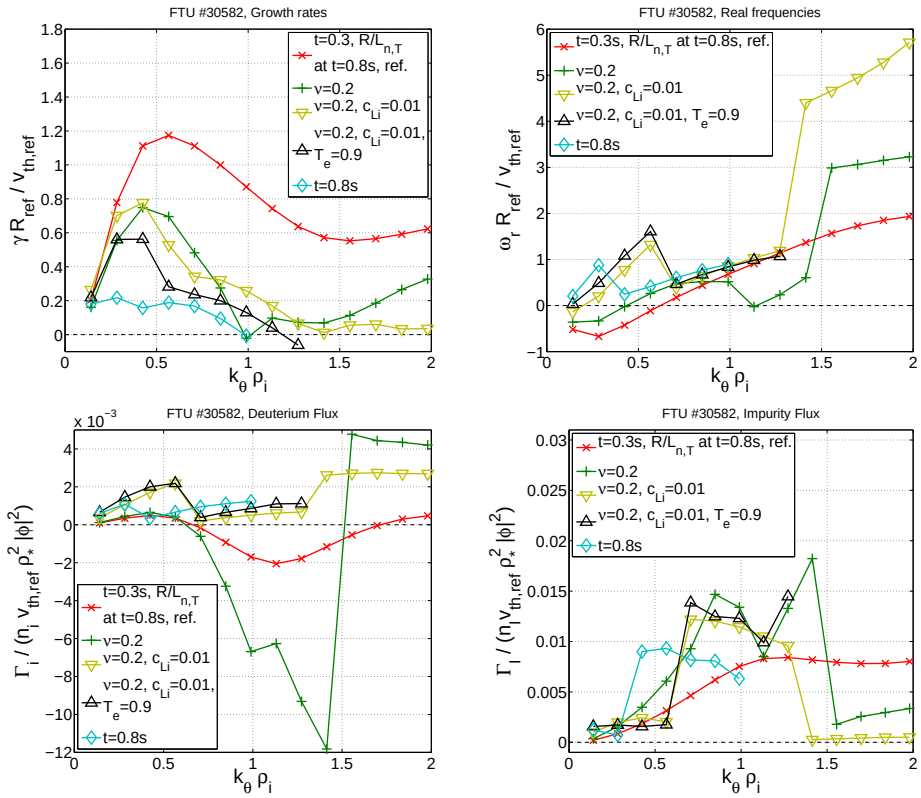

Figure 3.10: Approaching the $t = 0.8$s case (cyan diamonds) by increasing the gradients (red x-es), collisionality (green crosses), decreasing the lithium concentration (yellow down triangle) and electron temperature (black up triangle) from their respective values at $t = 0.3$s.

3.11). At $t = 0.3$s D-ITG and Li-ITG modes are not as clearly separated in the bi-normal wavenumber spectrum (figure 3.3), they are expected to be mixed ITG modes sensitive to the temperature gradients of both ion species [44]. However, the presence of the lithium ions changes the phase difference between the deuterium density and potential fluctuations in a way that it produces an inward deuterium flux (figure 3.4). This effect is different from the collisionality effect described in [55]: Fable et al. showed that collisionality provides an outward contribution to the radial deuterium flux in a plasma with trace impurities, whereas in the present case larger lithium concentration leads to inward deuterium transport despite the increasing collisionality. However, if the collisionality is sufficiently high, the reduction of the impurity concentration towards the trace limit leads to outward main ion flux, in agreement with [55].

The typical spatial scale of the impurity ITG modes can be separated from

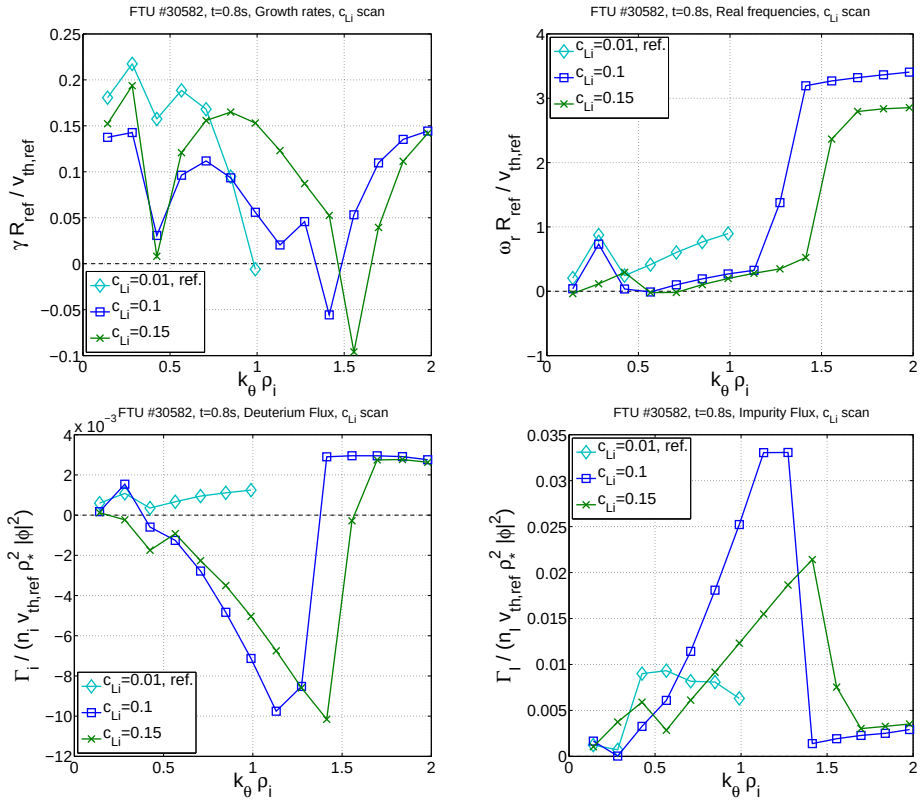

Figure 3.11: Lithium concentration scan of growth rate (top left), real frequency (top right), quasi-linear deuterium (bottom left) and lithium (bottom right) flux as a function of bi-normal wavenumber at $t = 0.8$s.

those of the deuterium by reducing the impurity temperature, and thus their Larmor-radius: $\rho_{\mathrm{Li}}/\rho_{\mathrm{D}} = Z_{\mathrm{D}}/Z_{\mathrm{Li}}\sqrt{m_{\mathrm{Li}}T_{\mathrm{Li}}/(m_{\mathrm{D}}T_{\mathrm{D}})}$. Figure 3.12 shows the effect of changing the $T_{\mathrm{Li}}/T_{\mathrm{D}}$ temperature ratio from 1 down to 0.5 (green circles) and 0.2 (blue squares). At 50% reduced lithium temperature all ion modes are stabilized highlighting their mixed nature. The ion peak in the growth rate spectrum becomes wider as the modes at higher k_θ values are destabilized as a result of the smaller lithium Larmor-radius. A further cooling of the impurity species almost completely stabilizes the lithium modes due to their significantly increased collisionality. However, the peak of the lithium driven modes is now shifted even further away from the main D-ITG region.

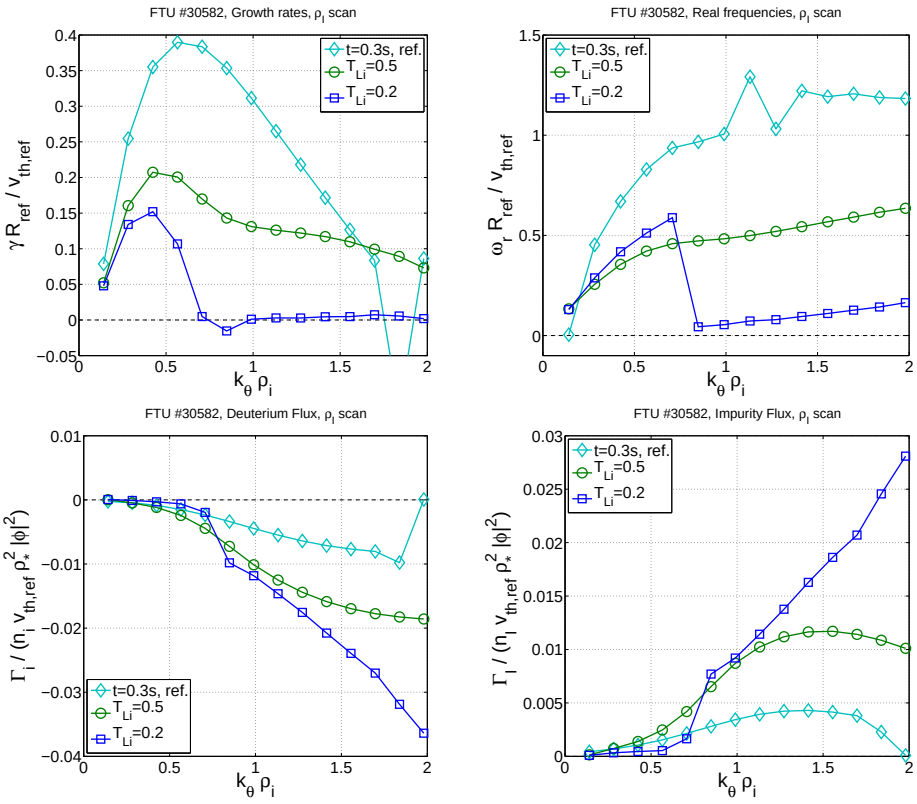

Figure 3.12: Effect of changing the impurity Larmor-radius on the growth rate (top left), real frequency (top right), quasi-linear deuterium (bottom left) and lithium (bottom right) flux as a function of the bi-normal wavenumber at $t = 0.3$s.

3.1.3 Non-linear Gyrokinetic Analysis

A non-linear gyrokinetic study of the FTU #30582 discharge has been carried out with GKW in order to support the linear gyrokinetic and fluid results. Figure 3.13 shows four electro-static simulations of the radial particle flux of the species driven by the ITG modes as a function of time at $t = 0.3$s and $r/a = 0.6$. The top left panel is the reference, it corresponds to the experimental lithium concentration $c_{\mathrm{Li}} = 0.15$, while the top right panel to the reduced $c_{\mathrm{Li}} = 0.01$ impurity concentration. In both cases the full collision operator has been adopted. The simulation of the reference case has been performed with 21 bi-normal modes equally spaced up to $k_\theta \rho_{\mathrm{i}} = 1.6$ and 83 radial modes, yielding a box size of $\sim 75\rho_{\mathrm{i}}$ in both perpendicular directions. In the reduced lithium case the maximum wavenumber has been decreased to $k_\theta \rho_{\mathrm{i}} = 1.4$ in order to match the transition point from ITG to TEM in the corresponding linear spectrum. The resolution along the remaining dimensions is 16 points per

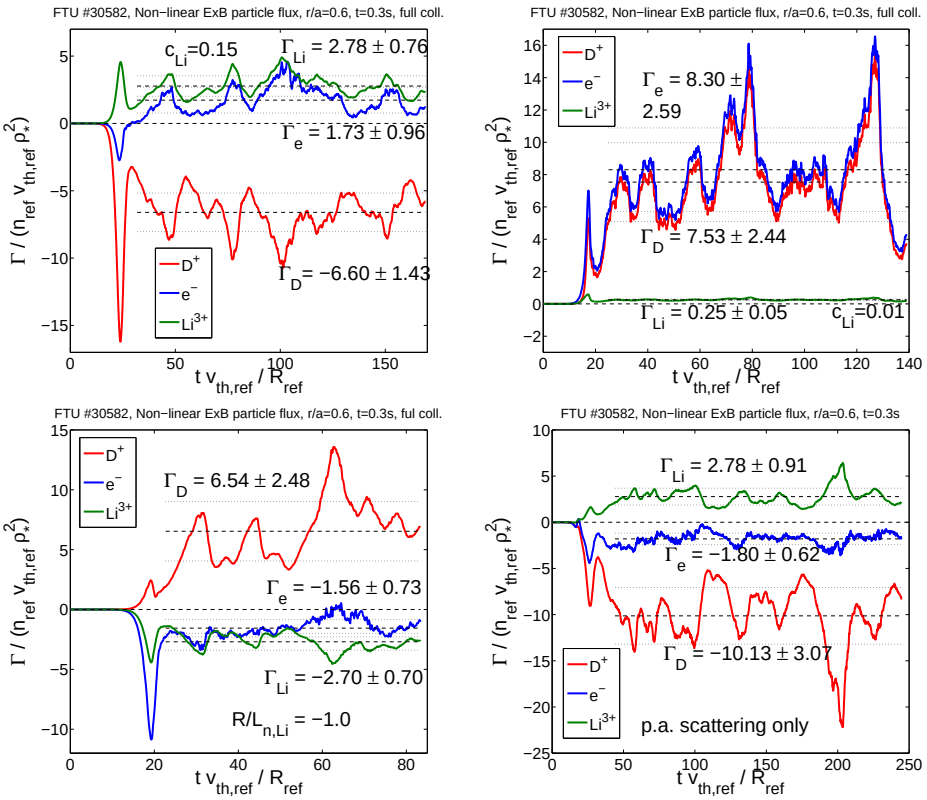

Figure 3.13: Non-linear simulation of the radial particle flux driven by ITG modes as a function of time in FTU #30582 at $t = 0.3$s and $r/a = 0.6$, using the full collision operator, with the experimental ($c_{\mathrm{Li}} = 0.15$, top left) and with reduced ($c_{\mathrm{Li}} = 0.01$, top right) lithium concentration. The experimental case with negative impurity density gradient $R_{\mathrm{ref}}/L_{\mathrm{n,Li}} = -1.0$ and with pitch-angle scattering only are shown on the bottom left and right panels.

period in parallel direction, 10 points in magnetic moment and 48 points in parallel velocity space. The fluxes are expressed in units of $n_{\mathrm{ref}} v_{\mathrm{th,ref}} \rho_*^2 \approx 7.9 \cdot 10^{18} \mathrm{s}^{-1} \mathrm{m}^{-2}$.

The reference case (top left) shows that the deuterium and lithium flux maintain their directions as predicted by the linear analysis. However, the electron flux changes from inward to outward when progressing into the saturated phase. This suggests that the electron flux is determined by the fast growing modes above $k_\theta \rho_{\mathrm{i}} \approx 0.5$ in the linear phase (see figure 3.4, top right) but they are overtaken by the low-k modes in the saturated phase. Therefore, quasi-linear methods for estimating electron transport have to be employed with caution in this particular case.

The same non-linear simulation using pitch-angle scattering only (figure 3.13, bottom right) gives approximately the same value for the lithium flux: 2.78 ± 0.91,

and values reduced by approximately the same number for both deuterium and electron fluxes: -10.13 ± 3.07 and -1.80 ± 0.62, respectively. This reduction is again in agreement with the expected outward contribution of the collisions [55]. The different direction of the simulated electron flux with the full collision operator and pitch-angle scattering only is due to the fact that the electron transport is near zero. In this case the additional outward component of the flux provided by the energy scattering and friction terms is sufficient to change the direction of the turbulent electron transport.

If the impurity density gradient is negative on the analysed flux surface (figure 3.13, bottom left), the ion species flow in the opposite radial direction compared to the experimental case, as anticipated from the linear results (figure 3.6). The electron flux also becomes negative due to the reduced electron density gradient ($R_{\mathrm{ref}}/L_{\mathrm{n,e}} = 1.1$).

When the lithium concentration is reduced to $c_{\mathrm{Li}} = 0.01$ (figure 3.13, top right) both the deuterium and electron fluxes are outward and the lithium flux is negligible. The value of the outward electron flux in this case (8.30 ± 2.59) is almost a factor of five larger than in the experimental case (1.73 ± 0.96). The deuterium flux is thus reversed and the electron flux is significantly reduced by the high lithium concentration, as suggested by figure 3.4 in the linear analysis. The heat flux of the species (not shown) is also lower by approximately a factor of two at $c_{\mathrm{Li}} = 0.15$ than at $c_{\mathrm{Li}} = 0.01$ which can be attributed to the stabilization of the ITG modes.

The electron flux can be estimated from the time evolution of the density profile by solving the transport equation $\partial_t n(\psi) = -\nabla_\psi \cdot \Gamma(\psi) + S(\psi)$, where ψ is the radial coordinate. Calculating the fluxes for the transport equation with gyrokinetic method at a reasonable radial resolution is a comuptationally expensive project and it has not been done for this thesis. However, this calculation has been performed with the JETTO [56] transport code using a fluid model to approximate the fluxes and assuming the source term S to be zero. The results of this simulation have been plotted in figure 3.14. The left panel shows the experimental electron flux profile at $t = 0.3$s, and the right panel the time traces of the flux at $r/a = 0.6$. Since the estimated electron flux is much larger than the simulated one in the reference case (figure 3.13, top left), especially towards the edge, it suggests that there is significant electron source in the plasma at this time. However, the simulated electron flux in the reduced lithium concentration case is of the same magnitude as the estimated one, and thus it would effectively counteract the source term. The lithium induced electron flux reduction therefore seems to be an important factor in achieving a highly peaked electron density profile. The time traces of the estimated electron flux

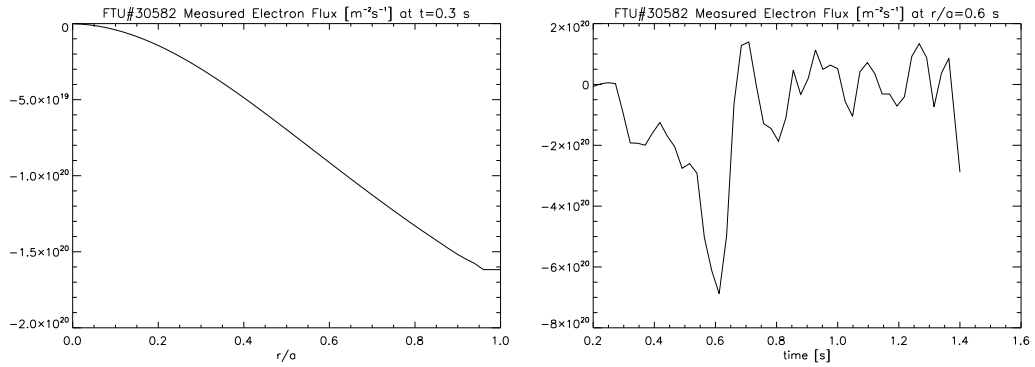

Figure 3.14: Estimate of the radial electron flux based on time evolution of the measured electron density profile. Left: flux profile at t=0.3s. Right: time traces of the flux at $r/a = 0.6$.

(figure 3.14, right) show that the electron density increases until $t = 0.6$s, after which an oscillation around zero occurs in the stady-state phase of the discharge. The ion density profiles are not measured directly, the same analysis is not immediately available. However, since the average Z_{eff} of the plasma decreases to near unity during the experiment, the deuterium profile must reach approximately the same degree of peaking as the electrons.

Since FTU #30582 is an Ohmically heated discharge with relatively low temperature and high magnetic field, the Ware-pinch is expected to contribute to the total particle flux with a significant margin. The neoclassical particle transport has been estimated with the Neoart code [57]. The turbulent electron flux predicted by GKW in physical units is $\Gamma_{\text{e}}^{\text{turb}} \approx 1.34 \cdot 10^{19}\text{s}^{-1}\text{m}^{-2}$. The overall neoclassical electron flux is calculated as $\Gamma_{\text{e}}^{\text{neo}} \approx -0.87 \cdot 10^{19}\text{s}^{-1}\text{m}^{-2}$ of which the flux due to the Ware-pinch is $\Gamma_{\text{e}}^{\text{Ware}} \approx -0.99 \cdot 10^{19}\text{s}^{-1}\text{m}^{-2}$. The turbulent and neoclassical values are thus comparable and the neoclassical contribution further reduces the electron transport.

Peaking could also be caused by a larger electron source in the core originating from an increased number of lithium atoms. However, a crude estimate of the neutral lithium penetration depth shows that lithium atoms can only travel approximately 0.5 cm before ionization under plasma conditions at $r/a = 0.6$ and $t = 0.3$s. The penetration depth is certainly larger near the edge, this result nonetheless suggests that the electron source term in the core is not significantly increased by lithium atoms coming from the limiter during the density ramp-up phase of the discharge. The estimate is based on the formula $\lambda_{\text{iz}} = v_{\text{n}}/(n_{\text{e}}\overline{\sigma v_{\text{iz}}}(T_{\text{e}}))$, where λ_{iz} is the penetration depth, v_{n} is the velocity of the neutrals and $\overline{\sigma v_{\text{iz}}}(T_{\text{e}})$ is the tem-

MAST parameters	Value	Dim.
Plasma diameter	3	m
Plasma volume	8	m^3
Plasma current	1.3	MA
Toroidal magnetic field	0.6	T
Pulse length	1	s

Table 3.3: Typical parameters of the MAST tokamak. Data from http://www.ccfe.ac.uk/MAST.aspx

perature dependent electron ionization coefficient [58]. The ionization coefficient for lithium can be found in [59], in the range of $T_e \approx 0.57$ keV its value is approximately $\overline{\sigma v_{iz}}(T_e) \approx 5 \cdot 10^{-14}$ m^3/s. The neutral velocity for hydrogen atoms has been estimated in [60] as $v_n \approx 1.7 \cdot 10^4$ m/s by assuming Franck–Condon atoms. The same value has been used for lithium which, albeit not accurate, provides a conservative estimate for the penetration depth, since the lithium neutral velocity is expected to be lower.

3.2 Analysis of MAST #24541

MAST is a medium size spherical tokamak located in Culham Science Centre, UK, its characteristic parameters are summarized in table 3.3. Due to their compact shapes, spherical tokamaks are capable of operating at much lower toroidal magnetic field, and typically higher plasma beta, than the conventional tokamaks. The effects of high plasma beta and finite magnetic perturbations on turbulent transport are investigated with a series of gyrokinetic simulations of the MAST discharge #24541. The role of light impurities in determining mode stability and transport in high-beta plasmas is also discussed.

Plasma beta impacts the turbulence in two major ways. First, by enabling magnetic perturbations it gives rise to magnetic flutter and fluctuating grad-B velocities, as introduced in chapter 2, and leads to electro-magnetic eigenmodes. Second, it has an effect on the magnetic equilibrium: the Shafranov-shift α is proportional to the radial derivative of beta, and therefore high-beta tokamak plasmas are characterized by strongly shifted flux surfaces. This mainly affects the vertical drift frequency and therefore has an impact of the response of the species. The circular, non-shifted geometry, that has been applied in the previous section, is not a sufficient approximation of the magnetic structure. The magnetic equilibrium required

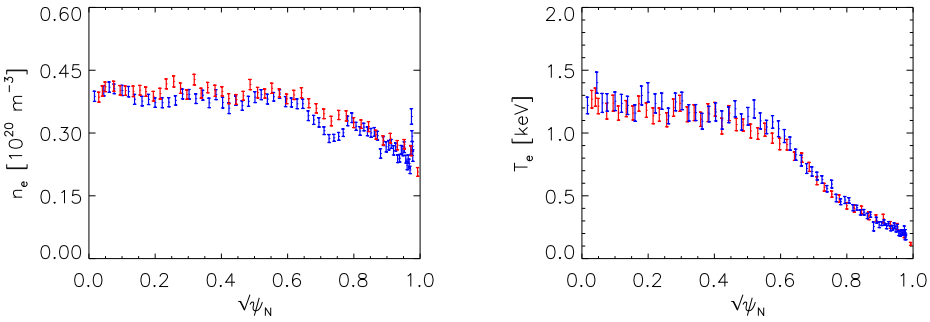

Figure 3.15: Electron density (left) and temperature profiles (right) at $t = 0.317$s as a function of the square root of the normalized poloidal flux $\sqrt{\psi_N}$. Blue points indicate measurements on the inboard and red ones on the outboard side.

for the GKW simulations of this MAST discharge is calculated using the CHEASE [61] Grad–Shafranov solver code. In this thesis only the first effect of high plasma beta is investigated.

3.2.1 Experimental Features of MAST #24541

The discharge selected for the analysis is a typical ELMy H-mode MAST plasma without any particular instability in the core causing additional complexity. The plasma beta is moderate ($\beta_{\text{ref}} \sim 3.6\%$ locally on the magnetic surface) but it is sufficient to provide non-negligible magnetic perturbations. The radial electron density and temperature profiles at $t = 0.317$s are indicated on figure 3.15 (figure courtesy of Luca Garzotti), where the radial coordinate is the square root of the normalized poloidal flux ψ_N. The profiles are flat in most of the core plasma, typical to H-mode discharges, the gradient region is located outside $\sqrt{\psi_N} \approx 0.6$.

The magnetic equilibrium has been reconstructed with the CHEASE code. The input required for a CHEASE run consists of the coordinates of the last closed flux surface, the pressure and the current (or q) profiles. These can be specified numerically with the measured values, or with analytical formulae. In the present case the measured coordinates of the last closed flux surface has been used, and the profiles have been approximated by 8th degree polynomial expressions. The poloidal cross section of the magnetic equilibrium as calculated by CHEASE is shown in figure 3.16. As it has been mentioned above, the magnetic equilibrium is sensitive to changes in plasma beta, and it should be consistently recalculated for simulations scanning over different beta values. However, the analysis of the geometrical effects

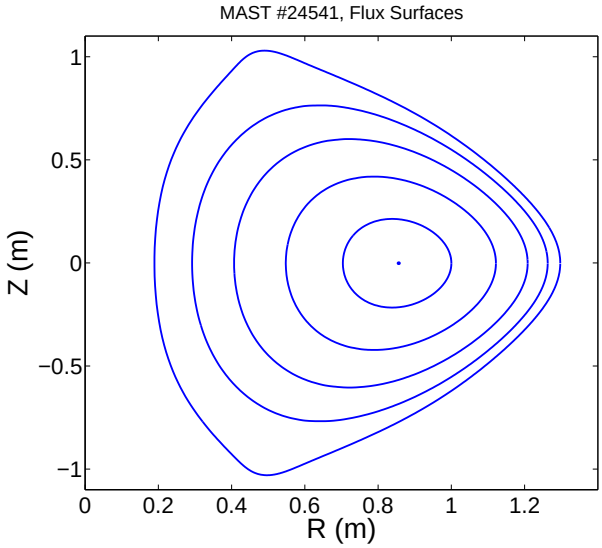

Figure 3.16: Flux surfaces of MAST #24541 as reconstructed by the CHEASE equilibrium code.

on turbulence is not within the focus of this thesis, and the gyrokinetic simulations have all been performed with the same equilibrium.

The discharge was heated by two beams of Neutral Beam Injection (NBI) depositing $P_{\mathrm{NBI}} \sim 3.5$MW heating power into the plasma. The toroidal rotation velocity of the plasma caused by NBI heating is of the order of $v_{\mathrm{tor}} \sim 10^5$ m/s (profile shown on figure 3.17). Although plasma rotation is expected to have a stabilising property on the ITG modes, the effect of rotation on the turbulence is outside the main scope of this thesis and the simulations have been performed assuming stationary plasma.

3.2.2 Linear Gyrokinetic Analysis

The simulations have been performed at $t = 0.317$s at the radial position of $\psi_{\mathrm{N}} = 0.8$, including carbon impurities. The relevant plasma parameters are listed in table 3.4. Similar to the FTU analysis, the reference density is chosen to be the electron density, and the reference temperature is the deuterium temperature.

The spectra of growth rates (top left), frequencies (top right), quasi-linear deuterium and impurity flux (bottom left and right) are shown on figure 3.18 for five different values of β_{ref}. The reference value, as calculated from the measured quantities, is $\beta_{\mathrm{ref}} = 0.036$. The points above $k_\theta \rho_{\mathrm{i}} \approx 1$ of the reference curve are stable. The fluxes plotted here are driven by the fluctuating ExB velocity, corre-

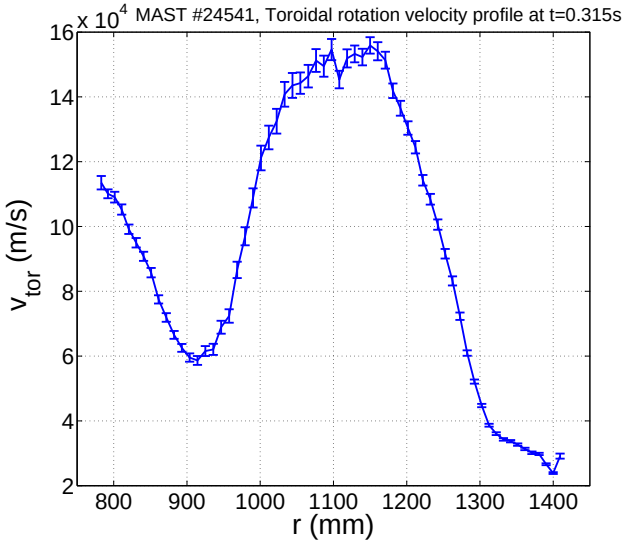

Figure 3.17: Measured toroidal rotation velocity profile of MAST #24541 at $t = 0.315$s.

	$n[10^{19}\mathrm{m}^{-3}]$	$T[\mathrm{keV}]$	$-\frac{R_{\mathrm{ref}}\nabla T}{T}$	$-\frac{R_{\mathrm{ref}}\nabla n}{n}$
		$t = 0.317$s		
D^+	2.52	0.58	7.85	2.09
e^-	2.96	0.43	6.06	1.17
C^{6+}	0.073	0.58	7.85	-4.12
	$B_{\mathrm{ref}} = 0.56$T	$R_{\mathrm{ref}} = 0.93$m	$\nu_{\mathrm{ii,N}} = 0.0088$	$Z_{\mathrm{eff}} = 1.74$

Table 3.4: Plasma parameters of MAST #24541 at $\psi_{\mathrm{N}} = 0.8$ and $t = 0.317$s.

sponding to the first term of equation 2.80. This is the only term present in an electro-static simulations, and even in high beta electro-magnetic runs it remains the dominant part in the total quasi-linear flux. The terms associated with the perturbed magnetic flutter and grad-B drift velocities are still at least one order of magnitude smaller, as shown on figure 3.20. The top left panel of figure 3.18 shows a strongly increasing mode growth when β_{ref} is raised from 2% to 10%. The growth rates of the $\beta_{\mathrm{ref}} = 0.02$ and $\beta_{\mathrm{ref}} = 0.036$ cases are similar below $k_\theta \rho_{\mathrm{i}} = 1$. However, the frequency plots (top right panel) indicate that they are different modes. At $\beta_{\mathrm{ref}} = 0.02$ all the modes rotate in the ion diamagnetic direction, whereas at $\beta_{\mathrm{ref}} = 0.036$ the mode frequency changes sign at $k_\theta \rho_{\mathrm{i}} \approx 0.4$. At $\beta_{\mathrm{ref}} = 0.05$ there is

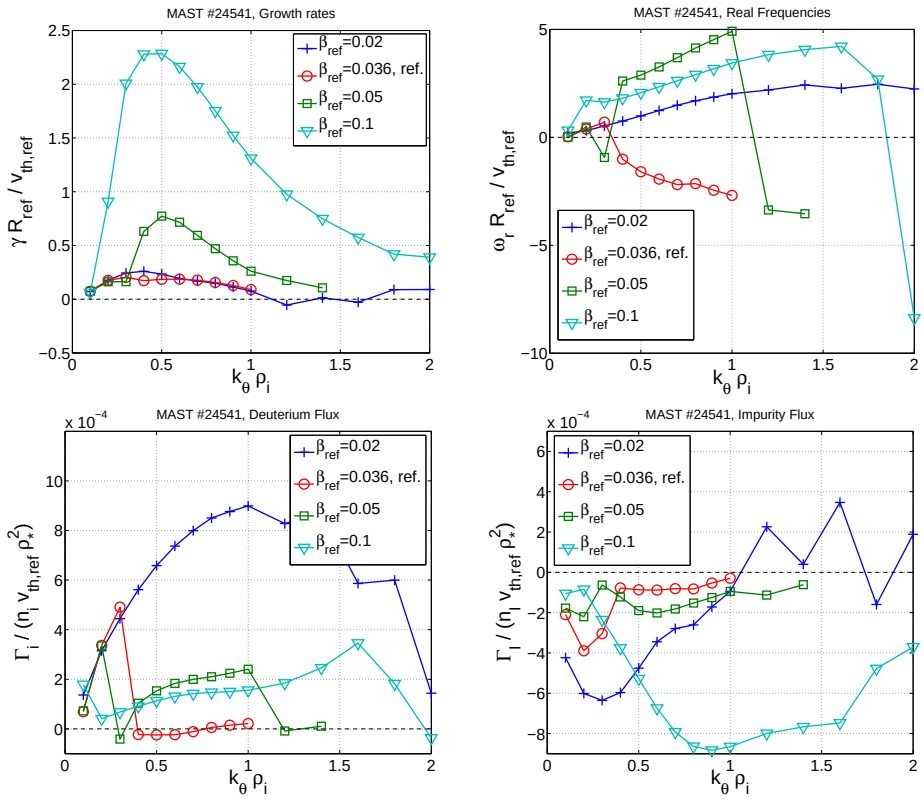

Figure 3.18: β_{ref} scan of growth rate (top left), real frequency (top right), quasi-linear ExB driven deuterium (bottom left) and carbon (bottom right) flux as a function of the bi-normal wavenumber.

a narrow region in the spectrum where the modes rotate in the electron direction at $k_\theta \rho_{\mathrm{i}} \approx 0.3$, and again above $k_\theta \rho_{\mathrm{i}} \approx 1$. At $\beta_{\mathrm{ref}} = 0.1$ a similar transition occurs at $k_\theta \rho_{\mathrm{i}} \approx 1.9$.

In order to elucidate this behaviour it is useful to take a look at the parallel structure of the various modes, also called the parallel eigenfunctions, and how they change with varying plasma beta. Figure 3.19 illustrates the linear electro-static potential Φ and parallel vector potential $A_{\parallel}$ responses of the most unstable bi-normal modes ($k_\theta \rho_{\mathrm{i}} = 0.3 - 0.4$) at three different beta values as a function of the parallel coordinate s. The centre of the graphs ($s = 0$) is the outboard midplane around which the modes are typically localized, and the values are normalized to $|\Phi(s = 0)|$. In three of the included cases (at $\beta_{\mathrm{ref}} = 0.036$ and $k_\theta \rho_{\mathrm{i}} = 0.3$, $\beta_{\mathrm{ref}} = 0.02$ and $k_\theta \rho_{\mathrm{i}} = 0.4$, $\beta_{\mathrm{ref}} = 0.05$ and $k_\theta \rho_{\mathrm{i}} = 0.4$) the real part of the electro-static potential perturbation is an even function of the parallel coordinate accompanied by an anti-symmetric (odd) vector-potential perturbation. These are characteristic

properties of the electro-static ITG, TEM and ETG modes, as well as the electro-magnetic Kinetic Ballooning Modes (KBM) [40]. In the fourth case the shape of the eigenmodes is the opposite: the scalar potential becomes odd and the vector potential is approximately even, which is the signature of the electro-magnetic micro-tearing mode (MTM) [41]. MTM-s are also typically more elongated along the magnetic field lines than the ITG modes. It can be shown that the even shape of the vector potential eigenfunction $A_{\parallel}(s)$ leads to tearing of the magnetic field lines and generation of magnetic islands [41]. Therefore, the odd parallel Φ mode structure is also sometimes referred to as tearing mode parity. Micro-tearing modes are also distinguished from ITG modes by having negative real frequencies. In conclusion, figure 3.19 shows that at $\beta_{\text{ref}} = 0.036$ the spectrum changes from ITG mode to micro-tearing mode (insted of TEM/ETG) dominated regime at $k_\theta \rho_{\text{i}} = 0.4$. Micro-tearing modes are commonly observed in MAST due to its relatively high beta operation [41].

In figure 3.21 a more detailed β_{ref} scan of the fastest growing mode at $k_\theta \rho_{\text{i}} = 0.4$ is shown. At low plasma beta a typical ITG driven mode is observed. As β_{ref} increases the mode is slightly stabilized, but at $\beta_{\text{ref}} \approx 0.04$ the trend changes. As the ITG mode becomes less unstable it eventually transitions into a micro-tearing mode at $\beta_{\text{ref}} \approx 0.4$. If the plasma beta is further increased the mode changes again and turns into a kinetic kallooning mode characterized by growth rates strongly increasing with β_{ref} [40]. In the reference case the plasma beta ($\beta_{\text{ref}} = 0.036$) is close to the transition point of the fastest growing mode between the ITG and KBM regimes. This is the point when the ion modes are the most stable and hence a micro-tearing dominated spectrum occurs above $k_\theta \rho_{\text{i}} \approx 0.4$, as observed on figure 3.18. At lower beta ($\beta_{\text{ref}} = 0.02$) the ITG modes remain dominant across the spectrum up to $k_\theta \rho_{\text{i}} = 2$. At $\beta_{\text{ref}} = 0.05$ the ITG mode stabilization is stronger and therefore the transition point occurs at a lower wavenumber value, at $k_\theta \rho_{\text{i}} \approx 0.3$. First a narrow region of micro-tearing modes is observed followed by the destabilization of KBM-s rotating in the ion diamagnetic direction. At the second transition point, at $k_\theta \rho_{\text{i}} \approx 1$, the spectrum becomes dominated by micro-tearing modes again as KBM-s are stabilized at smaller length scales. In the highest beta case included in this analysis at $\beta_{\text{ref}} = 0.1$ the modes obtain a KBM nature already at the lowest wavenumber values, a change from KB to micro-tearing modes can be observed at $k_\theta \rho_{\text{i}} \approx 1.9$ due to the stronger drive of the kinetic ballooning modes.

The quasi-linear electro-static deuterium flux driven by the ITG modes (bottom left, figure 3.18) align with each other at all four values of plasma beta, following the $\beta_{\text{ref}} = 0.02$ curve. The deuterium transport points outward, and the

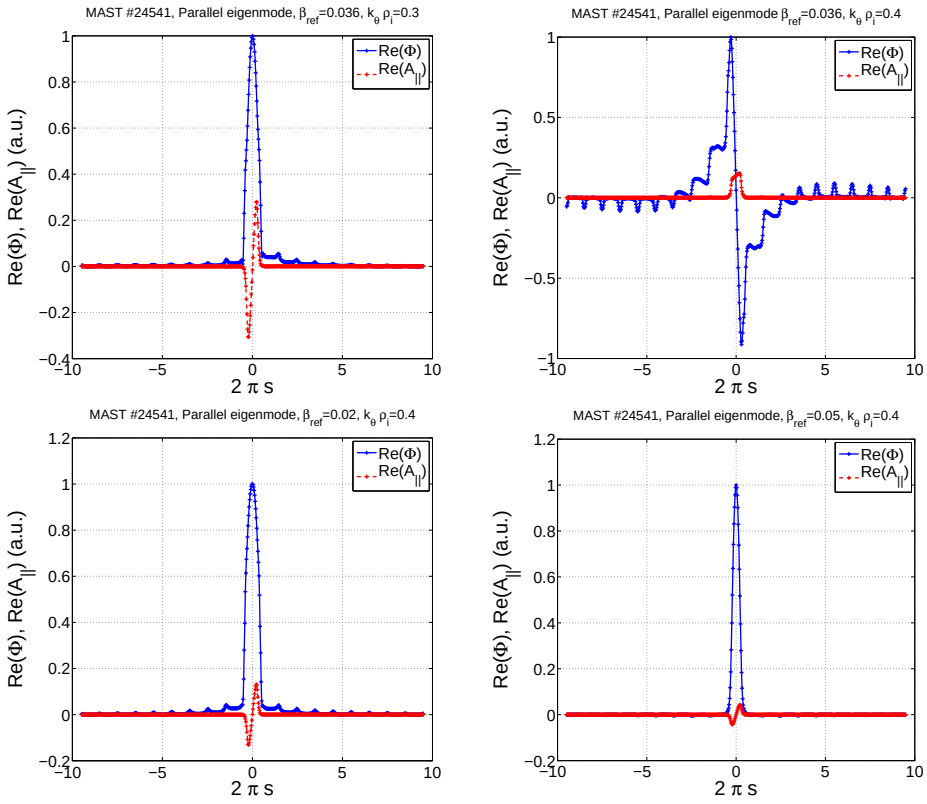

Figure 3.19: Parallel mode structure of the real part of the normalized electro-static (blue) and parallel vector potential (red) perturbations. Top left: $\beta_{\rm ref} = 0.036$, $k_\theta \rho_{\rm i} = 0.3$, Top right: $\beta_{\rm ref} = 0.036$, $k_\theta \rho_{\rm i} = 0.4$ (tearing parity), Bottom left: $\beta_{\rm ref} = 0.02$, $k_\theta \rho_{\rm i} = 0.4$, Bottom right: $\beta_{\rm ref} = 0.05$, $k_\theta \rho_{\rm i} = 0.4$.

phase difference between the potential and density perturbations is reduced when the modes transition to the micro-tearing (in the $\beta_{\rm ref} = 0.036$ case) or to the KB (in the $\beta_{\rm ref} = 0.05$ and 0.1 cases) regime. The carbon flux (bottom fight, figure 3.18) points inward in all four cases, and becomes reduced with increasing plasma beta in the ITG driven regime. However, the KBM-s appear to generate stronger phase difference when $\beta_{\rm ref}$ is increased.

The magnetic flutter component of the quasi-linear ion flux (top and bottom left, figure 3.20) driven by the ITG modes ($\beta_{\rm ref} = 0.02$, crosses) generates an outward particle transport. When KBM-s appear due to the increasing plasma beta the linear flux becomes less negative and eventually changes direction at $\beta_{\rm ref} = 0.1$. The deuterium flux driven by the micro-tearing dominated modes both in the $\beta_{\rm ref} = 0.036$ and $\beta_{\rm ref} = 0.05$ cases provide an outward contribution. While the flux associated with the magnetic flutter velocity is qualitatively similar for the two ion species, the

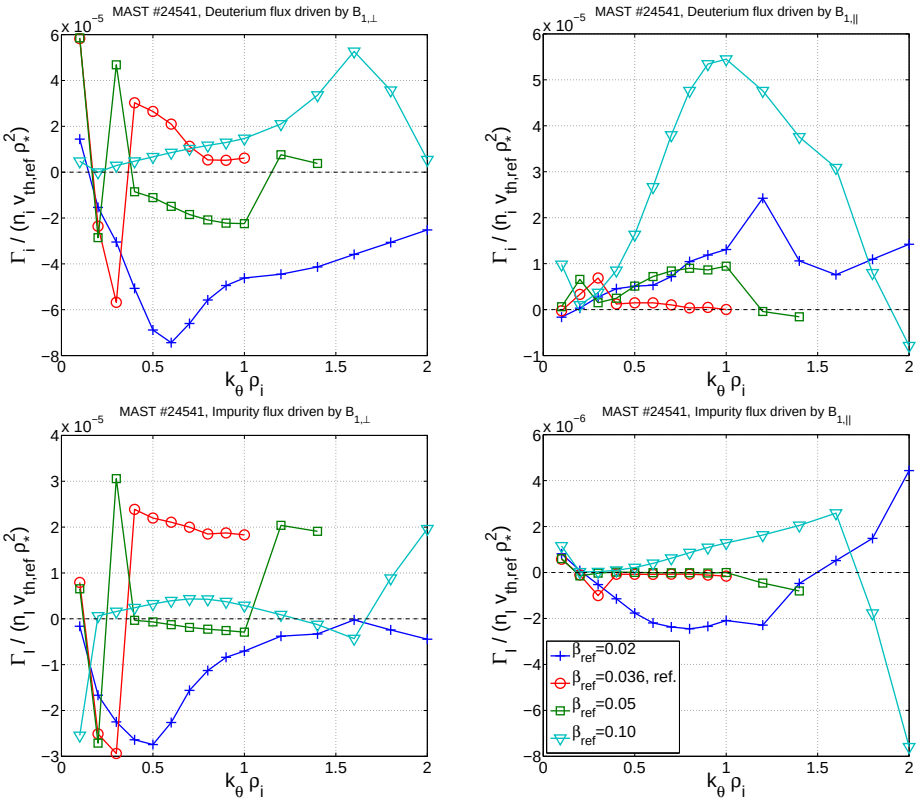

Figure 3.20: β_{ref} scan of deuterium (top) and carbon (bottom) flux driven by the magnetic flutter (left) and compressional grad-B drift (right) velocities as a function of the bi-normal wavenumber.

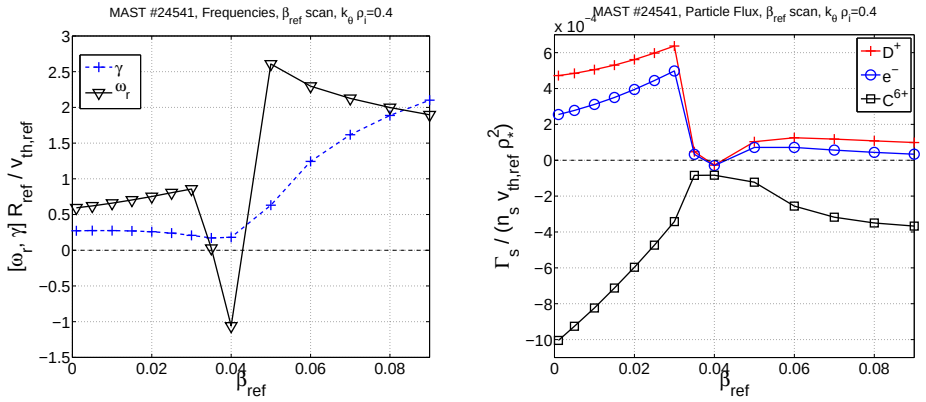

Figure 3.21: β_{ref} scan of the fastest growing mode at $k_\theta \rho_{\mathrm{i}} = 0.4$. Left: growth rate (dashed, cross) and real frequency (solid, triangle), right: ExB driven quasi-linear particle flux of deuterium (cross), electron (circle) and carbon (square) species.

flux due to magnetic compression (top and bottom right, 3.20) shows different behaviour: the ITG modes drive an outward deuterium and inward impurity transport reinforcing, although only with a small margin, the electro-static fluxes. The KBM driven deuterium transport is outward and increases with β_{ref}. The KBM driven impurity transport is negligible at $\beta_{\mathrm{ref}} = 0.05$ but grows positive as plasma beta is further increased.

In the remaining part of this section the effect of light impurities on the linear ITG and KB modes will be discussed. Since in the experimental case the plasma beta ($\beta_{\mathrm{ref}} = 0.036$) is close to the critical beta for the onset of the KB modes ($\beta_{\mathrm{ref,C}} \approx 0.04$), the $\beta_{\mathrm{ref}} = 0.02$ case has been selected for the ITG analysis. The KBM-s are studied in the $\beta_{\mathrm{ref}} = 0.1$ case.

Figure 3.22 shows the growth rate, electro-static quasi-linear electron, deuterium and impurity flux spectra in five different settings in the ITG dominated regime (the reference curve is the $\beta_{\mathrm{ref}} = 0.02$ case, crosses). Increasing the carbon concentration from the original $c_{\mathrm{C}} = n_{\mathrm{C}}/n_{\mathrm{e}} = 0.025$ value (crosses) to $c_{\mathrm{C}} = 0.05$ (circles, $Z_{\mathrm{eff}} = 2.5$) destabilizes the Carbon-ITG modes around $k_\theta \rho_{\mathrm{i}} \sim 1.5$ and stabilizes the the D-ITG peak, in a way analogous to the lithium effect in the FTU analysis. The deuterium flux is only slightly affected by the increased carbon concentration. However, the inward impurity flux driven by the D-ITG modes has been significantly decreased compared to the reference curve, and an outward transport above $k_\theta \rho_{\mathrm{i}} \approx 0.6$ can be observed. If the carbon ions in the $c_{\mathrm{C}} = 0.05$ case are replaced by lithium while keeping the same deuterium dilution ($c_{\mathrm{Li}} = 0.1$, $Z_{\mathrm{eff}} = 1.6$, squares), the modes are destabilized in a wide region around $k_\theta \rho_{\mathrm{i}} \approx 1$. The stabilization of the D-ITG is less pronounced due to the lower Z_{eff}. The impurity flux is similar to that in the $c_{\mathrm{C}} = 0.05$ case, however, in the region where the lithium affects the growth rate spectrum the deuterium flux is also strongly reduced. This effect is not observed in presence of the heavier carbon impurity. In all five cases the variation of the impurity concentration has a negligible effect on the electron flux. This is explained by the fact that in typical tokamak conditions the electromagnetic fluctuations provide the main mechanism driving a non-adiabatic electron response [62]. Already at $\beta_{\mathrm{ref}} = 0.02$ the electron flux is not reduced by the presence of impurities and therefore an ion flow separation, as observed in every cases of the FTU analysis, does not necessarily occur.

The cases discussed so far are all characterized by a negative impurity density gradient, and an impurity flux driven inward by the low-k ITG modes. In the remaining two cases in figure 3.22 the effect of a centrally peaked impurity density profile (i.e. positive local density gradient) is tested. First, the density gradient of

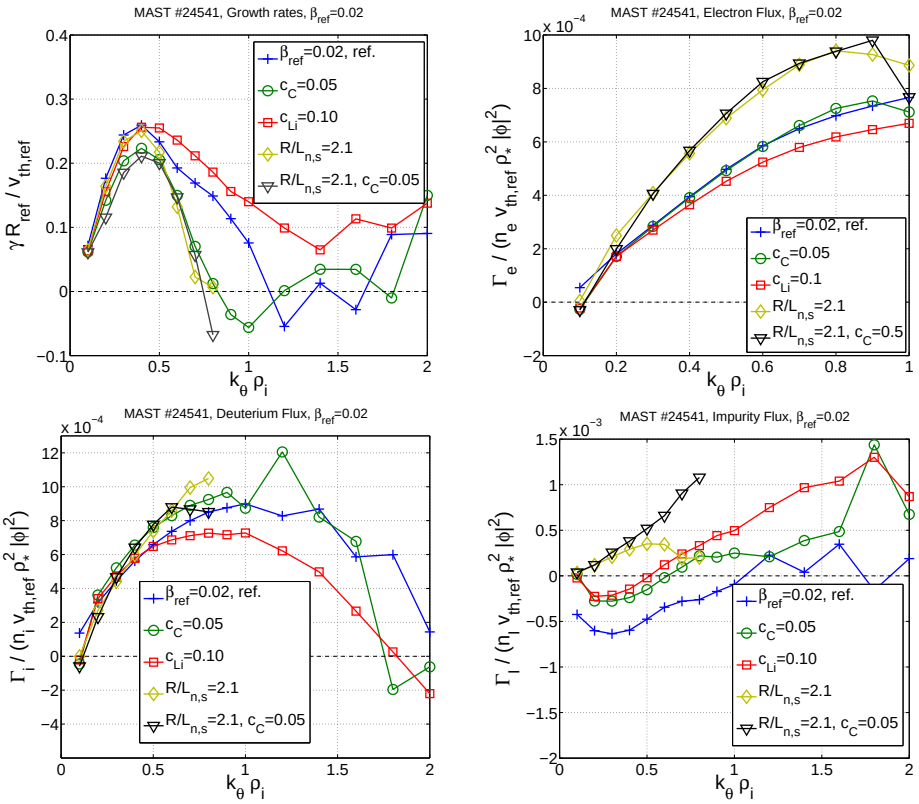

Figure 3.22: Growth rate (top left), quasi-linear ExB driven electron (top right), deuterium (bottom left) and impurity (bottom right) flux as a function of bi-normal wavenumber in an ITG mode dominated spectrum. The reference beta is $\beta_{\rm ref} = 0.02$ (crosses), the reference carbon concentration is $c_{\rm C} = 0.025$.

the species is set uniformly to $R_{\rm ref}/L_{\rm n,s} = 2.1$ (diamonds), that is the density gradient of the deuterium species in the experimental case. This causes the stabilization of the ITG peak above $k_\theta \rho_{\rm i} \approx 0.6$. The deuterium flux is not strongly affected by this change, but the carbon flux reverses its direction from inward to outward. However, this is not followed by an inversion of the deuterium transport, in contrast with the results of the FTU analysis. Even when the carbon concentration is increased to $c_{\rm C} = 0.05$ while keeping the density gradients of the species at $R_{\rm ref}/L_{\rm n,s} = 2.1$ (triangles), although the outward impurity flux is enhanced, there is no significant change in the deuterium flux.

The same analysis described above has been carried out for a KBM dominated spectrum, at $\beta_{\rm ref} = 0.1$. Figure 3.23 indicates that the KBM growth rates and real frequencies are much less sensitive to the changes of the impurity species, impurity concentration or impurity density gradient, they show the same trend in

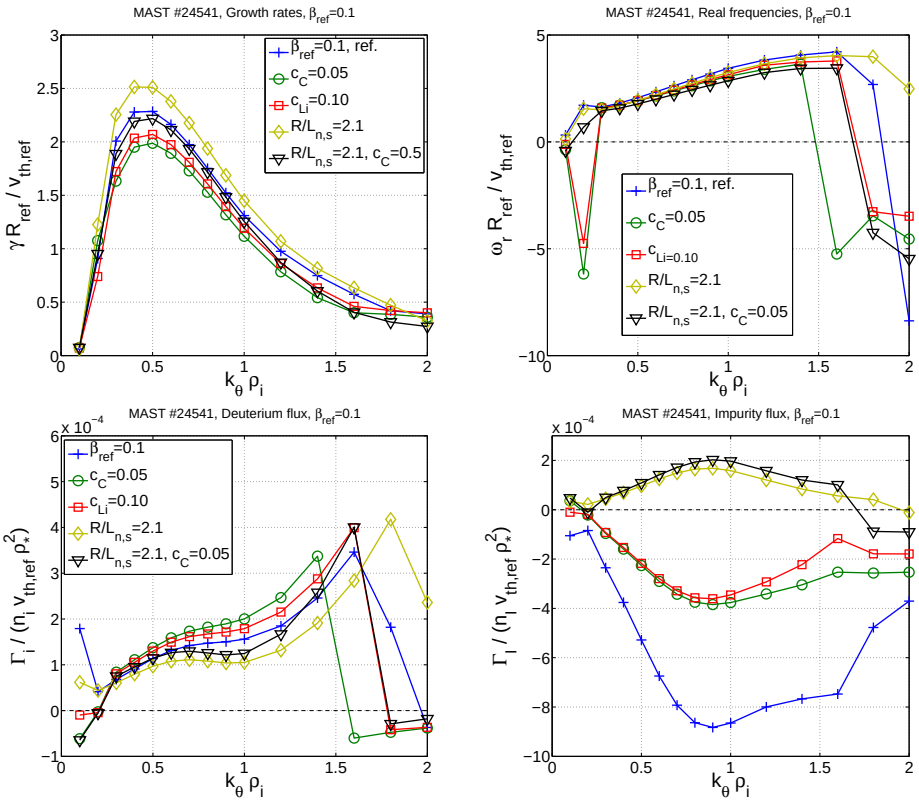

Figure 3.23: Growth rate (top left), real frequency (top right), quasi-linear ExB driven deuterium (bottom left) and impurity (bottom right) flux as a function of bi-normal wavenumber in an KBM dominated spectrum. The reference beta is $\beta_{\rm ref} = 0.1$ (crosses), the reference carbon concentration is $c_{\rm C} = 0.025$.

all five cases. The transition point from KB to TE modes is slightly shifted towards lower $k_\theta \rho_{\rm i}$ values by the increased $Z_{\rm eff}$, and towards higher $k_\theta \rho_{\rm i}$ by the modified impurity and electron density gradients. The KBM driven impurity flux also changes direction in the two cases with positive impurity density gradients. Similarly to the ITG analysis, this is not followed by a reversal of the deuterium transport.

3.3 Summary of the Chapter

In this chapter the gyrokinetic mode stability and particle transport analysis of two discharges have been presented.

The first case is a liquid lithium limiter FTU discharge characterized by increased density peaking and improved particle confinement compared to the typical standard metallic limiter experiments. Local gyrokinetic simulations performed

with GKW at mid radius during the density ramp-up phase show that the presence of a high concentration, centrally peaked lithium profile reverses the deuterium flux from outward to inward. This reversal is not a result of higher collisionality, since the increased Z_{eff} leads to increased effective collision frequencies which are expected to give an outward contribution to the particle transport. At the same time, the lithium is transported radially outward resulting in the decontamination of the plasma. In the reference case the electron flux remains outward even in the presence of large lithium concentration, but it is significantly reduced due to the fact that quasi-neutrality at the ion scales can be satisfied with the two ion species. At the reduced level the turbulent electron flux becomes comparable to the inward neoclassical electron flux dominated by the Ware-pinch term. The core electron source is not expected to be strongly modified by the presence of lithium, therefore the reduced electron transport leads to a more peaked electron density profile. An other consequence of the low electron flux is that its direction becomes sensitive to effects that modify transport. In this particular analysis, neglecting the energy scattering and friction terms in the GKW collision operator was sufficient to drive an inward electron flux. The build-up of the deuterium and electron profiles can, of course, not go on forever. At a later time stage, in the density plateau phase, the discharge is characterized by higher density gradients, low impurity concentration and an outward flux of all three species. However, if the lithium concentration is artificially increased, a reversal of the deuterium transport can be obtained again.

The effect of light impurities on particle transport has also been analysed in the MAST #24541 discharge. MAST is a spherical tokamak characterized by much lower toroidal magnetic field compared to FTU, significantly higher plasma beta and strongly shaped flux surfaces. The main impurity species are carbon, and the impurity density gradient is measured to be negative at the selected flux surface, which is also in contrast with the FTU analysis. Simulations show that at low plasma beta the turbulence is dominated by ITG modes, but the increasing beta gives rise to a Kinetic Ballooning Mode (KBM) dominated regime. In simulations of a non-rotating plasma micro-tearing modes can be observed at intermediate beta values, between the ITG and KBM dominated regime. However, plasma rotation is known to have a significant stabilizing property on ITG modes, while it does not affect the micro-tearing instabilities. This is why in this analysis a micro-tearing mode dominated regime, typically observed in MAST experiments [41], has not been reproduced. Both in the ITG and KBM dominated cases the majority of the flux is driven by the fluctuating ExB velocity, the electro-magnetic terms are at least an order of magnitude smaller. The inward impurity transport can be reduced

by increasing impurity concentration, in the ITG driven case even a reversal can be achieved in the k_θ range where the impurity modes have a strong effect on the modes. The direction of the impurity transport is sensitive to the sign of the density gradient, a reversal from inward to outward in the whole spectrum is achieved with a centrally peaked impurity density profile. However, this is not followed by deuterium flux reversal in this case due the electro-magnetic perturbation driving a strong non-adiabatic electron response. The described effects are similar but more pronounced when carbon is replaced by lithium impurities.

Chapter 4

Derivation of a Fluid Model for Anomalous Particle Transport in Low-Beta Multiple Ion Species Tokamak Plasma

4.1 Introduction

In this section a fluid model is introduced that, although lacks the small scale physics present in a gyrokinetic calculation, captures the main aspects of the ion particle transport and allows us to analyse the effects of impurities in more detail. Since GKW is an initial value code, it only provides information about the fastest growing eigenmode at every k_θ value, while the fluid model describes all eigenmodes present in the system. This is, of course, possible with gyrokinetic eigenvalue solvers, such as QuaLiKiz [63] or GENE [64], we decided to use a fluid approach for its computational effectiveness and intuitive results.

It has been pointed out by a number of authors that the effective particle transport in magnetized fusion plasmas is determined by a delicate balance between several contributing factors [63, 65, 66, 67]. The particle flux can be formally separated into a diffusive part explicitly proportional to the density gradient, a thermodiffusive part proportional to the temperature gradient, and a residual term often called the particle pinch [65]. These contributions have been analysed in detail by both quasi-linear fluid and gyrokinetic methods in terms of their dependences on magnetic shear [51, 52, 53, 68], magnetic curvature [50, 65], collisionality [69, 70], impurity concentration and charge number [28, 50, 52, 53, 71, 72], and whether the

dominant instability driving the small scale turbulence is an ion or electron mode [55, 65, 73, 74]. In rotating plasmas an additional term, the rotodiffusion, is also taken into account [75, 76]. Each of these terms are functions of essentially all the plasma parameters and either of them can provide radially inward or outward contributions to the flux depending on the circumstances. An other advantage of using a fluid model is that, compared to gyrokinetic simulations, it provides a straightforward way of separating the flux into diffusion, thermodiffusion and particle pinch terms and evaluate their roles independently.

In impurity transport studies a commonly applied technique is the so called trace-impurity approximation. Under this assumption one may say that the amount of impurity ions in the system is small enough that they can be omitted from the quasi-neutrality equation. As it will be shown later, this method greatly simplifies the dispersion relation and, moreover, leads to a linear relationship between the impurity transport coefficients and impurity gradients [65]. While in many experimental situations this approximation is indeed applicable, in a typical FTU-LLL discharge the lithium concentration can reach values up to $n_{\mathrm{Li}}/n_{\mathrm{e}} \approx 15\%$. In such scenarios the impurity species have a strong effect on the transport of the other plasma constituents and must be fully taken into account in the quasi-neutrality equation.

A multiple ion-species fluid model with adiabatic electrons for ITG modes in toroidal geometry has been developed by Fröjdh et al. [50]. They have shown that the presence of impurities stabilize the main ITG modes in a wide range of the parameter $L_{\mathrm{n}}/L_{\mathrm{B}}$, the equilibrium density length scale over the magnetic curvature, and that the particle flux driven by these modes is accordingly reduced. The direction of the radial transport of the two ion species is always in the opposite direction due to ambi-polarity, and it is sensitive to the density gradients of both constituents. Determining the direction of the ion transport in FTU-LLL discharges is a key element of this thesis, as well. However, as it has been observed in the gyrokinetic analysis in chapter 3, as the impurity concentration is reduced significant electron transport occurs. The ambi-polarity condition is relaxed and the two ion species can move in the same direction. In order to include this effect into a fluid model a non-adiabatic electron response is required.

In toroidal geometry the electron species are separated into trapped and passing electron fractions depending on their particle orbits. Passing electrons are commonly assumed adiabatic and the density response of the trapped electrons is used to obtain finite electron transport. In a slab-like configuration, where there is no trapping condition, a non-adiabatic electron response is achieved by either

keeping finite electron inertia, including electron collisions or electro-magnetic perturbations [62]. In order to keep the dispersion relation relatively simple three non-adiabatic species, main and impurity ions and trapped electrons, and adiabatic passing electrons will be included for modelling the FTU-LLL discharges.

Fluctuations in FTU plasmas are dominantly electro-static and therefore magnetic perturbations will be neglected. This means that the model is not applicable for analysis of high-β experiments, such as those in MAST. A fluid model for two plasma constituents including electro-magnetic fluctuations have been developed by Hein et al. [77]. Adding magnetic perturbations to the present model is subject of future work.

As it was mentioned in chapter 3, one particular feature of FTU plasmas is high collisionality due to their relatively low temperature and high density values. Although our model is based on the collisionless Braginskii equations [13], collisions are introduced for the trapped electrons according to Nilsson and Weiland [78].

The fluid closure applied is that of the Weiland model [15]: the energy balance equation is closed by assuming diamagnetic heat flux. The final system is similar to the one used by Moradi et al. [52] for impurity transport studies. The main difference is the treatment of the Finite Larmor Radius (FLR) terms: as detailed by Tardini in his doctoral thesis [79], they introduce a flute-mode equation between potential and pressure fluctuations and thus confine the FLR terms to appear only as corrections to the potential in the continuity equation. We do not introduce such a simplification and, as it will be seen in the following sections, the FLR corrections present themselves symmetrically in the potential, density, temperature and velocity fluctuation terms. This has purely a formal importance, the effect of this separation on the numerical results is negligible.

4.2 The Fluid Model

4.2.1 Derivation of the Model Equations

Our starting equations for the ions are the collisionless Braginskii equations. The two ion species are described by the same set of equations and they will be denoted by subscript s. The density fluctuation is obtained by solving the set of their continuity (4.1), momentum balance (4.2) and energy balance equations (4.3):

$$\frac{\partial n_\mathrm{s}}{\partial t} + \nabla \cdot (n_\mathrm{s} \mathbf{v}_\mathrm{s}) = 0 \tag{4.1}$$

$$m_{\mathrm{s}} n_{\mathrm{s}} \frac{\mathrm{d}\mathbf{v}_{\mathrm{s}}}{\mathrm{d}t} + \nabla p_{\mathrm{s}} + \nabla \cdot \pi_{\mathrm{s}}^{\mathrm{gv}} - Z_{\mathrm{s}} e n_{\mathrm{s}} (\mathbf{E} + \mathbf{v}_{\mathrm{s}} \times \mathbf{B}) = 0 \tag{4.2}$$

$$\frac{3}{2} \frac{\mathrm{d}p_{\mathrm{s}}}{\mathrm{d}t} + \frac{5}{2} p_{\mathrm{s}} \nabla \cdot \mathbf{v}_{\mathrm{s}} + \nabla \cdot \mathbf{q}_{*\mathrm{s}} = 0 \tag{4.3}$$

where $\frac{\mathrm{d}}{\mathrm{d}t} = (\frac{\partial}{\partial t} + \mathbf{v}_{\mathrm{s}} \cdot \nabla)$ is the total time derivative, $\mathbf{v}_{\mathrm{s}}$ is the fluid velocity of the species, p_{s} is the scalar pressure, π_s^{gv} is the gyro-viscous part of the pressure tensor (the other parts are collisional), and the heat flux in the energy balance equations has been approximated by the diamagnetic heat flux $\mathbf{q}_{*\mathrm{s}}$ (diamagnetic closure [15])

$$\mathbf{q}_{*\mathrm{s}} = \frac{5}{2} \frac{p_{\mathrm{s}}}{m_{\mathrm{s}} \omega_{\mathrm{c,s}}} \mathbf{b} \times \nabla T_{\mathrm{s}} \tag{4.4}$$

where $\omega_{\mathrm{c,s}} = Z_{\mathrm{s}} e B / m_{\mathrm{s}}$ is the cyclotron frequency of the species. Magnetic perturbations are neglected and we write $\mathbf{E} = -\nabla \phi$.

A right-handed coordinate system of parallel ($\mathbf{b}$), radial ($\mathbf{r}$) and bi-normal ($\mathbf{y}$) vectors is used: $\mathbf{b} \times \mathbf{r} = \mathbf{y}$. The radial basis vector points from the central column of the tokamak towards the low-field-side and the bi-normal base vector on the low-field-side points downwards. The model is radially local, i.e. it is only applicable in a narrow radial region in which the profiles and gradients can be considered constant (similar to the flux tube nature of GKW).

The quantities are separated into equilibrium and fluctuating parts $n_{\mathrm{s}} = n_{\mathrm{s0}} + n_{\mathrm{s1}}$, and the equations are linearized for the fluctuations. Only parallel and bi-normal fluctuations are considered. For simplicity, fluctuations in the radial direction are neglected. This can be motivated by noting that radial potential fluctuations would give rise to a bi-normal ExB velocity which would not contribute to the radial transport. The solution of the equations is assumed to be of the Fourier-form:

$$n_{\mathrm{s1}} = \hat{n}_{\mathrm{s1}} \mathrm{e}^{-i\omega t + i k_{\mathrm{y}} \mathrm{y} + i k_{\parallel} \mathrm{z}}. \tag{4.5}$$

The perpendicular derivative of the fluctuations is ordered as $k_{\mathrm{y}} \sim 1/\rho_{\mathrm{ref}}$ while that of the equilibrium is as $\nabla_{\perp} \sim 1/R_{\mathrm{ref}}$, where $\rho_{\mathrm{ref}} = m_{\mathrm{ref}} v_{\mathrm{th,ref}} / (e B_{\mathrm{ref}})$ is the reference Larmor radius (typically the main ion Larmor radius) and R_{ref} is the reference macroscopic length scale, often chosen as the minor or major radius of the tokamak. In order for the fluid treatment to be adequate $k_{\mathrm{y}} \rho_{\mathrm{ref}} < 1$ is required. The parallel gradient of the fluctuations are taken to be $k_{\parallel} \sim 1/R_{\mathrm{ref}}$ and the parallel variation of the equilibrium is neglected. The time scale of the fluctuations are considered slow compared to the ion cyclotron frequency: $\omega \sim \rho_* \omega_{\mathrm{c,i}}$, with $\rho_* = \rho_{\mathrm{ref}} / R_{\mathrm{ref}} \ll 1$ being the ratio of the reference Larmor radius and the reference length scale and used as our ordering parameter. We also assume zero electric field and parallel flow

in equilibrium.

An iterative solution of the perpendicular component of momentum equation (4.2) yields

$$\mathbf{v}_\mathrm{s} = \frac{\mathbf{b}\times\nabla\phi}{B} + \frac{\mathbf{b}\times\nabla p_\mathrm{s}}{Z_\mathrm{s} e n_\mathrm{s} B} + \frac{\mathbf{b}\times\nabla\cdot\pi_\mathrm{s}^\mathrm{gv}}{Z_\mathrm{s} e n_\mathrm{s} B} + \frac{1}{\omega_\mathrm{c,s}}\mathbf{b}\times\frac{\mathrm{d}\mathbf{v}_\mathrm{s}}{\mathrm{d}t} \tag{4.6}$$

where the terms are the well known ExB velocity, diamagnetic drift, drift due to the gyro-viscous force and the polarization drift, respectively.

Under the drift ordering assumption [11], the first two velocities are of order $\mathcal{O}(\rho_* v_\mathrm{th,ref})$ and the latter two are both $\mathcal{O}(\rho_*^2 v_\mathrm{th,ref})$, where $v_\mathrm{th,ref}$ is the reference thermal velocity (typically the main ion thermal velocity). Note, however, that both the continuity and energy balance equations contain the divergence of the fluid velocity. In these terms the divergence of the polarization term will be the same order as that of the ExB and diamagnetic contributions.

In the momentum equation the gyro-viscous cancellation is applied. The conventional derivation shown in [80] is applicable in slab magnetic geometry and at constant temperature, and expresses that the total diamagnetic contribution in the polarization velocity is partially cancelled with the gyro-viscous force. In the present study a different version of the cancellation suggested by Chang and Callen [81] is applied. It does not require uniform temperature profile and therefore it is more relevant for ITG modelling. The main difference between the two cases is that in the latter result only the convective diamagnetic part of the polarization term takes part in the cancellation:

$$n_\mathrm{s} m_\mathrm{s} \mathbf{v}_{*\mathrm{s}}\cdot\nabla_\perp\mathbf{v}_\mathrm{s} + \nabla\cdot\pi_\mathrm{s}^\mathrm{gv} = (\nabla + 2\mathbf{b}\nabla_\parallel)\chi_\mathrm{s} + \frac{p_\mathrm{s}}{\omega_\mathrm{c,s}}(\mathbf{b}\times\nabla)\nabla_\parallel v_{\parallel\mathrm{s}} \tag{4.7}$$

where χ_s is a higher order pressure correction and will be neglected in the remaining of the derivation. The divergence of the polarization term after the cancellation is

$$\nabla\cdot\mathbf{v}_\mathrm{p,s} = \nabla_\perp\cdot\frac{\mathbf{b}}{\omega_\mathrm{c,s}}\times\left(\frac{\partial}{\partial t} + \mathbf{v}_\mathrm{ExB}\cdot\nabla_\perp\right)\mathbf{v}_\mathrm{s} - \frac{p_\mathrm{s}}{n_\mathrm{s} m_\mathrm{s}\omega_\mathrm{c,s}^2}\nabla_\perp^2\nabla_\parallel v_{\parallel\mathrm{s}}. \tag{4.8}$$

Note, that although this result also requires slab magnetic geometry, the variation of the polarization velocity due to magnetic curvature is a higher order correction and can be omitted. The divergence of the polarization velocity after linearizing and Fourier transforming becomes

$$\nabla\cdot\mathbf{v}_\mathrm{p,s}^1 = -i\omega\frac{1}{2}k_\mathrm{y}^2\rho_\mathrm{th,s}^2\left(\frac{Z_\mathrm{s} e}{T_\mathrm{s}}\hat{\phi}_1 + \frac{\hat{p}_{\mathrm{s}1}}{p_{\mathrm{s}0}}\right) + ik_\parallel\frac{1}{2}k_\mathrm{y}^2\rho_\mathrm{th,s}^2\hat{v}_{\parallel\mathrm{s}}^1 \tag{4.9}$$

where $\rho_{\mathrm{th,s}}$ is the thermal Larmor radius of the species.

The divergence term appearing in the continuity equation (4.1) can be reformulated with the vector calculus identity $\nabla \cdot (\mathbf{A} \times \mathbf{B}) = \mathbf{B} \cdot \nabla \times \mathbf{A} - \mathbf{A} \cdot \nabla \times \mathbf{B}$. With this we can write

$$\begin{aligned} \nabla \cdot (n_{\mathrm{s}} \mathbf{v}_{\mathrm{ExB}}) &= \nabla n_{\mathrm{s}} \cdot \frac{\mathbf{b} \times \nabla \phi}{B} - n_{\mathrm{s}} \frac{\nabla B}{B} \cdot \frac{\mathbf{b} \times \nabla \phi}{B} + n_{\mathrm{s}} \frac{\nabla \phi \cdot \nabla \times \mathbf{b}}{B} \\ &= \mathbf{v}_{\mathrm{ExB}} \cdot \nabla n_{\mathrm{s}} + \frac{Z_{\mathrm{s}} e}{T_{\mathrm{s}}} \nabla \phi \cdot \frac{T_{\mathrm{s}}}{Z_{\mathrm{s}} e B} \left(\mathbf{b} \times \frac{\nabla B}{B} + \nabla \times \mathbf{b} \right) \\ &= \mathbf{v}_{\mathrm{ExB}} \cdot \nabla n_{\mathrm{s}} + \frac{Z_{\mathrm{s}} e}{T_{\mathrm{s}}} \mathbf{v}_{\mathrm{D,s}} \cdot \nabla \phi \end{aligned} \tag{4.10}$$

where the notation $\mathbf{v}_{\mathrm{D,s}}$ has been introduced for the magnetic drift velocity of the species accounting for the grad-B and curvature drifts. Similarly for the diamagnetic term of the divergence one obtains

$$\nabla \cdot (n_{\mathrm{s}} \mathbf{v}_{*\mathrm{s}}) = \frac{1}{T_{\mathrm{s}}} \mathbf{v}_{\mathrm{D,s}} \cdot \nabla p_{\mathrm{s}}. \tag{4.11}$$

After linearizing and substituting Fourier-mode solution for the fluctuations, the continuity equation can be written as

$$\begin{aligned} &\frac{\hat{n}_{\mathrm{s,1}}}{n_{\mathrm{s0}}} \left(2\omega_{\mathrm{D,s}} - \omega - \omega \frac{1}{2} k_{\mathrm{y}}^2 \rho_{\mathrm{th,s}}^2 \right) + \frac{\hat{T}_{\mathrm{s,1}}}{T_{\mathrm{s0}}} \left(2\omega_{\mathrm{D,s}} - \omega \frac{1}{2} k_{\mathrm{y}}^2 \rho_{\mathrm{th,s}}^2 \right) + \\ &\frac{Z_{\mathrm{s}} e}{T_{\mathrm{s0}}} \hat{\phi}_1 \left(2\omega_{\mathrm{D,s}} - \omega_{*\mathrm{s}}^{\mathrm{n}} - \omega \frac{1}{2} k_{\mathrm{y}}^2 \rho_{\mathrm{th,s}}^2 \right) + k_{\parallel} \hat{v}_{\parallel \mathrm{s}}^1 \left(1 + \frac{1}{2} k_{\mathrm{s}}^2 \rho_{\mathrm{th,s}}^2 \right) = 0 \end{aligned} \tag{4.12}$$

where $p_{\mathrm{s}} = n_{\mathrm{s}} T_{\mathrm{s}}$ has been used and the drift and diamagnetic frequencies have been introduced:

$$2\omega_{\mathrm{D,s}} = k_{\mathrm{y}} \mathbf{y} \cdot \mathbf{v}_{\mathrm{D,s}} \qquad \omega_{*\mathrm{s}}^{\mathrm{n}} = -\frac{k_{\mathrm{y}} T_{\mathrm{s}}}{Z_{\mathrm{s}} e B L_{\mathrm{n,s}}}. \tag{4.13}$$

Here, $L_{\mathrm{n,s}} = -\frac{n_{\mathrm{s}}}{\nabla n_{\mathrm{s}}}$ is the density gradient length scale and the minus sign in 4.13 indicates that the ion diamagnetic velocity points in the negative bi-normal direction. Also note that only the $n_{\mathrm{s0}} \nabla \cdot \mathbf{v}_{\mathrm{p,s}}^1$ term is kept as $\nabla n_{\mathrm{s0}} \cdot \mathbf{v}_{\mathrm{p,s}}^1$ is higher order in ρ_*.

The linear Fourier-transformed equation for the parallel velocity fluctuation is

$$-\frac{m_{\mathrm{s}}}{T_{\mathrm{s}}} \omega \hat{v}_{\parallel \mathrm{s}}^1 + k_{\parallel} \left(\frac{\hat{n}_{\mathrm{s1}}}{n_{\mathrm{s0}}} + \frac{\hat{T}_{\mathrm{s1}}}{T_{\mathrm{s0}}} + \frac{Z_{\mathrm{s}} e}{T_{\mathrm{s0}}} \hat{\phi}_1 \right) = 0. \tag{4.14}$$

Similarly to the perpendicular wavenumber, the condition $k_{\parallel} \rho_{\mathrm{ref}} < 1$ is required in order for the fluid treatment to be adequate. In tokamaks the modes exhibit an elongated structure along the magnetic field lines, and this condition is typically

satisfied.

In the energy equation (4.3) we substitute $\nabla\cdot\mathbf{v}_\mathrm{s} = -\frac{1}{n_\mathrm{s}}\left(\frac{\mathrm{d}n_\mathrm{s}}{\mathrm{d}t} + \nabla n_\mathrm{s}\cdot\mathbf{v}_\mathrm{s}\right)$ from the continuity equation 4.1 and keep only the leading order $\mathbf{v}_\mathrm{ExB}$ and $\mathbf{v}_{*\mathrm{s}}$ velocities in the expression. The divergence of the diamagnetic heat flux can be written as

$$\nabla\cdot\mathbf{q}_{*\mathrm{s}} = \frac{5}{2}n_\mathrm{s}\nabla T_\mathrm{s}\cdot\left(\mathbf{v}_\mathrm{D,s} - \mathbf{v}_{*\mathrm{s}}\right). \tag{4.15}$$

Note, that $\mathbf{v}_{*\mathrm{s}}\cdot\nabla p_\mathrm{s} = 0$ which removes the diamagnetic convective term and also causes a cancellation between the diamagnetic term of the divergence of the heat flux and the term containing $\nabla n_\mathrm{s}\cdot\mathbf{v}_{*\mathrm{s}}$. Linearization removes the parallel convective term as there are no parallel equilibrium gradients. The linearized Fourier-transformed energy equation takes the form

$$\left(\frac{10}{3}\omega_\mathrm{D,s} - \omega\right)\frac{\hat{T}_\mathrm{s1}}{T_\mathrm{s0}} + \frac{2}{3}\omega\frac{\hat{n}_\mathrm{s1}}{n_\mathrm{s0}} - \frac{Z_\mathrm{s}e}{T_\mathrm{s}}\hat{\phi}_1\omega^\mathrm{n}_{*\mathrm{s}}\left(\eta_\mathrm{s} - \frac{2}{3}\right) = 0 \tag{4.16}$$

where $\eta_\mathrm{s} = L_\mathrm{n,s}/L_\mathrm{T,s}$ is the ratio of the density and temperature gradient length scales.

These equations are the same as found in the thesis by Tardini [79] with the difference that, while he introduces a flute mode equation between the potential and pressure FLR terms, we keep them separated so they appear as a correction for every fluctuating quantities.

The above equations can also be used to describe non-adiabatic passing electron response due to finite electron inertia [62] which allows the simulation of ETG modes. However, the system is prone to numerical instabilities when solved for the typical ITG driven long wavelength modes. This problem can be overcome by assuming adiabatic passing electron response and including trapped electrons with negligible bounce-averaged parallel motion.

Following the simplified model suggested by Nielsson and Weiland [78] collisions of the trapped electron fraction is included in order to recover the dissipative Trapped Electron Modes (TEM). The continuity and energy balance equations for the trapped electrons neglecting electron FLR corrections can be expressed as

$$\frac{\hat{n}_\mathrm{s,1}}{n_\mathrm{s0}}\left(2\omega_\mathrm{D,s} - \omega - \mathrm{i}\nu_\mathrm{th}\right) + \frac{\hat{T}_\mathrm{s,1}}{T_\mathrm{s0}}2\omega_\mathrm{D,s} + \frac{Z_\mathrm{s}e}{T_\mathrm{s0}}\hat{\phi}_1\left(2\omega_\mathrm{D,s} - \omega^\mathrm{n}_{*\mathrm{s}} - \mathrm{i}\nu_\mathrm{th}\Gamma\right) = 0 \tag{4.17}$$

and

$$\left(\frac{10}{3}\omega_\mathrm{D,s} - \omega\right)\frac{\hat{T}_\mathrm{s1}}{T_\mathrm{s0}} + \frac{\hat{n}_\mathrm{s1}}{n_\mathrm{s0}}\left(\frac{2}{3}\omega - \beta\mathrm{i}\nu_\mathrm{th}\right) - \frac{Z_\mathrm{s}e}{T_\mathrm{s}}\hat{\phi}_1\left[\omega^\mathrm{n}_{*\mathrm{s}}\left(\eta_\mathrm{s} - \frac{2}{3}\right) + \beta\mathrm{i}\nu_\mathrm{th}\right] = 0 \tag{4.18}$$

where $\nu_{th} = \nu_{\rm ei}/\epsilon$, $\epsilon = r/R$ the inverse aspect ratio, $\Gamma = 1 + \frac{\alpha\eta_{\rm e}\omega^{\rm n}_{*\rm e}}{\omega - \omega_{\rm D,e} + {\rm i}\nu_{\rm th}}$. $\alpha \approx 1$ and $\beta \approx 1.5$ are factors determined in [78] in order to recover the strongly collisional TEM dynamics using the simplified collision operator.

4.2.2 Derivation of the Dispersion Relation

The system of equations 4.12, 4.14 and 4.16 yields the density response of the species as

$$\begin{aligned}\frac{\hat{n}_{\rm s1}}{n_{\rm s0}} &= -\frac{Z_{\rm s}e}{T_{\rm s0}}\hat{\phi}_1 \left\{ \left[2\omega_{\rm D,s} - C^{\rm s}_{\rm FLR}\omega + \frac{T_{\rm s}}{m_{\rm s}}\frac{k_\parallel^2}{\omega}(1 + C^{\rm s}_{\rm FLR}) \right] \times \right. \\ &\left[\frac{10}{3}\omega_{\rm D,s} - \omega + \omega^{\rm n}_{*\rm s}\left(\eta_{\rm s} - \frac{2}{3}\right) \right] - \frac{10}{3}\omega_{\rm D,s}\omega^{\rm n}_{*\rm s} + \omega^{\rm n}_{*\rm s}\omega \Big\} / \\ &\left\{ \left[2\omega_{\rm D,s} - C^{\rm s}_{\rm FLR}\omega + \frac{T_{\rm s}}{m_{\rm s}}\frac{k_\parallel^2}{\omega}(1 + C^{\rm s}_{\rm FLR}) \right] \left(\frac{10}{3}\omega_{\rm D,s} - \frac{5}{3}\omega \right) - \right. \\ &\left. \frac{10}{3}\omega_{\rm D,s}\omega + \omega^2 \right\} \end{aligned} \tag{4.19}$$

where $\frac{1}{2}k_{\rm y}^2\rho^2_{\rm th,s}$ has been replaced with $C^{\rm s}_{\rm FLR}$. The expression can be split into adiabatic and non-adiabatic parts to give

$$\begin{aligned}\frac{\hat{n}_{\rm s1}}{n_{\rm s0}} &= -\frac{Z_{\rm s}e}{T_{\rm s0}}\hat{\phi}_1 \left\{ 1 + \left\{ \left[2\omega_{\rm D,s} - C^{\rm s}_{\rm FLR}\omega + \frac{T_{\rm s}}{m_{\rm s}}\frac{k_\parallel^2}{\omega}(1 + C^{\rm s}_{\rm FLR}) \right] \times \right. \right. \\ &\left[\frac{2}{3}\omega + \omega^{\rm n}_{*\rm s}\left(\eta_{\rm s} - \frac{2}{3}\right) \right] + (\omega - \omega^{\rm n}_{*\rm s}) \left(\frac{10}{3}\omega_{\rm D,s} - \omega \right) \Big\} / \\ &\left\{ \left[2\omega_{\rm D,s} - C^{\rm s}_{\rm FLR}\omega + \frac{T_{\rm s}}{m_{\rm s}}\frac{k_\parallel^2}{\omega}(1 + C^{\rm s}_{\rm FLR}) \right] \left(\frac{10}{3}\omega_{\rm D,s} - \frac{5}{3}\omega \right) - \right. \\ &\left. \left. \omega\left(\frac{10}{3}\omega_{\rm D,s} - \omega \right) \right\} \right\} \end{aligned} \tag{4.20}$$

showing that the main sources of non-adiabaticity is $\eta_{\rm s}$ and the difference between the mode frequency and the diamagnetic frequency.

The effect of magnetic geometry is contained in the magnetic drift frequency $\omega_{\rm D}$. It is taken into account in a simplified way according to Hirose [82]: the norms of the parallel and perpendicular differential operators are estimated by taking the average of an ad-hoc strongly ballooning eigenfunction in the ballooning space, resulting $k_\parallel = 1/\sqrt{3(qR)^2}$, $k_\perp = k_{\rm y}\sqrt{1 + (\pi^2/3 - 5/2)\hat{s}^2}$ replacing $k_{\rm y}$ in the FLR terms, $\omega_{\rm D,s} = -k_{\rm y}T_{\rm s0}(2/3 + 5/9\hat{s})/(Z_{\rm s}eR) = -k_{\rm y}T_{\rm s0}\lambda_{\rm s}/(Z_{\rm s}eR)$ and $\omega_{\rm D,e} = -k_{\rm y}T_{\rm e0}(1/4 + 2/3\hat{s})/(Z_{\rm e}eR) = -k_{\rm y}T_{\rm e0}\lambda_{\rm e}/(Z_{\rm e}eR)$ in the ion and trapped

electron magnetic drift frequencies, respectively [68]. R is the tokamak major radius, q is the safety factor, $\hat{s} = r/q\ \mathrm{d}q/\mathrm{d}r$ is the magnetic shear.

The frequencies are normalized with the ion drift frequency taken at the reference length scale R_{ref} and at $\lambda_{\mathrm{i}} = 1$: $\omega_{\mathrm{D,i}}^{\mathrm{ref}} = -k_{\mathrm{y}} T_{\mathrm{i0}}/(Z_{\mathrm{i}} e R_{\mathrm{ref}})$. The factors $F_{\mathrm{s}} = \frac{T_{\mathrm{s0}}}{T_{\mathrm{i0}}} \frac{Z_{\mathrm{i}}}{Z_{\mathrm{s}}}$ are introduced appearing in the $\frac{\omega_{\mathrm{D,s}}}{\omega_{\mathrm{D,i}}}$ and $\frac{\omega_{*\mathrm{s}}}{\omega_{\mathrm{D,i}}}$ terms. The normalization rules as outlined in section 2.3.6 are followed: $n_{\mathrm{s0}} = n_{\mathrm{ref}} n_{\mathrm{N,s}}$, $T_{\mathrm{s0}} = T_{\mathrm{ref}} T_{\mathrm{N,s}}$, $B = B_{\mathrm{ref}} B_{\mathrm{N}}$, $k_{\mathrm{y}} = k_{\mathrm{y,N}}/\rho_*$, and $k_{\parallel} = k_{\parallel \mathrm{N}}/R_{\mathrm{ref}}$ is chosen. The notations $J_{\mathrm{s}} = \frac{2 Z_{\mathrm{i}}^2 T_{\mathrm{s,N}} B_{\mathrm{N}} k_{\parallel \mathrm{N}}^2}{T_{\mathrm{i,N}}^2 m_{\mathrm{s,N}} k_{\mathrm{y,N}}^2}$ appearing during the normalization of the parallel terms, and $\omega_{\mathrm{N}} = \omega/\omega_{\mathrm{D,i}}^{\mathrm{ref}}$ are also introduced. The density response (equation 4.19) with these modifications becomes

$$\begin{aligned}
\frac{\hat{n}_{\mathrm{s1}}}{n_{\mathrm{s0}}} \quad = \quad & -\frac{Z_{\mathrm{s}} e}{T_{\mathrm{s0}}} \hat{\phi}_1 \left\{ \left[2F_{\mathrm{s}} \lambda_{\mathrm{s}} \frac{R_{\mathrm{ref}}}{R} \omega_{\mathrm{N}} - C_{\mathrm{FLR}}^{\mathrm{s}} \omega_{\mathrm{N}}^2 + J_{\mathrm{s}} (1 + C_{\mathrm{FLR}}^{\mathrm{s}}) \right] \times \right. \\
& \left[\frac{10}{3} F_{\mathrm{s}} \lambda_{\mathrm{s}} \frac{R_{\mathrm{ref}}}{R} - \omega_{\mathrm{N}} + F_{\mathrm{s}} \frac{R_{\mathrm{ref}}}{L_{\mathrm{n,s}}} \left(\eta_{\mathrm{s}} - \frac{2}{3} \right) \right] - \omega_{\mathrm{N}} F_{\mathrm{s}} \frac{R_{\mathrm{ref}}}{L_{\mathrm{n,s}}} \left(\frac{10}{3} F_{\mathrm{s}} \lambda_{\mathrm{s}} \frac{R_{\mathrm{ref}}}{R} - \omega_{\mathrm{N}} \right) \Bigg\} / \\
& \left\{ \left[2F_{\mathrm{s}} \lambda_{\mathrm{s}} \frac{R_{\mathrm{ref}}}{R} \omega_{\mathrm{N}} - C_{\mathrm{FLR}}^{\mathrm{s}} \omega_{\mathrm{N}}^2 + J_{\mathrm{s}} (1 + C_{\mathrm{FLR}}^{\mathrm{s}}) \right] \frac{5}{3} \left(2F_{\mathrm{s}} \lambda_{\mathrm{s}} \frac{R_{\mathrm{ref}}}{R} - \omega_{\mathrm{N}} \right) - \right. \\
& \left. \left. \omega_{\mathrm{N}}^2 \left(\frac{10}{3} F_{\mathrm{s}} \lambda_{\mathrm{s}} \frac{R_{\mathrm{ref}}}{R} - \omega_{\mathrm{N}} \right) \right\} . \right. \qquad (4.21)
\end{aligned}$$

Evaluating the brackets gives a third degree polynomial in ω_{N} in both the numerator and the denominator and the density response can be written in a compact form as

$$\frac{\hat{n}_{\mathrm{s1}}}{n_{\mathrm{s0}}} = -\frac{Z_{\mathrm{s}} e}{T_{\mathrm{s0}}} \hat{\phi}_1 \frac{A_{3\mathrm{s}} \omega_{\mathrm{N}}^3 + A_{2\mathrm{s}} \omega_{\mathrm{N}}^2 + A_{1\mathrm{s}} \omega_{\mathrm{N}} + A_{0\mathrm{s}}}{B_{3\mathrm{s}} \omega_{\mathrm{N}}^3 + B_{2\mathrm{s}} \omega_{\mathrm{N}}^2 + B_{1\mathrm{s}} \omega_{\mathrm{N}} + B_{0\mathrm{s}}} = -\frac{Z_{\mathrm{s}} e}{T_{\mathrm{s0}}} \hat{\phi}_1 \frac{P_{\mathrm{A,s}}}{P_{\mathrm{B,s}}} \qquad (4.22)$$

with the coefficients

$$\begin{aligned}
A_{3\mathrm{s}} \quad &= \quad C_{\mathrm{FLR}}^{\mathrm{s}} \\
A_{2\mathrm{s}} \quad &= \quad -F_{\mathrm{s}} \left[\left(\frac{10}{3} C_{\mathrm{FLR}}^{\mathrm{s}} + 2 \right) \lambda_{\mathrm{s}} \frac{R_{\mathrm{ref}}}{R} + \frac{R_{\mathrm{ref}}}{L_{\mathrm{n,s}}} \left(\eta_{\mathrm{s}} - \frac{2}{3} \right) C_{\mathrm{FLR}}^{\mathrm{s}} - \frac{R_{\mathrm{ref}}}{L_{\mathrm{n,s}}} \right] \\
A_{1\mathrm{s}} \quad &= \quad 2F_{\mathrm{s}}^2 \left[\frac{10}{3} \frac{R_{\mathrm{ref}}}{R} \lambda_{\mathrm{s}} + \frac{R_{\mathrm{ref}}}{L_{\mathrm{n,s}}} \left(\eta_{\mathrm{s}} - \frac{7}{3} \right) \right] \frac{R_{\mathrm{ref}}}{R} \lambda_{\mathrm{s}} - J_{\mathrm{s}} (1 + C_{\mathrm{FLR}}^{\mathrm{s}}) \\
A_{0\mathrm{s}} \quad &= \quad F_{\mathrm{s}} J_{\mathrm{s}} (1 + C_{\mathrm{FLR}}^{\mathrm{s}}) \left[\frac{10}{3} \frac{R_{\mathrm{ref}}}{R} \lambda_{\mathrm{s}} + \frac{R_{\mathrm{ref}}}{L_{\mathrm{n,s}}} \left(\eta_{\mathrm{s}} - \frac{2}{3} \right) \right]
\end{aligned}$$

$$
\begin{aligned}
B_{3\mathrm{s}} &= \frac{5}{3}C^{\mathrm{s}}_{\mathrm{FLR}} + 1 \\
B_{2\mathrm{s}} &= -\frac{10}{3}\frac{R_{\mathrm{ref}}}{R}\lambda_{\mathrm{s}}F_{\mathrm{s}}\left(2 + C^{\mathrm{s}}_{\mathrm{FLR}}\right) \\
B_{1\mathrm{s}} &= \frac{5}{3}\left[\left(\frac{R_{\mathrm{ref}}}{R}\lambda_{\mathrm{s}}\right)^2 4F_{\mathrm{s}}^2 - J_{\mathrm{s}}(1 + C^{\mathrm{s}}_{\mathrm{FLR}})\right] \\
B_{0\mathrm{s}} &= \frac{10}{3}\frac{R_{\mathrm{ref}}}{R}F_{\mathrm{s}}\lambda_{\mathrm{s}}J_{\mathrm{s}}(1 + C^{\mathrm{s}}_{\mathrm{FLR}}).
\end{aligned} \tag{4.23}
$$

Collisionless trapped electron response can be recovered by assuming $J_{\mathrm{e}} = 0$ and multiplying n_{e} with the trapped electron fraction f_{t}. The density response of the collisional trapped electrons are derived in a straightforward way using equations 4.17 and 4.18. The resulting coefficients are

$$
\begin{aligned}
A_{3\mathrm{e}} &= 0 \\
A_{2\mathrm{e}} &= F_{\mathrm{e}}\frac{R_{\mathrm{ref}}}{L_{\mathrm{n,e}}} - 2F_{\mathrm{e}}\lambda_{\mathrm{e}}\frac{R_{\mathrm{ref}}}{R} + 2N_{\mathrm{e}} \\
A_{1\mathrm{e}} &= \frac{26}{3}F_{\mathrm{e}}^2\left(\frac{R_{\mathrm{ref}}}{R}\lambda_{\mathrm{e}}\right)^2 + F_{\mathrm{e}}^2\lambda_{\mathrm{e}}\frac{R_{\mathrm{ref}}}{R}\frac{R_{\mathrm{ref}}}{L_{\mathrm{n,e}}}\left(2\eta_{\mathrm{e}} - \frac{17}{3}\right) + N_{\mathrm{e}}^2 - \\
&\quad F_{\mathrm{e}}\lambda_{\mathrm{e}}\frac{R_{\mathrm{ref}}}{R}N_{\mathrm{e}}\left(\frac{19}{3} + 2\beta\right) + F_{\mathrm{e}}\frac{R_{\mathrm{ref}}}{L_{\mathrm{n,e}}}N_{\mathrm{e}}(1 + \alpha\eta_{\mathrm{e}}) \\
A_{0\mathrm{e}} &= 2F_{\mathrm{e}}\lambda_{\mathrm{e}}\frac{R_{\mathrm{ref}}}{R}\left\{-\frac{10}{3}\left(\frac{R_{\mathrm{ref}}}{R}\lambda_{\mathrm{e}}\right)^2 F_{\mathrm{e}}^2 - F_{\mathrm{e}}^2\lambda_{\mathrm{e}}\frac{R_{\mathrm{ref}}}{R}\frac{R_{\mathrm{ref}}}{L_{\mathrm{n,e}}}\left(\eta_{\mathrm{e}} - \frac{7}{3}\right) + F_{\mathrm{e}}\lambda_{\mathrm{e}}\frac{R_{\mathrm{ref}}}{R}N_{\mathrm{e}}(5 + \beta) + \right. \\
&\quad \left. F_{\mathrm{e}}\frac{R_{\mathrm{ref}}}{L_{\mathrm{n,e}}}N_{\mathrm{e}}\left[\left(1 - \frac{5}{3}\alpha\right)\eta_{\mathrm{e}} - \frac{7}{3}\right] - N_{\mathrm{e}}^2\left(\frac{5}{3} + \beta\right)\right\} \\
B_{3\mathrm{e}} &= 1 \\
B_{2\mathrm{e}} &= -\frac{23}{3}F_{\mathrm{e}}\frac{R_{\mathrm{ref}}}{R}\lambda_{\mathrm{e}} + 2N_{\mathrm{e}} \\
B_{1\mathrm{e}} &= \frac{40}{3}F_{\mathrm{e}}^2\left(\frac{R_{\mathrm{ref}}}{R}\lambda_{\mathrm{e}}\right)^2 + F_{\mathrm{e}}\lambda_{\mathrm{e}}\frac{R_{\mathrm{ref}}}{R}N_{\mathrm{e}}(2\beta - 11) + N_{\mathrm{e}}^2 \\
B_{0\mathrm{e}} &= 2F_{\mathrm{e}}\lambda_{\mathrm{e}}\frac{R_{\mathrm{ref}}}{R}\left[-\frac{10}{3}F_{\mathrm{e}}^2\left(\frac{R_{\mathrm{ref}}}{R}\lambda_{\mathrm{e}}\right)^2 + F_{\mathrm{e}}\lambda_{\mathrm{e}}\frac{R_{\mathrm{ref}}}{R}N_{\mathrm{e}}(5 - \beta) + N_{\mathrm{e}}^2\left(\beta - \frac{5}{3}\right)\right]
\end{aligned} \tag{4.24}
$$

where the notation $N_{\mathrm{e}} = -\frac{i}{\epsilon}\left(\nu_{\mathrm{ei}}\frac{R_{\mathrm{ref}}}{v_{\mathrm{th,ref}}}\right)\frac{2Z_{\mathrm{i}}B_{\mathrm{N}}}{k_{\mathrm{y,N}}T_{\mathrm{i,N}}}$ for the normalized collision frequency has been introduced. Note, that it is not immediately evident that the coefficients in 4.24 are equivalent to those in equation 4.23 in case of zero collision frequency. However, if N_{e} is set to zero, both polynomials can be divided by $\omega_{\mathrm{N}} - F_{\mathrm{e}}\frac{R_{\mathrm{ref}}}{R}$ and the previous result can be obtained.

The system of equations 4.12, 4.14 and 4.16 is closed by the quasi-neutrality

condition

$$\sum_{\mathrm{s}} Z_{\mathrm{s}} n_{\mathrm{s}} = 0. \tag{4.25}$$

Substituting the density fluctuations of the species into equation 4.25 the dispersion relation can be expressed as

$$\sum_{\mathrm{s}} \frac{Z_{\mathrm{s}}^2 n_{\mathrm{s,N}}}{T_{\mathrm{s,N}}} \frac{A_{3\mathrm{s}}\omega_{\mathrm{N}}^3 + A_{2\mathrm{s}}\omega_{\mathrm{N}}^2 + A_{1\mathrm{s}}\omega_{\mathrm{N}} + A_{0\mathrm{s}}}{B_{3\mathrm{s}}\omega_{\mathrm{N}}^3 + B_{2\mathrm{s}}\omega_{\mathrm{N}}^2 + B_{1\mathrm{s}}\omega_{\mathrm{N}} + B_{0\mathrm{s}}} = 0. \tag{4.26}$$

In order to obtain a dispersion relation in polynomial form equation 4.26 is multiplied by the denominators of its terms. In case of adiabatic passing electron response and in presence of trapped electrons this leads to a ninth degree polynomial, the roots of which provide the frequencies and growth rates of the physical modes as a function of the parameters and wavenumbers: $\omega_{\mathrm{N}} = \omega_{\mathrm{N}}(n_{\mathrm{s}}, T_{\mathrm{s}}, R_{\mathrm{ref}}/L_{\mathrm{T,s}}, R_{\mathrm{ref}}/L_{\mathrm{T,s}}, m_{\mathrm{s}}, Z_{\mathrm{s}}, B, R, k_{\mathrm{y}}, k_{\parallel})$. Although it is straightforward to calculate, for the sake of completeness the coefficients of this polynomial are given in appendix B.1[1]. The dispersion relation is evaluated numerically with the commercial Matlab mathematical software package.

4.2.3 Quasi-linear Particle Flux

The radial quasi-linear particle flux of the species is given by the formula

$$\begin{aligned} \Gamma_{\mathrm{s,r}} &= \langle n_{\mathrm{s1}} \mathbf{r} \cdot \mathbf{v}_{\mathrm{s1}} \rangle = \langle \sum_{l=-\infty}^{\infty} \hat{n}_{\mathrm{s1}}^{l} \mathrm{e}^{i\mathbf{k}_l \cdot \mathbf{x}} \sum_{m=-\infty}^{\infty} \mathbf{r} \cdot \hat{\mathbf{v}}_{\mathrm{s1}}^{m} \mathrm{e}^{i\mathbf{k}_m \cdot \mathbf{x}} \rangle \\ &= 2\mathrm{Re}\left(\sum_{l=0}^{\infty} \hat{n}_{\mathrm{s1}}^{l} (\mathbf{r} \cdot \hat{\mathbf{v}}_{\mathrm{s1}}^{l})^{*} \right) \end{aligned} \tag{4.27}$$

where the angled brackets mean flux-surface averaging, and the $*$ superscript indicates complex conjugate. The same argument is applied here as described earlier in section 2.3.7: since both the density and velocity fluctuations are expressed as series of Fourier-components in space, when their product is taken, every term containing different modes will be nullified by the averaging operator. However, when a mode is multiplied by its complex conjugate pair, it will give a constant non-zero contribution to the sum and thus to the flux-surface average [31], allowing to evaluate the flux driven by individual modes $\Gamma_{\mathrm{s,r}}^{k}$.

Substituting equation 4.22 and the leading order terms from equation 4.6

[1] The ten coefficients for the case with non-adiabatic passing electrons and no trapping can be recovered analogously.

yields

$$\begin{aligned}\Gamma^k_{\mathrm{s,r}} &= 2\mathrm{Re}\left\{-\frac{Z_\mathrm{s}e}{T_\mathrm{s0}}\hat{\phi}^k_1 n_\mathrm{s0}\frac{A_\mathrm{3s}\omega^3_\mathrm{N}+A_\mathrm{2s}\omega^2_\mathrm{N}+A_\mathrm{1s}\omega_\mathrm{N}+A_\mathrm{0s}}{B_\mathrm{3s}\omega^3_\mathrm{N}+B_\mathrm{2s}\omega^2_\mathrm{N}+B_\mathrm{1s}\omega_\mathrm{N}+B_\mathrm{0s}}\left(\frac{-ik_\mathrm{y}\hat{\phi}^k_1}{B}\right)^*\right\} \\ &= 2\mathrm{Im}\left\{\frac{Z_\mathrm{s}e}{T_\mathrm{s0}}n_\mathrm{s0}|\hat{\phi}^k_1|^2\frac{k_\mathrm{y}}{B}\frac{A_\mathrm{3s}\omega^3_\mathrm{N}+A_\mathrm{2s}\omega^2_\mathrm{N}+A_\mathrm{1s}\omega_\mathrm{N}+A_\mathrm{0s}}{B_\mathrm{3s}\omega^3_\mathrm{N}+B_\mathrm{2s}\omega^2_\mathrm{N}+B_\mathrm{1s}\omega_\mathrm{N}+B_\mathrm{0s}}\right\}. \qquad (4.28)\end{aligned}$$

Note, that the diamagnetic velocity does not give a contribution to the flux. Formally, this is because it is proportional to the density fluctuation, there is no phase difference between the two, and therefore the imaginary part of the flux surface average of their product is zero. The physical reason is that the diamagnetic drift is not an actual particle velocity, it only arises as a consequence of particle gyration in finite background density gradient.

For estimating the magnitude of the potential perturbation the Weiland-model [15] is applied and, assuming isotropic turbulence in the saturated phase, the potential is written as $|\phi^k_1| = \frac{\gamma B}{k^2_\mathrm{y}}$. Although there exist more complex and accurate saturation models [63], it has been shown by Wágner [83] that applying various quasi-linear rules does not result in qualitatively different particle fluxes. Finally, normalization leads to

$$\Gamma^k_{\mathrm{s,r}} = \mathrm{Im}\left\{\frac{A_\mathrm{3s}\omega^3_\mathrm{N}+A_\mathrm{2s}\omega^2_\mathrm{N}+A_\mathrm{1s}\omega_\mathrm{N}+A_\mathrm{0s}}{B_\mathrm{3s}\omega^3_\mathrm{N}+B_\mathrm{2s}\omega^2_\mathrm{N}+B_\mathrm{1s}\omega_\mathrm{N}+B_\mathrm{0s}}\right\}\frac{Z_\mathrm{s}n_\mathrm{s,N}}{T_\mathrm{s,N}}\frac{T^2_\mathrm{i,N}}{Z^2_\mathrm{i}}\frac{\gamma^2_\mathrm{N}}{k_\mathrm{y,N}B_\mathrm{N}}n_\mathrm{ref}v_\mathrm{th,ref}\rho^2_*. \qquad (4.29)$$

The particle flux can formally be split into terms explicitly proportional to the normalized density and temperature gradients ($R_\mathrm{ref}/L_\mathrm{n,s}$ and $R_\mathrm{ref}/L_\mathrm{T,s}$) of the species, and a residual term. These contributions are often called as diffusive, thermo-diffusive and pinch terms, and the flux can be expressed as

$$\Gamma^k_{\mathrm{s,r}} = \frac{n_\mathrm{s,0}}{R_\mathrm{ref}}\left(D_\mathrm{n,s}\frac{R_\mathrm{ref}}{L_\mathrm{n,s}} + D_\mathrm{T,s}\frac{R_\mathrm{ref}}{L_\mathrm{T,s}} + R_\mathrm{ref}V_\mathrm{p,s}\right) \qquad (4.30)$$

where $D_\mathrm{n,s}$ is the diffusion coefficient, $D_\mathrm{T,s}$ the thermo-diffusion coefficient and $V_\mathrm{p,s}$ the pinch velocity [71]. Note, however, that this splitting is purely formal: due to the complex dependence of the mode frequency on the plasma parameters, the above coefficients depend on the gradients themselves, and in general the transport can not be treated as a linear problem. Nonetheless, these terms provide useful additional information about the main driving mechanisms of particle transport. The flux can be further separated into terms containing the magnetic curvature and those appearing even in slab geometry. In stationary plasmas with zero particle

flux, the thermo-diffusion and pinch coefficients are often expressed as

$$C_{\mathrm{T,s}} = \frac{D_{\mathrm{T,s}}}{D_{\mathrm{n,s}}} \qquad C_{\mathrm{P,s}} = \frac{R_{\mathrm{ref}} V_{\mathrm{p,s}}}{D_{\mathrm{n,s}}}.$$

The advantage of C_{T} and C_{P} is that their values are independent of the normalization scheme applied in a linear simulation (typically in gyrokinetics). These definitions will be used when comparing the fluid results with the literature.

4.3 Limiting Cases

In this section standard limiting cases of the fluid equations are considered and compared with previous numerical and analytical results. The physical modes described by the model in these cases are identified and the impact of the added features on mode stability is estimated.

Three limiting cases are analysed: (i.) two-fluid model in slab geometry with one ion species adiabatic electrons, (ii.) two-fluid model in slab geometry with one ion species and non-adiabatic passing electrons and (iii.) three-fluid model in toroidal geometry with two ion species, adiabatic electrons and no parallel dynamics. All cases in this section are collisionless.

Adiabatic electron response can be achieved by setting the electron mass and temperature fluctuation to zero in the parallel momentum equation. However, applying this limit in the dispersion relation 4.26 is not sufficient as the full density response contains terms from the energy and continuity equations, as well. One has to set both the $P_{\mathrm{A,s}}$ and $P_{\mathrm{B,s}}$ polynomials of the electrons in equation 4.22 to unity: $A_{3\mathrm{e}} = A_{2\mathrm{e}} = A_{1\mathrm{e}} = 0,\ A_{0\mathrm{e}} = 1$ and $B_{3\mathrm{e}} = B_{2\mathrm{e}} = B_{1\mathrm{e}} = 0,\ B_{0\mathrm{e}} = 1$. For the zero impurity case $n_{\mathrm{I,N}} = R_{\mathrm{ref}}/L_{\mathrm{n,I}} = 0$ as well as $B_{3\mathrm{I}} = B_{2\mathrm{I}} = B_{1\mathrm{I}} = 0,\ B_{0\mathrm{I}} = 1$ are required[2]. In slab geometry R_{ref}/R must be set to zero. Electron finite Larmor-radius effects are typically neglected for ITG modelling which is obtained simply by $C^{\mathrm{e}}_{\mathrm{FLR}} = 0$.

4.3.1 Two-fluid Model with Adiabatic Electrons

First, the simple two-fluid ITG model with adiabatic electrons in slab geometry with uniform magnetic field is considered. This limit is detailed in [11]. The dispersion relation is

$$\omega\left(\omega + \frac{T_{\mathrm{e}}}{T_{\mathrm{i}}}\omega^{\mathrm{n}}_{*\mathrm{i}}\right) = \frac{T_{\mathrm{e}}}{m_{\mathrm{i}}} k_{\parallel}^2 \left[\frac{5}{3}\frac{T_{\mathrm{i}}}{T_{\mathrm{e}}} + 1 - \frac{\omega^{\mathrm{n}}_{*\mathrm{i}}}{\omega}\left(\eta_{\mathrm{i}} - \frac{2}{3}\right)\right] \tag{4.31}$$

[2]The latter condition is needed because the 9th degree dispersion relation is derived by multiplying equation 4.26 by its denominators.

which can be derived from the model equations (4.12, 4.14, 4.16 and 4.25) by neglecting the toroidal and FLR terms, setting the impurity density to zero and calculating the electron density response from the parallel momentum equation 4.14 assuming zero electron mass. It can be easily shown that, as a third degree polynomial with real coefficients, it has either three real or one real and two complex roots that are complex conjugates of each other, describing three distinct physical modes. As a limiting case of our model, the dispersion relation is evaluated by setting $P_{\mathrm{A,e}} = P_{\mathrm{B,e}} = P_{\mathrm{B,I}} = 1$ and zero impurity concentration.

The spectrum of real frequencies and growth rates of the three modes as a function of the normalized bi-normal wavenumber $k_{\mathrm{y,N}} = k_{\mathrm{y}}\rho_{\mathrm{ref}}$ at $k_{\parallel \mathrm{N}} = k_{\parallel}R_{\mathrm{ref}} = 1.0$, $T_{\mathrm{e}}/T_{\mathrm{i}} = 1.2$, $R_{\mathrm{ref}}/L_{\mathrm{n,i}} = R_{\mathrm{ref}}/L_{\mathrm{n,e}} = 4$ and $R_{\mathrm{ref}}/L_{\mathrm{T,i}} = R_{\mathrm{ref}}/L_{\mathrm{T,e}} = 9$ is plotted on the left panel of figure 4.1. The spectrum is calculated up to $k_{\mathrm{y,N}} = 1$ even though the validity of the fluid description breaks down approaching $k_{\mathrm{y,N}} \sim 1$. The right panel shows a scan of the parallel wavenumber $k_{\parallel}$ of the unstable mode (mode 3) at $k_{\mathrm{y,N}} = 0.4$ with the same physical parameters. This graph shows good qualitative agreement to the behaviour of the ITG mode described in [11] on page 161-162, and mode 3 is therefore identified as the Ion Temperature Gradient driven eigenmode. The real frequency of the ITG mode is negative due to the normalization applied in the model, corresponding to the ion diamagnetic direction. The oscillating mode (mode 1) is characterized by a frequency linear in k_{y} and therefore proportional to the electron diamagnetic frequency. The mode is identified as a modified electron drift wave [11]. The stability criterion of the ITG mode when $\omega \sim k_{\parallel}\frac{T_{\mathrm{e}}}{m_{\mathrm{i}}} \ll \omega^{\mathrm{n}}_{*\mathrm{i}}$ is expected to be $\eta_{\mathrm{i}} > \frac{2}{3}$ [11]. This can be easily expressed using equation 4.31 keeping only the terms proportional to $\omega^{\mathrm{n}}_{*\mathrm{s}}$, and it is confirmed by a scan of $R_{\mathrm{ref}}/L_{\mathrm{T,i}}$ at $k_{\mathrm{y,N}} = 0.4$ and $k_{\parallel \mathrm{N}} = 0.1$ shown on figure 4.2.

If the parallel wavenumber, and together with it the mode frequency, is increased, the stabilizing terms on the right hand side of equation 4.31 are becoming more important. This leads to the shifting of the instability towards higher k_{y} values. The same effect can be obtained by increasing $T_{\mathrm{i}}/T_{\mathrm{e}}$.

The FLR corrections do not increase the degree of the dispersion relation in this case due to the fixed adiabatic response of the electrons. They have a weak stabilizing effect on the ITG driven modes at $k_{\mathrm{y,N}} < 1$ (figure 4.3, left). Not shown on this figure, but at the same time they limit the bi-normal wavenumber range where the instability occurs to $k_{\mathrm{y,N}} \sim 1$, whereas without the FLR correction the mode stays unstable even at much higher $k_{\mathrm{y,N}}$ values. This, of course, is just in a mathematical sense as the fluid description becomes invalid as $k_{\mathrm{y,N}}$ approaches unity. The frequency of the electron drift mode is significantly reduced at high k_{y}

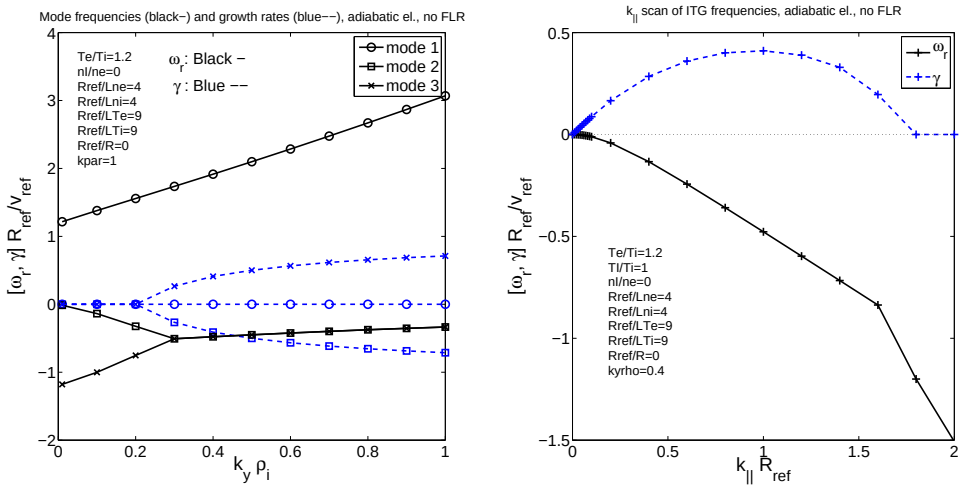

Figure 4.1: Two-Fluid Model with Adiabatic Electrons. Left: Real frequency (black) and growth rate (blue) spectrum of the three physical modes as a function of the bi-normal wavenumber. Right: $k_{||}$ scan of mode 3 (ITG mode) at $k_{\mathrm{y,N}} = 0.4$.

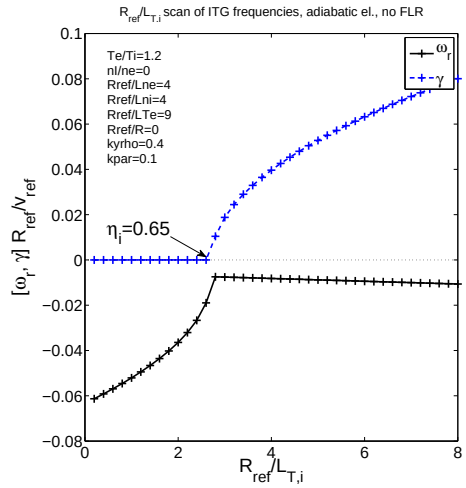

Figure 4.2: Two-Fluid Model with Adiabatic Electrons. $R/L_{\mathrm{T,i}}$ scan of the real frequency (black) and growth rate (blue) of the $k_{\mathrm{y,N}} = 0.4$, $k_{||}/R = 0.1$ mode.

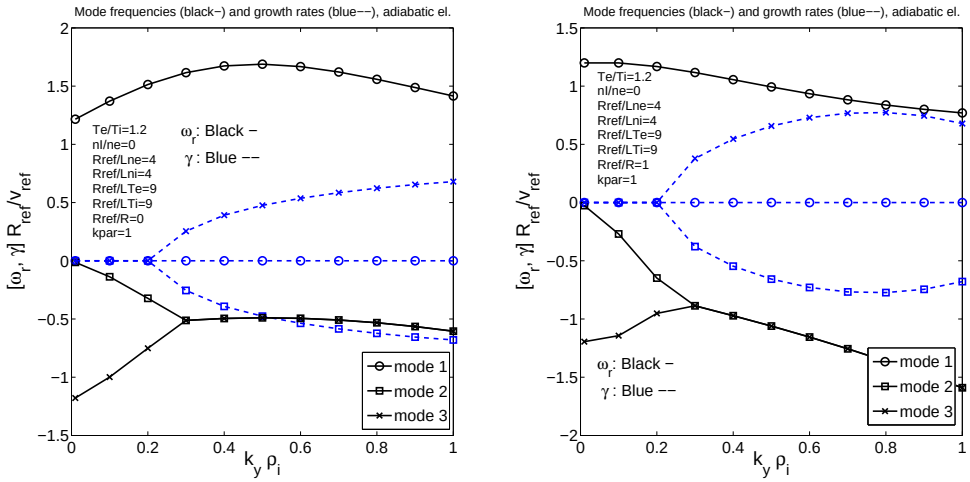

Figure 4.3: Two-Fluid Model with Adiabatic Electrons. Real frequency (black) and growth rate (blue) spectrum of the three physical modes as a function of the bi-normal wavenumber with FLR corrections in slab (left) and toroidal (right) geometry.

and the absolute value of unstable ITG mode frequency becomes linearly increasing, commonly observed in gyro-kinetic simulations (see for example [44]).

Including curvature corrections in equation 4.21 also does not change the degree of the dispersion relation. Qualitatively, the mode structure remains the same but the occurrence of the unstable ITG modes is further limited in the bi-normal wavenumber range (figure 4.3, right). A scan over the toroidicity parameter of the $k_{\mathrm{y,N}} = 0.4$ mode at $k_{\parallel} = 0$ and $\lambda_{\mathrm{s}} = 1$, shown on the left of figure 4.4, reveals that the growth rate of a typical ITG mode increases with R_{ref}/R, in accordance with the expectation on the bad curvature side. The growth rate curve is also in qualitative agreement with the results of Jarmén et al. [84] who obtained a similar dependence in a circular tokamak geometry solving the eigenvalue problem in ballooning space. In the simple case of $\lambda_{\mathrm{s}} R_{\mathrm{ref}}/R = 1$ with $k_{\parallel} = 0$ and no FLR corrections the dispersion relation is quadratic and the stability criterion reduces to the expression

$$\left(\frac{R_{\mathrm{ref}}}{L_{\mathrm{n,i}}}\right)^2 - 4\left[1 + \frac{10}{3}\frac{T_{\mathrm{i,N}}}{T_{\mathrm{e,N}}} - \frac{14}{3}\frac{T_{\mathrm{i,N}}}{T_{\mathrm{e,N}}}\right]\frac{R_{\mathrm{ref}}}{L_{\mathrm{n,i}}} + 4 + \frac{160}{9}\left(\frac{T_{\mathrm{i,N}}}{T_{\mathrm{e,N}}}\right)^2 < 8\frac{T_{\mathrm{i,N}}}{T_{\mathrm{e,N}}}\frac{R_{\mathrm{ref}}}{L_{\mathrm{n,i}}}\eta_{\mathrm{i}} \qquad (4.32)$$

giving $\eta_{\mathrm{i}} > 1.28$ with $R_{\mathrm{ref}}/L_{\mathrm{n,i}} = 4$ and $T_{\mathrm{e,N}}/T_{\mathrm{i,N}} = 1.2$, confirmed by the right panel of figure 4.4.

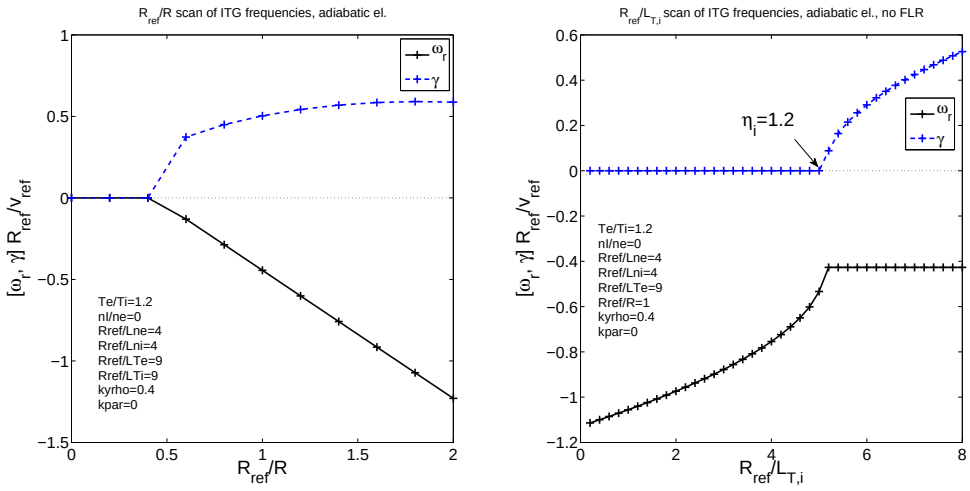

Figure 4.4: Two-Fluid Model with Adiabatic Electrons. $R_{\rm ref}/R$ (left) and $R_{\rm ref}/L_{\rm n,i}$ (right) scan of the real frequencies (black, solid) and growth rates (blue, dashed) of mode 3 (ITG mode) at $k_{\|} = 0$.

4.3.2 Two-fluid Model with Non-adiabatic Electrons

The impact of turning on non-adiabatic electron response due to finite electron inertia in the slab model with the same parameters as those for figure 4.1 is that of completely stabilizing the bi-normal modes. The reason can be understood by looking at the dispersion relation including both ion and electron dynamics in case of no FLR and no toroidal effects. In this limit one obtains

$$A_{3\rm s} = 0, \quad A_{2\rm s} = F_{\rm s}\frac{R_{\rm ref}}{L_{\rm n,s}}, \quad A_{1\rm s} = -J_{\rm s}, \quad A_{0\rm s} = F_{\rm s}J_{\rm s}\frac{R_{\rm ref}}{L_{\rm n,s}}\left(\eta_{\rm s} - \frac{2}{3}\right)$$
$$B_{3\rm s} = 1, \quad B_{2\rm s} = 0, \quad B_{1\rm s} = -\frac{5}{3}J_{\rm s}, \quad B_{0,\rm s} = 0$$

leading to a fifth degree polynomial. However, the zeroth order term is zero and the highest order coefficient $\frac{R_{\rm ref}}{L_{\rm n,i}} - \frac{R_{\rm ref}}{L_{\rm n,e}}$ cancels due to quasi-neutrality leaving, effectively, a third degree problem. Setting $n_{\rm i,N} = n_{\rm e,N}$, $Z_{\rm i} = -Z_{\rm e} = 1$ and realizing that typically $\frac{J_{\rm i}}{J_{\rm e}} \sim \frac{m_{\rm e}}{m_{\rm i}}\frac{T_{\rm i}}{T_{\rm e}} \ll 1$ one can write

$$\omega_{\rm N}\left(\omega_{\rm N} + \tau\frac{R_{\rm ref}}{L_{\rm n,i}}\left(\eta_{\rm e}+1\right)\right) = \frac{5}{3}J_{\rm i}\left(\tau + 1 + \frac{\tau}{\omega_{\rm N}}\frac{R_{\rm ref}}{L_{\rm n,i}}\left(\eta_{\rm e} - \eta_{\rm i}\right)\right) \tag{4.33}$$

with $\tau = T_{\mathrm{e,N}}/T_{\mathrm{i,N}}$. Note, that $\tau J_{\mathrm{i}} = \frac{T_{\mathrm{e}}}{m_{\mathrm{i}}} \frac{k_{\parallel}^2}{(\omega_{\mathrm{D,i}}^{\mathrm{mod}})^2}$. Using now the limit $\omega \sim k_{\parallel} \frac{T_{\mathrm{e}}}{m_{\mathrm{i}}} \ll \omega_{*\mathrm{i}}^{\mathrm{n}}$ again and assuming $(\eta_{\mathrm{e}} - \eta_{\mathrm{i}}) \sim 1$ gives

$$\omega_{\mathrm{N}}^2 = \frac{5}{3} J_{\mathrm{i}} \frac{\eta_{\mathrm{e}} - \eta_{\mathrm{i}}}{\eta_{\mathrm{e}} + 1} \tag{4.34}$$

leading to $\eta_{\mathrm{i}} > \eta_{\mathrm{e}}$ as the instability criterion. If $(\eta_{\mathrm{e}} - \eta_{\mathrm{i}}) \ll 1$ then the dispersion relation is the first order expression

$$\omega_{\mathrm{N}} \tau \frac{R_{\mathrm{ref}}}{L_{\mathrm{n,i}}} (\eta_{\mathrm{e}} + 1) = \frac{5}{3} J_{\mathrm{i}} (\tau + 1) \tag{4.35}$$

which means the mode is always stable. This cancellation is the consequence of the symmetry between the ion and electron dynamics. This limit, however, is not typical in experimental conditions. The presence of trapped electrons, as additional species, or impurity particles breaks the symmetry and gives rise to unstable modes even when $\eta_{\mathrm{i}} = \eta_{\mathrm{e}}$.

Turning on the FLR terms maintains a similar stability criterion for the ITG modes. Comparing the left panel of figure 4.5, showing the ITG spectrum with non-adiabatic electrons response, with figure 4.3 shows that the stabilizing effect of the electrons is still present despite the stronger drive for the ITG mode. In case of $\eta_{\mathrm{e}} > \eta_{\mathrm{i}}$ ETG modes appear at $k_{\mathrm{y}}\rho_{\mathrm{i}} \approx 10$ (figure 4.5, right). The detailed analysis of these modes is beyond the scope of this thesis.

4.3.3 Three-fluid Model with Adiabatic Electrons

The system describing two ion species in toroidal geometry with adiabatic electrons and without parallel dynamics has been studied in detail by Fröjdh et al. in [50]. The presence of impurity species leads to impurity ITG modes that, as it is shown below, either co-exist or compete with the main ion ITG modes. In this work we are investigating the effect of low-Z impurities on turbulence and therefore only fully ionized particles will be considered (unless otherwise stated).

Figure 4.6 shows a case when two distinct ion ITG modes, associated with deuterium and carbon species, are present. The relevant parameters are $R_{\mathrm{ref}}/L_{\mathrm{n,s}} = 4$, $R_{\mathrm{ref}}/L_{\mathrm{T,e}} = R_{\mathrm{ref}}/L_{\mathrm{T,I}} = 9$, $R_{\mathrm{ref}}/L_{\mathrm{T,i}} = 12$, $T_{\mathrm{e}}/T_{\mathrm{i}} = 1.2$, $T_{\mathrm{I}}/T_{\mathrm{i}} = 1.0$, $n_{\mathrm{I}}/n_{\mathrm{e}} = 0.05$, $R_{\mathrm{ref}}/R = 1$ and $k_{\parallel} = 0$. The $k_{\mathrm{y,N}}$ range of this plot has been extended up to 2 as the fully ionized carbon ions have a Larmor-radius about 2.4 times smaller than that of the deuterium. The right panel of the same figure shows the $R_{\mathrm{ref}}/L_{\mathrm{T,i}}$ scan of the main ion ITG and the $R_{\mathrm{ref}}/L_{\mathrm{T,I}}$ scan of the impurity ITG mode at $k_{\mathrm{y,N}} = 0.4$. Both modes present the expected dependence on η_{s} as observed in

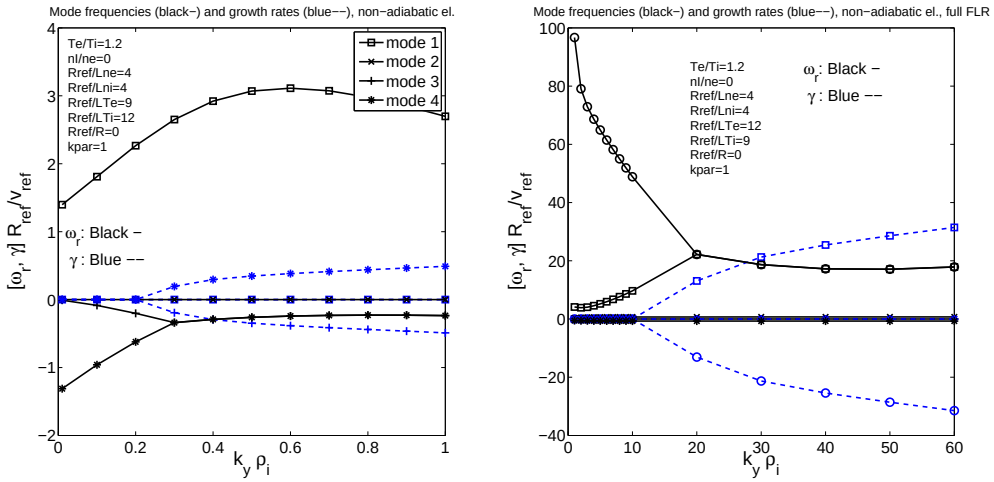

Figure 4.5: Two-Fluid Model with Non-Adiabatic Electrons. Real frequency (black) and growth rate (blue) spectrum of the ITG (left) and ETG (right) modes as a function of the bi-normal wavenumber with non-adiabatic electron response and FLR corrections in slab geometry.

section 4.3.1 in figure 4.2. A similar bi-normal mode spectrum can be achieved with the same physical parameters using neon impurities. Figure 4.7 shows that with a lower main ion concentration, either due to higher Z impurity species or larger amount of impurity particles, the threshold of the main ITG branch is shifted towards higher temperature gradients. This plot is in good qualitative agreement with figure 2 of [50].

When lithium impurities are used the frequency spectrum of the bi-normal modes with the same physical parameters (4.8, left) shows a qualitatively different picture. In this case only one unstable mode is obtained at any bi-normal wavenumber value, but, between $k_{\mathrm{y,N}} \sim 1.0 - 1.5$, a secondary branch of unstable modes appears driven by the impurity temperature gradient. Although these modes are not, strictly speaking, within the regime of interest of our model ($k_{\mathrm{y}}\rho_{\mathrm{th,i}} < 1$), the structural difference compared to the spectra obtained with higher Z impurities within the same limit is peculiar.

In order to give an analytical explanation for this behaviour one would have to treat a fourth degree problem, any further reduction would mean that the model can not describe two unstable modes simultaneously. This, in general, can be quite demanding and is beyond the scope of the present work. However, deriving the coefficients of dispersion relation without FLR corrections (appendix B.2) shows that only two quantities are significantly affected when different impurity species

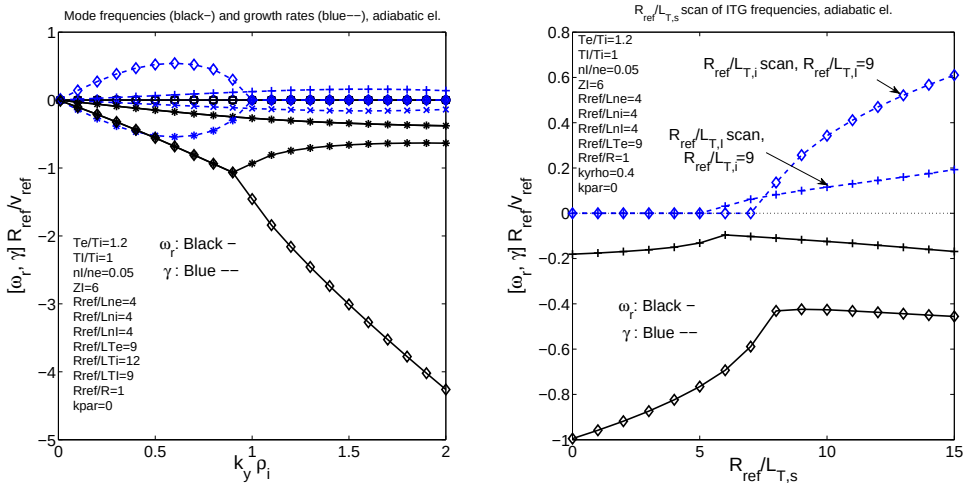

Figure 4.6: Left: Real frequency (black) and growth rate (blue) spectrum of the ITG modes as a function of the bi-normal wavenumber with carbon impurity, FLR corrections and adiabatic electrons in toroidal geometry. Right: $R_{\rm ref}/L_{\rm T,i}$ and $R_{\rm ref}/L_{\rm T,I}$ scans of the two ITG modes at $k_{\rm y,N} = 0.4$.

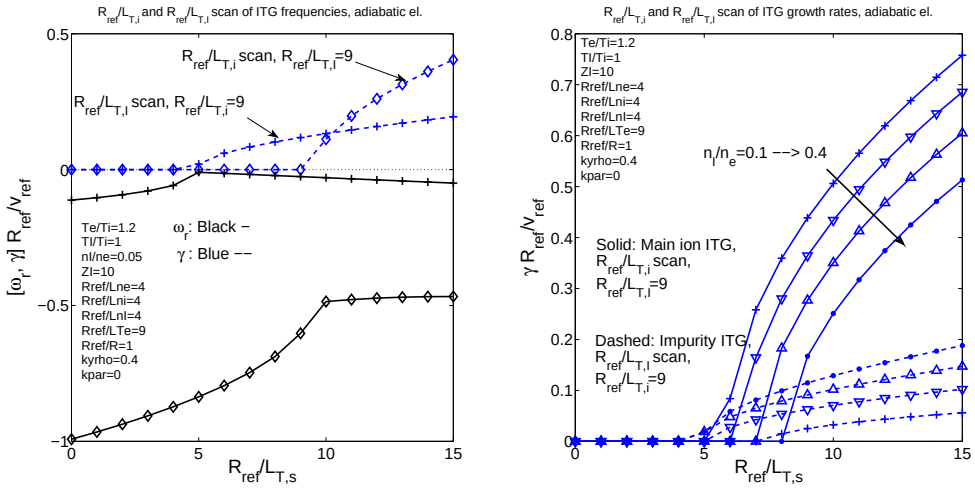

Figure 4.7: $R_{\rm ref}/L_{\rm T,i}$ and $R_{\rm ref}/L_{\rm T,I}$ scans of growth rates and frequencies of the two ITG modes at $k_{\rm y,N} = 0.4$ with neon impurities at $n_{\rm I}/n_{\rm e} = 0.05$ (left) and growth rates at four different values of $n_{\rm I}/n_{\rm e} = 0.01, 0.02, 0.03, 0.04$ (right).

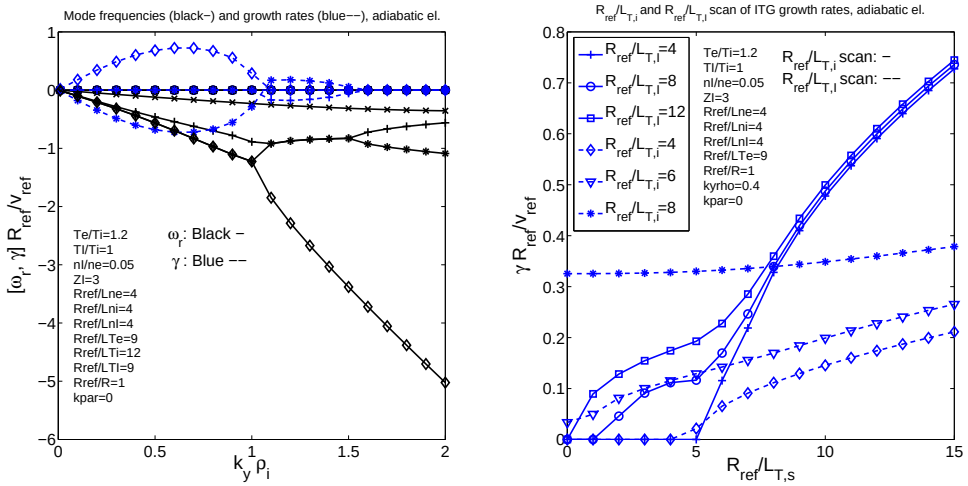

Figure 4.8: Left: Real frequency (black) and growth rate (blue) spectrum of the ITG modes as a function of the bi-normal wavenumber with lithium impurity, FLR corrections and adiabatic electrons in toroidal geometry. Right: $R_{\rm ref}/L_{\rm T,i}$ and $R_{\rm ref}/L_{\rm T,I}$ scans of the ITG modes at $k_{\rm y,N} = 0.5$ and $k_{\rm y,N} = 1.3$.

are included in the system: the main ion density (through quasi-neutrality) and $F_{\rm I} = (T_{\rm I}/T_{\rm i})(Z_{\rm i}/Z_{\rm I})$. The FLR terms would also change but their contribution is small at low $k_{\rm y}$ values and the present phenomenon occurs without them, as well. Using heavier impurities while keeping the same impurity concentration means that the effective charge number ($Z_{\rm eff} = Z_{\rm i}^2 n_{\rm i} + Z_{\rm I}^2 n_{\rm I}$) increases. This can also be achieved by a larger amount of lighter impurities. In our present example, increasing $n_{\rm Li}$ in order to maintain the $Z_{\rm eff}$ value obtained by 5% carbon concentration does not change the qualitative features of the spectrum of figure 4.8. However, decreasing the lithium temperature to $T_{\rm Li}/T_{\rm i} = 0.3$ increases the value of $F_{\rm I}$ and compensates for the difference due to the smaller $Z_{\rm Li}$. With the reduced impurity temperature the two ITG modes co-exist again at low $k_{\rm y,N}$ values and a spectrum much similar to that in figure 4.6 is produced. Accordingly, if the temperature of carbon species (or any higher Z impurities) is sufficiently increased, a spectrum similar to that in figure 4.8 is obtained.

In the case when there is only one instability, the mode is a mixture of main and impurity ITG-s. The two mechanisms compete with each other, and the one with the stronger drive dominates. This behaviour is shown on the right panel of figure 4.8: If the impurity temperature gradient is low, the $R_{\rm ref}/L_{\rm T,i}$ scan gives the previously observed dependence of the main ITG growth rates. Similarly, when the main ion temperature gradient is low, the $R_{\rm ref}/L_{\rm T,I}$ scan reveals that the same bi-

normal mode is driven unstable by the impurity temperature gradient. In this case the secondary instability branch, observed on the left panel only at $k_{\mathrm{y,N}} \sim 1.0 - 1.5$ above the main ITG modes, appears at a wide range of the bi-normal spectrum, much the same as the impurity mode in figure 4.6 without the dominant mode. Above $R_{\mathrm{ref}}/L_{\mathrm{T,i}} \sim 8$ increasing the impurity temperature gradient has only a weak effect on the growth rates but between $0 < R_{\mathrm{ref}}/L_{\mathrm{T,i}} < 5$ the impurities clearly play an important role in destabilizing the modes. The impurity ITG-s (dashed) are more sensitive to the main ion temperature gradient. Increasing $R_{\mathrm{ref}}/L_{\mathrm{T,i}}$ from 4 to 8 the mode almost completely loses its dependence on $R_{\mathrm{ref}}/L_{\mathrm{T,I}}$.

These findings suggest that the reason for this qualitative difference is related to the ratio of the Larmor-radii of the main and impurity ions and the typical length scale of their associated ITG modes. In case of lithium impurities at $T_{\mathrm{Li}}/T_{\mathrm{i}} = 1.0$ this ratio is relatively small, $\rho_{\mathrm{i}}/\rho_{\mathrm{Li}} \sim 1.7$, and the two species are expected to show similar dynamics. Fluctuations, represented by the imposed bi-normal Fourier-modes, that have a spatial extent similar to the deuterium Larmor radius will also be perceived by the lithium ions and, within the framework of this model, only one unstable eigenmode appears. When the difference between the Larmor-radii of the two ion species is larger either due to higher Z_{I} ($\rho_{\mathrm{i}}/\rho_{\mathrm{C}} \sim 2.4$) or lower $T_{\mathrm{I}}/T_{\mathrm{i}}$ ($\rho_{\mathrm{i}}/\rho_{\mathrm{Li}} \sim 1.7\sqrt{T_{\mathrm{i}}/T_{\mathrm{I}}}$), the fluctuations typically driving main ion ITG modes will not affect the impurities, and vica versa. In this case two distinct unstable modes exist with the impurity mode being sub-dominant at $k_{\mathrm{y}}\rho_{\mathrm{i}} < 1$.

The quasi-linear radial particle flux corresponding to this limit will always exhibit the ambi-polarity of the two ion species due to the adiabatic electron response. Figure 4.9 shows the flux as a function of the bi-normal wavenumber driven by the two unstable modes in presence of carbon impurities. The spectrum is not peaked, the lowest k_{y} mode gives the largest contribution to the particle flux. When both the deuterium and carbon density profiles are centrally peaked (positive density gradients, left) both ITG modes drive an outward impurity, and consequently, an inward deuterium flux. If the impurity density profile is peaked on the outside (negative density gradient), then the direction of the D-ITG flux reverses, in accordance with the results of [50]. The impurity ITG modes still drive the particles in the inward direction but their effect is subdominant compared to the D-ITG modes.

4.4 Summary of the Chapter

In this chapter a Weiland-type fluid model has been introduced that captures the main aspects of the particle transport properties of the FTU Liquid Lithium Limiter

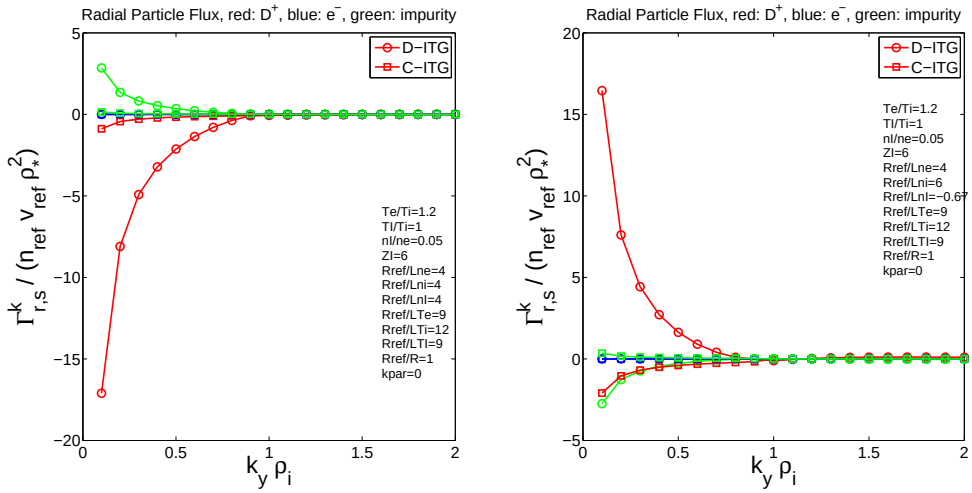

Figure 4.9: Radial particle flux spectrum of the deuterium (red), impurity ion (green) and electron (blue) species as a function of the bi-normal wavenumber driven by the main ion (circles) and impurity (squares) ITG modes, with centrally peaked (left) and reversed (right) impurity density profile.

discharges. For this purpose, two non-trace impurity species and non-adiabatic electron response are required. The non-adiabatic electron dynamics can be provided either by a trapped electron fraction in toroidal geometry or finite passing electron inertia. Electron collisions are included in order to stabilize trapped electron modes and obtain an ITG dominated turbulent regime. The dispersion relation obtained from the model is written in a polynomial form and its roots are evaluated numerically. The quasi-linear particle flux is calculated using Weiland's model for the saturated electrostatic potential [15].

In order to check the validity of the model, three simple limiting cases have been presented. The first case, with one ion species and adiabatic electrons in slab geometry, is the simplest case when ITG modes can be excited. The dispersion relation can be evaluated analytically when the mode frequency is sufficiently low, and the numerical results show good agreement with the theoretical formula. In the second case non-adiabatic passing electron response was included. Although this model can capture ETG modes, since we are aiming to study ITG mode driven transport, it is not relevant for the present work. However, it provides a useful analytical benchmark against the numerical results. The third case, with two non-trace ion species in toroidal geometry without parallel dynamics, is a comparison with the work of Fröjdh et al. in [50]. It is shown that two separate eigenmodes, associated with the deuterium and impurity ITG modes, are present when the typical

spatial scale of the two ion modes are sufficiently far from each other. In a lithium doped plasma with thermal equilibrium between the two ion species, only one mixed ITG mode exists. Its growth rate is dominated by the mode with the stronger drive and therefore it is sensitive to the temperature gradient of both ion species. The ion particle flux is ambi-polar and, in agreement with the results of [50], its direction is determined by the sign of the impurity density gradient.

The above cases provide a baseline of benchmarks of the model and its numerical implementation. The effect of trapped electrons, electron collisions and magnetic geometry will be investigated in the following chapter in relation with the analysis of the experimental cases.

Chapter 5

Multi-Fluid Particle Flux Analysis of Non-trace Impurity Doped Tokamak Plasmas

The local gyrokinetic transport analysis of the FTU #30582 discharge presented in chapter 3 is repeated here using the quasi-linear fluid model introduced in chapter 4. Emphasis is placed on separating the unstable eigenmodes of the system, and identifying the role of the diffusion, thermodiffusion and pinch terms of the ion particle flux under the different cases. The main results of this chapter have been published in [45].

5.1 Analysis of FTU #30582

5.1.1 The Density Ramp-up Phase

The spectra of growth rates of the two most unstable modes and the total particle flux of the deuterium, trapped electron and lithium species as functions of the bi-normal wavenumber k_y are plotted on the top left and right panels of figure 5.1, respectively. The remaining eigenmodes are completely stable and omitted from the graph. The deuterium and lithium fluxes driven by the ITG modes split into diffusive, thermo-diffusive and pinch terms are shown on the bottom left and right panels. The slab (solid) and curvature driven (dashed) terms are also indicated separately. The plasma parameters at $t = 0.3$s have been used (table 3.2). Although the electron flux is not expected to be accurately captured by a quasi-linear model, for the sake of completeness it is also included in the total flux plot.

The modes of the lower-k peak in the growth rate spectrum located between

$0.1 < k_{\mathrm{y}}\rho_{\mathrm{i}} < 1.2$ rotate in the ion diamagnetic direction and they are associated with ITG modes. The real frequency of the other eigenmode has the opposite sign, indicating TE modes. Compared with the linear gyrokinetic simulation of the same case (figure 3.3), one can see that the maxima of the ITG growth rates are in close agreement, but the TE modes are predicted to be much more unstable by the fluid calculation. They become the most unstable eigenmode at $k_{\mathrm{y}}\rho_{\mathrm{i}} \approx 0.7$ in the fluid model, while they do not appear in the corresponding gyrokinetic spectrum below $k_\theta\rho_{\mathrm{i}} = 2$. The deuterium flux driven by the ITG mode is directed inward across the whole spectrum except for the longest wavelength mode included in the analysis, at $k_y\rho_{\mathrm{i}} = 0.1$. These observations suggest that the effect of collisionality in the fluid model is underestimated at high, and overestimated at low k_{y} values due to the $1/k_{\mathrm{y}}$ scaling of the collision operator.

Although a precise quantitative agreement between the fluid and gyrokinetic results are not expected, the ratio of the deuterium and lithium fluxes in the linear gyrokinetic, non-linear gyrokinetic and quasi-linear fluid calculations at the fastest growing mode, at $k_{\mathrm{y}}\rho_{\mathrm{i}} = 0.4$, are all between -0.5 and -0.3. The coefficient $C_{\mathrm{T},\sigma} = D_{\mathrm{T},\sigma}/D_{\mathrm{n},\sigma}$, as calculated from the fluid model, takes a value between approximately -0.28 and -0.43 for deuterium ions in the region $0.3 < k_\theta\rho_{\mathrm{i}} < 0.5$, where the largest flux is observed. These values are similar to those found in [85] for a metallic limiter FTU scenario.

If the collision frequency is sufficiently low, TEM-s become the dominant mode, but the ITG driven deuterium flux remains to be directed inward (collisionless case shown in figure 5.2). An ITG dominated spectrum driving inward deuterium flux can be obtained at low collisionality by manually reducing the trapped electron fraction, showing that the deuterium pinch is not caused by collisions.

The effect of reducing the lithium concentration of the plasma to $c_{\mathrm{Li}} = 0.01$ at the $t = 0.3$s case while keeping the reference $\nu_{e,N} = 0.049$ collision frequency is shown on figure 5.3. The ITG modes become more unstable but occupy a narrower region in the bi-normal spectrum, similarly to the gyrokinetic results (figure 3.4). The TE modes are also more unstable reflecting the effect of the impurity screening on the electron driven modes [48]. The distribution of the deuterium particle flux driven by the ITG modes between the various channels (bottom left panel) shows a similar picture as in the reference $c_{\mathrm{Li}} = 0.15$ case. However, the slab diffusive component stays dominant in a wider region of the k_θ space resulting in a strong outward particle transport up until $k_\theta\rho_{\mathrm{i}} \approx 0.5$ and a weak inward flux above.

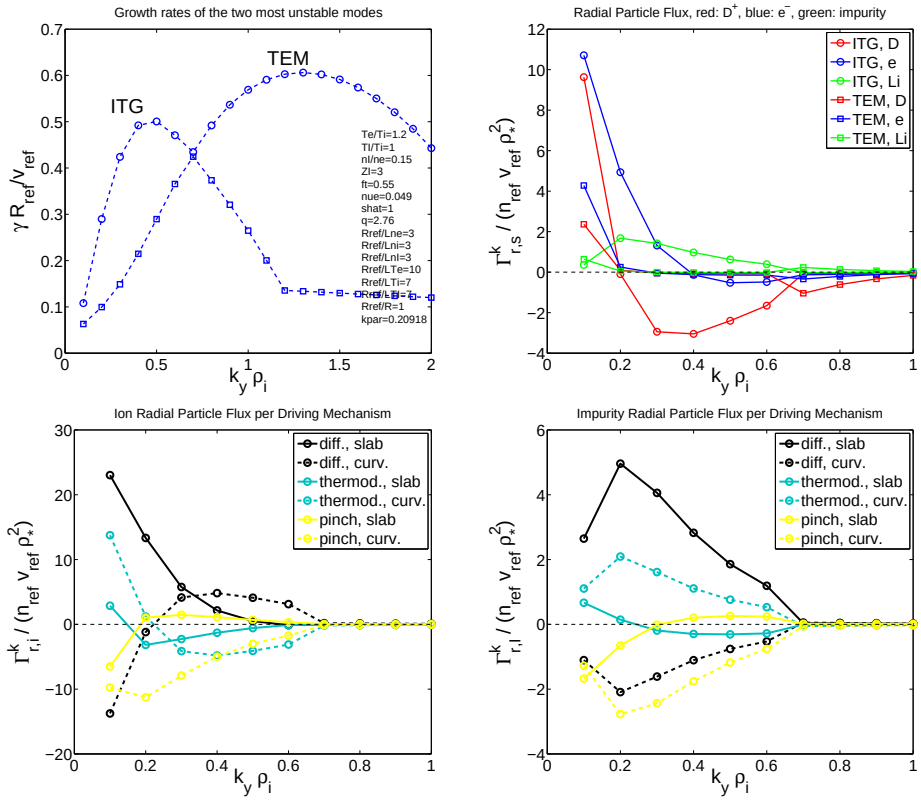

Figure 5.1: Fluid analysis at $t = 0.3$s with the reference $c_{\mathrm{Li}} = 0.15$ lithium concentration. Growth rates of the two most unstable modes (ITG and TEM, top left), total flux of the species driven by ITG and TE modes (top right), deuterium (bottom left) and lithium (bottom right) particle flux by slab (solid) and curvature (dashed) terms of the diffusive (black), thermo-diffusive (cyan) and pinch (yellow) contributions driven by ITG modes as a function of the bi-normal wavenumber.

5.1.2 The Density Plateau Phase

The fluid analysis of the $t = 0.8$s case with the experimental parameters (figure 5.4) shows that the fastest growing eigenmode is associated with ITG modes below $k_{\mathrm{y}}\rho_{\mathrm{i}} \approx 0.6$. This case is characterized by strong collisionality ($\nu_{e,N} = 0.46$) that stabilizes TEM-s and destabilizes drift modes rotating in the ion diamagnetic direction. Ion drift modes have also been observed in the gyrokinetic analysis (figure 3.11) but, in contrast with the fluid results, they are completely stable. However, due to the inverse scaling of the flux with the bi-normal wavenumber according to the mixing length theory, these modes are expected to contribute little to the overall particle transport. Electron and deuterium fluxes are similar due to the low lithium concentration, both of them are dominated by the outward slab diffusive term.

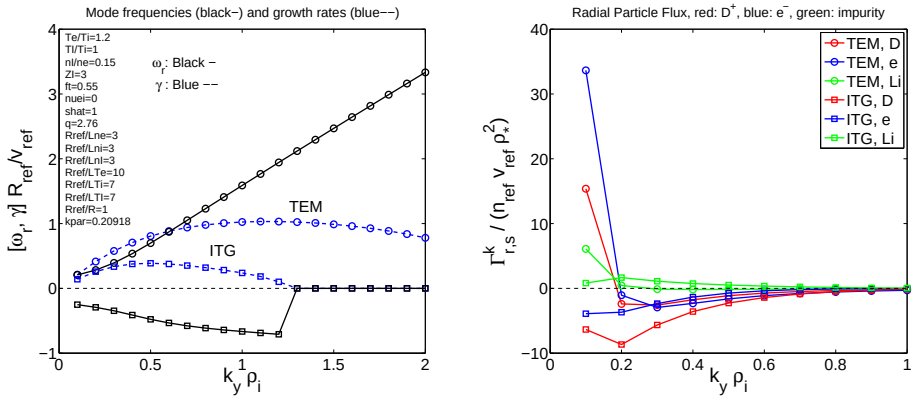

Figure 5.2: Fluid analysis at $t = 0.3$s without collisions. Growth rates (dashed) and real frequencies (solid) of the two most unstable modes (ITG and TEM, left) and the total particle flux of the species driven by ITG and TE modes (right).

If the high lithium concentration ($c_{\mathrm{Li}} = 0.15$) is artificially restored in the $t = 0.8$s case, it again causes a deuterium pinch similarly to the gyrokinetic result (figure 3.11). The low-k ITG modes are slightly stabilized allowing the TEM-s to become the most unstable eigenmodes below $k_{\mathrm{y}}\rho_{\mathrm{i}} \approx 0.5$. However, the majority of the flux remains to be driven by the ITG modes. In contrast with the previous fluid results, the slab diffusion term of the quasi-linear deuterium flux is now inward in most of the bi-normal spectrum, and the main outward drive comes from the curvature diffusion term. The thermo-diffusion and pinch terms of the low-k modes, however, provide a strong inward contribution and produce an overall inward deuterium flux. The distribution of the impurity flux between the various channels are the same as in the experimental case, but the magnitude is, of course, significantly larger due to the higher lithium concentration.

5.1.3 Separating the Ion Eigenmodes

In all of the previous cases only a single unstable eigenmode rotating in the ion diamagnetic direction has been observed at low wavenumbers (below $k_{\mathrm{y}}\rho_{\mathrm{i}} \approx 0.5$). The expected deuterium and lithium ITG modes did not appear separately, they generated one mixed deuterium-lithium ITG mode. In the linear gyrokinetic analysis the D-ITG and Li-ITG dominated modes have been separated in the bi-normal spectrum by decreasing the relative impurity temperature and thus their Larmor-radius. The same idea is used with the fluid model: The $t = 0.3$s case with a reduced lithium and deuterium temperature ratio $T_{\mathrm{Li}}/T_{\mathrm{D}} = 0.5$ is plotted on figure 5.6. The

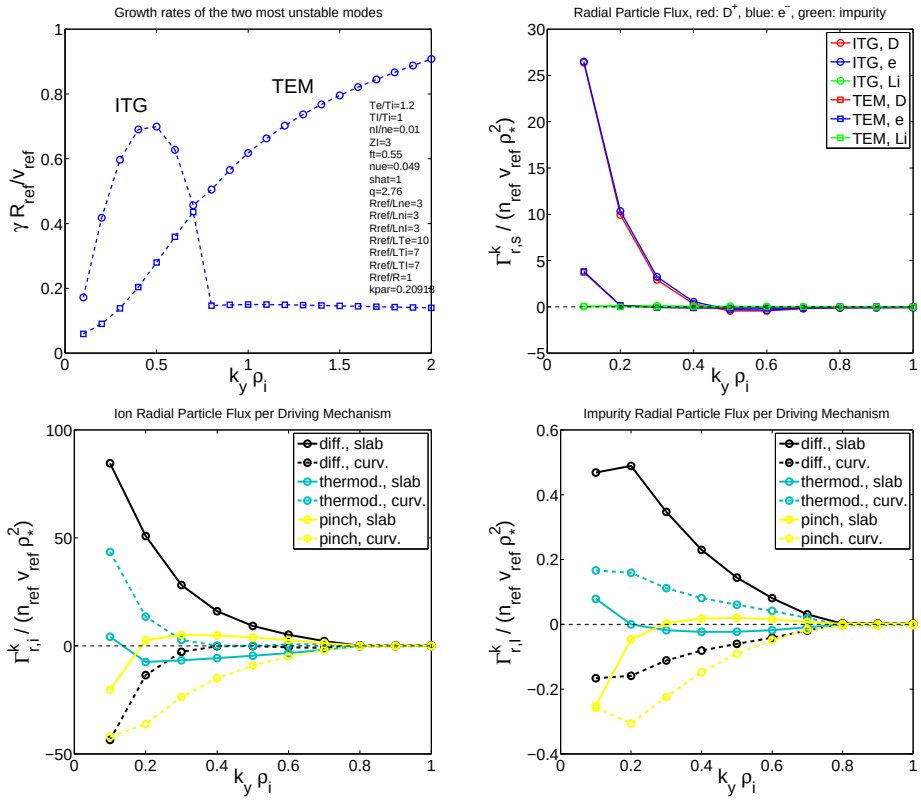

Figure 5.3: Fluid analysis at $t = 0.3$s with reduced $c_{\mathrm{Li}} = 0.01$ lithium concentration. Growth rates of the two most unstable modes (ITG and TEM, top left), total flux of the species driven by ITG and TE modes (top right), deuterium (bottom left) and lithium (bottom right) particle flux by slab (solid) and curvature (dashed) terms of the diffusive (black), thermo-diffusive (cyan) and pinch (yellow) contributions driven by ITG modes as a function of the bi-normal wavenumber.

growth rate spectrum (top left) shows three unstable eigenmodes, two of which rotate in the ion diamagnetic and one in the electron diamagnetic direction below $k_{\mathrm{y}}\rho_{\mathrm{i}} \approx 0.5$, associated with D-ITG, Li-ITG and TE modes, respectively. At higher wavenumber values the D-ITG modes become stable and the third most unstable eigenmode becomes an electron drift mode. If compared with the gyrokinetic results on figure 3.12, it can be seen that the deuterium and lithium ITG growth rates follow a similar pattern in the two models: the D-ITG maximum is located around $k_{\mathrm{y}}\rho_{\mathrm{i}} \approx 0.4$ and the Li-ITG modes are peaked around $k_{\mathrm{y}}\rho_{\mathrm{i}} \approx 1$ in both cases. The growth rates in the fluid calculation are slightly overestimated, probably due to the fact that only electron collisions are included, and the fluid model also predicts the presence of fast growing TE modes above $k_{\mathrm{y}}\rho_{\mathrm{i}} \approx 0.5$ missing from the gyrokinetic

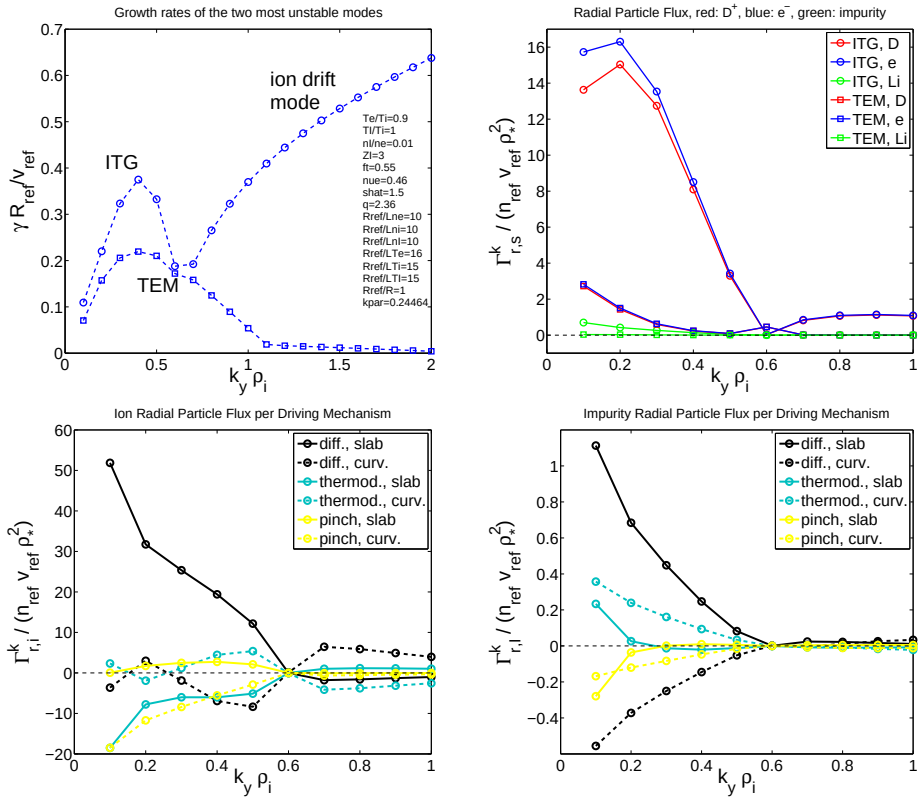

Figure 5.4: Fluid analysis at $t = 0.8$s with the reference $c_{\mathrm{Li}} = 0.01$ lithium concentration. Growth rates of the two most unstable modes (ITG and TEM, top left), total flux of the species driven by ITG and TE modes (top right), deuterium (bottom left) and lithium (bottom right) particle flux by slab (solid) and curvature (dashed) terms of the diffusive (black), thermo-diffusive (cyan) and pinch (yellow) contributions driven by ITG modes as a function of the bi-normal wavenumber.

spectrum. The total deuterium flux, as shown on the top right panel, driven by both ITG eigenmodes modes is still inward between $0.2 < k_{\mathrm{y}}\rho_{\mathrm{i}} < 0.6$, but the pinch is less pronounced than in the experimental case (figure 5.1). The bottom left and right panels show the deuterium flux distributed among the different channels, driven by the D-ITG and Li-ITG eigenmodes, respectively. The D-ITG modes produce a deuterium flux determined by the balance of the outward slab diffusive and inward slab thermo-diffusive and curvature pinch terms. The deuterium flux driven by the Li-ITG modes resemble in structure the $t = 0.8$s case with increased lithium concentration (figure 5.5): the slab diffusion and curvature pinch terms are directed inward while the curvature diffusion is outward. This indicates that the ITG eigenmode in figure 5.5 is indeed an Li-ITG dominated mode, as suggested

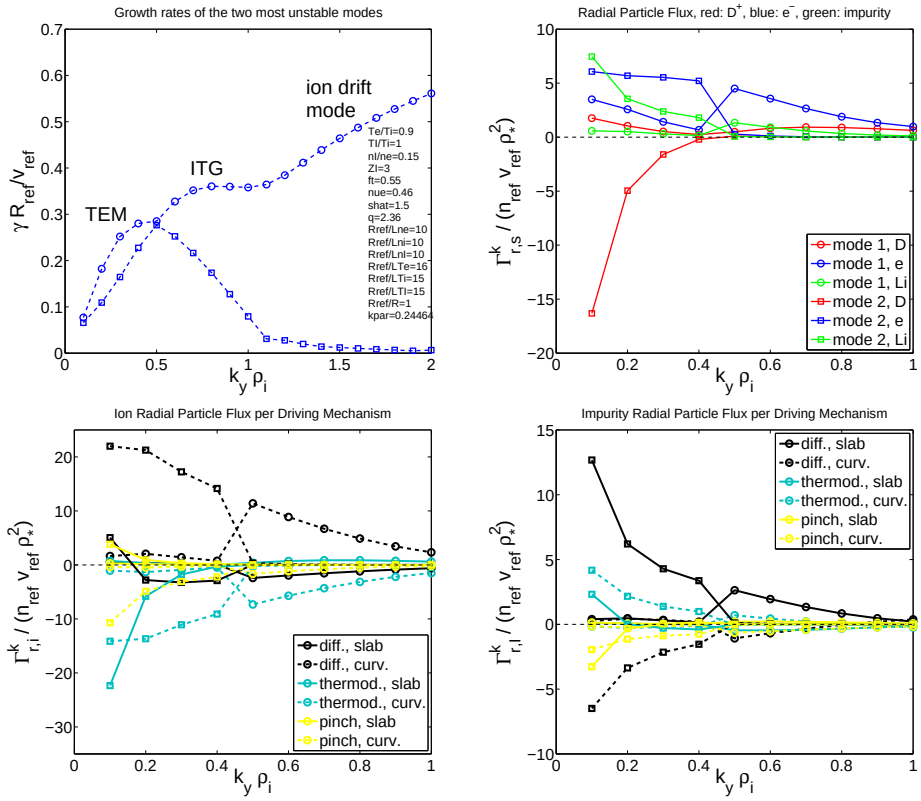

Figure 5.5: Fluid analysis at $t = 0.8$s with increased $c_{\mathrm{Li}} = 0.15$ lithium concentration. Growth rates of the two most unstable modes (ITG and TEM, top left), total flux of the species driven by ITG and TE modes (top right), deuterium (bottom left) and lithium (bottom right) particle flux by slab (solid) and curvature (dashed) terms of the diffusive (black), thermo-diffusive (cyan) and pinch (yellow) contributions driven by ITG modes as a function of the bi-normal wavenumber.

by the gyrokinetic results in figure 3.11. The lithium-ITG modes, whether or not distinguished from the D-ITG as a separate eigenmode, generate a phase difference between deuterium density and potential fluctuation in a way that it drives an inward flux. The lithium transport driven by both ITG modes is similar as observed in the previous cases.

The same effect can be achieved when the lithium impurities are replaced by carbon while keeping the same deuterium concentration (figure 5.7). The TE and electron drift modes appear to be more stable compared to the lithium case (figure 5.6) due to higher $Z_{\mathrm{eff}} = 3.25$, but the two ITG eigenmodes show similar behaviour in terms of both stability and transport.

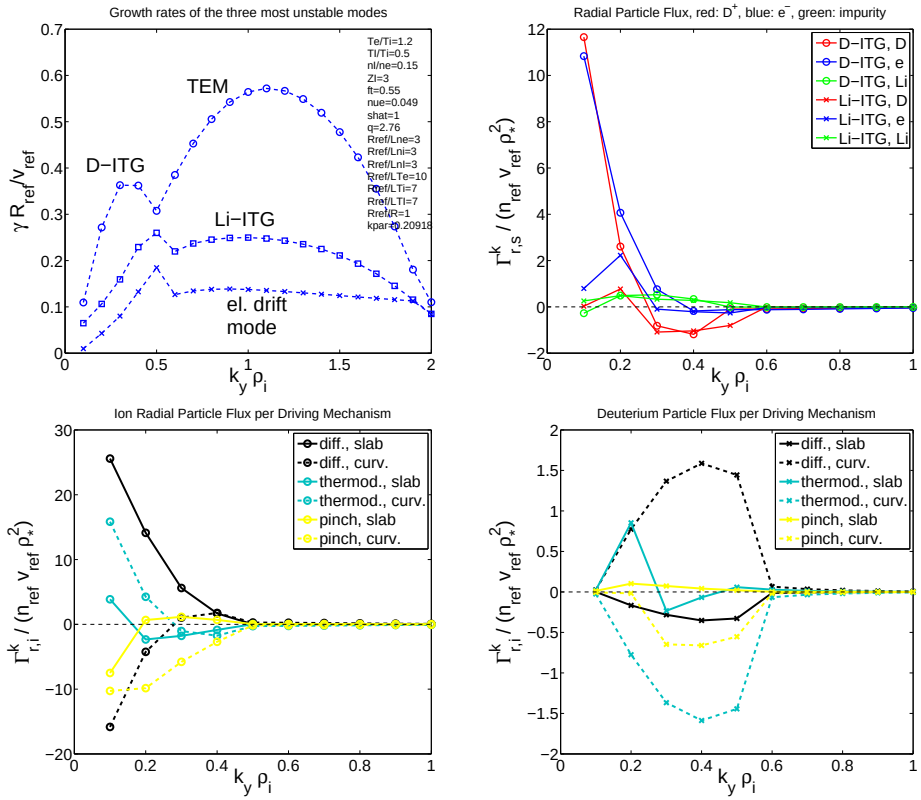

Figure 5.6: Fluid analysis at $t = 0.3$s with decreased $T_{\mathrm{Li}}/T_{\mathrm{D}} = 0.5$. Growth rates of the three most unstable modes (top left), total flux of the species driven by D-ITG and Li-ITG modes (top right), deuterium particle flux by slab (solid) and curvature (dashed) terms of the diffusive (black), thermo-diffusive (cyan) and pinch (yellow) contributions driven by D-ITG (bottom left) and Li-ITG (bottom right) modes as a function of the bi-normal wavenumber.

5.1.4 Reduced Impurity Density Gradient Case

The effect of the centrally peaked impurity density gradient is tested also in the fluid calculation. Figures 5.8 and 5.9 show plots with reduced but positive ($R_{\mathrm{ref}}/L_{\mathrm{n,Li}} = 1$) and with negative ($R_{\mathrm{ref}}/L_{\mathrm{n,Li}} = -1$) lithium density gradient. In both cases the diffusive part (both slab and curvature) of the impurity flux (bottom right) changes approximately proportionally with the prescribed density gradient, that is, the lithium behaves as if it was present only in trace amounts. The change in the other components of the impurity flux is small. Consequently, the overall outward flux of the lithium ions becomes reduced at $R_{\mathrm{ref}}/L_{\mathrm{n,Li}} = 1$, then turns inward at $R_{\mathrm{ref}}/L_{\mathrm{n,Li}} = -1$, which is qualitatively consistent with the gyrokinetic results (figure 3.6). The deuterium flux reacts with an increased diffusive and thermo-diffusive

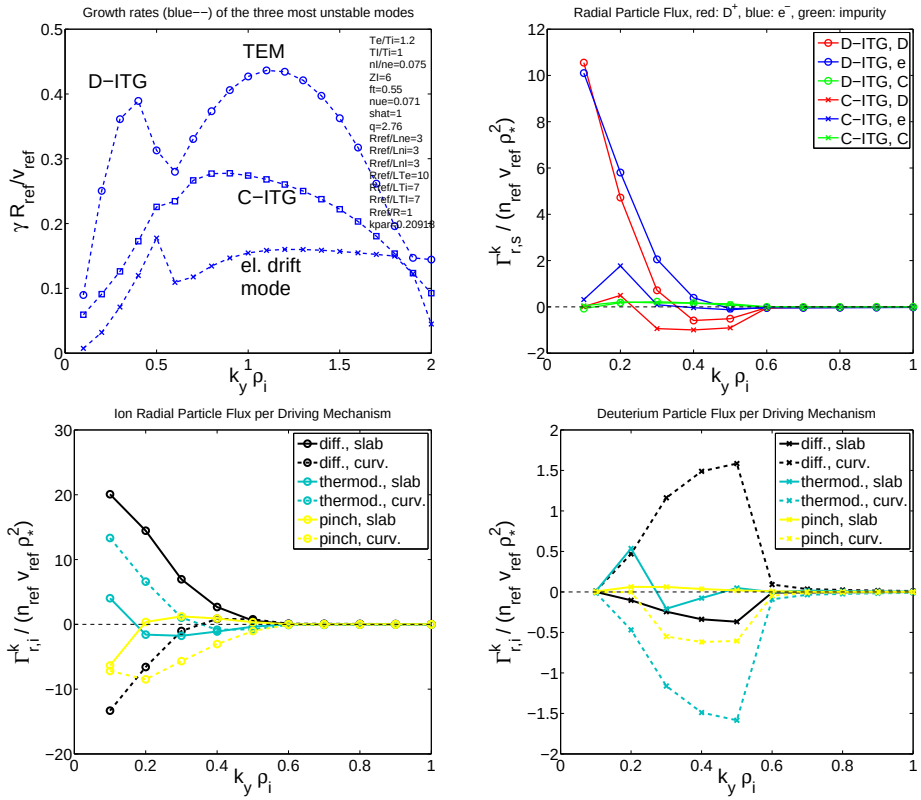

Figure 5.7: Fluid analysis at $t = 0.3$s with carbon impurities at constant deuterium dilution. Growth rates of the two most unstable modes (ITG and TEM, top left), total flux of the species driven by D-ITG and C-ITG modes (top right), deuterium particle flux by slab (solid) and curvature (dashed) terms of the diffusive (black), thermo-diffusive (cyan) and pinch (yellow) contributions driven by D-ITG (bottom left) and C-ITG (bottom right) modes as a function of the bi-normal wavenumber.

drive, while the pinch terms remain similar to the reference case. However, the curvature diffusive and thermo-diffusive parts still cancel, and the increase of the slab diffusive term is larger than that of the slab thermo-diffusion, leading to an overall outward deuterium flux.

5.1.5 A MAST-like Case

Although the fluid model does not contain all the physics required for the accurate modelling of particle transport in MAST, in this section the model is applied to analyse a MAST-like case. That is, we are still looking at an electro-static, circular plasma but the physical parameters are taken from the gyrokinetic analysis of the MAST discharge #24541 (table 3.4). Figure 5.10 shows the reference case with 5%

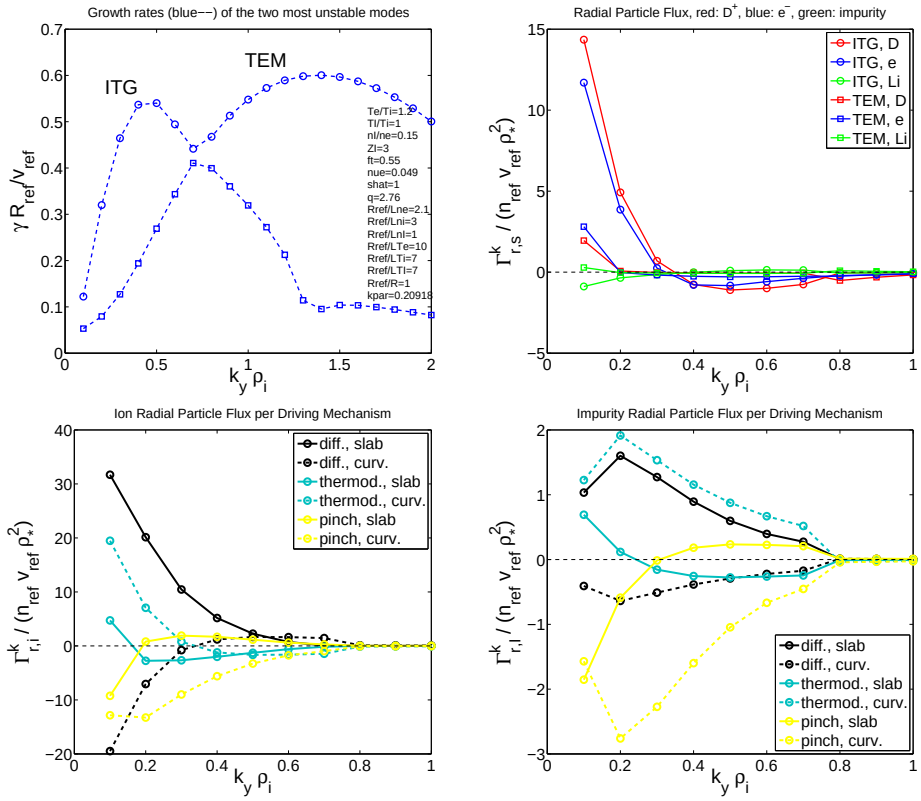

Figure 5.8: Fluid analysis at $t = 0.3$s with reduced lithium density gradient $R_{\rm ref}/L_{\rm n,Li} = 1$. Growth rates of the two most unstable modes (ITG and TEM, top left), total flux of the species driven by ITG and TE modes (top right), deuterium (bottom left) and lithium (bottom right) particle flux by slab (solid) and curvature (dashed) terms of the diffusive (black), thermo-diffusive (cyan) and pinch (yellow) contributions driven by ITG modes as a function of the bi-normal wavenumber.

carbon concentration in order to increase the effect of the impurity species. Compared with figure 3.22, a good qualitative agreement is found with the gyrokinetic result of the corresponding case. The locations of the main ITG peaks coincide, although the growth rate is consistently overestimated by the fluid model due to the lack of ion collisions. The presence of TE modes is also a common feature in the fluid results not observed in the gyrokinetic spectrum. However, the unstable modes around $k_{\rm y}\rho_{\rm i} \sim 1$ driven unstable by the carbon ITG are present in both models.

The direction of the particle fluxes predicted by the two models are also in agreement: the carbon pinch is accompanied by outward deuterium flow. The impurity flux is characterized by an inward diffusive contribution, but it is mainly driven by the inward pinch terms. The point at which the carbon flux changes sign

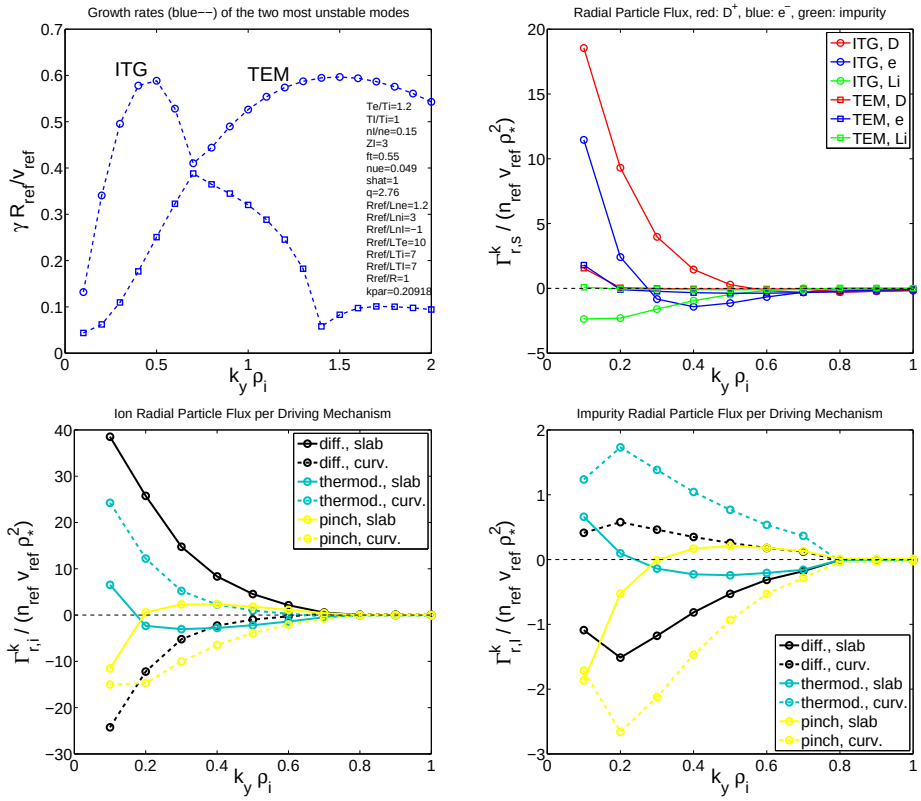

Figure 5.9: Fluid analysis at $t = 0.3$s with negative lithium density gradient $R_{\mathrm{ref}}/L_{\mathrm{n,Li}} = -1$. Growth rates of the two most unstable modes (ITG and TEM, top left), total flux of the species driven by ITG and TE modes (top right), deuterium (bottom left) and lithium (bottom right) particle flux by slab (solid) and curvature (dashed) terms of the diffusive (black), thermo-diffusive (cyan) and pinch (yellow) contributions driven by ITG modes as a function of the bi-normal wavenumber.

from negative to positive is $k_{\mathrm{y}}\rho_{\mathrm{i}} \approx 0.4$ in both cases.

If the carbon density gradient is set to positive, i.e. a centrally peaked profile is assumed (figure 5.11), the main difference again occurs in the impurity diffusive term: both the slab and curvature diffusion changes approximately proportionally with the carbon density gradient, driving the impurities more towards the edge. However, in contrast with the lithium case, the effect of carbon ions on the deuterium flux is weak, and the outward deuterium flow remains.

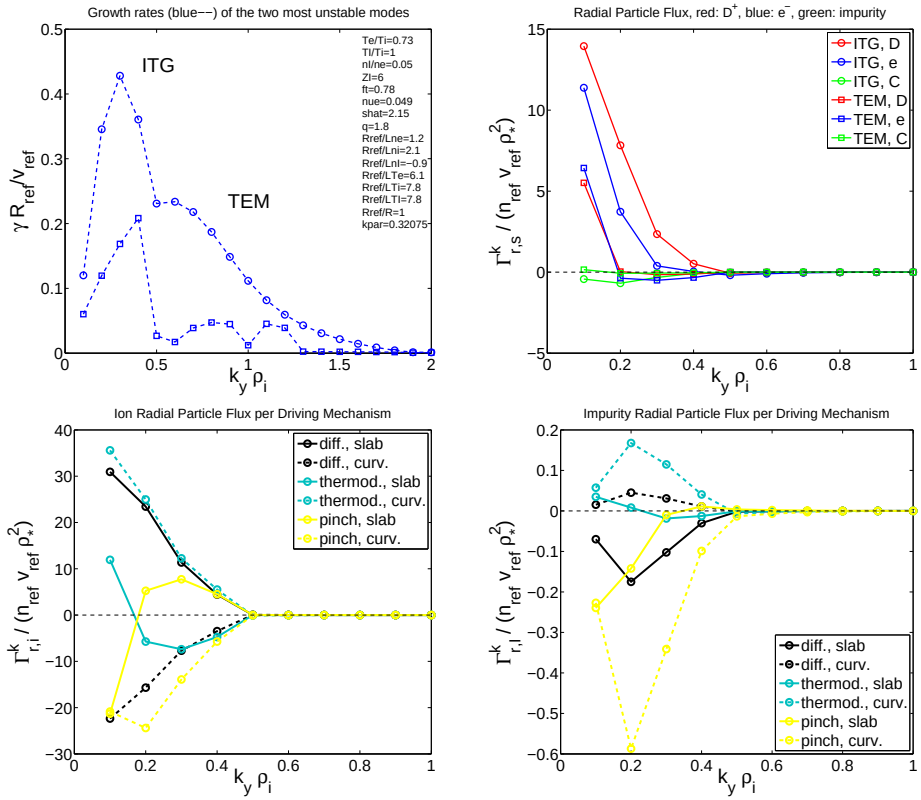

Figure 5.10: Fluid analysis of a MAST-like case with carbon concentration of $c_C = 0.05$. Growth rates of the two most unstable modes (ITG and TEM, top left), total flux of the species driven by ITG and TE modes (top right), deuterium (bottom left) and lithium (bottom right) particle flux by slab (solid) and curvature (dashed) terms of the diffusive (black), thermo-diffusive (cyan) and pinch (yellow) contributions driven by ITG modes as a function of the bi-normal wavenumber.

5.2 Summary of the Chapter

In this chapter the microstability and transport analysis of the FTU #30582 discharge with a Weiland-type fluid model has been presented. The stability of the ITG modes show good agreement with the gyrokinetic results, and the direction of the particle flux driven by the ITG modes is also accurately captured. The growth rate of the TE modes is systematically overestimated due to the $1/k_y$ scaling of the simplified electron collision operator.

Separating the particle flux into diffusive, thermo-diffusive and pinch terms as well as slab and curvature related parts shows that in presence of a centrally peaked lithium profile the deuterium transport is driven inward, against the density gradient, primarily by the curvature pinch. Reducing the lithium concentration is

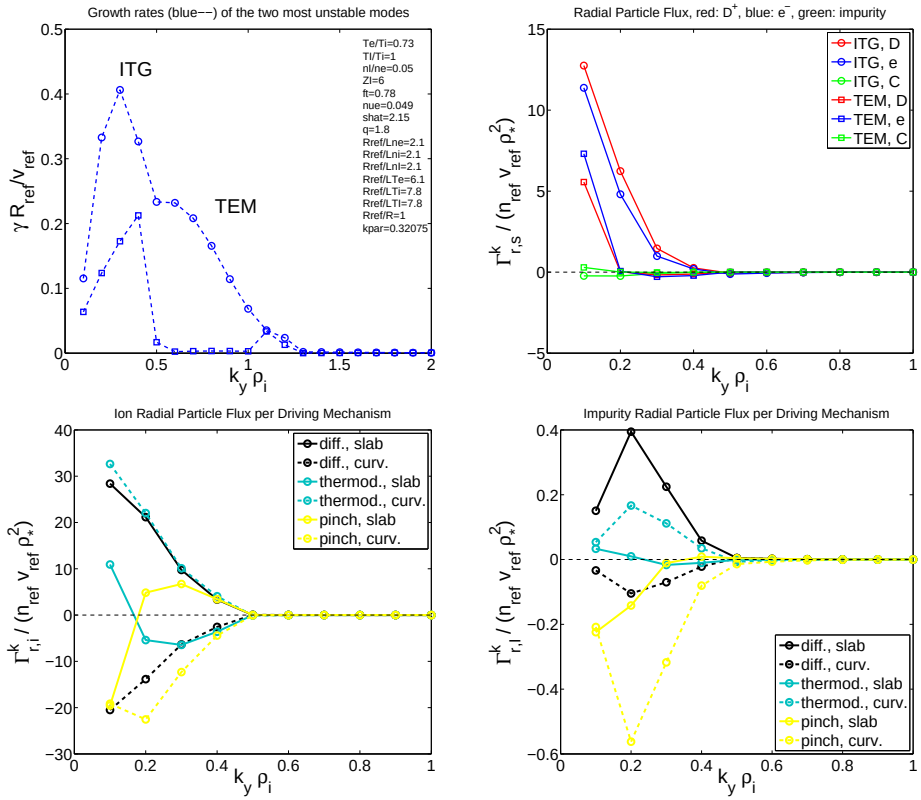

Figure 5.11: Fluid analysis of a MAST-like case with carbon concentration of $c_C = 0.05$ and a centrally peaked impurity density profile. Growth rates of the two most unstable modes (ITG and TEM, top left), total flux of the species driven by ITG and TE modes (top right), deuterium (bottom left) and lithium (bottom right) particle flux by slab (solid) and curvature (dashed) terms of the diffusive (black), thermo-diffusive (cyan) and pinch (yellow) contributions driven by ITG modes as a function of the bi-normal wavenumber.

accompanied by a relative increase of the outward slab diffusive contribution to the deuterium transport.

Despite its high concentration in the density ramp-up phase, the lithium has been found to act like trace impurity species when varying its density gradient value. That is, the diffusive part of the lithium flux (both slab and curvature) changes proportionally with $R_{\mathrm{ref}}/L_{\mathrm{n,Li}}$, while the other components are weakly affected. When reducing the lithium density gradient, and thus its outward flux, the deuterium flux reacts by a relative increase of the diffusive transport again.

Two separate eigenmodes for the deuterium-ITG and lithium-ITG modes could be obtained when the relative impurity temperature, and thus the lithium Larmor-radius, has been reduced. In this case the overall outward lithium and the

inward deuterium flux have both been found less pronounced. The same effect is observed when the lithium is replaced by carbon impurities. The detailed analysis of the particle transport shows that when the lithium-ITG eigenmode appears it is characterized by inward deuterium slab diffusive and outward curvature diffusive terms, in contrast with the typical pattern of the deuterium-ITG eigenmodes. Even when the two ITG eigenmodes are not separated, and appear as a mixed eigenmode, the effect of the impurities on the deuterium flux is analogous: the slab diffusive term is reduced.

The analysis of a MAST-like case shows that the main features of the ITG growth rates and fluxes, as obtained with gyrokinetic simulations, can be captured with the fluid model despite its obvious shortcomings in accurately modelling geometrical and electro-magnetic effects. This indicates that the observed separation of the ion flow is not strongly influenced by these mechanisms, it is mostly determined by the densities, temperatures and gradients of the species.

Chapter 6

Conclusions

In this thesis the particle transport properties of light impurity seeded core tokamak plasmas have been investigated. The main motivation of this work was provided by the Liquid Lithium Limiter experiments in the FTU tokamak, in which a significantly improved electron density peaking was consistently observed. Analysis of a low-beta FTU-LLL discharge and a high-beta MAST discharge has been presented in order to assess the electro-magnetic effects on particle transport.

A local gyrokinetic analysis of an FTU-LLL discharge during the density ramp-up and density plateau phases in the high gradient region of the plasma core (approximately mid-radius) has been performed. The simulations confirm that the large lithium concentration has a major impact on the linear spectrum of the turbulence and the associated anomalous particle transport. In a mainly electro-static, ITG dominated turbulence the electron response remains close to adiabatic. The electron flux thus becomes small compared to the ion fluxes, enabling the ions to flow in opposite direction in order to maintain quasi-neutrality. This has not been observed when tritium was used instead of lithium, due to the similar dynamics of the deuterium and tritium species. However, with any other impurities heavier than tritium the ion flow separation occurs. In order to obtain an inward deuterium (and/or tritium) transport, the outward drive of the impurity flux must be stronger than that of the main ion species. This can be achieved by sufficiently high impurity concentration and density gradient, which conditions are satisfied during the density ramp-up phase of the analysed FTU-LLL discharge.

These features of the turbulent particle transport in a lithiated FTU plasma indicate a better confinement of the deuterium and electron species, improved even further by the relatively strong Ware-pinch contribution. Since the turbulent transport is likely to be quenched deeper in the core plasma due to the weaker drive of the drift-instabilities, the reduced electron flux is expected to lead to a more peaked

density profile. However, since the gyrokinetic analysis is local, no quantitative prediction regarding the profile evolution of the species can be made.

Gyrokinetic simulations of an H-mode MAST discharge have also been performed in order to provide inter-machine comparison of the effect of impurities, and to assess the role of magnetic perturbations on particle transport. Although both an inward and outward impurity flux has been observed in the simulations both in ITG and KBM dominated turbulence depending mainly on the direction of the impurity density gradient, this has not been followed by an ion flow separation as in the FTU analysis. The deuterium flux has consistently been found to be inward. This is attributed to the fact that, although the electro-magnetic perturbations provide negligible contribution to the ion transport, they drive a strong non-adiabatic electron response.

The fluid analysis of the FTU-LLL experiment provided information regarding the distribution of the particle transport between the diffusive, thermo-diffusive and pinch channels. It has been found that the lithium behaves as trace species despite its high concentration in the plasma. That is, the diffusive part of the lithium transport changes approximately proportionally with the lithium density gradient, while the other contributions to the flux remain unaffected by the changes in $R_{\mathrm{ref}}/L_{\mathrm{n,Li}}$. In every case when an inward deuterium flux is enforced by an outward lithium transport, it is mainly the outward diffusive term of the deuterium flux that responds by taking a reduced value. In the reference case only one unstable eigenmode is found rotating in the ion diamagnetic direction. However, separate deuterium-ITG and lithium-ITG eigenmodes can be obtained by decreasing the relative lithium temperature and thus separating the typical spatial scale of the two modes from each other. A similar splitting of the modes is achieved with carbon impurities. When the Larmor-radii of the two ion species are further apart, the impact of the impurities on the main ion transport is weaker. However, the impurity-ITG mode still drives an inward deuterium flux and it is characterized by an inward slab diffusive contribution.

The described mechanism driving inward deuterium transport during the ramp-up phase of the discharge is not a collisional effect. It has been observed in simulations with reduced collisionality, and not been observed in clean plasma with increased Z_{eff} to model the effect of higher collisionality. Furthermore, collisions provide an outward contribution in and ITG driven turbulent flux for all the species. This indicates that light impurity seeding during the startup of a discharge might lead to improved deuterium and tritium density peaking also in higher temperature tokamak experiments.

Appendix A

Integrals Involving Products of Bessel Functions

The following three types of integrals involving products of Bessel functions, exponential and algebraic terms appear in the derivation of the gyrocentre Maxwell's equations:

$$1. \quad \int_0^\infty J_0^2(\lambda)\mathrm{e}^{-\frac{\mu B_0}{T}}\mathrm{d}\mu \tag{A.1}$$

$$2. \quad \int_0^\infty \mu J_0(\lambda)\hat{J}_1(\lambda)\mathrm{e}^{-\frac{\mu B_0}{T}}\mathrm{d}\mu \tag{A.2}$$

$$3. \quad \int_0^\infty \mu^2 \hat{J}_1^2(\lambda)\mathrm{e}^{-\frac{\mu B_0}{T}}\mathrm{d}\mu \tag{A.3}$$

where $\hat{J}_1(\lambda) = \frac{2}{\lambda}J_1(\lambda)$. In all three cases the new variable $x = \frac{\mu B_0}{T}$ is introduced according to Dannert [30], which also leads to $\lambda = \sqrt{2xb}$ where $b = -\rho_{th}^2\nabla_\perp^2$. The Jacobian is simply $\frac{T}{B_0}$ and the integrals can be written as

$$1. \quad \frac{T}{B_0}\int_0^\infty J_0^2(\sqrt{2xb})\mathrm{e}^{-x}\mathrm{d}x$$

$$2. \quad \frac{T^2}{B_0^2}\frac{2}{\sqrt{2b}}\int_0^\infty \sqrt{x}J_0(\sqrt{2xb})J_1(\sqrt{2xb})\mathrm{e}^{-x}\mathrm{d}x$$

$$3. \quad \frac{T^3}{B_0^3}\frac{2}{b}\int_0^\infty xJ_1^2(\lambda)\mathrm{e}^{-\frac{\mu B_0}{T}}\mathrm{d}x.$$

The first integral can be solved using the formula 6.615 on page 710 of [86]:

$$\int_0^\infty \mathrm{e}^{-\alpha x} J_\nu(2\beta\sqrt{x}) J_{nu}(2\gamma\sqrt{x})\mathrm{d}x = \frac{1}{\alpha} I_\nu\left(\frac{2\beta\gamma}{\alpha}\right) \mathrm{e}^{-\frac{\beta^2+\gamma^2}{\alpha^2}}$$

which immedately gives

$$1. \qquad \frac{T}{B_0}\int_0^\infty J_0^2(\sqrt{2xb})\mathrm{e}^{-x}\mathrm{d}x = I_0(b)\mathrm{e}^{-b}.$$

In the two remaining integrals let us use the new variable $y = \sqrt{2bx}$. The Jacobian is $\frac{y}{b}$ and therefore it leads to

$$2. \qquad \frac{T^2}{B_0^2}\frac{2}{\sqrt{2b}}\int_0^\infty \sqrt{x} J_0(\sqrt{2xb}) J_1(\sqrt{2xb})\mathrm{e}^{-x}\mathrm{d}x = \frac{T^2}{B_0^2}\frac{1}{b^2}\int_0^\infty y^2 J_0(y) J_1(y)\mathrm{e}^{-hy^2}\mathrm{d}y$$

$$3. \qquad \frac{T^3}{B_0^3}\frac{2}{b}\int_0^\infty x J_1^2(\lambda)\mathrm{e}^{-\frac{\mu B_0}{T}}\mathrm{d}\mu = \frac{T^3}{B_0^3}\frac{1}{b^3}\int_0^\infty y^3 J_1^2(y)\mathrm{e}^{-hy^2}\mathrm{d}y$$

where $h = \frac{1}{2b}$ was used in the exponentials.

The second integral (leaving the prefactors for now) can be further written as

$$\begin{aligned}
\int_0^\infty y^2 J_0(y) J_1(y)\mathrm{e}^{-hy^2}\mathrm{d}y &= \frac{\partial}{\partial h}\left(-\int_0^\infty \mathrm{e}^{-hy^2} J_0(y) J_1(y)\right)\mathrm{d}y \\
&= \frac{1}{2}\frac{\partial}{\partial h}\left(\int_0^\infty \mathrm{e}^{-hy^2}\frac{\mathrm{d}}{\mathrm{d}y}\left(J_0^2(y)\right)\right)\mathrm{d}y \\
&= \frac{1}{2}\frac{\partial}{\partial h}\left(\underbrace{\left[J_0^2(y)\mathrm{e}^{-hy^2}\right]_0^\infty}_{1} + 2h\int_0^\infty J_0^2(y) y \mathrm{e}^{-hy^2}\mathrm{d}y\right)
\end{aligned}$$

where the relation $\frac{\mathrm{d}J_0(y)}{\mathrm{d}y} = -J_1(y)$ was applied (see [39]). The integral can be found in [87] on page 395 and it gives

$$\int_0^\infty y J_0^2(y)\mathrm{e}^{-hy^2}\mathrm{d}y = \frac{1}{2h}\mathrm{e}^{-\frac{1}{2h}} I_0\left(\frac{1}{2h}\right). \tag{A.4}$$

Taking the derivative with respect to h and using the identity $\frac{\mathrm{d}I_0(z)}{\mathrm{d}z} = I_1(z)$ results

$$\begin{aligned}\int_0^\infty y^2 J_0(y) J_1(y) \mathrm{e}^{-hy^2} \mathrm{d}y &= \frac{1}{4h^2} \mathrm{e}^{-\frac{1}{2h}} \left(I_0\left(\frac{1}{2h}\right) - I_1\left(\frac{1}{2h}\right)\right) \\ &= b^2 \mathrm{e}^{-b} \left(I_0(b) - I_1(b)\right). \end{aligned} \tag{A.5}$$

And with the prefactors:

$$2. \quad \int_0^\infty \mu J_0(\lambda) \hat{J}_1(\lambda) \mathrm{e}^{-\frac{\mu B_0}{T}} \mathrm{d}\mu = \frac{T^2}{B_0^2} \mathrm{e}^{-b} \left(I_0(b) - I_1(b)\right). \tag{A.6}$$

The third integral (without the prefactors) is integrated by parts first to get

$$\begin{aligned}\int_0^\infty y^3 J_1^2(y) \mathrm{e}^{-hy^2} \mathrm{d}y &= -\frac{1}{2h} \int_0^\infty (-2hy) \mathrm{e}^{-hy^2} y^2 J_1(y) \mathrm{d}y \\ &= -\frac{1}{2h} \left(\underbrace{\left[\mathrm{e}^{-hy^2} y^2 J_1^2(y)\right]_0^\infty}_{0} - 2 \int_0^\infty \mathrm{e}^{-hy^2} \left(y J_1^2(y) + y^2 J_1(y) \frac{\mathrm{d}J_1(y)}{\mathrm{d}y} \right) \right). \end{aligned}$$

Using the relation $\frac{\mathrm{d}J_1(y)}{\mathrm{d}y} = J_0(y) - \frac{1}{y} J_1(y)$ (see [39]) two of the terms cancel out and the integral simplifies to

$$\int_0^\infty y^3 J_1^2(y) \mathrm{e}^{-hy^2} \mathrm{d}y = \frac{1}{h} \int_0^\infty y^2 J_0(y) J_1(y) \mathrm{e}^{-hy^2} \mathrm{d}y.$$

Using equation (A.5) the third integral can be written as

$$\int_0^\infty y^3 J_1^2(y) \mathrm{e}^{-hy^2} \mathrm{d}y = 2b^3 \mathrm{e}^{-b} \left(I_0(b) - I_1(b)\right) \tag{A.7}$$

and with prefactors:

$$3. \quad \int_0^\infty \mu^2 \hat{J}_1^2(\lambda) \mathrm{e}^{-\frac{\mu B_0}{T}} \mathrm{d}\mu = \frac{T^3}{B_0^3} 2\mathrm{e}^{-b} \left(I_0(b) - I_1(b)\right). \tag{A.8}$$

Appendix B

Coefficients of the Dispersion Relation Polynomial

B.1 9th Degree Coefficients

$$
\begin{aligned}
c_9 \;=\; & \frac{Z_{\mathrm{i}}^2 n_{\mathrm{i,N}}}{T_{\mathrm{i,N}}}(A_{3\mathrm{i}}B_{3\mathrm{I}}B_{3\mathrm{e}}) + \frac{Z_{\mathrm{I}}^2 n_{\mathrm{I,N}}}{T_{\mathrm{I,N}}}(A_{3\mathrm{I}}B_{3\mathrm{i}}B_{3\mathrm{e}}) + \\
& \frac{Z_{\mathrm{e}}^2 n_{\mathrm{e,N}} f_{\mathrm{t}}}{T_{\mathrm{e,N}}}(A_{3\mathrm{e}}B_{3\mathrm{I}}B_{3\mathrm{i}}) + \frac{Z_{\mathrm{e}}^2 n_{\mathrm{e,N}}(1-f_{\mathrm{t}})}{T_{\mathrm{e,N}}}(B_{3\mathrm{e}}B_{3\mathrm{I}}B_{3\mathrm{i}})
\end{aligned}
$$

$$
\begin{aligned}
c_8 \;=\; & \frac{Z_{\mathrm{i}}^2 n_{\mathrm{i,N}}}{T_{\mathrm{i,N}}}(A_{3\mathrm{i}}B_{3\mathrm{I}}B_{2\mathrm{e}} + A_{3\mathrm{i}}B_{2\mathrm{I}}B_{3\mathrm{e}} + A_{2\mathrm{i}}B_{3\mathrm{I}}B_{3\mathrm{e}}) + \\
& \frac{Z_{\mathrm{I}}^2 n_{\mathrm{I,N}}}{T_{\mathrm{I,N}}}(A_{3\mathrm{I}}B_{3\mathrm{i}}B_{2\mathrm{e}} + A_{3\mathrm{I}}B_{2\mathrm{i}}B_{3\mathrm{e}} + A_{2\mathrm{I}}B_{3\mathrm{i}}B_{3\mathrm{e}}) + \\
& \frac{Z_{\mathrm{e}}^2 n_{\mathrm{e,N}} f_{\mathrm{t}}}{T_{\mathrm{e,N}}}(A_{3\mathrm{e}}B_{3\mathrm{I}}B_{2\mathrm{i}} + A_{3\mathrm{e}}B_{2\mathrm{I}}B_{3\mathrm{i}} + A_{2\mathrm{e}}B_{3\mathrm{I}}B_{3\mathrm{i}}) + \\
& \frac{Z_{\mathrm{e}}^2 n_{\mathrm{e,N}}(1-f_{\mathrm{t}})}{T_{\mathrm{e,N}}}(B_{3\mathrm{e}}B_{3\mathrm{I}}B_{2\mathrm{i}} + B_{3\mathrm{e}}B_{2\mathrm{I}}B_{3\mathrm{i}} + B_{2\mathrm{e}}B_{3\mathrm{I}}B_{3\mathrm{i}})
\end{aligned}
$$

$$
\begin{aligned}
c_7 \;=\;& \frac{Z_{\mathrm{i}}^2 n_{\mathrm{i,N}}}{T_{\mathrm{i,N}}}(A_{3\mathrm{i}}B_{3\mathrm{I}}B_{1\mathrm{e}} + A_{3\mathrm{i}}B_{1\mathrm{I}}B_{3\mathrm{e}} + A_{1\mathrm{i}}B_{3\mathrm{I}}B_{3\mathrm{e}} + A_{3\mathrm{i}}B_{2\mathrm{I}}B_{2\mathrm{e}} + A_{2\mathrm{i}}B_{3\mathrm{I}}B_{2\mathrm{e}} + A_{2\mathrm{i}}B_{2\mathrm{I}}B_{3\mathrm{e}}) + \\
& \frac{Z_{\mathrm{I}}^2 n_{\mathrm{I,N}}}{T_{\mathrm{I,N}}}(A_{3\mathrm{I}}B_{3\mathrm{i}}B_{1\mathrm{e}} + A_{3\mathrm{I}}B_{1\mathrm{i}}B_{3\mathrm{e}} + A_{1\mathrm{I}}B_{3\mathrm{i}}B_{3\mathrm{e}} + A_{3\mathrm{I}}B_{2\mathrm{i}}B_{2\mathrm{e}} + A_{2\mathrm{I}}B_{3\mathrm{i}}B_{2\mathrm{e}} + A_{2\mathrm{I}}B_{2\mathrm{i}}B_{3\mathrm{e}}) + \\
& \frac{Z_{\mathrm{e}}^2 n_{\mathrm{e,N}} f_{\mathrm{t}}}{T_{\mathrm{e,N}}}(A_{3\mathrm{e}}B_{3\mathrm{I}}B_{1\mathrm{i}} + A_{3\mathrm{e}}B_{1\mathrm{I}}B_{3\mathrm{i}} + A_{1\mathrm{e}}B_{3\mathrm{I}}B_{3\mathrm{i}} + A_{3\mathrm{e}}B_{2\mathrm{I}}B_{2\mathrm{i}} + A_{2\mathrm{e}}B_{3\mathrm{I}}B_{2\mathrm{i}} + A_{2\mathrm{e}}B_{2\mathrm{I}}B_{3\mathrm{i}}) + \\
& \frac{Z_{\mathrm{e}}^2 n_{\mathrm{e,N}} (1-f_{\mathrm{t}})}{T_{\mathrm{e,N}}}(B_{3\mathrm{e}}B_{3\mathrm{I}}B_{1\mathrm{i}} + B_{3\mathrm{e}}B_{1\mathrm{I}}B_{3\mathrm{i}} + B_{1\mathrm{e}}B_{3\mathrm{I}}B_{3\mathrm{i}} + B_{3\mathrm{e}}B_{2\mathrm{I}}B_{2\mathrm{i}} + B_{2\mathrm{e}}B_{3\mathrm{I}}B_{2\mathrm{i}} + B_{2\mathrm{e}}B_{2\mathrm{I}}B_{3\mathrm{i}})
\end{aligned}
$$

$$
\begin{aligned}
c_6 \;=\;& \frac{Z_{\mathrm{i}}^2 n_{\mathrm{i,N}}}{T_{\mathrm{i,N}}}(A_{3\mathrm{i}}B_{3\mathrm{I}}B_{0\mathrm{e}} + A_{3\mathrm{i}}B_{0\mathrm{I}}B_{3\mathrm{e}} + A_{0\mathrm{i}}B_{3\mathrm{I}}B_{3\mathrm{e}} + A_{3\mathrm{i}}B_{2\mathrm{I}}B_{1\mathrm{e}} + A_{3\mathrm{i}}B_{1\mathrm{I}}B_{2\mathrm{e}} + \\
& A_{2\mathrm{i}}B_{3\mathrm{I}}B_{1\mathrm{e}} + A_{1\mathrm{i}}B_{3\mathrm{I}}B_{2\mathrm{e}} + A_{2\mathrm{i}}B_{1\mathrm{I}}B_{3\mathrm{e}} + A_{1\mathrm{i}}B_{2\mathrm{I}}B_{3\mathrm{e}} + A_{2\mathrm{i}}B_{2\mathrm{I}}B_{2\mathrm{e}}) + \\
& \frac{Z_{\mathrm{I}}^2 n_{\mathrm{I,N}}}{T_{\mathrm{I,N}}}(A_{3\mathrm{I}}B_{3\mathrm{i}}B_{0\mathrm{e}} + A_{3\mathrm{I}}B_{0\mathrm{i}}B_{3\mathrm{e}} + A_{0\mathrm{I}}B_{3\mathrm{i}}B_{3\mathrm{e}} + A_{3\mathrm{I}}B_{2\mathrm{i}}B_{1\mathrm{e}} + A_{3\mathrm{I}}B_{1\mathrm{i}}B_{2\mathrm{e}} + \\
& A_{2\mathrm{I}}B_{3\mathrm{i}}B_{1\mathrm{e}} + A_{1\mathrm{I}}B_{3\mathrm{i}}B_{2\mathrm{e}} + A_{2\mathrm{I}}B_{1\mathrm{i}}B_{3\mathrm{e}} + A_{1\mathrm{I}}B_{2\mathrm{i}}B_{3\mathrm{e}} + A_{2\mathrm{I}}B_{2\mathrm{i}}B_{2\mathrm{e}}) + \\
& \frac{Z_{\mathrm{e}}^2 n_{\mathrm{e,N}} f_{\mathrm{t}}}{T_{\mathrm{e,N}}}(A_{3\mathrm{e}}B_{3\mathrm{I}}B_{0\mathrm{i}} + A_{3\mathrm{e}}B_{0\mathrm{I}}B_{3\mathrm{i}} + A_{0\mathrm{e}}B_{3\mathrm{I}}B_{3\mathrm{i}} + A_{3\mathrm{e}}B_{2\mathrm{I}}B_{1\mathrm{i}} + A_{3\mathrm{e}}B_{1\mathrm{I}}B_{2\mathrm{i}} + \\
& A_{2\mathrm{e}}B_{3\mathrm{I}}B_{1\mathrm{i}} + A_{1\mathrm{e}}B_{3\mathrm{I}}B_{2\mathrm{i}} + A_{2\mathrm{e}}B_{1\mathrm{I}}B_{3\mathrm{i}} + A_{1\mathrm{e}}B_{2\mathrm{I}}B_{3\mathrm{i}} + A_{2\mathrm{e}}B_{2\mathrm{I}}B_{2\mathrm{i}}) + \\
& \frac{Z_{\mathrm{e}}^2 n_{\mathrm{e,N}} (1-f_{\mathrm{t}})}{T_{\mathrm{e,N}}}(B_{3\mathrm{e}}B_{3\mathrm{I}}B_{0\mathrm{i}} + B_{3\mathrm{e}}B_{0\mathrm{I}}B_{3\mathrm{i}} + B_{0\mathrm{e}}B_{3\mathrm{I}}B_{3\mathrm{i}} + B_{3\mathrm{e}}B_{2\mathrm{I}}B_{1\mathrm{i}} + B_{3\mathrm{e}}B_{1\mathrm{I}}B_{2\mathrm{i}} + \\
& B_{2\mathrm{e}}B_{3\mathrm{I}}B_{1\mathrm{i}} + B_{1\mathrm{e}}B_{3\mathrm{I}}B_{2\mathrm{i}} + B_{2\mathrm{e}}B_{1\mathrm{I}}B_{3\mathrm{i}} + B_{1\mathrm{e}}B_{2\mathrm{I}}B_{3\mathrm{i}} + B_{2\mathrm{e}}B_{2\mathrm{I}}B_{2\mathrm{i}})
\end{aligned}
$$

$$
\begin{aligned}
c_5 \;=\;& \frac{Z_{\mathrm{i}}^2 n_{\mathrm{i,N}}}{T_{\mathrm{i,N}}}(A_{3\mathrm{i}}B_{2\mathrm{I}}B_{0\mathrm{e}} + A_{3\mathrm{i}}B_{0\mathrm{I}}B_{2\mathrm{e}} + A_{2\mathrm{i}}B_{3\mathrm{I}}B_{0\mathrm{e}} + A_{0\mathrm{i}}B_{3\mathrm{I}}B_{2\mathrm{e}} + A_{2\mathrm{i}}B_{0\mathrm{I}}B_{3\mathrm{e}} + A_{0\mathrm{i}}B_{2\mathrm{I}}B_{3\mathrm{e}} + \\
& A_{3\mathrm{i}}B_{1\mathrm{I}}B_{1\mathrm{e}} + A_{1\mathrm{i}}B_{3\mathrm{I}}B_{1\mathrm{e}} + A_{1\mathrm{i}}B_{1\mathrm{I}}B_{3\mathrm{e}} + A_{2\mathrm{i}}B_{2\mathrm{I}}B_{1\mathrm{e}} + A_{2\mathrm{i}}B_{1\mathrm{I}}B_{2\mathrm{e}} + A_{1\mathrm{i}}B_{2\mathrm{I}}B_{2\mathrm{e}}) + \\
& \frac{Z_{\mathrm{I}}^2 n_{\mathrm{I,N}}}{T_{\mathrm{I,N}}}(A_{3\mathrm{I}}B_{2\mathrm{i}}B_{0\mathrm{e}} + A_{3\mathrm{I}}B_{0\mathrm{i}}B_{2\mathrm{e}} + A_{2\mathrm{I}}B_{3\mathrm{i}}B_{0\mathrm{e}} + A_{0\mathrm{I}}B_{3\mathrm{i}}B_{2\mathrm{e}} + A_{2\mathrm{I}}B_{0\mathrm{i}}B_{3\mathrm{e}} + A_{0\mathrm{I}}B_{2\mathrm{i}}B_{3\mathrm{e}} + \\
& A_{3\mathrm{I}}B_{1\mathrm{i}}B_{1\mathrm{e}} + A_{1\mathrm{I}}B_{3\mathrm{i}}B_{1\mathrm{e}} + A_{1\mathrm{I}}B_{1\mathrm{i}}B_{3\mathrm{e}} + A_{2\mathrm{I}}B_{2\mathrm{i}}B_{1\mathrm{e}} + A_{2\mathrm{I}}B_{1\mathrm{i}}B_{2\mathrm{e}} + A_{1\mathrm{I}}B_{2\mathrm{i}}B_{2\mathrm{e}}) + \\
& \frac{Z_{\mathrm{e}}^2 n_{\mathrm{e,N}} f_{\mathrm{t}}}{T_{\mathrm{e,N}}}(A_{3\mathrm{e}}B_{2\mathrm{I}}B_{0\mathrm{i}} + A_{3\mathrm{e}}B_{0\mathrm{I}}B_{2\mathrm{i}} + A_{2\mathrm{e}}B_{3\mathrm{I}}B_{0\mathrm{i}} + A_{0\mathrm{e}}B_{3\mathrm{I}}B_{2\mathrm{i}} + A_{2\mathrm{e}}B_{0\mathrm{I}}B_{3\mathrm{i}} + A_{0\mathrm{e}}B_{2\mathrm{I}}B_{3\mathrm{i}} + \\
& A_{3\mathrm{e}}B_{1\mathrm{I}}B_{1\mathrm{i}} + A_{1\mathrm{e}}B_{3\mathrm{I}}B_{1\mathrm{i}} + A_{1\mathrm{e}}B_{1\mathrm{I}}B_{3\mathrm{i}} + A_{2\mathrm{e}}B_{2\mathrm{I}}B_{1\mathrm{i}} + A_{2\mathrm{e}}B_{1\mathrm{I}}B_{2\mathrm{i}} + A_{1\mathrm{e}}B_{2\mathrm{I}}B_{2\mathrm{i}}) + \\
& \frac{Z_{\mathrm{e}}^2 n_{\mathrm{e,N}} (1-f_{\mathrm{t}})}{T_{\mathrm{e,N}}}(B_{3\mathrm{e}}B_{2\mathrm{I}}B_{0\mathrm{i}} + B_{3\mathrm{e}}B_{0\mathrm{I}}B_{2\mathrm{i}} + B_{2\mathrm{e}}B_{3\mathrm{I}}B_{0\mathrm{i}} + B_{0\mathrm{e}}B_{3\mathrm{I}}B_{2\mathrm{i}} + B_{2\mathrm{e}}B_{0\mathrm{I}}B_{3\mathrm{i}} + B_{0\mathrm{e}}B_{2\mathrm{I}}B_{3\mathrm{i}} + \\
& B_{3\mathrm{e}}B_{1\mathrm{I}}B_{1\mathrm{i}} + B_{1\mathrm{e}}B_{3\mathrm{I}}B_{1\mathrm{i}} + B_{1\mathrm{e}}B_{1\mathrm{I}}B_{3\mathrm{i}} + B_{2\mathrm{e}}B_{2\mathrm{I}}B_{1\mathrm{i}} + B_{2\mathrm{e}}B_{1\mathrm{I}}B_{2\mathrm{i}} + B_{1\mathrm{e}}B_{2\mathrm{I}}B_{2\mathrm{i}})
\end{aligned}
$$

$$
\begin{aligned}
c_4 \;=\;& \frac{Z_{\mathrm{i}}^2 n_{\mathrm{i,N}}}{T_{\mathrm{i,N}}}(A_{3\mathrm{i}}B_{1\mathrm{I}}B_{0\mathrm{e}} + A_{3\mathrm{i}}B_{0\mathrm{I}}B_{1\mathrm{e}} + A_{1\mathrm{i}}B_{3\mathrm{I}}B_{0\mathrm{e}} + A_{0\mathrm{i}}B_{3\mathrm{I}}B_{1\mathrm{e}} + A_{1\mathrm{i}}B_{0\mathrm{I}}B_{3\mathrm{e}} + A_{0\mathrm{i}}B_{1\mathrm{I}}B_{3\mathrm{e}} + \\
& A_{2\mathrm{i}}B_{1\mathrm{I}}B_{1\mathrm{e}} + A_{1\mathrm{i}}B_{2\mathrm{I}}B_{1\mathrm{e}} + A_{1\mathrm{i}}B_{1\mathrm{I}}B_{2\mathrm{e}} + A_{2\mathrm{i}}B_{2\mathrm{I}}B_{0\mathrm{e}} + A_{2\mathrm{i}}B_{0\mathrm{I}}B_{2\mathrm{e}} + A_{0\mathrm{i}}B_{2\mathrm{I}}B_{2\mathrm{e}}) + \\
& \frac{Z_{\mathrm{I}}^2 n_{\mathrm{I,N}}}{T_{\mathrm{I,N}}}(A_{3\mathrm{I}}B_{1\mathrm{i}}B_{0\mathrm{e}} + A_{3\mathrm{I}}B_{0\mathrm{i}}B_{1\mathrm{e}} + A_{1\mathrm{I}}B_{3\mathrm{i}}B_{0\mathrm{e}} + A_{0\mathrm{I}}B_{3\mathrm{i}}B_{1\mathrm{e}} + A_{1\mathrm{I}}B_{0\mathrm{i}}B_{3\mathrm{e}} + A_{0\mathrm{I}}B_{1\mathrm{i}}B_{3\mathrm{e}} + \\
& A_{2\mathrm{I}}B_{1\mathrm{i}}B_{1\mathrm{e}} + A_{1\mathrm{I}}B_{2\mathrm{i}}B_{1\mathrm{e}} + A_{1\mathrm{I}}B_{1\mathrm{i}}B_{2\mathrm{e}} + A_{2\mathrm{I}}B_{2\mathrm{i}}B_{0\mathrm{e}} + A_{2\mathrm{I}}B_{0\mathrm{i}}B_{2\mathrm{e}} + A_{0\mathrm{I}}B_{2\mathrm{i}}B_{2\mathrm{e}}) + \\
& \frac{Z_{\mathrm{e}}^2 n_{\mathrm{e,N}} f_{\mathrm{t}}}{T_{\mathrm{e,N}}}(A_{3\mathrm{e}}B_{1\mathrm{I}}B_{0\mathrm{i}} + A_{3\mathrm{e}}B_{0\mathrm{I}}B_{1\mathrm{i}} + A_{1\mathrm{e}}B_{3\mathrm{I}}B_{0\mathrm{i}} + A_{0\mathrm{e}}B_{3\mathrm{I}}B_{1\mathrm{i}} + A_{1\mathrm{e}}B_{0\mathrm{I}}B_{3\mathrm{i}} + A_{0\mathrm{e}}B_{1\mathrm{I}}B_{3\mathrm{i}} + \\
& A_{2\mathrm{e}}B_{1\mathrm{I}}B_{1\mathrm{i}} + A_{1\mathrm{e}}B_{2\mathrm{I}}B_{1\mathrm{i}} + A_{1\mathrm{e}}B_{1\mathrm{I}}B_{2\mathrm{i}} + A_{2\mathrm{e}}B_{2\mathrm{I}}B_{0\mathrm{i}} + A_{2\mathrm{e}}B_{0\mathrm{I}}B_{2\mathrm{i}} + A_{0\mathrm{e}}B_{2\mathrm{I}}B_{2\mathrm{i}}) + \\
& \frac{Z_{\mathrm{e}}^2 n_{\mathrm{e,N}}(1-f_{\mathrm{t}})}{T_{\mathrm{e,N}}}(B_{3\mathrm{e}}B_{1\mathrm{I}}B_{0\mathrm{i}} + B_{3\mathrm{e}}B_{0\mathrm{I}}B_{1\mathrm{i}} + B_{1\mathrm{e}}B_{3\mathrm{I}}B_{0\mathrm{i}} + B_{0\mathrm{e}}B_{3\mathrm{I}}B_{1\mathrm{i}} + B_{1\mathrm{e}}B_{0\mathrm{I}}B_{3\mathrm{i}} + B_{0\mathrm{e}}B_{1\mathrm{I}}B_{3\mathrm{i}} + \\
& B_{2\mathrm{e}}B_{1\mathrm{I}}B_{1\mathrm{i}} + B_{1\mathrm{e}}B_{2\mathrm{I}}B_{1\mathrm{i}} + B_{1\mathrm{e}}B_{1\mathrm{I}}B_{2\mathrm{i}} + B_{2\mathrm{e}}B_{2\mathrm{I}}B_{0\mathrm{i}} + B_{2\mathrm{e}}B_{0\mathrm{I}}B_{2\mathrm{i}} + B_{0\mathrm{e}}B_{2\mathrm{I}}B_{2\mathrm{i}})
\end{aligned}
$$

$$
\begin{aligned}
c_3 \;=\;& \frac{Z_{\mathrm{i}}^2 n_{\mathrm{i,N}}}{T_{\mathrm{i,N}}}(A_{3\mathrm{i}}B_{0\mathrm{I}}B_{0\mathrm{e}} + A_{0\mathrm{i}}B_{3\mathrm{I}}B_{0\mathrm{e}} + A_{0\mathrm{i}}B_{0\mathrm{I}}B_{3\mathrm{e}} + A_{2\mathrm{i}}B_{1\mathrm{I}}B_{0\mathrm{e}} + A_{1\mathrm{i}}B_{2\mathrm{I}}B_{0\mathrm{e}} + \\
& A_{2\mathrm{i}}B_{0\mathrm{I}}B_{1\mathrm{e}} + A_{1\mathrm{i}}B_{0\mathrm{I}}B_{2\mathrm{e}} + A_{0\mathrm{i}}B_{2\mathrm{I}}B_{1\mathrm{e}} + A_{0\mathrm{i}}B_{1\mathrm{I}}B_{2\mathrm{e}} + A_{1\mathrm{i}}B_{1\mathrm{I}}B_{1\mathrm{e}}) + \\
& \frac{Z_{\mathrm{I}}^2 n_{\mathrm{I,N}}}{T_{\mathrm{I,N}}}(A_{3\mathrm{I}}B_{0\mathrm{i}}B_{0\mathrm{e}} + A_{0\mathrm{I}}B_{3\mathrm{i}}B_{0\mathrm{e}} + A_{0\mathrm{I}}B_{0\mathrm{i}}B_{3\mathrm{e}} + A_{2\mathrm{I}}B_{1\mathrm{i}}B_{0\mathrm{e}} + A_{1\mathrm{I}}B_{2\mathrm{i}}B_{0\mathrm{e}} + \\
& A_{2\mathrm{I}}B_{0\mathrm{i}}B_{1\mathrm{e}} + A_{1\mathrm{I}}B_{0\mathrm{i}}B_{2\mathrm{e}} + A_{0\mathrm{I}}B_{2\mathrm{i}}B_{1\mathrm{e}} + A_{0\mathrm{I}}B_{1\mathrm{i}}B_{2\mathrm{e}} + A_{1\mathrm{I}}B_{1\mathrm{i}}B_{1\mathrm{e}}) + \\
& \frac{Z_{\mathrm{e}}^2 n_{\mathrm{e,N}} f_{\mathrm{t}}}{T_{\mathrm{e,N}}}(A_{3\mathrm{e}}B_{0\mathrm{I}}B_{0\mathrm{i}} + A_{0\mathrm{e}}B_{3\mathrm{I}}B_{0\mathrm{i}} + A_{0\mathrm{e}}B_{0\mathrm{I}}B_{3\mathrm{i}} + A_{2\mathrm{e}}B_{1\mathrm{I}}B_{0\mathrm{i}} + A_{1\mathrm{e}}B_{2\mathrm{I}}B_{0\mathrm{i}} + \\
& A_{2\mathrm{e}}B_{0\mathrm{I}}B_{1\mathrm{i}} + A_{1\mathrm{e}}B_{0\mathrm{I}}B_{2\mathrm{i}} + A_{0\mathrm{e}}B_{2\mathrm{I}}B_{1\mathrm{i}} + A_{0\mathrm{e}}B_{1\mathrm{I}}B_{2\mathrm{i}} + A_{1\mathrm{e}}B_{1\mathrm{I}}B_{1\mathrm{i}}) + \\
& \frac{Z_{\mathrm{e}}^2 n_{\mathrm{e,N}}(1-f_{\mathrm{t}})}{T_{\mathrm{e,N}}}(B_{3\mathrm{e}}B_{0\mathrm{I}}B_{0\mathrm{i}} + B_{0\mathrm{e}}B_{3\mathrm{I}}B_{0\mathrm{i}} + B_{0\mathrm{e}}B_{0\mathrm{I}}B_{3\mathrm{i}} + B_{2\mathrm{e}}B_{1\mathrm{I}}B_{0\mathrm{i}} + B_{1\mathrm{e}}B_{2\mathrm{I}}B_{0\mathrm{i}} + \\
& B_{2\mathrm{e}}B_{0\mathrm{I}}B_{1\mathrm{i}} + B_{1\mathrm{e}}B_{0\mathrm{I}}B_{2\mathrm{i}} + B_{0\mathrm{e}}B_{2\mathrm{I}}B_{1\mathrm{i}} + B_{0\mathrm{e}}B_{1\mathrm{I}}B_{2\mathrm{i}} + B_{1\mathrm{e}}B_{1\mathrm{I}}B_{1\mathrm{i}})
\end{aligned}
$$

$$
\begin{aligned}
c_2 \;=\;& \frac{Z_{\mathrm{i}}^2 n_{\mathrm{i,N}}}{T_{\mathrm{i,N}}}(A_{2\mathrm{i}}B_{0\mathrm{I}}B_{0\mathrm{e}} + A_{0\mathrm{i}}B_{2\mathrm{I}}B_{0\mathrm{e}} + A_{0\mathrm{i}}B_{0\mathrm{I}}B_{2\mathrm{e}} + A_{1\mathrm{i}}B_{1\mathrm{I}}B_{0\mathrm{e}} + A_{1\mathrm{i}}B_{0\mathrm{I}}B_{1\mathrm{e}} + A_{0\mathrm{i}}B_{1\mathrm{I}}B_{1\mathrm{e}}) + \\
& \frac{Z_{\mathrm{I}}^2 n_{\mathrm{I,N}}}{T_{\mathrm{I,N}}}(A_{2\mathrm{I}}B_{0\mathrm{i}}B_{0\mathrm{e}} + A_{0\mathrm{I}}B_{2\mathrm{i}}B_{0\mathrm{e}} + A_{0\mathrm{I}}B_{0\mathrm{i}}B_{2\mathrm{e}} + A_{1\mathrm{I}}B_{1\mathrm{i}}B_{0\mathrm{e}} + A_{1\mathrm{I}}B_{0\mathrm{i}}B_{1\mathrm{e}} + A_{0\mathrm{I}}B_{1\mathrm{i}}B_{1\mathrm{e}}) + \\
& \frac{Z_{\mathrm{e}}^2 n_{\mathrm{e,N}} f_{\mathrm{t}}}{T_{\mathrm{e,N}}}(A_{2\mathrm{e}}B_{0\mathrm{I}}B_{0\mathrm{i}} + A_{0\mathrm{e}}B_{2\mathrm{I}}B_{0\mathrm{i}} + A_{0\mathrm{e}}B_{0\mathrm{I}}B_{2\mathrm{i}} + A_{1\mathrm{e}}B_{1\mathrm{I}}B_{0\mathrm{i}} + A_{1\mathrm{e}}B_{0\mathrm{I}}B_{1\mathrm{i}} + A_{0\mathrm{e}}B_{1\mathrm{I}}B_{1\mathrm{i}}) + \\
& \frac{Z_{\mathrm{e}}^2 n_{\mathrm{e,N}}(1-f_{\mathrm{t}})}{T_{\mathrm{e,N}}}(B_{2\mathrm{e}}B_{0\mathrm{I}}B_{0\mathrm{i}} + B_{0\mathrm{e}}B_{2\mathrm{I}}B_{0\mathrm{i}} + B_{0\mathrm{e}}B_{0\mathrm{I}}B_{2\mathrm{i}} + B_{1\mathrm{e}}B_{1\mathrm{I}}B_{0\mathrm{i}} + B_{1\mathrm{e}}B_{0\mathrm{I}}B_{1\mathrm{i}} + B_{0\mathrm{e}}B_{1\mathrm{I}}B_{1\mathrm{i}})
\end{aligned}
$$

$$
\begin{aligned}
c_1 \quad = \quad & \frac{Z_{\mathrm{i}}^2 n_{\mathrm{i,N}}}{T_{\mathrm{i,N}}}(A_{1\mathrm{i}}B_{0\mathrm{I}}B_{0\mathrm{e}} + A_{0\mathrm{i}}B_{1\mathrm{I}}B_{0\mathrm{e}} + A_{0\mathrm{i}}B_{0\mathrm{I}}B_{1\mathrm{e}}) + \\
& \frac{Z_{\mathrm{I}}^2 n_{\mathrm{I,N}}}{T_{\mathrm{I,N}}}(A_{1\mathrm{I}}B_{0\mathrm{i}}B_{0\mathrm{e}} + A_{0\mathrm{I}}B_{1\mathrm{i}}B_{0\mathrm{e}} + A_{0\mathrm{I}}B_{0\mathrm{i}}B_{1\mathrm{e}}) + \\
& \frac{Z_{\mathrm{e}}^2 n_{\mathrm{e,N}} f_{\mathrm{t}}}{T_{\mathrm{e,N}}}(A_{1\mathrm{e}}B_{0\mathrm{I}}B_{0\mathrm{i}} + A_{0\mathrm{e}}B_{1\mathrm{I}}B_{0\mathrm{i}} + A_{0\mathrm{e}}B_{0\mathrm{I}}B_{1\mathrm{i}}) + \\
& \frac{Z_{\mathrm{e}}^2 n_{\mathrm{e,N}} (1-f_{\mathrm{t}})}{T_{\mathrm{e,N}}}(B_{1\mathrm{e}}B_{0\mathrm{I}}B_{0\mathrm{i}} + B_{0\mathrm{e}}B_{1\mathrm{I}}B_{0\mathrm{i}} + B_{0\mathrm{e}}B_{0\mathrm{I}}B_{1\mathrm{i}})
\end{aligned}
$$

$$
\begin{aligned}
c_0 \quad = \quad & \frac{Z_{\mathrm{i}}^2 n_{\mathrm{i,N}}}{T_{\mathrm{i,N}}}(A_{0\mathrm{i}}B_{0\mathrm{I}}B_{0\mathrm{e}}) + \frac{Z_{\mathrm{I}}^2 n_{\mathrm{I,N}}}{T_{\mathrm{I,N}}}(A_{0\mathrm{I}}B_{0\mathrm{i}}B_{0\mathrm{e}}) + \\
& \frac{Z_{\mathrm{e}}^2 n_{\mathrm{e,N}} f_{\mathrm{t}}}{T_{\mathrm{e,N}}}(A_{0\mathrm{e}}B_{0\mathrm{I}}B_{0\mathrm{i}}) + \frac{Z_{\mathrm{e}}^2 n_{\mathrm{e,N}} (1-f_{\mathrm{t}})}{T_{\mathrm{e,N}}}(B_{0\mathrm{e}}B_{0\mathrm{I}}B_{0\mathrm{i}})
\end{aligned}
$$

B.2 4th Degree Coefficients

$$
\begin{aligned}
c_4 &= \frac{Z_\mathrm{e}^2}{T_{\mathrm{e},0}} \\
c_3 &= \frac{Z_\mathrm{i}^2}{T_{\mathrm{i},0}}\frac{n_{\mathrm{i},0}}{n_{\mathrm{e},0}}\left\{-F_\mathrm{i}\left(2-\frac{R_\mathrm{ref}}{L_{\mathrm{n,i}}}\right)\right\}+\frac{Z_\mathrm{I}^2}{T_{\mathrm{I},0}}\frac{n_{\mathrm{I},0}}{n_{\mathrm{e},0}}\left\{-F_\mathrm{I}\left(2-\frac{R_\mathrm{ref}}{L_{\mathrm{n,I}}}\right)\right\}+\frac{Z_\mathrm{e}^2}{T_\mathrm{e}}\left\{-\frac{20}{3}\left(F_\mathrm{i}+F_\mathrm{I}\right)\right\} \\
c_2 &= \frac{Z_\mathrm{i}^2}{T_{\mathrm{i},0}}\frac{n_{\mathrm{i},0}}{n_{\mathrm{e},0}}\left\{2F_\mathrm{i}^2\left[\frac{10}{3}+\frac{R_\mathrm{ref}}{L_{\mathrm{n,i}}}\left(\eta_\mathrm{i}-\frac{7}{3}\right)\right]+\frac{20}{3}F_\mathrm{i}F_\mathrm{I}\left(2-\frac{R_\mathrm{ref}}{L_{\mathrm{n,i}}}\right)\right\}+ \\
&\quad \frac{Z_\mathrm{I}^2}{T_{\mathrm{I},0}}\frac{n_{\mathrm{I},0}}{n_{\mathrm{e},0}}\left\{2F_\mathrm{I}^2\left[\frac{10}{3}+\frac{R_\mathrm{ref}}{L_{\mathrm{n,I}}}\left(\eta_\mathrm{I}-\frac{7}{3}\right)\right]+\frac{20}{3}F_\mathrm{i}F_\mathrm{I}\left(2-\frac{R_\mathrm{ref}}{L_{\mathrm{n,I}}}\right)\right\}+ \\
&\quad \frac{Z_\mathrm{e}^2}{T_\mathrm{e}}\frac{20}{3}\left\{F_\mathrm{i}^2+F_\mathrm{I}^2+\frac{20}{3}F_\mathrm{i}F_\mathrm{I}\right\} \\
c_1 &= \frac{Z_\mathrm{i}^2}{T_{\mathrm{i},0}}\frac{n_{\mathrm{i},0}}{n_{\mathrm{e},0}}\left\{-\frac{20}{3}F_\mathrm{i}F_\mathrm{I}^2\left(2-\frac{R_\mathrm{ref}}{L_{\mathrm{n,i}}}\right)-\frac{40}{3}F_\mathrm{i}^2F_\mathrm{I}\left[\frac{10}{3}+\frac{R_\mathrm{ref}}{L_{\mathrm{n,i}}}\left(\eta_\mathrm{i}-\frac{7}{3}\right)\right]\right\}+ \\
&\quad \frac{Z_\mathrm{I}^2}{T_{\mathrm{I},0}}\frac{n_{\mathrm{I},0}}{n_{\mathrm{e},0}}\left\{-\frac{20}{3}F_\mathrm{I}F_\mathrm{i}^2\left(2-\frac{R_\mathrm{ref}}{L_{\mathrm{n,I}}}\right)-\frac{40}{3}F_\mathrm{I}^2F_\mathrm{i}\left[\frac{10}{3}+\frac{R_\mathrm{ref}}{L_{\mathrm{n,I}}}\left(\eta_\mathrm{I}-\frac{7}{3}\right)\right]\right\}+ \\
&\quad \frac{Z_\mathrm{e}^2}{T_\mathrm{e}}\left\{-\frac{400}{9}\left(F_\mathrm{i}F_\mathrm{I}^2+F_\mathrm{I}F_\mathrm{i}^2\right)\right\} \\
c_0 &= \frac{Z_\mathrm{i}^2}{T_{\mathrm{i},0}}\frac{n_{\mathrm{i},0}}{n_{\mathrm{e},0}}\left\{\frac{40}{3}F_\mathrm{i}^2F_\mathrm{I}^2\left[\frac{10}{3}+\frac{R_\mathrm{ref}}{L_{\mathrm{n,i}}}\left(\eta_\mathrm{i}-\frac{7}{3}\right)\right]\right\}+ \\
&\quad \frac{Z_\mathrm{I}^2}{T_{\mathrm{I},0}}\frac{n_{\mathrm{I},0}}{n_{\mathrm{e},0}}\left\{\frac{40}{3}F_\mathrm{i}^2F_\mathrm{I}^2\left[\frac{10}{3}+\frac{R_\mathrm{ref}}{L_{\mathrm{n,I}}}\left(\eta_\mathrm{I}-\frac{7}{3}\right)\right]\right\}+ \\
&\quad \frac{Z_\mathrm{e}^2}{T_\mathrm{e}}\frac{400}{9}F_\mathrm{i}^2F_\mathrm{I}^2
\end{aligned}
$$

Bibliography

[1] C.M.H. Smith, A Textbook of Nuclear Physics, p 223 (Pergamon, Oxford, 1965)

[2] J. Wesson, Tokamaks, p4 (Clarendon Press, Oxford, 1987)

[3] J. D. Lawson, Proceedings of the Physical Society B, **70**, 6 (1957)

[4] H.P. Furth, Nucl. Fusion **15**, 487 (1975)

[5] P. Helander, D.J. Sigmar, Collisional Transport in Magnetized Plasmas (Cambridge University Press 2002)

[6] B. Lehnert, Plasma Physics **9**, 301 (1967)

[7] W. Horton, Rev. Mod. Phys. **71** 735 (1999)

[8] E.J. Doyle et al., Nucl. Fusion **47**, S18-S127 (2007)

[9] B. Coppi, M.N. Rosenbluth, R.Z. Sagdeev, Phys. Fluids **10**, 582 (1967)

[10] S.C. Cowley, R.M. Kulsrud, R. Sudan, Phys. Fluids B **3**, 2767 (1991)

[11] R.D. Hazeltine, F.L. Waelbroeck, The Framework of Plasma Phyiscs (Perseus Book, 1998)

[12] A.J. Brizard, T.S. Hahm, Rev. Mod. Phys. **79**, 421 (2007)

[13] S.I. Braginskii, Chapter 3, Reviews of Plasma Physics, Vol. 1 (Consultants Bureau, New York, 1965)

[14] R.D. Hazeltine, J.D. Meiss, Plasma Confinement (Courier Dover Publications, 2003)

[15] J. Weiland et al., Nucl. Fusion **29**, 10 (1989)

[16] C. Gormezano et al., Fusion Sci. Technol. **45**, no. 3 (2004)

[17] M.L. Apicella et al., J. Nucl. Materials **363-365**, 1346 (2007)

[18] A. Tuccillo et al., Nucl. Fusion **49**, 104013 (2009)

[19] G. Mazzitelli et al. (including G. Szepesi), Nucl. Fusion **51**, 073006 (2011)

[20] V. Evitkin et al., Fusion Eng. Des. **56-57**, 363 (2001)

[21] R. Majeski et al., Phys. Rev. Letters **97**, 075002 (2006)

[22] D. K. Mansfield et al., Phys. Plasmas **3**, 1892 (1996)

[23] D. A. Gates et al., Nucl. Fusion **49**, 104016 (2009)

[24] R. Maingi et al., Phys. Rev. Letters **103**, 075001 (2009)

[25] M. Murakami et al., Nucl. Fusion **41**, 317 (2001)

[26] G.R. McKee et al., Phys. Plasmas **7**, 1870 (2000)

[27] R.R. Weynants, Nucl. Fusion **39**, 1637 (1999)

[28] C. Estrada-Mila et al., Phys. Plasmas **12**, 022305 (2005)

[29] A. Darke et al., MAST: a mega ampère spherical tokamak, Proc. 18th Symposium on Fusion Technology (1994)

[30] T. Dannert: Gyrokinetische Simulation von Plasmaturbulenz mit gefangenen Teilchen und Elektromagnetischen Effekten (Doctoral Thesis, Technische Universität München, 2005)

[31] A.G. Peeters et al. (including G. Szepesi), Comput. Phys. Commun. **180**, 2650 (2009)

[32] P.M. Bellan, Fundamentals of Plasma Physics (Cambridge University Press, 2006)

[33] R.G. Littlejohn, Phys. Fluids **24**, 1730 (1981)

[34] M. Fecko Differential Geometry and Lie Groups for Physicists (Cambridge University Press, 2006)

[35] R.G. Littlejohn, J. Math. Phys. **23**, 742 (1982)

[36] A.G. Peeters et al., Phys. Plasmas **16**, 042310 (2009)

[37] B. Scott: Introduction to Gyrokinetic Field Theory (Lecture notes, GOTiT course at IPP Garching, 2008 November)

[38] F.J. Casson et al. (including G. Szepesi), Phys. Plasmas **17**, 102305 (2010)

[39] M. Abramowitz, I.A. Stegun, eds., Handbook of Mathematical Functions with Formulas, Graphs, and Mathematical Tables, (New York: Dover Publications, 1972)

[40] F. Jenko, W. Dorland, Plasma Phys. Control. Fusion **43**, A141 (2001)

[41] D J Applegate et al., Plasma Phys. Control. Fusion **49**, 1113 (2007)

[42] M. Kotschenreuther, G. Rewoldt, and M. W. Tang, Comput. Phys. Commun. **88**, 128 (1995)

[43] C. Karney, Comp. Phys. Rep. **4** 183, (1986)

[44] M. Romanelli, et al. (including G. Szepesi), Nucl. Fusion **51**, 103008 (2011)

[45] G. Szepesi et al., Nucl. Fusion **53**, 033007 (2013)

[46] X. Lapillone et al., Phys. Plasmas **16**, 032308 (2009)

[47] M. Romanelli et al., Phys. Plasmas **14**, 082305 (2007)

[48] M. Reshko, C.M. Roach, Plasma Phys. Control. Fusion **50**, 115002 (2008)

[49] B. Coppi et al., Phys. Fluids **19**, 1144 (1976)

[50] M. Fröjdh et al., Nucl. Fusion **31**, 419 (1992)

[51] J.E. Kinsey et al., Phys. Plasmas **13**, 022305 (2006)

[52] S. Moradi et al., Phys. Plasmas **17**, 012101 (2010)

[53] H Nordman et al., Phys. Plasmas **14**, 052303 (2007)

[54] B. Coppi et al., Phys. Fluids **2**, 2322 (1990)

[55] E. Fable et al., Plasma Phys. Control. Fusion **52**, 015007 (2010)

[56] G. Cenacchi, A. Taroni, Rapporto ENEA RT/TIB 88, 5 (1988)

[57] A.G. Peeters, Phys. Plasmas **7**, 268 (2000)

[58] P.C. Stangeby, The Plasma Boundary of Magnetic Fusion Devices (Taylor & Francis, 2000)

[59] K.L. Bell et al., J. Phys. Chem. Ref. Data **12**, 891 (1983)

[60] F. Militello, W. Fundamenski, Plasma Phys. Control. Fusion **53**, 095002 (2011)

[61] H. Lütjens et al., Comput. Phys. Commun. **97**, 219 (1996)

[62] F. Militello, W. Fundamenski, Plasma Phys. Control. Fusion **53**, 095002 (2011)

[63] C. Bourdelle et al., Phys. Plasmas **14**, 112501 (2007)

[64] F. Jenko et al., Phys. Plasmas **7**, 1904 (2000)

[65] C. Angioni et al., Plasma Phys. Control. Fusion **51**, 124017 (2009)

[66] C. Bourdelle et al., Plasma Phys. Control. Fusion **47**, A317 (2005)

[67] X. Garbet et al., Phys. Rev. Letters **91**, 035001-1 (2003)

[68] H Nordman et al., Plasma Phys. Control. Fusion **49**, 985 (2007)

[69] C. Angioni et al., Phys. Plasmas **12**, 112310 (2005)

[70] C. Angioni et al., Phys. Rev. Letters **90**, 205003 (2003)

[71] C. Angioni, A.G. Peeters, Phys. Rev. Letters **96**, 095003 (2006)

[72] A. Skyman et al., Phys. Plasmas **19**, 032313 (2012)

[73] M. Fröjdh, A. Jarmén, Nucl. Fusion **35**, 575 (1995)

[74] C. Angioni et al., Plasma Phys. Control. Fusion **49**, 2027 (2007)

[75] Y. Camenen et al., Phys. Rev. Lett. **102**, 125001 (2009)

[76] C. Angioni et al., Nucl. Fusion **51**, 023006 (2011)

[77] T. Hein, C. Angioni, Phys. Plasmas **17**, 012307 (2010)

[78] J. Nilsson, J. Weiland, Nucl. Fusion **34**, 803 (1994)

[79] G. Tardini: Validation of Theory Based Transport Models in Tokamak Plasmas (Doctoral Thesis, Technische Universtät München, 2003)

[80] R.D. Hazeltine, J.D. Meiss, Phys. Rep. **121**, No. 1 (1985)

[81] Z. Chang, J.D. Callen, Phys. Fluids B **4**, 1766 (1992)

[82] A. Hirose, Phys. Fluids B **5**, 230 (1993)

[83] D. Wágner at al., Plasma Phys. Control. Fusion **54**, 085018 (2012)

[84] A. Jarmén et al., Nucl. Fusion **27**, 941 (1987)

[85] M. Romanelli et al., Plasma Phys. Control. Fusion **49**, 935 (2007)

[86] I.S. Gradshteyn, I.M. Ryzhik: Table of Integrals, Series, and Products (Academic Press, 1965)

[87] E.T. Whittaker, G.N. Watson, A Course of Modern Analysis (Cambridge University Press, 4th edition, 1927)